Universidad
Carlos III de Madrid

High Temperature Mechanical Behavior of Al/SiC Nanoscale Multilayers

Author:

Saeid Lotfian

Supervisors:

Dr. Jon M. Molina-Aldareguía

Dr. Javier Llorca

A Dissertation submitted for the degree of Doctor of Philosophy at the
Department of Materials Science and Engineering
and Chemical Engineering

Universidad Carlos III de Madrid

Leganés, June 2014

TESIS DOCTORAL

High Temperature Mechanical Behavior of Al/SiC Nanoscale Multilayers

Autor: **Saeid Lotfian**

Director: **Dr. Jon M. Molina-Aldareguía**

Dr. Javier Llorca

Firma del Tribunal Calificador:

Firma

Presidente:	Dr. José Manuel Torralba Castelló
Vocal:	Dr. Pedro Alberto Poza Gómez
Secretario:	Dr. Ignacio Jiménez Guerrero

Calificación:

Leganés 30 de Junio de 2014

"Science is based on experiment; on a willingness to challenge old dogma; on an openness to see the universe as it really is. Accordingly, science sometimes requires courage - at the very least the courage to question the conventional wisdom"

Carl Sagan

Abstract

Nanoscale Al/SiC composite laminates are metal-ceramic multilayers with unique mechanical properties at ambient temperature, such as high strength, high toughness, and damage tolerance, due to the nm scale thickness of their layers. Nevertheless, nothing is known about their high temperature mechanical properties and this is a key issue both from the fundamental viewpoint as well as from the in-service behavior. This lack of information is mainly due to the difficulties associated with the characterization of the mechanical behavior of thin-films at high temperature, a rather unexplored area.

High temperature instrumented nanoindentation and micropillar compression were carried out in this thesis to study the mechanical properties of Al/SiC nanolaminates as a function of layer thickness from room temperature up to 300ºC. Mechanical tests were complemented with detailed transmission electron microscopy (TEM) analysis of the deformed structures to elucidate the effect of temperature on the deformation mechanisms at the nm scale. In addition, finite element simulations of the multilayer deformation were used to clarify the influence of the Al flow stress and of the interface properties (strength, friction coefficient) on the overall stress-strain response of Al/SiC multilayers.

The combination of nanoindentation, micropillar compression tests, TEM observations and numerical simulations provided a better understanding of the key parameters influencing the high temperature mechanical behavior of Al/SiC nanoscale multilayers. It was found that the mechanical behavior at ambient temperature was controlled by the high strength of the Al nanograins and the constraint induced by the stiff SiC nanolayers on the Al plastic flow. Changes in the Al-SiC interface behavior, in the form of interface sliding, limited the constraint on plastic flow at 100ºC. This phenomenon, together with the softening of the Al nanolayers, resulted in a marked reduction in the flow stress and in the strain hardening capacity of the nanoscale multilayers. The role of the Al-SiC interfaces in plastic flow was also apparent in the creep activation energies, which showed a marked decrease with the reduction in Al layer thicknesses, reaching values

close to the activation energy for grain boundary diffusion in Al for layer thicknesses of 10 nm.

Finally, above 200ºC, chemical reactions between Al and SiC promoted a large degradation in the mechanical properties of the nanoscale multilayers.

Resumen

Los nanolaminados de Al/SiC son materiales multicapa metal-cerámicos con propiedades mecánicas singulares a temperatura ambiente, combinando alta resistencia, alta tenacidad y tolerancia al daño, debido al espesor nanométrico de las capas. Sin embargo, su comportamiento mecánico a alta temperatura no es conocido y éste es un aspecto clave tanto desde el punto de vista fundamental como para su comportamiento en servicio. Ello es principalmente debido a la dificultad inherente a la caracterización mecánica a altas temperaturas de películas delgadas, un área que está en desarrollo en la actualidad.

En este trabajo, se han empleado técnicas de nanoindentación instrumentada y compresión de micropilares a alta temperatura para estudiar las propiedades mecánicas de nanolaminados de Al/SiC, en función del espesor de las capas, entre temperatura ambiente y 300ºC. Los ensayos mecánicos se complementaron con una caracterización detallada de las microestructuras deformadas mediante microscopía electrónica de transmisión (TEM), con el objetivo de determinar el efecto de la temperatura en los mecanismos de deformación. Por último, se han empleado simulaciones por elementos finitos para entender mejor la influencia de la tensión de fluencia del Al y de las propiedades de las intercaras (resistencia, coeficiente de fricción) en el comportamiento global tensión-deformación de los nanolaminados de Al/SiC.

La resultados obtenidos en los estudios de nanoindentación, compresión de micropilares, caracterización por TEM y simulaciones numéricas permitieron adquirir una mejor compresión de los parámetros que determinan el comportamiento mecánico a alta temperatura de nanolaminados de Al/SiC. Se concluyó que el comportamiento mecánico a temperatura ambiente está controlado por la alta resistencia plástica de las nanocapas de Al y la restricción a la deformación impuesta por las capas rígidas de SiC. A 100ºC, se observó un cambio en el comportamiento de la intercaras Al/SiC, dando lugar a la aparición de deslizamiento en las intercaras, limitando así la restricción

a la deformación plástica de las capas de Al. Este cambio, junto al ablandamiento de las nanocapas de Al, dio lugar a una abrupta reducción de la tensión de fluencia y de la tasa de endurecimiento por deformación de los nanolaminados. El efecto de las intercaras Al-SiC en la deformación plástica también fue notable en las energías de activación a fluencia lenta, que decrecieron con la reducción del espesor de las capas de Al, hasta alcanzar valores cercanos a la energía de activación para difusión en las fronteras de grano del Al, para espesores de capa de 10 nm.

Por último, por encima de 200ºC, reacciones químicas entre las capas de Al y SiC dieron lugar a una reducción importante de las propiedades mecánicas de los nanolaminados.

Preface

This dissertation is submitted for the degree of Doctor of Philosophy in the Universidad Carlos III de Madrid. The research described in this thesis was carried out at IMDEA Materials Institute (Madrid, Spain) during the period September 2010 to June 2014 under the supervision of Dr. Jon M. Molina-Aldareguía, senior researcher at IMDEA Materials Institute and Adjunct professor in the Carlos III University, and Prof. Javier Llorca, director of IMDEA Materials Institute and professor in the Department of Materials Science, Polytechnic University of Madrid.

The results obtained during the course of this thesis have been published in peer-reviewed international journals in Materials Science, including Acta Materialia, Philosophical Magazine Letters, Journal of Electronic Materials, International Journal of Precision Engineering and Manufacturing, and Thin Solid Films. Moreover, this work has been well received at international conferences and workshops on nanolaminates and nanomechanics.

To the best of my knowledge, the work described in this dissertation is original, except where due reference has been made to the work of others, and nothing is included which is the outcome of work done in collaboration, unless otherwise stated. No part of this dissertation, or any similar to it, has been, or is currently being, submitted for any degree or other qualification at any other university.

Saeid Lotfian

Madrid

June 2014

Acknowledgements

I gratefully acknowledge the provision of financial support for the work described in this dissertation by IMDEA Materials Institute. This investigation was supported by the National Science Foundation of the US and the Spanish Ministry of Economy and Competitiveness under the Materials World Network Program through the project “High temperature mechanical behavior of metal/ceramic nanolaminate composites”. Additional support from Altare S.L. through the project “High Temperature Nanoindentation” is also gratefully acknowledged.

I would also like to thank a number of people for their help and support during this PhD. Firstly, I wish to thank my supervisors, Dr Jon Mikel Molina-Aldareguía and Professor Javier Llorca, for their expert guidance, patience, and assistance in all aspects of this research. Their enthusiasm for doing and communicating research of quality has been inspirational. Their scientific guidance and consideration were not limited to my PhD work but also touched other aspects of my life.

I sincerely thank Professor Nikhilesh Chawla, from Arizona State University, for collaborating during this research and sharing the wealth of his expertise with me, which greatly helped to accomplish this investigation. I would also extend grateful thanks to Dr. Amit Misra, scientist and director of CMIME from Los Alamos National Laboratory for his collaboration during this research.

Special thanks to Dr. Miguel Monclus for helping and encouraging me during experiments, and being always available for stimulating discussion on my findings. I acknowledge Dr. Marcos Rodríguez de la Peña for tutoring my learning of finite element modeling and for very useful discussions.

I would like to thank all the members (past and present) of IMDEA Materials Institute for creating a very pleasant working environment. The friendly supportive atmosphere inherent to the whole institute contributed to the final outcome of my studies, not only during the working hours at the institute but also during the free time. To all of them, I am truly grateful.

I greatly acknowledge my friends, Mahmoud and Alireza, for their helpful assistance during this time.

I sincerely thank all my friends those who have helped me throughout my PhD study, and throughout my life.

My deep and humble appreciation goes to my family, in particular my parents, Shahnaz and Ali and my brothers, Sajjad and Masoud for their unconditional love and encouragement. I acknowledge my parents-in-law, sisters-in-law and brothers-in-law for their support. And finally, I owe my deepest gratitude to Mahshid, that her companionship, understanding, solidarity, and patience were the driving forces that kept me going in difficult moments. This thesis is dedicated to her with deep love.

List of Abbreviation and Symbols

AFM	Atomic Force Microscopy
ARB	Accumulative Roll Bonding
CVD	Chemical Vapor Deposition
EDS	Energy Dispersive x-ray Spectroscopy
FIB	Focused Ion Beam
GB	Grain Boundary
HREM	High Resolution Electron Microscopy
PVD	Physical Vapor Deposition
SEM	Scanning Electron Microscopy
TEM	Transmission Electron Microscopy
fcc	face center cubic
bcc	body center cubic
hcp	hexagonal close packed
a	Radius of the contact area of indentation (nm)
a_c	Contact area (m^2)
a_c^{real}	Real Contact area (m^2)
A	Pre-factor in equation 3-12
$A(h)$	Cross-sectional area of the indenter with the distance from its tip (m^2)
A_c	Contact area (m^2)
A_0	Micropillar initial cross-sectional area (m^2)
A_p	Micropillar cross/sectional area (m^2)
b	Burgers vector (m)
C	Pre-factor in equation 3-15
$C_{Sneddon}$	Sneddon compliance

d	Interface damage parameter
E	Elastic modulus (GPa)
E_a	Apparent activation energy (kJ/mol)
E_{base}	Elastic modulus of the base material (GPa)
E_i	Elastic modulus of indenter (GPa)
E_l	Longitudinal nanolaminate elastic modulus (GPa)
E_r	Reduced indentation elastic modulus (GPa)
E_t	Transverse nanolaminate elastic modulus (GPa)
E_{Al}	Elastic moduli of Al (GPa)
E_{SiC}	Elastic moduli of SiC (GPa)
G	Shear modulus (GPa)
h	Individual layer thickness (nm)
$h(t)$	Instantaneous indenter displacement (nm)
h_0	Initial indentation depth during dwell time at maximum load (nm)
h_c	Contact depth of indentation (nm)
h_f	The final depth of a residual hardness impression (nm)
h_{max}	Maximum depth of penetration of an indenter (nm)
h_s	Displacement of the surface at the perimeter of the indentation (nm)
H	Hardness (GPa)
H_0	Extrapolated hardness (GPa)
k	Boltzmann constant (J/K)
K	Initial stiffness in cohesive law(GPa/m)
L_0	Initial length (m)
L_{crit}	Critical layer thickness (nm)
m	Strain rate sensitivity

n	Stress exponent
P	Indentation load (N)
P_{max}	Maximum indentation load (N)
Q	Activation energy (kJ/mol)
R	Universal gas constant (J $mol^{-1}K^{-1}$)
S	Stiffness of the indentation contact (N/m)
t	Total stress in cohesive law (MPa)
t	Time (sec)
t_0	Necessary time to reach the maximum load (sec)
t_n	Normal stress in cohesive law (MPa)
t_s	Shear stress in cohesive law (MPa)
t^c	Interface critical strength in cohesive law (MPa)
t_n^c	Interface normal strength in cohesive law (MPa)
t_s^c	Interface shear strength in cohesive law (MPa)
T	Temperature (K)
T_m	Melting temperature (K)
u_{pillar}	Plastic deformation in pillar (m)
u_{punch}	Elastic deformation in diamond indenter (m)
u_{sink}	Sneddon's elastic sink-in (m)
u_{TOTAL}	Measured displacement of the flat punch (m)
V	Volume fraction
V^*	Activation volume (b^3)
V_{Al}	Volume fraction of Al
V_{SiC}	Volume fraction of SiC
x	Fitting parameter in equation 3-17

y	Fitting parameter in equation 3-17
z	Fitting parameter in equation 3-17
Γ	Interface fracture toughness (J/m^2)
δ	Displacement jump in cohesive law (m)
δ_n	Normal displacement jump in cohesive law (m)
δ_s	Shear displacement jump in cohesive law (m)
ε	strain
ε	Indenter geometrical constant
$\dot{\varepsilon}$	Strain rate
$\dot{\varepsilon}_{ind}$	Indentation strain rate
Λ	Bilayer thickness or periodicity of the multilayer (nm)
μ	Friction coefficient
ν	Poisson's ratio
ν_{base}	Poisson's ratio of the base material
ν_i	Poisson's ratio of the indenter
σ	Applied stress (MPa)
σ_y	Yield stress (MPa)
$\langle \quad \rangle$	Macaulay brackets

Table of contents

1 Introduction

1.1. Background: nanoscale multilayers

Laminated composites consist of alternating layers of two or more materials in different combinations, namely: metal-metal [1-7], ceramic-ceramic [8-12], and metal-ceramic [13-20]. They present outstanding mechanical properties (strength, toughness, and fatigue resistance) when the layer thicknesses are smaller than 100 nm. In this case, they are also referred to as nanoscale multilayers or nanolaminates. By proper choice of the constituent materials, their layer thickness and their microstructure, multilayers have shown superior performance than their bulk counterparts in many applications where multifunctionality is important, as summarized in table 1-1 [21].

In this context, metal-ceramic nanolaminates offer a good combination of hardness and toughness, leading to excellent wear resistance for protective coatings. In electronic applications, metal (Cu, Al) - ceramic (SiO2, CDO) multilayers have been widely used in advanced packaging technology for more than 30 years [22-24]. In addition, new electronic devices (like MEMS, Micro Electro Mechanical Systems) often combine metal-ceramic layers at the interconnect level. More recently, metal/ceramic multilayers

have also found applications as optically absorbing coatings in solar collectors for thermo-solar energy generation [25]. Finally, the development of cellular phones has pushed the research towards base-metal electrode multilayer ceramic capacitors due to their high capacitance at large frequencies [26-28].

Table 1-1: Applications in which nanolaminates have shown superior performance, including one example of the material combination proposed in each case [21].

Ultra-high strength materials (Cu/Nb) [29]	Magnetic transducers-GMR (Co/Cu) [30]
High performance tribological coatings (Cr/CrN) [31]	EUV, Soft X-ray and X-ray optics spectroscopy (Ni/Mg) [32]
Coatings for gas turbine engines (Thermal Barrier Coatings) [33]	Magneto-optic read/write memory (Pt/Co) [34]
Coatings for medical applications (porous-coated Co/Cr) [35]	High performance visible optics (Indium Tin Oxide/Silica) [36]
High performance capacitors for energy storage (MnO_2/Ni/graphite/paper) [37]	New smart materials for sensors (SnO_2/SiO_2) [38]
Capacitor structures for industrial applications (Graphene/h-BN) [39]	Imaging and microcircuit lithography development (Photoresist/SiO_2/Si) [40]
Integrated circuit interconnects (Au/Cu) [41]	

Even in those cases where metal-ceramic nanolaminates are selected on the basis of their electrical or optical properties, their mechanical reliability is also a concern, particularly at high temperature. This is because nanolaminates will be often subjected to high stresses and temperatures under normal operation conditions, as in the case of electrical interconnects or solar coatings. However, very little is known about the mechanical behavior of metal-ceramic nanoscale multilayers at high temperature, due to the lack of techniques available up to date to explore the mechanical properties of thin-films at high temperature.

1.2. Motivation for the thermomechanical study of nanolaminates

Recent progress in instrumented nanoindentation has opened the possibility to carry out nanoindentation tests at high temperatures. Current knowledge about the effect of temperature on the mechanical properties of nanoscale multilayers is scarce. This information is important from the engineering viewpoint but also from the fundamental perspective as the dominant mechanisms controlling the deformation and fracture of nanoscale multilayers (interface strength, dislocation plasticity) are often thermally activated.

However, quantifying the stress-strain behavior of small volumes from indentation tests is still a challenge. Despite the popularity of indentation tests, they still present some intrinsic shortcomings. The main problem is that indentation involves a complex stress-strain field underneath the indenter that depends on the specific tip geometry. In consequence, extracting the uniaxial stress-strain constitutive relationship, although possible, requires difficult iterative methods. To overcome this problem, alternative nanomechanical testing methods that lead to a more uniform stress state in the tested volume have been developed during the last decade. Among these, micropillar compression has been extensively studied recently [42-45]. This technique uses a nanoindenter with a flat punch to compress a small cylindrical volume to obtain uniaxial stress-strain behavior. The main advantage of this method is that the imposed stress field is uniform. However, it requires the fabrication of micropillars whose dimension in length, in this case, is limited by the coating thickness, usually just a few micrometers. Machining this type of micrometer size pillars requires the use of focused ion beam (FIB) methods. Since microcompression testing is a relatively new technique, there has been very limited use of this technique at high temperatures, and even less in the case of nanoscale multilayers.

1.3. Aim of the study and summary of the work

Based on the above, the main objective of this work has been exploiting the recently developed capabilities in high temperature nanomechanical testing to study the thermomechanical properties of metal-ceramic nanolaminates. The study has focused on Al/SiC multilayers. Al/SiC multilayers constitute an interesting metal-ceramic multilayer model system, but are also technologically relevant, due to their high strength, high toughness and high damage tolerance at room temperature [46, 47]. These nanolaminated composites were fabricated by magnetron sputtering of aluminum (Al) and silicon carbide (SiC) onto Si substrates.

Multilayers with varying individual layer thicknesses, in the range of 10 to 100 nm, were grown. Their deformation behavior was studied by high temperature nanoindentation and micropillar compression from room temperature up to 300ºC. The high temperature behavior, unknown up to date, provided the basis for understanding the controlling deformation and fracture mechanisms at different temperatures, by analyzing the deformation mechanisms, using focused ion beam (FIB) and transmission electron

microscopy (TEM). Based on the experimental observations, numerical simulations provided further evidence of the key microstructural parameters determining the mechanical behavior of these nanolaminates.

1.4. Outline of the thesis

The thesis is divided into six core chapters dealing with various aspects related to this investigation. Chapter 2 summarizes the current knowledge on the mechanical properties of nanolaminate composites. Chapter 3 briefly introduces the most important nanomechanical testing techniques used in this work, together with the experimental parameters used for the processing of the Al/SiC nanolaminates and their microstructural characterization techniques, namely, atomic force microscopy (AFM), scanning electron microscopy (SEM), energy dispersive x-ray spectroscopy (EDS), transmission electron microscopy (TEM), and focused ion beam (FIB). Since nanomechanical testing at high temperature is not currently a well-established technique, large efforts were devoted in this work to establish the optimum testing conditions. The challenges and best practices developed as a result of this work for carrying out nanomechanical testing at high temperature are thus summarized in Chapter 4. The main results obtained using these techniques in Al/SiC nanolaminates are summarized in the following chapters. Chapter 5 is focused on the effects of layer thickness and temperature on strength and creep of Al/SiC nanolaminates by using high temperature nanoindentation. In chapter 6, the effect of temperature on the controlling deformation mechanisms is studied in more detail by micropillar compression of selected nanolaminates. Based on the experimental results, a finite element model was used to simulate the mechanical behavior of Al/SiC nanolaminates, which is presented in Chapter 7. Finally, the conclusions extracted from this work and some recommendations for future studies are summarized in chapter 8.

2 State of the art

2.1. Nanolaminate composites

Nanolaminates can be produced with layer thicknesses varying from the sub-nanometer scale to hundreds of nanometers. Their mechanical strength and the operating deformation mechanisms have been found to depend strongly on layer thickness. Koehler [48] was the first to propose that a multilayered structure was expected to display ultra-high strength and high resistance to brittle fracture. Based on his pioneering ideas, there have been many theoretical and experimental studies based on the use of multilayered structures to improve strength and ductility, namely:

- The use of one interlayer or several interlayers to enhance the adhesion of coatings by reducing the mismatch in mechanical, chemical, or thermal properties between coatings and substrate.
- The use of multilayered structures to control the residual strain and therefore the tensile stress within coatings, most commonly to enhance the effective adhesion and strength.

- Alternating layers that can improve the fracture toughness either by introducing interfaces that stop cracks or providing a tough medium through which propagation of cracks is prohibited.
- Alternating hard and brittle layers along with ductile and tough layers to avoid the significant stress concentrations that may occur with thick hard coatings.
- Nanoscale multilayers that inhibit dislocation motion, and thereby possess extremely high strength.
- Individual layers that provide distinct physical or electrical properties, such as diffusion, thermal, or insulating barriers.

It appears, therefore, that the potential benefits of multilayered structures depend strongly on the nature of the materials used for making the layers. In the following sections, the state-of-the-art in the mechanical properties of metal-metal and ceramic-ceramic multilayers is reviewed, to finish with the case of metal-ceramic multilayers, which are the object of this thesis.

2.1.1. Metal-metal nanolaminates

To date, metal-metal nanolaminates seem to be the most widely studied due to their outstanding mechanical properties. It has been found that changes in the plastic deformation mechanisms appear when the individual layer thickness is below 100 nm. Under these conditions, the high density of interfaces impedes dislocation glide and the dimensions of the individual layer thickness become comparable to the length of dislocation sources [49, 50]. As a result, metal-metal nanolaminates typically display much larger strengths than their monolithic counterparts, which strongly depend on the modulation periodicity (Λ) (thickness of a bilayer). Several strengthening mechanisms have been proposed to explain their ultra high strength, depending on the layer combinations [51-54], such as:

- **Misfit dislocation strengthening**: if the lattice parameters of the two components are different, an array of misfit dislocations will develop at the interfaces. They act as a barrier to the motion of gliding dislocations across the interfaces.
- **Coherency strain strengthening**: for a small lattice mismatch between the layers and a small layer thickness, it might become energetically favored for the layers to elastically strain to a common in-plane lattice parameter, rather than to

nucleate an array of misfit dislocations. In these cases, large in-plane coherency stresses that alternate from tensile to compressive between the layers give rise to a periodic resistance to dislocation motion.

- **Structure barrier strengthening**: in some cases, especially for very thin layers, the crystal structure of one of the layers can serve as a template for the nucleation of the other layer through heteroepitaxy. This can lead to the stabilization of metastable phases, which can be harder than the stable phase.
- **Elastic mismatch (Koehler stress)**: for multilayers with large shear modulus mismatch between layers, a dislocation in the lower modulus (hence, lower line energy) phase may need to overcome a large repulsive image stress from the higher modulus phase before slip can be transmitted across layers.

In all these cases, the strength that can be achieved is very sensitive to the chemical intermixing at the interface and to the layer thickness [55, 56]. Unlike sharp interfaces usually formed in multilayer thin films with positive enthalpy of mixing, intermixing at interface due to negative enthalpy of mixing can reduce the effectiveness of the interface as dislocation motion barrier and thus weaken the hardness/strength of the multilayer thin film. Regarding the layer thickness dependency, it has been found that at large layer thicknesses, typically above 100 nm, the yield strength follows a Hall-Petch type dependency, with the strength increasing with the inverse root of layer thickness. However, a large deviation from the Hall-Petch behavior has been reported at smaller layer thicknesses, of the order of tens of nm, as shown in figure 2-1 for Cu/Nb nanoscale multilayers.

Misra *et al*. [50, 57] rationalized the strength of metal-metal nanolaminates from the point of view of the operating deformation mechanisms as a function of layer thickness, as summarized in figure 2-2.

- At large layer thicknesses, generally above 100 nm, the layers are thick enough to form dislocation pile-ups that can help to overcome the interface barrier. As a result, a Hall-Petch type relationship between strength and layer thickness develops in this regime, so that the yield stress $\sigma_y \propto 1/\sqrt{h}$, where h is layer thickness.
- For layer thicknesses in the order of a few nanometers to tens of nanometers, the layers are no longer thick enough to accommodate dislocation pile-ups,

resulting in a breakdown of the Hall-Petch regime. At these layer thicknesses, threading dislocations are thought to be the primary deformation mechanism. Threading dislocations are glide dislocations that are formed during layer growth. Typically these dislocations originate at surface defects in the substrate and extend from the substrate to the next layer. In multilayer systems, the threading dislocations in each layer are inherited from the previous layer during growth. In this regime, deformation is thought to occur by dislocation bowing (Orowan bowing) within each individual layer, a mechanism that has been named confined layer slip [58]. The restrictions imposed by the interfaces and the smaller layer thicknesses limit the motion of the threading dislocations to two dimensions, which brings about a logarithmic strength dependency with layer thickness (h), of the type $\sigma_y \propto \ln(h/b)/h$, where b is the burgers vector.

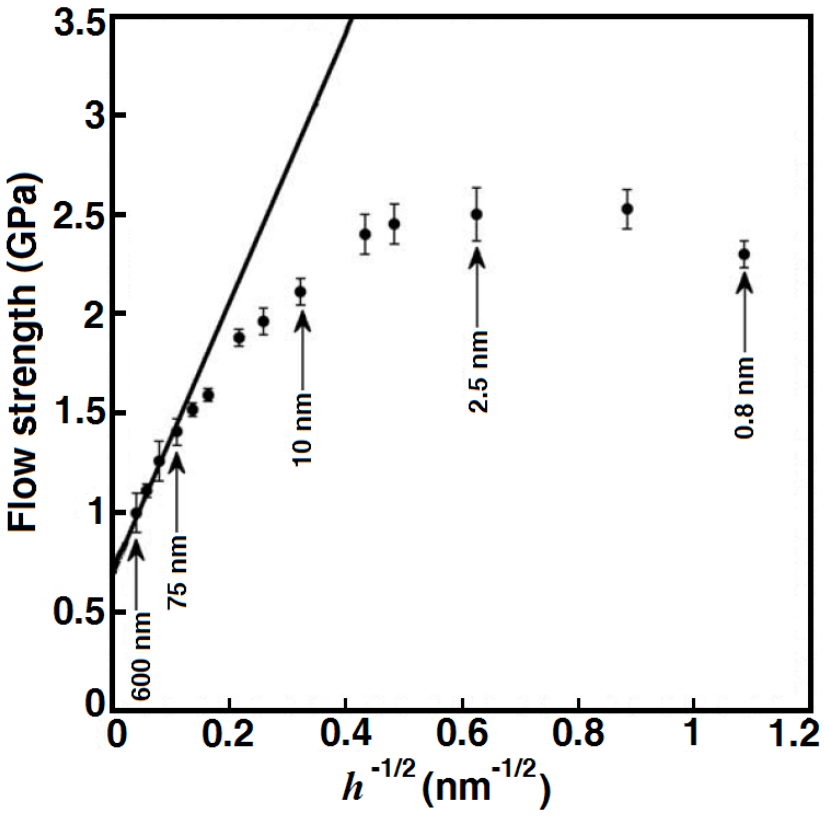

Figure 2-1: Flow strength of Cu/Nb multilayers (estimated as hardness divided *b*y 2.7) as a function of $h^{-0.5}$ where h is the individual layer thickness. The solid line stands for a linear fit of the experimental data consistent with a Hall-Petch type behavior [51].

- Finally, when the layer thickness is of the order of a few nanometers, it has been proposed that the stress required for confined layer slip is so large, that transmission of dislocations across the interface might become favorable,

reaching a plateau in strength. In this regime, it seems that interface/dislocation interactions and interfacial shearing become important.

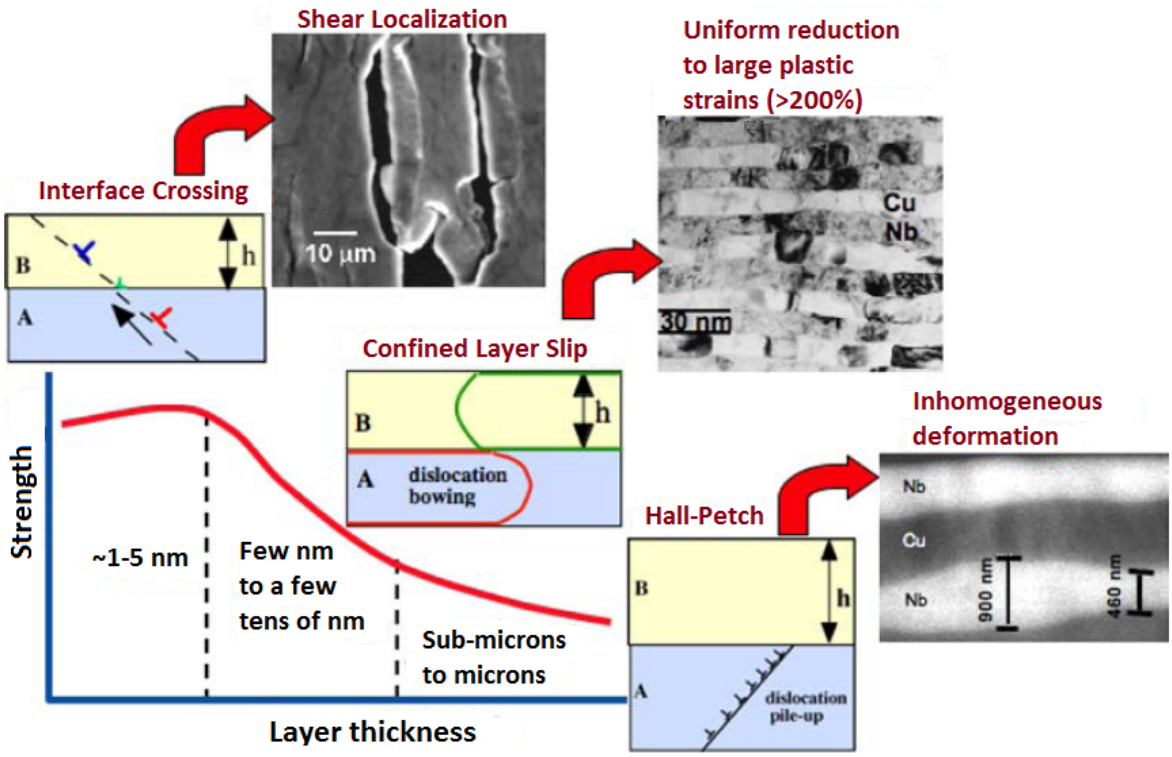

Figure 2-2: Deformation mechanisms in metallic multilayers as a function of layer thickness [50, 57, 58].

Several experimental observations support the operation of these deformation mechanisms in metallic multilayers. For instance, in-situ deformation experiments inside the TEM in Cu/Ni nanolaminates (Foecke *et al*. [3]) showed confined layer slip followed by unstable crack growth, due to fracture of interfaces and layers, with a large plastic zone ahead of crack tip. Similarly, the yield stress of Ag/Cu multilayers increased with decreasing layer thickness, down to extremely small layer thicknesses, at which ductility was lost, triggering brittle fracture [59].

Interestingly, the interface character plays a major role on the maximum strength of metallic multilayers [51]. The most important factor determining the interface character is the crystal structure of each layer (see the figure 2-3) [60]:

- **Coherent or semicoherent interfaces**: a coherent (figure 2-4 (a)) or semicoherent (figure 2-4 (b)) interface is formed when the two layers present the same crystal structure, as it is the case of fcc/fcc multilayers like Cu/Ni. The interface strengthening mechanisms are mainly elastic mismatch plus coherency

strains or misfit dislocation strengthening, depending on whether the layers are fully coherent or semicoherent.

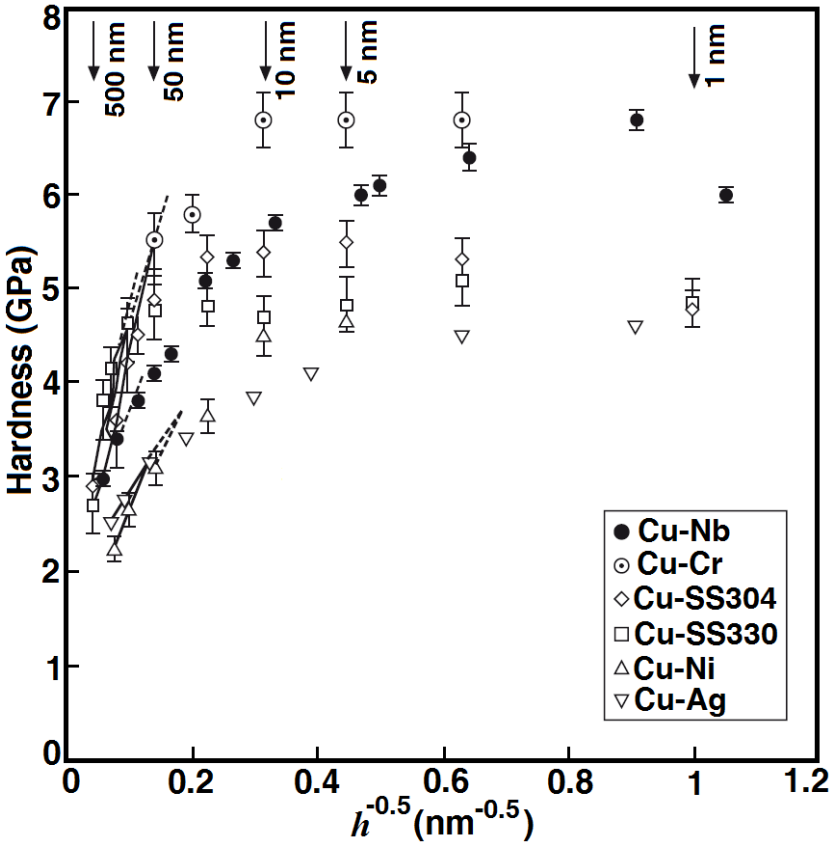

Figure 2-3: Hardness of a number of Cu-based nanolaminates with coherent or semicoherent interfaces (Cu/Ni, Cu/Ag, Cu/SS304, and Cu/SS304) and incoherent interfaces (Cu/Nb and Cu/Cr). h is the layer thickness or one-half of the bilayer period. The solid lines stand for a linear fit of the each experimental data set consistent with a Hall-Petch type behavior [51].

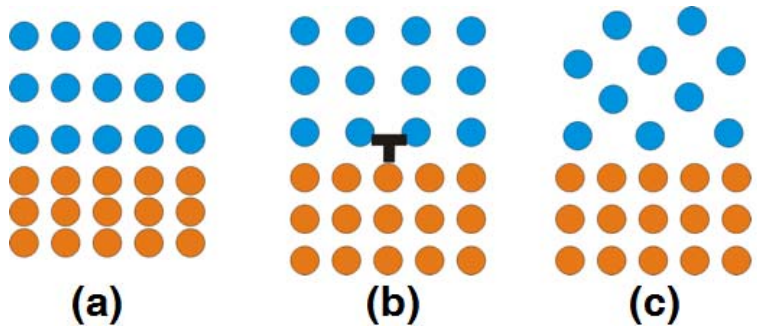

Figure 2-4: Schematic of (a) coherent interface, (b) semicoherent interface, and (c) incoherent interface [60].

- **Incoherent interfaces**: fully incoherent interfaces (figure 2-4 (c)) are found in multilayers combining layers with different crystal structures, like Cu/Nb, where

Cu is fcc and Nb is bcc. They have shown superior strength and, on top of the strengthening mechanisms mentioned above, the incoherent interfaces act as dislocation sinks. In other words, dislocations tend to get trapped at incoherent interfaces, requiring larger stresses for dislocation transmission, and thus providing a larger strengthening capability than coherent or semicoherent interfaces, as shown in figure 2-3 for Cu/Nb and Cu/Cr multilayers.

2.1.2. Ceramic-ceramic nanolaminates

Ceramic-ceramic nanolaminates have also been the subject of large research efforts, mainly driven by the cutting tool industry. Making artificial materials that match or exceed the hardness of the two hardest known materials (diamond and cubic boron nitride) has been a dream from both the fundamental and the technological viewpoint. Ceramic-ceramic nanolaminates (also referred to as ceramic superlattices) typically show strengths near to theoretical strength limit, and as such, fall in the so-called category of ultra-hard materials. The most studied systems have been:

- Nitrides: TiN/NbN [11], AlN/CrN [61], TiN/ZrN [8], Ti/VN [62], TiAlN/CrN [63], that are usually grown by reactive sputtering.
- Oxides: Al_2O_3/TiO_2 [64], Y_2O_3/Zr_2O_3 [65], Al_2O_3/Zr_2O_3 [66].
- Carbides: like TiC/CrC [67, 68]

There are many investigations on nitrides nanolaminates, while the other two (oxides and carbides) remain less explored. Recently, some non-isostructural systems like nitride/carbide (AlN/SiC [69], TiN/TiB_2 [70]) multilayers have also been studied.

The ultra-high hardness of ceramic nanolaminates has been attributed to two factors associated with the nanometer thick dimensions of the layers. Firstly, similar dislocation strengthening mechanisms to those described in metallic multilayers are expected to operate, as a function of elastic and lattice mismatch between the layers. Secondly, ceramics are inherently brittle and a reduction in individual layer thickness and an increase in interface density can also improve the crack propagation resistance.

For instance, Shinn *et al*. [71, 72] studied the hardness of epitaxial TiN/NbN nanolaminates grown by reactive magnetron sputtering with bilayer thicknesses, Λ, ranging from 1.6 to 450 nm. Cross-sectional TEM studies showed well-defined superlattice layers and relatively sharp interfaces, with semi-coherent interfaces

containing misfit dislocations for $\Lambda > 9.4$ nm that became fully coherent for $\Lambda < 4.6$ nm. The hardness was found to increase rapidly with decreasing Λ, reaching a peak value of 52 GPa at $\Lambda = 4.6$, which was around 30 GPa larger than that of the TiN film. Further reductions in Λ below 4.6 nm also led to a reduction in hardness (see figure 2-5). The hardening mechanisms were explained by a combination of two effects that inhibited dislocation motion across the layers. The primary mechanism of hardness enhancement was related to the difference in the dislocation line energies between TiN and NbN layers. A secondary mechanism was related to coherency strains. The maximum hardness occurred where the layers were too thin for coherency-strain relaxation or dislocation motion.

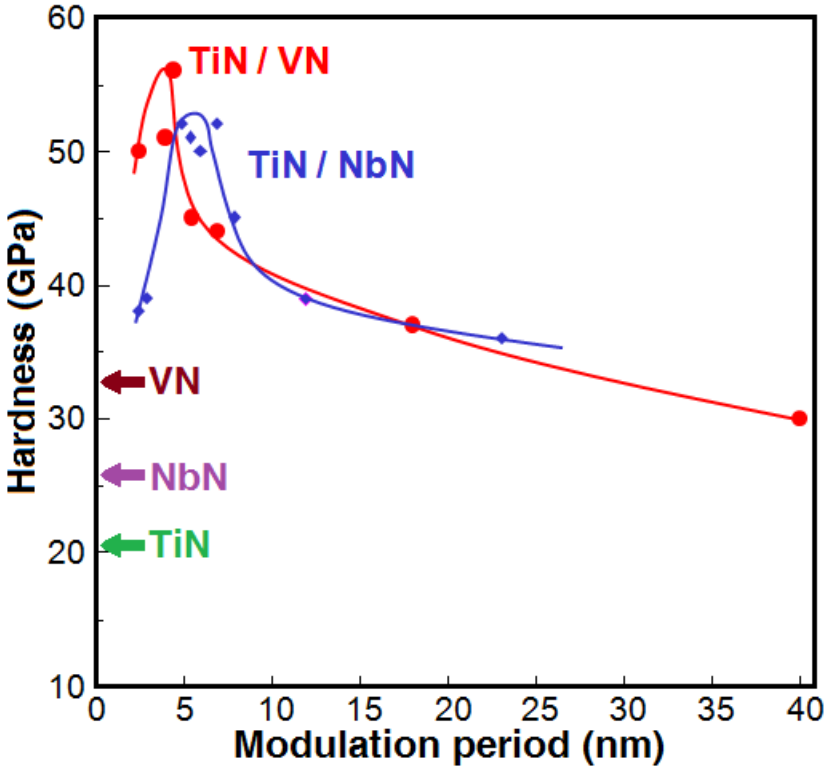

Figure 2-5: Hardness of different combinations of nitride superlattices [72].

Similar effects were found in another single-crystal TiN/VN strained-layer superlattice (SLS) system by Helmersson *et al*. [62]. The hardness of the SLS structures increased rapidly with reduction the superlattice period and reached a maximum of 56 GPa at $\Lambda = 5.2$ nm. Further increases in Λ resulted in a rapid decrease in hardness to 44 GPa at $\Lambda = 7.5$ nm and only in a relatively slow decrease in hardness at higher wavelengths. The highest hardness measured was more than 2.5 times higher than that of the TiN component. These results are summarized in figure 2-5.

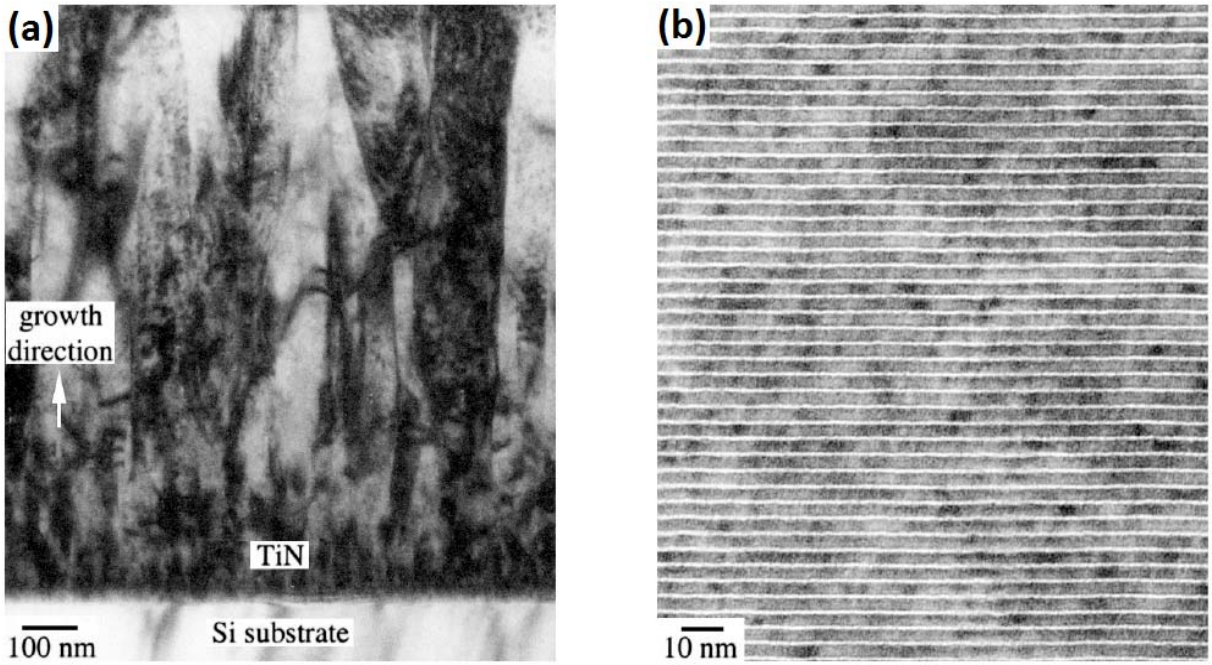

Figure 2-6: TEM images showing (a) columnar TiN film grown on Si(001); (b) small region from a TiN/SiNx multilayer grown on Si(001) in similar conditions. The lighter layers are SiNx. In (a) the contrast arises from the different crystallographic orientations of the grains. Small, equiaxed grains form near the substrate but, as the film grows, preferentially grain growth in favorable orientations leads to a columnar structure. The introduction of amorphous layers in (b) results in a much greater degree of control over the orientation and shape of the grains, as each amorphous layer interrupts grain growth and each TiN layer is forced to renucleate, eliminating the columnar growth and reducing the roughness [60].

Additionally, nanolaminates often present an improved microstructure as compared with thin films of one material (figure 2-6). The layers contribute to the suppression of columnar growth and to a reduction of porosity associated with columnar boundaries that often limit the mechanical strength of ceramic coatings [60].

2.1.3. Metal-ceramic nanolaminates

Metal-ceramic nanolaminates have not been studied in depth. However, they are expected to display an attractive combination of strength, hardness, and toughness, due to several reasons:

- Metal-ceramic multilayers present a large elastic, lattice and shear strength mismatch between the layers, which is expected to constrain the plastic deformation of the softer metallic layers.
- The metallic layers are very thin and thus are expected to yield at very high stresses.

- The ceramic layers are very thin and thus are expected to show very high fracture stresses.
- The different physical nature of each layer can contribute to the suppression of columnar boundaries or other coating defects that propagate throughout the thickness in monolithic coatings, as shown in figure 2-6.
- The high density of interfaces may lead to the activation of toughening mechanisms based on crack arrest and/or crack deflection at the interfaces.

These effects have been demonstrated in several systems. For instance, the hardness of Ti/TiN nanolaminates was found to depend on layer thickness, with hardness peaking for a bilayer thickness of 50 nm (figure 2-7 (a)) [73]. Similar results have also been found in Cr/CrN [74] (figure 2-7 (b)), and Al/AlN (figure 2-7 (c)) multilayers [75, 76]. In general, the peak hardness of the nanolaminates was higher than that of the nitride, indicating that the strength of the metallic layers was greatly enhanced by the nanolaminate architecture.

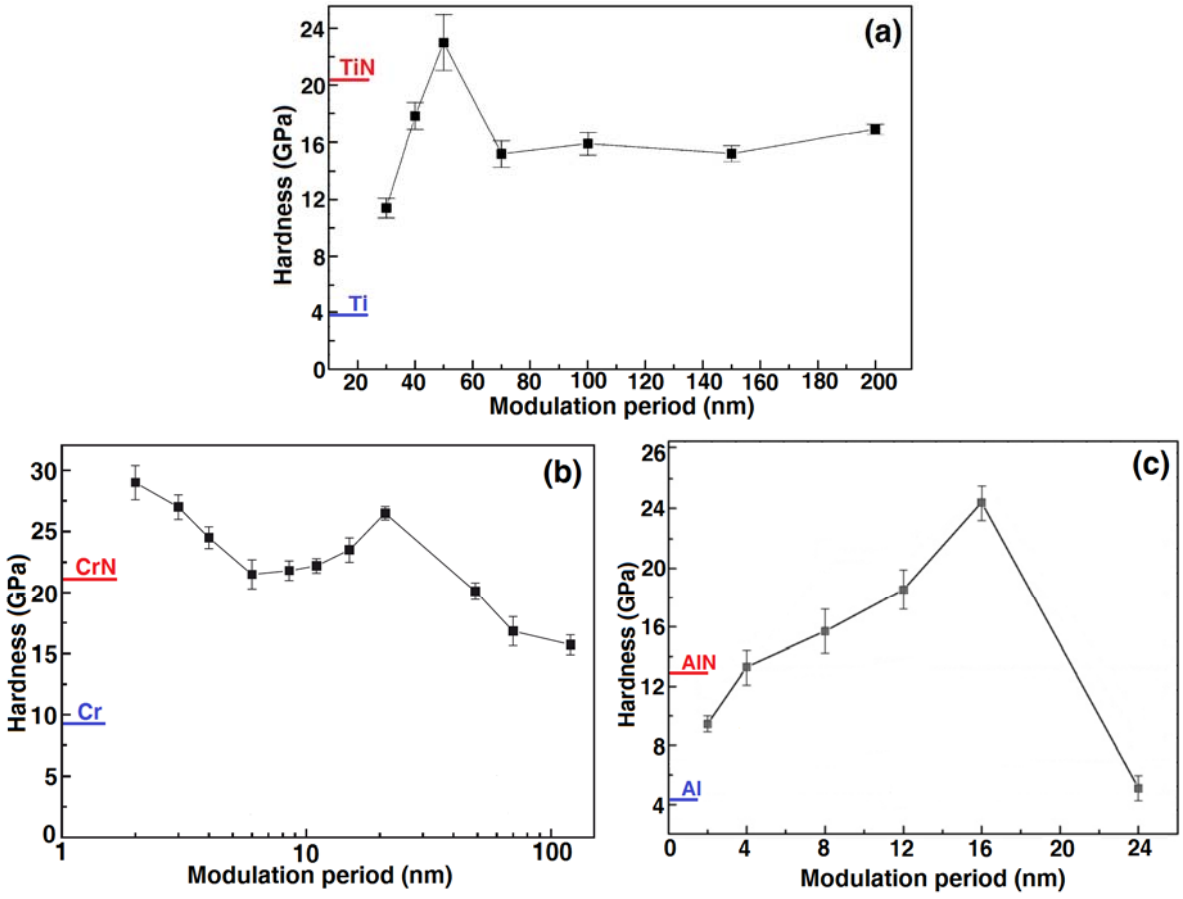

Figure 2-7: Hardness of (a) Ti/TiN, (b) Cr/CrN, and (c) Al/AlN multilayers as a function of the modulation period [73-76]. The hardness of the constituents is also shown in the figures for comparison.

Another recent study was devoted to study the mechanical properties of Cu/Cu-Zr, in which Cu-Zr is an amorphous metallic glass [16]. Bulk metallic glasses usually display limited ductility due to shear localization and strain softening. However, significant increase in ductility was found in the case of metal/metallic glass nanolaminates, compared with Cu/304 stainless steel crystalline multilayers with an individual layer thickness of 25 nm and pure nanocrystalline Cu with an average grain size of ≈ 30 nm (figure 2-8). The study showed that, when the amorphous layers were sufficiently small (thickness ≈ 5 nm), they can act as sinks for dislocations and are no longer affected by shear banding instability.

Finally, improvements in damage tolerance associated with nanometer thick ceramic layers have also been observed in Cu/TiN multilayers [77]. Cross-sectional studies across indentation imprints showed that the material deformed by extensive plastic deformation of Cu and bending of the ceramic TiN layers to substantial strains without fracture. Deformation by rotation of Cu grains was also observed (figure 2-9).

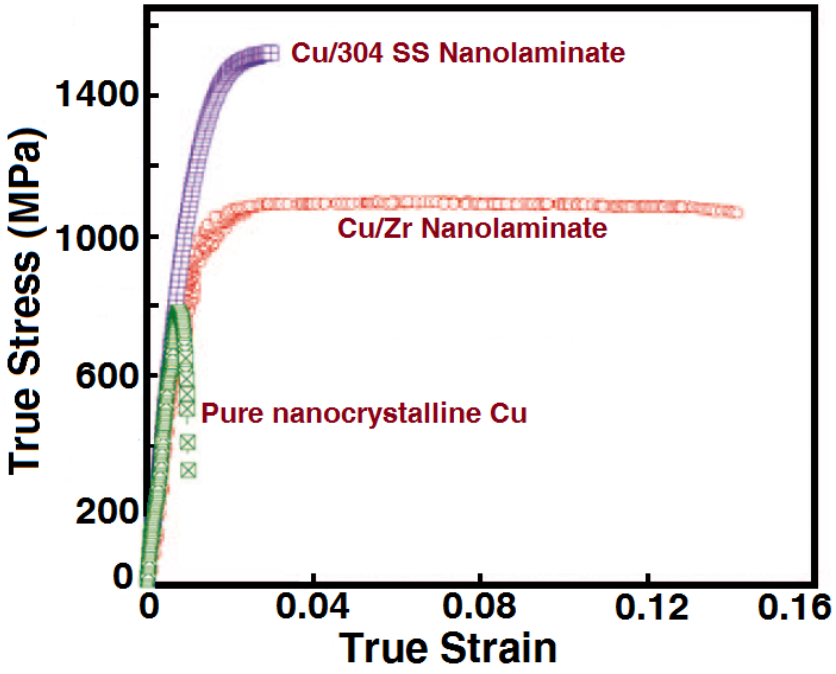

Figure 2-8: Room-temperature tensile true stress–strain curves of the nanocrystalline – amorphous nanolaminate at the strain rate of 10^{-4} s^{-1}, in comparison with those of Cu/304 stainless steel crystalline multilayers with an individual layer thickness of 25 nm and pure nanocrystalline Cu with an average grain size of ≈ 30 nm. The curve for pure nanocrystalline Cu is an engineering stress–strain plot [78]. The Cu/Zr nanolaminate has an average tensile elongation to failure of 13.8 ± 1.7% and a steady-state flow stress of 1090 ± 20 MPa, in contrast with the low ductility (<2%) seen in conventional crystalline nanolaminates (Cu/304 SS) and pure nanocrystalline Cu [16].

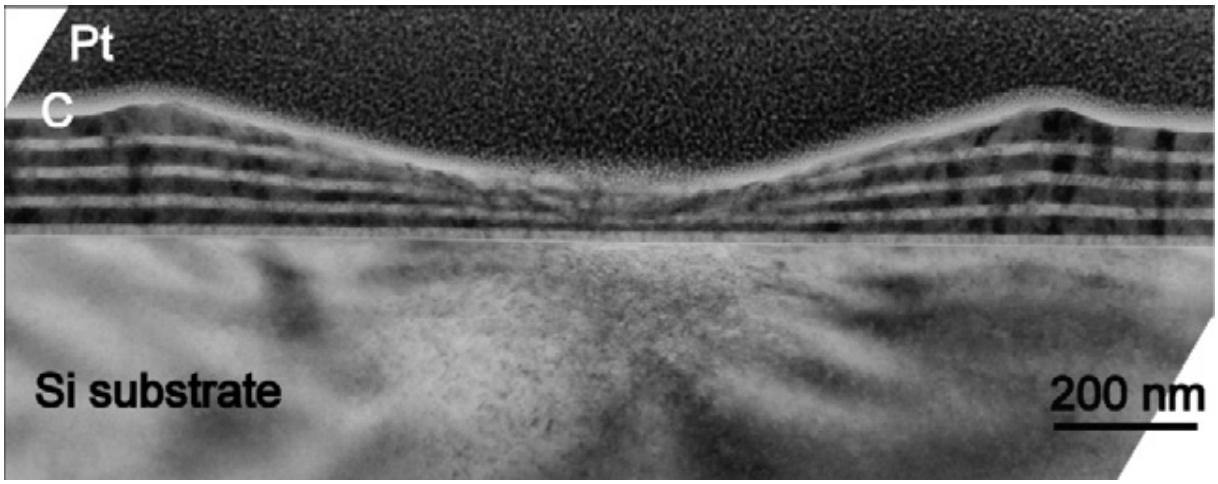

Figure 2-9: FIB-TEM cross-section image showing a cross-section of the indented region of the Cu/TiN multilayer with $\Lambda = 50$ nm deposited on a Si substrate. The TiN layers bend elastically, and constrain the upward plastic flow of copper [77].

2.2. Strength of nanolaminates at high temperature

The current knowledge about the effect of temperature on the mechanical properties of nanoscale multilayers is scarce, as most of the experimental work has been carried out at ambient temperature. This information is important from the engineering viewpoint but also from a fundamental perspective as the dominant mechanisms controlling the deformation and fracture of nanoscale multilayers (interface strength, dislocation plasticity) are thermally activated.

Cu/Nb nanolaminates has been one of the only laminate systems for which the high temperature mechanical properties have been investigated. Mara *et al*. [79, 80] tested freestanding Cu/Nb multilayers with 60 nm layer thicknesses. The Cu/Nb samples contained 125 bilayers to form 15 μm foils and were sputtered on Si wafers. After deposition, the foils were carefully peeled from their substrate, clamped into a fixture and ground into dogbone-shaped tensile specimens with a gauge length of 2 mm and a gauge width of 1 mm to a finish on the edges better than 1 μm. The samples were tested at temperature ranging from 20°C to 700°C at strain rates on the order of $10^{-4}s^{-1}$. The layered morphology of the composite was stable in the whole temperature range. At room temperature, the nanolaminate exhibited high strength (1.2 GPa) and a strain to failure close to 10%. At 700°C, the flow stress of the nanolaminate was ≈ 200 MPa, while the strain to failure reached 30% (figure 2-10). The high strength of the nanolaminate was attributed to the fine scale of the microstructure, and to the ability of the Cu/Nb interfaces to function as barriers to dislocation motion. The confined layer slip

model is able to explain the mechanical response up to 500ºC, and the reduction in the work hardening contribution with increasing temperature is due to enhanced dislocation mobility at elevated temperatures. At 600°C and above, thermally activated processes such as dislocation climb and cross slip across Cu/Nb interfaces diminish the work hardening, leading to uniform strains of 30% at 700ºC.

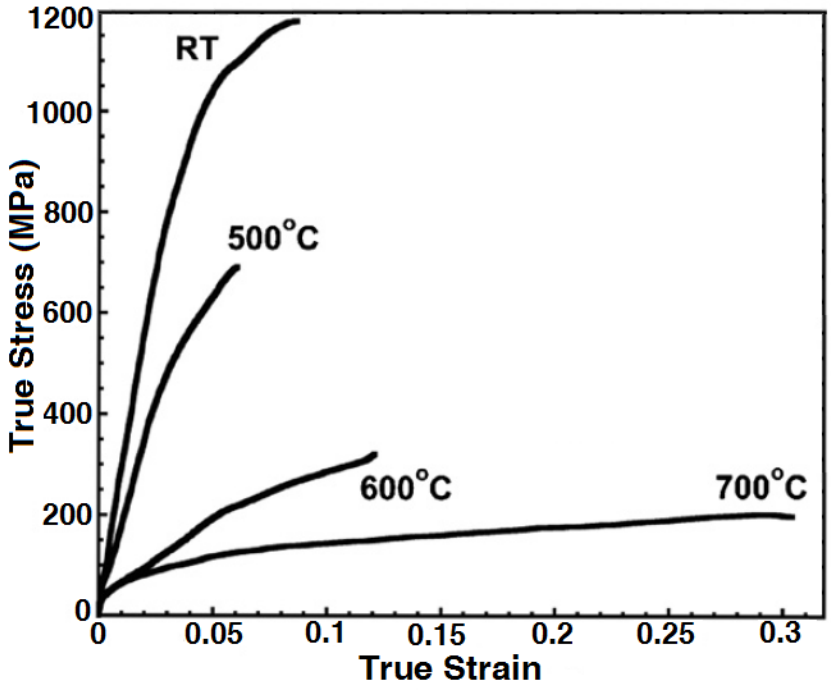

Figure 2-10: Influence of the temperature in the tensile stress-strain curve of Cu/Nb nanolaminates tested at a strain rate of 10^{-4} s^{-1} [79, 80].

Recently, Monclus *et al.* [81] used high temperature nanoindentation to reveal nano-layer size effects on the hardness of Cu/Nb nanolaminates. They reported the effect of nano-layer thickness and interface structure on the high temperature mechanical behavior of Cu/Nb nanolaminates with different thicknesses and processing history: physical vapor deposition (PVD) Cu/Nb thin films and accumulative roll bonded (ARB) Cu/Nb sheets. They showed that the PVD samples are consistently harder than the ARB samples at all temperatures, which is in agreement with the trends observed in ambient temperature studies on Cu/Nb nanolaminates (figure 2-11).

In addition, their study revealed the existence of a critical layer thickness L_{crit} at which the material is more resistant to softening at elevated temperature. L_{crit} depends on interface structure, which provides indirect evidence that L_{crit} corresponds to the layer thickness at which the main deformation mechanism changes from confined layer slip to

interface crossing. These results imply that layer thickness and interface structure can be tuned to achieve optimal high-temperature strength in layered nanocomposite structures.

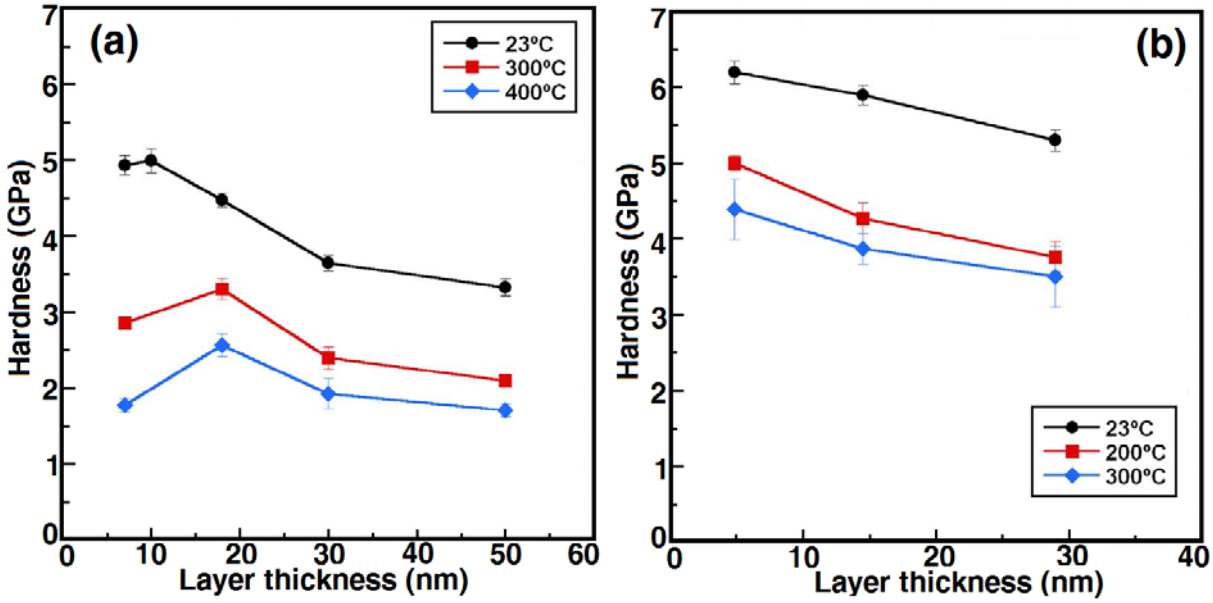

Figure 2-11: Indentation hardness vs. layer thickness L for the (a) ARB Cu/Nb nanolaminates at 23°C, 300°C, and 400°C; (b) PVD Cu/Nb multilayers at 23°C, 200°C, and 300°C [81].

With the recent progress in instrumented nanoindentation, it is now possible to carry out nanomechanical testing at high temperatures. This work aims at exploiting this new technique to explore the high temperature mechanical properties of Al/SiC nanolaminates as a model multilayer system combining metallic and ceramic layers.

3 Materials and experimental techniques

3.1. Multilayer processing

Except for accumulative roll bonding (ARB), that has demonstrated the ability to manufacture bulk metallic laminate plates with layer thicknesses as small as 10 nm, most of the techniques for nanolaminate fabrication rely on thin-film deposition technology. Metal-ceramic nanoscale laminates can be processed by a range of thin-film deposition techniques, like chemical vapor deposition (CVD), physical vapor deposition (PVD), sol-gel synthesis, electroplating, *etc*. The Al/SiC nanolaminates studied in this work were deposited by magnetron sputter deposition (a form of PVD). Sputter deposition is one of the most versatile and widely used fabrication techniques for nanoscale multilayers [4, 5, 9, 10, 13, 17]. The wide acceptance of this technique is based on the ability to deposit a wide variety of materials (both conducting and non-conducting elements as well as alloys can be sputtered) together with a good process control (required to control layer thickness at the nano scale) and high deposition rates

(needed to manufacture relatively thick laminates) [82]. The conditions used for the deposition of the Al/SiC nanolaminates and the set of multilayers deposited are briefly described below.

3.1.1. Deposition of the Al/SiC nanolaminates by magnetron sputtering

The Al/SiC nanoscale multilayers were grown on thermally oxidized (111) oriented single-crystal silicon (Si) wafers. The films were deposited in Los Alamos National Laboratory using a sputter unit made up of a high vacuum chamber with dual sputter guns (figure 3-1).

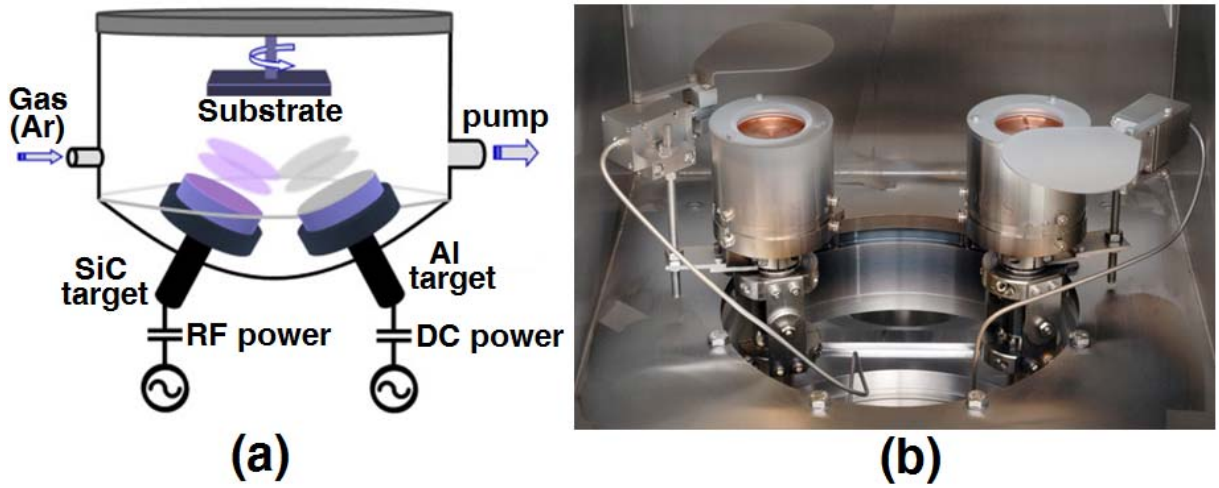

Figure 3-1: (a) Schematic of sputter unit, (b) vacuum chamber with dual sputter guns.

The base pressure of the sputtering unit was 10^{-7} Torr. Argon (Ar) was used as the sputter gas and all depositions were carried out at an Ar working pressure of 3.0 mTorr (0.4 Pa). The pure aluminum target (>99.99% purity, Kurt J. Lesker, Clairton, PA) was sputtered at a DC power of 95 W. SiC layers were deposited from a SiC target made by hot isostatic pressing (>99.5% purity, Kurt J. Lesker, Clairton, PA) using identical argon pressure and a RF sputter power of 215 W. The targets were pre-sputtered for about 10 min at 40 W for Al and 95 W for SiC to remove any oxides and contamination prior to film deposition. The sample holder was continuously rotated during sputtering to obtain a uniform layer thickness. The deposition rates were approximately 7.5 nm min^{-1} for Al and 3.9 nm min^{-1} for SiC. Alternating Al and SiC layers were deposited by means of a computer controlled shutter system to build up the multilayer structure [13, 14, 17, 83-85].

Four different series of nanolaminates were deposited for this work. In series 0, the Al and SiC layer were grown to an equal nominal thickness of 50 nm, to a total number of layers of 40, yielding a total coating thickness of approximately 2 μm. Using the same sputtering conditions, 1 μm thick monolithic thin films of Al and SiC were also deposited on Si substrates, to be used as reference materials.

Three additional series of samples (series 1 to 3 in table 3-1) were manufactured to investigate the effect of individual layer thickness and volume fraction on the mechanical response. The total number of layers in each nanolaminate was chosen to obtain a total coating thickness above 10 μm to reduce substrate effects during nanoindentation, as will be explained in section 3.4.

In series 1, the SiC layer thickness was kept constant at 50 nm and the Al layer thickness was varied between 10 and 100 nm. In series 2, the Al layer thickness was kept constant at 50 nm and the SiC layer thickness was ranged between 2 and 100 nm. Finally the volume fraction of both Al and SiC was fixed at 50% in series 3 and the layer thicknesses were varied between 10 and 100 nm. The code used to name the different nanolaminates refers to the nominal thickness, in nm, of each layer; for example Al10SiC50 refers to a nanolaminate containing 10 nm thick Al layers and 50 nm thick SiC layers. The last column in table 3-1 indicates the volume fraction of Al in each nanolaminate, according to the nominal layer thicknesses.

Table 3-1: Number of layers and layer thicknesses in the three series of nanolaminates under study.

Series	Sample	Thickness (μm)	Number of bilayers	t_{Al} (nm)	t_{SiC} (nm)	V_{Al}
S0	Al40SiC40	~2	20	40	40	0.5
	Al60SiC60	~2	20	60	60	0.5
	Al	~1	-	1000	-	1
	SiC	~1	-	-	1000	0
S1	Al10SiC50	~15	250	10	50	0.17
	Al25SiC50	~13.3	175	25	50	0.33
	Al50SiC50	~15	150	50	50	0.50
	Al100SiC50	~15	100	100	50	0.67
S2	Al50SiC2	~13.5	260	50	2	0.96
	Al50SiC10	~15	250	50	10	0.83
	Al50SiC25	~13	175	50	25	0.67
	Al50SiC100	~15	100	50	100	0.33
S3	Al100SiC100	~17	85	100	100	0.50
	Al25SiC25	~14	280	25	25	0.50
	Al10SiC10	~12	600	10	10	0.50

3.2. Microstructural characterization techniques

Microstructural characterization of the nanolaminates was carried out by scanning electron microscopy (SEM), energy dispersive x-ray spectroscopy (EDS), transmission electron microscopy (TEM), and atomic force microscopy (AFM).

SEM was carried out in either a SEM EVO® MA15 (Carl Zeiss Company) or a Helios 600i (FEI Company) dual beam system, both equipped with an Oxford INCA 350 EDS system for chemical analysis. AFM (Park XE-150) was employed to carry out a detailed analysis of the topography around nanoindentation imprints and to quantify the pile-up/sink-in effects as well as to study the shape changes of the indenter tip that can potentially occur during hot nanoindentation. Finally, TEM was employed for studying the deformation mechanisms, using three different microscopes: a FEI Tecnai F-20, at the LabMet Laboratory of Carlos III University, and the JEOL JEM 3000 and JEOL JEM 2100, at the National Laboratory for Electron Microscopy (CNME) of the Complutense University of Madrid. TEM sample preparation across nanoindentations and deformed nanopillars was carried out by focused ion beam (FIB) milling, as described in section 3.3.2.

3.3. Nanofabrication by FIB

Focused ion beam (FIB) milling has become an increasingly popular technique for the fabrication of various types of nanostructures for different applications. In this study, FIB milling, using a Helios 600i dual beam instrument (FEI Company) has been used with two purposes. The first one was to study the deformation mechanisms around indentations and deformed micropillars, as FIB is the only available method to prepare TEM specimens across selected locations. Secondly, for the fabrication of nanolaminate micropillars that were afterwards tested in compression. Since FIB nanofabrication is a relatively novel technique, the principle of operation is first presented in section 3.3.1, followed by a detailed description of the methods and conditions used for the TEM sample preparation (section 3.3.2) and the fabrication of the micropillars (section 3.3.3).

3.3.1. Principles of operation

Focused ion beam (FIB) microscopes are tools enabling inspection, characterization, structuring or manipulation of a broad range of materials. The basic concept is very similar to scanning electron microscope (SEM) but uses ions (charge atoms) instead of

electrons. For both instruments, the intensity of the secondary electrons produced at each raster position of the beam is displayed to create an image of the sample. A fine tungsten pin covered with liquid Gallium (Ga) is used as ion source from which Ga atoms are extracted and ionized via high voltage. The use of Ga is advantageous for two reasons. Firstly, Ga has a low melting point and hence exists in the liquid state near room temperature. Secondly, Ga can be focused to a very fine probe size, less than 10 nm in diameter. Such Ga^+ ions are then accelerated in the range of 0.5 - 50 keV and focused on the sample via electrostatic lenses. By controlling the strength of the electrostatic lenses and adjusting the effective aperture sizes, the probe current density (and therefore the beam diameter) may be varied from tens of pA to several nA corresponding to a beam diameter of ~ 5 nm to ~ 0.5 μm, respectively.

The impacting ions can interact with the specimen surface in many different ways, such as the emission of electrons, ions, atoms or clusters. An understanding of the sputtering process is important for the operation of FIB systems. When a Ga^+ ion is accelerated toward the target sample, it impacts the sample, creating a cascade of collision events that results in the emission of secondary electrons plus the ejection of sputtered particles (which may be ions or neutral atoms) and/or the generation of point and line defects. Therefore, the interaction with the ion beam can be used both for imaging, by the use of different detectors, and for removing material through sputtering in selected locations. Almost all materials can be structured by FIB, ranging from soft matter (polymers) to ultra hard material (diamond). However, when using FIBs for surface structuring it should be kept in mind that this method can lead to ion implantation, thermal stresses and defect formation. Another advantage of FIB systems is that they can also be used for ion-beam assisted chemical vapor deposition in selected locations. This is very useful for the deposition of metals in silicon semiconductor device repair, but also to protect selected locations from further interaction with the ion beam, and it is extensively used in SEM and TEM specimen preparation by FIB. To this end, a needle is brought to within 100–200 μm of the target surface. A suitable organometallic gas is injected through the needle and adsorbed onto the target surface. By scanning the area of interest with the Ga^+ beam, the gas can decompose, leaving a layer of deposited metal. Pt or W can be deposited in FIB systems using this method while the byproducts like CO are removed through the vacuum system [86, 87].

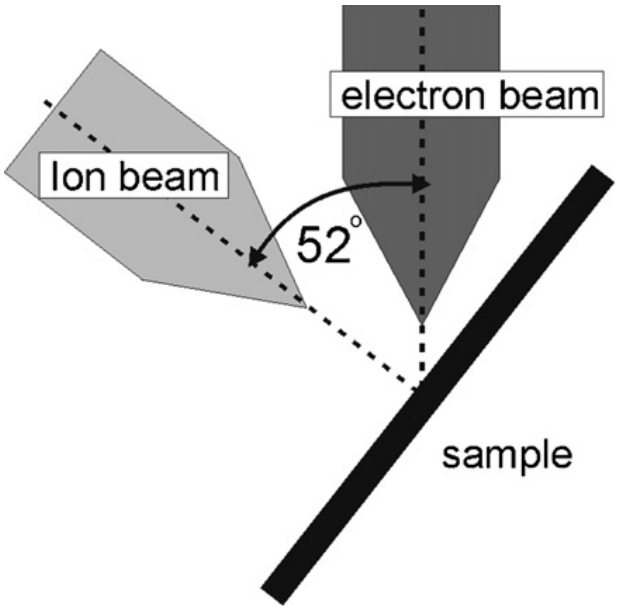

Figure 3-2: Schematic diagram of the configuration of the FIB/SEM dual beam apparatus. The sample is tilted to 52°, so ion milling occurs at 90° to the sample while electron imaging takes place at 52° to the sample [88].

Nowadays, most FIB microscopes are equipped with an additional scanning electron column, as depicted in figure 3-2. Such systems are extremely useful since they allow for in situ observation with the electron beam during ion beam induced surface structuring [86-94].

3.3.2. FIB milling techniques for TEM specimen preparation

The small beam size and imaging capabilities of the FIB make this instrument ideal for preparing SEM or TEM specimens in either cross-section or plan view in selected locations. The beam can be very accurately positioned on the sample at high current density to produce uniformly thin TEM specimens that may be prepared in just a couple of hours [86-89, 91-96]. There are basically two methods to prepare electron transparent lamellas using FIB:

a) **The cross-section method**: Initial specimen preparation must be performed before the sample is placed into the FIB using conventional TEM specimen preparation techniques. An area of interest is located and cut to less than 3 mm in length, so that it fits into the TEM holder. The sample is then mechanically polished as thin as possible (around 50 μm) to reduce the FIB time. The sample is mounted on a slotted TEM Cu grid that has been partially cut away (see figure 3.3). The sample is then positioned into the FIB and a window is thinned down using the Ga^+ beam. The preparation of plan

view specimens is similar to that for cross-section specimens. The plan view method essentially requires that the bulk sample be oriented so that planar interfaces are positioned parallel to the ion beam. For the preparation of TEM plan view specimens, the top edge of the specimen that contains the region of interest is polished and the bulk sample is cut and/or polished to the appropriate size using the same techniques mentioned above. The mounted sample is then positioned into the FIB so that the plane of interest is parallel to the ion beam and an electron transparent membrane is then FIB milled in a similar manner for the preparation of cross-section specimens.

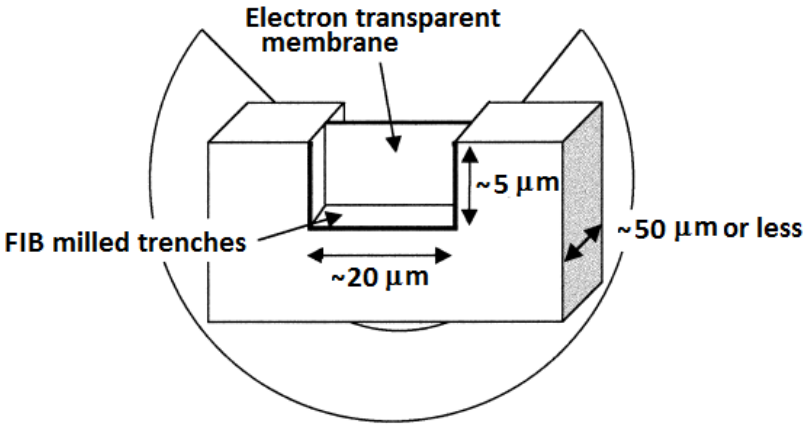

Figure 3-3: A schematic diagram of a TEM specimen prepared by FIB (drawing is not at scale) [92].

b) **The lift-out technique**: this technique requires little or no initial specimen preparation but the FIB system must be equipped with a micromanipulator or microprobe. A thin membrane is actually cut and removed from the bulk specimen and mounted in a TEM grid. The process starts with the deposition of a metal strip over the area of interest as in the conventional FIB method to protect the surface. A large stair-step FIB trench is cut on one side of the area of interest and a rectangular FIB trench is cut on the other side of the area of interest. Prior to final thinning, the sample is tilted to 45° with respect to the ion beam and then the bottom, left side, and a portion of the right side of the specimen is cut free. Then, the thin membrane is glued to the micromanipulator and then the remaining right side of the specimen is milled free and transferred to a TEM grid where is glued again depositing a metal pad. Once the membrane is transferred to the TEM grid, the final milling to electron transparency is completed using low ion beam currents. If the specimen is to be used for high resolution electron microscopy (HREM), a final FIB cut is performed ~1–2° with respect to the plane of the specimen surface. In this manner, the thinnest portion of the specimen lies

in the area of interest required for HREM analysis. The remaining right side of the specimen is milled free leaving the electron transparent membrane lying in the cut trenches. Plan view specimens may also be prepared using this technique. Lift-Out TEM specimens may be prepared within 3 h.

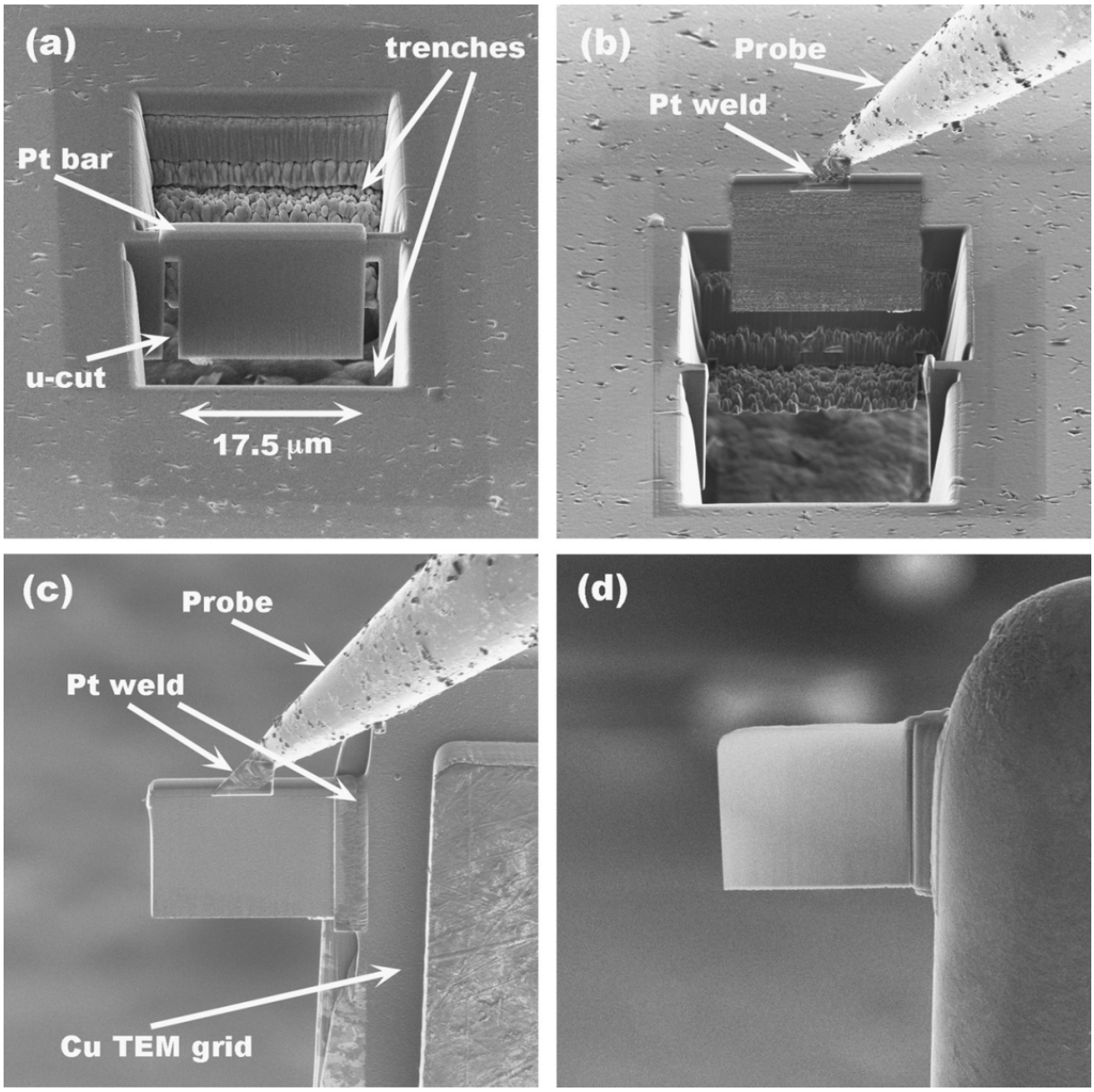

Figure 3-4: Focused ion beam (FIB) lift-out TEM sample preparation technique [80].

In this work, the lift-out technique was used to prepare electron transparent lamellas across nanoindentations in order to study the deformation mechanisms in the TEM. The process used to prepare cross-section surfaces suitable for TEM analysis is shown in figure 3-4. A Pt layer was deposited on the nanolaminate to minimize beam damage. This was followed by milling a wide trench in the region of interest at a decreasing high ion beam current (from 30 nA to 2.5 nA). A fair amount of beam damage was introduced

at this current. The region of interest was then finally thinned down at low currents (from 80 to 10 pA) to remove the damage introduced during the high current milling.

3.3.3. Micropillar fabrication by FIB

The micropillar compression technique was introduced by Uchic et al. [42-45] as a new method to characterize the mechanical behavior of micrometer scale volumes under uniaxial conditions. The technique, used for the first time to study size effects in strength in pure metals, is very well suited to study the mechanical behavior of thin-films and coatings under uniaxial loading. The technique relies on the ability to manufacture micropillars, whose size is limited by the total coating thickness. FIB milling is very well suited for this purpose and two main strategies can be used to manufacture micropillars by FIB:

a) Annular milling: The pillars are manufactured by milling concentric annular patterns, with the ion beam oriented parallel to the pillar axis, as schematically illustrated in figure 3-5 (a). The final result is a pillar located in the center of a trench whose dimensions have to be large enough to fit the flat punch that will be used for compressing the pillar. The main advantage of this technique is that it can be easily employed based on conventional milling patterns readily available in any FIB system. However, pillars fabricated by annular milling tend to present some taper, so that the diameter at the top is slightly smaller than the diameter at the base. This leads to a gradient on the applied stress along the micropillar and may induce potential artifacts in the stress-strain curves. The taper angle will vary with milling condition, but is generally within 2 to 5 degrees.

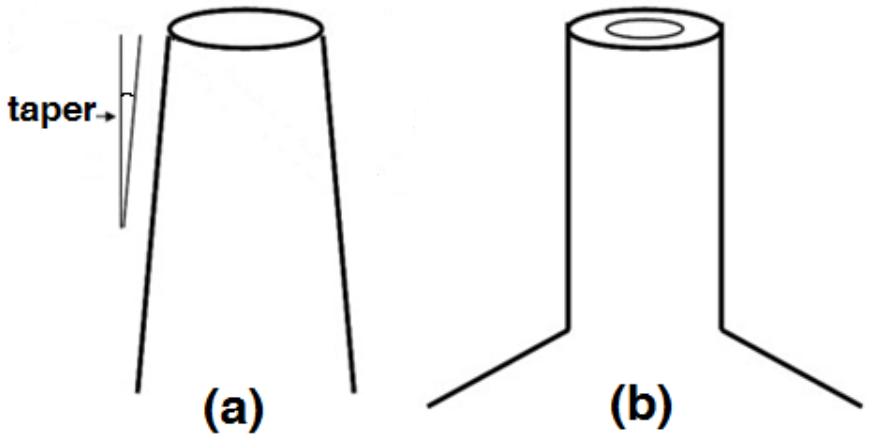

Figure 3-5: A schematic drawing of the approximate geometry for (a) annular milling, (b) lathe milling of micropillars.

b) Lathe milling: To avoid the potential artifacts associated with the taper, the micropillar walls can be subsequently polished with the ion beam at bevel angle to the bulk specimen surface, while rotating the pillar around its axis. This procedure, referred to as lathe milling, is time consuming, but provides micropillars with uniform cross-section and controlled aspect ratio (figure. 3-5 (b) and figure 3-6 (b) and (c)).

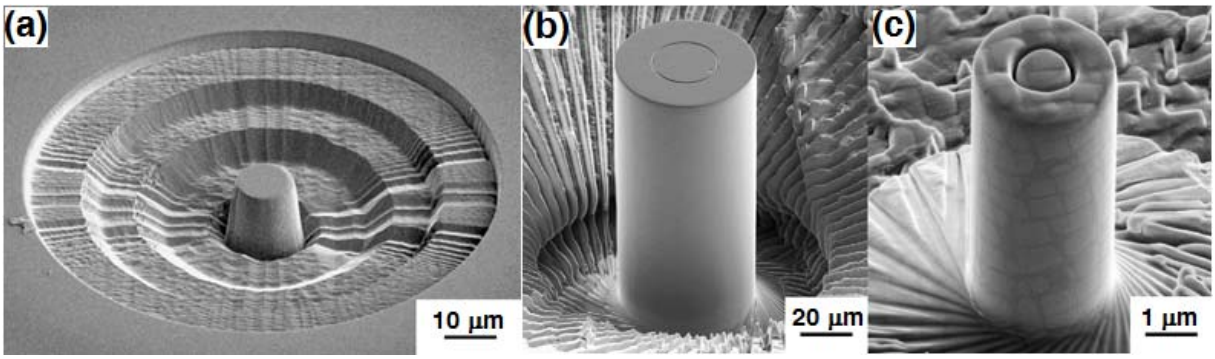

Figure 3-6: (a) Annular milling patterns have been used to FIB mill a roughly defined pillar and surrounding cavity, (b) and (c) micropillars fabricated by lathe milling [43].

In this work, the mechanical behavior of Al/SiC nanolaminates was investigated by micropillar compression (in addition to indentation). The micropillars were fabricated with a diameter of 1 μm and a length of 2 μm. Two types of manufacturing strategies were followed: annular milling and lathe milling, as shown in figure 3-7. The micropillars manufactured by annular milling presented slight taper (less than 4º), while lathe milling produced "taper-free" micropillars with vertical walls and negligible taper (< 1º). Milling of the tapered pillars was carried out in two steps. First, a relatively large pillar of 4 μm in diameter was milled with a relatively high ion current (7 nA). Final milling was carried out with an ion current of 50 pA, down to a final micropillar diameter of ~1 μm. "Taper-free" pillars were fabricated by initially milling a micropillar of ~3 μm in diameter using the annular milling technique described above. Afterwards, the sample surface was tilted to make a small angle with the initial sample surface (~28º), so that the ion beam overstepped the sample tangent to the surface. The sample was rotated in 5º intervals, and the milling operation was replicated with an ion current of 50 pA. A fixed mark at the top surface of the micropillar was introduced before starting the lathe milling for better aligning the sample. It is well known that Ga^+ ion implantation can cause irradiation damage, although the damage depth was estimated to be less than 60 nm at 30 kV beam under normal incidence [97, 98]. This is a small fraction of the total micropillar diameter (~1 μm).

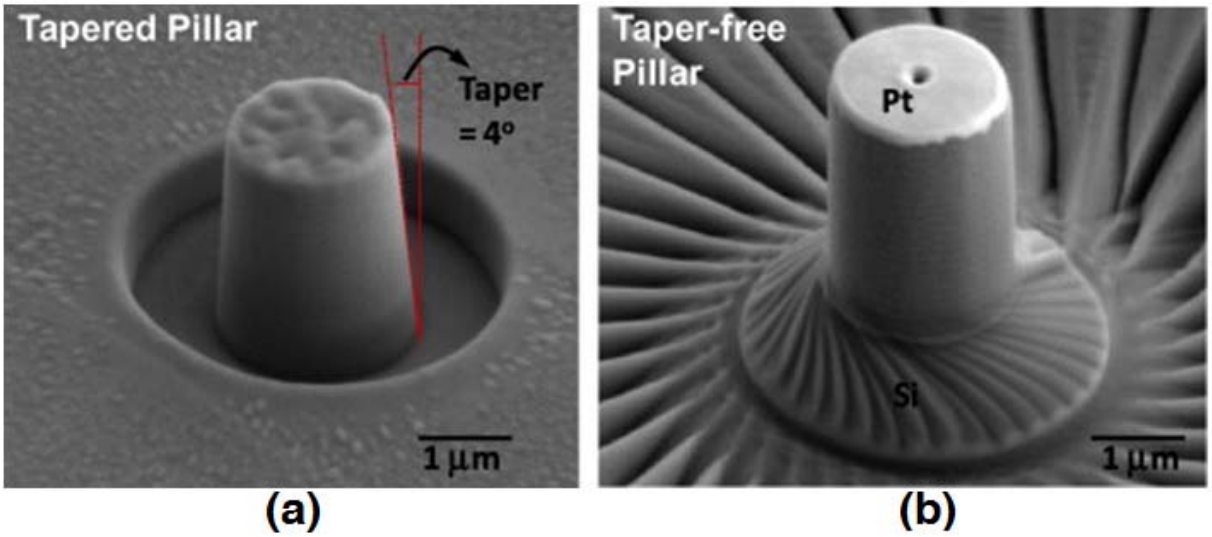

Figure 3-7: (a) Tapered micropillar of Al/SiC nanolaminate fabricated by FIB annular milling procedure, (b) Taper-free micropillar of Al/SiC nanolaminate manufactured by FIB lathe milling [85].

Ion beam-induced surface damage approaching the 50-60 nm in depth might have an influence on the micropillar compression behavior in the case of micropillars with very small diameter of monolithic materials [99]. The micropillar diameter does not influence the flow stress significantly In the case of Al/SiC nanolaminates since the characteristic length scale that controls the mechanical response is the layer thickness, that is much smaller than the micropillar diameter [84, 85]. For the reasons described above, it is assumed that the ion beam-induced surface damage should play a minor role on the deformation behavior of micropillars made of nanoscale multilayers.

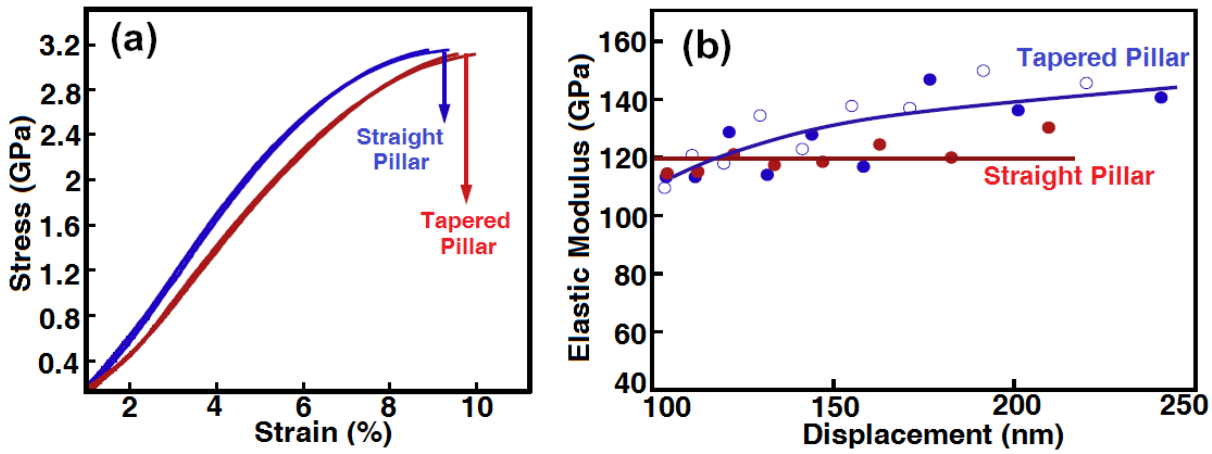

Figure 3-8: (a) Stress-strain curves in compression of Al/SiC nanoscale multilayers obtained by testing tapered and taper-free micropillars. (b) The elastic modulus determined for both micropillar geometry as a function of the applied displacement [85].

Figure 3-8 illustrates potential artifacts associated with the taper of the pillars by comparing the stress-strain curves for tapered and straight Al/SiC nanolaminate micropillars [85]. Tapered pillars tend to be somewhat more compliant than straight pillars and produce artifacts in the determination of the elastic modulus, due to the more inhomogeneous deformation and the stress concentration at the top of the pillar, resulting in plastic yielding at lower apparent stresses.

3.4. Nanomechanical testing

The aim of this work was to study the high temperature mechanical properties of Al/SiC nanoscale multilayers. This was achieved using three experimental nanomechanical testing approaches. Firstly, the hardness and elastic modulus of the nanolaminates was determined through instrumented nanoindentation. Secondly micropillar compression tests were carried out at elevated temperature in selected cases to get a better understanding of the deformation mechanisms. And finally, the creep behavior of these multilayers was also explored by the indentation creep technique. All three approaches are well established at room temperature, and hence are described below, together with a description of the experimental set-up used in this thesis. However, nanomechanical testing techniques at high temperature are not yet well established and required a large effort in order to find the best operating procedure. Hence, the extension of the techniques described below to elevated temperatures will be the subject of the next chapter and is one the original contributions of this thesis.

3.4.1. Description of experimental apparatus

Two types of commercial nanoindenter systems were used during this investigation:

- A TI 950 TriboIndenter^{TM} from Hysitron.
- A NanoTest^{TM} platform III from Micro Materials.

The Hysitron 950 TriboIndenter uses an axial-loading system based on a piezoelectric force transducer and capacitance depth-sensing indenter head (figure 3-9).

The indenter contains a granite base that supports other components of the system and is embedded on an active vibration isolation system. The system is equipped with automated motorized X-axis and Y-axis stages mounted on the bottom of the TriboIndenter base, while the Z-axis stage is mounted on the bridge (bracket). The

sample stage is connected directly to the XY stage. The Triboscanner (three axis piezo scanner and transducer) and optics are mounted to the Z stage. The positioning is provided by three axis piezo scanner that has much higher precision than the XYZ stage and can also be used for scanning the topography of the surface before and after indentation. The entire apparatus is placed inside an acoustic and thermal enclosure that has been designed to minimize the amount of acoustic noise that can get to the indenter during testing, that blocks air current and acts as a thermal buffer to help eliminate drift (figure 3-10).

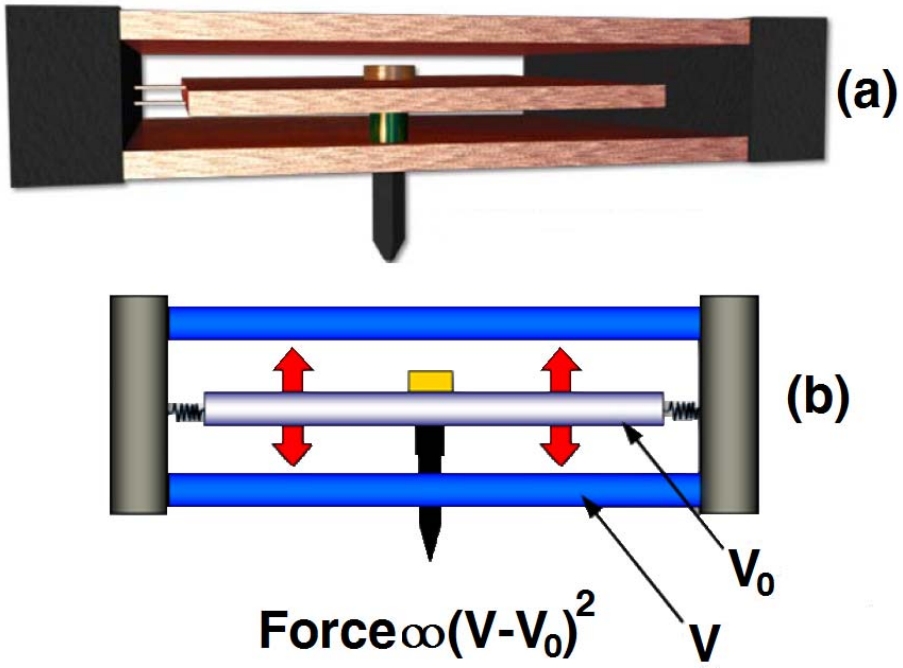

Figure 3-9: (a) Hysitron three-plate capacitive transducer. (b) Schematic of Hysitron three-plate capacitive transducer. Electrostatic actuation of the nanoindenter probe is realized by applying a known voltage between the movable center plate and the fixed lower outer plate of the force actuator sensor [100].

The NanoTest, however, operates with a horizontal loading configuration and utilizes a pendulum based loading system. The loading system is illustrated schematically in figure 3-11. By passing a current through the coil at the top, the pendulum rotates around a friction-less pivot towards the magnet, thus pushing the indenting tip into the sample. The displacement of the indenter into the sample surface is measured by a set of parallel plate capacitors, with one plate attached to the pendulum and the other to the main frame of the instrument. A set of damping plates located at the bottom provide air damping to minimize pendulum oscillation prior to measurements. The whole indentation setup is placed inside an environmental control chamber. Figure 3-12 shows

the seal chamber that can be purged with gas to perform the experiments in a controlled atmosphere.

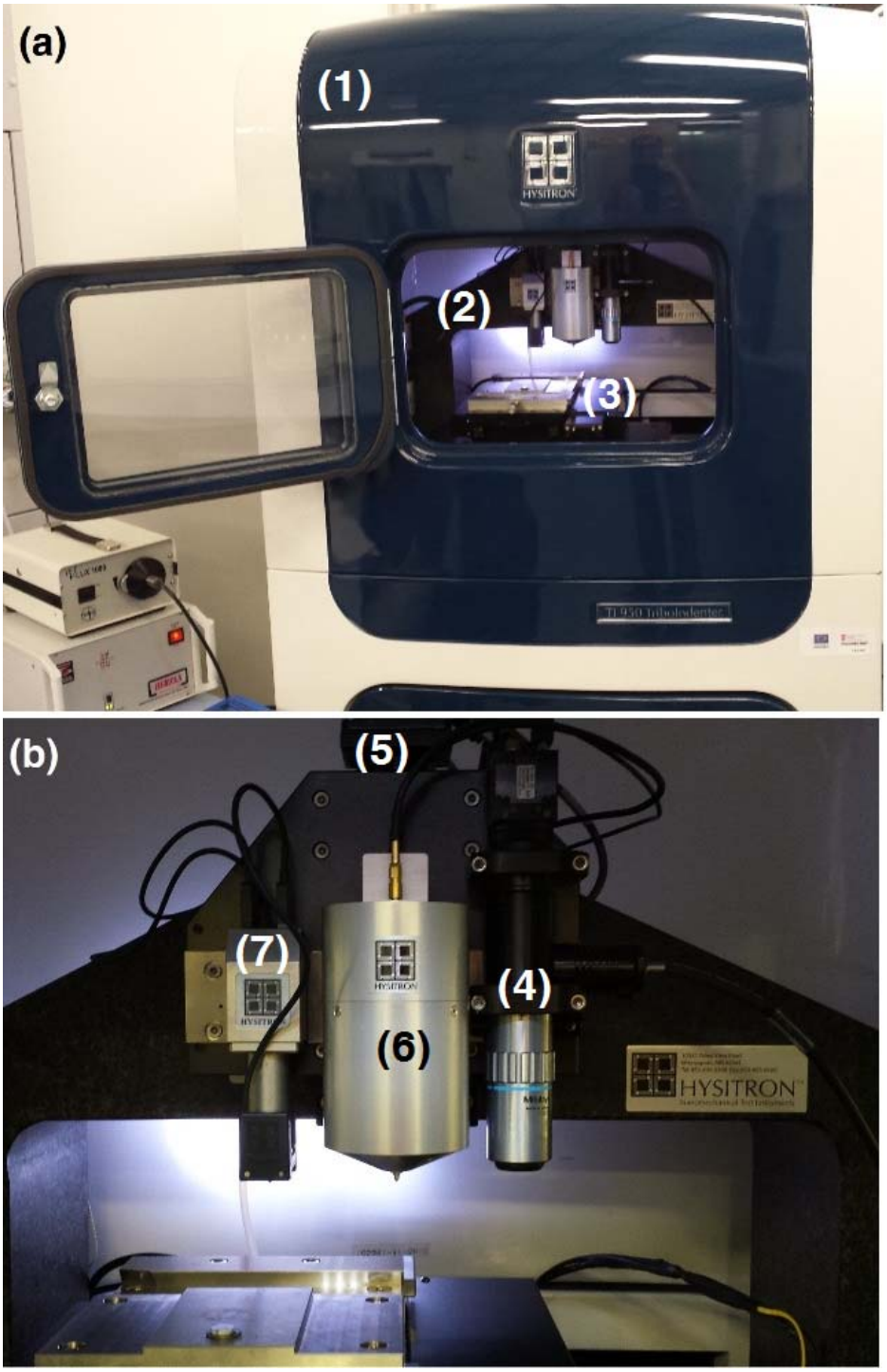

Figure 3-10: (a) Outside view of TriboIndenter cabinet, (b) Inside view of the TriboIndenter, (1) acoustic enclosure, (2) granite bridge, (3) XY-Stage, (4) Optic Objective, (5) Z-Axis stage, (6) high load transducer, (7) Triboscanner that contains piezo scanner and low load transducer.

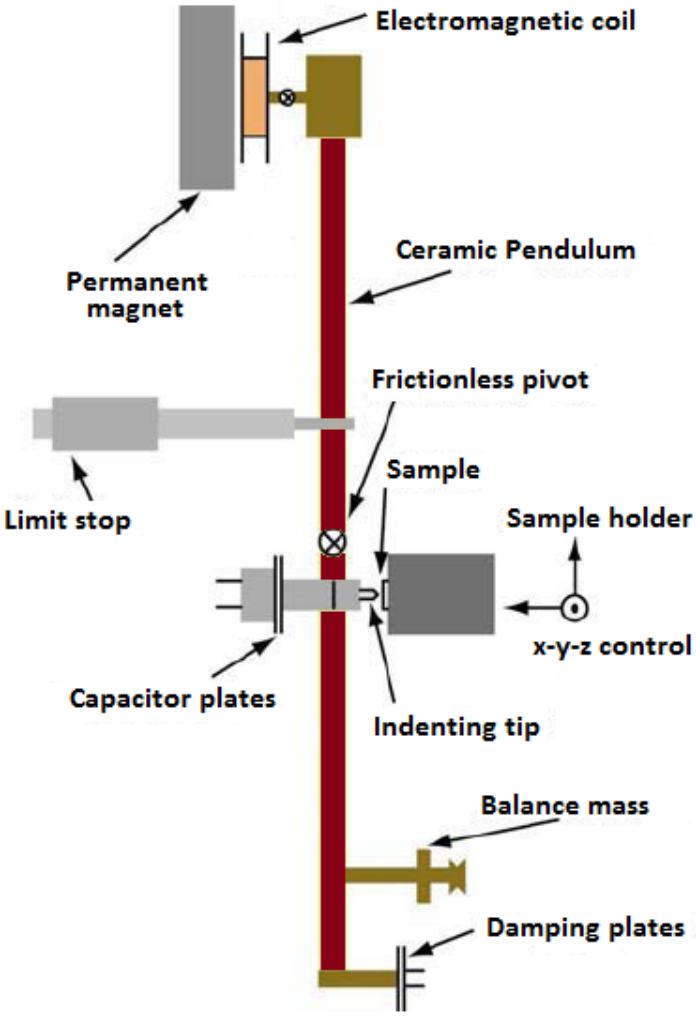

Figure 3-11: Schematic of NanoTest system based on horizontal loading of the specimen.

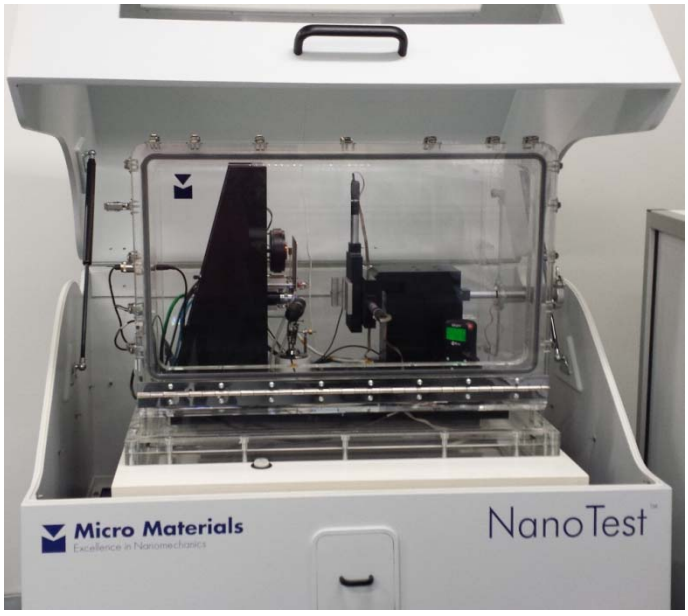

Figure 3-12: Outside view of NanoTest™ platform III from Micro Materials. The entire indentation setup lay on an environmental control chamber.

3.4.2. Basic principles of instrumented nanoindentation

In instrumented nanoindentation, force and depth are measured continuously during loading and unloading while a hard tip with a well defined geometry is pressed into the sample surface. Instrumented nanoindentation relies on the precise knowledge of the real shape of the indenter to estimate the contact area between the indenter and the flat surface from the loading-unloading sequence, allowing the hardness and elastic modulus to be derived. An important component of the indentation system is the probe tip. The indenter tip is generally made of single crystal diamond but other kind of hard materials such as sapphire, quartz, tungsten carbide, and cubic boron nitride can be used. Different shapes of tips are available depending on the type of experiment to carry out. Common geometries of the indenter tip are cones, spheres, four-sided pyramids, like Vickers, and three-sided pyramids, like Berkovich and Cube-Corner tips (figure 3-13). The most common tip in nanoscale testing for probing hardness and elastic modulus is the Berkovich tip, mainly due to two reasons. Firstly, pyramidal indenters have a self-similar geometry with depth, and therefore the type of elasto-plastic deformation induced by the indenter is independent of indentation depth. Secondly, three sided pyramids are easier to grind to a sharp point, allowing for very small indenter tip radius.

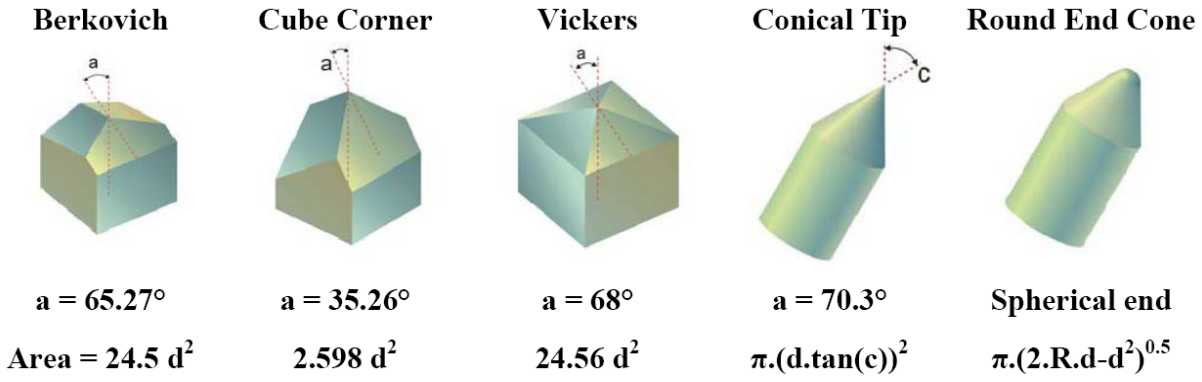

Figure 3-13: Various common indenter shapes and their projected cross-sectional area as a function of indentation depth [101].

3.4.2.1. Hardness and elastic modulus determination

The most commonly used method to analyze nanoindentation data for pyramidal indenters was developed by Oliver and Pharr in 1992 [102]. This method is based on analytical solutions for the elastic contact problem between an indenter and a flat surface. As the direct measurement of the contact area is not always accurate and

convenient, they proposed a procedure to determine the contact area based on the depth of indentation and the indenter shape function. The contact between an indenter and a flat surface can be modeled by the sequence of events illustrated in figure 3-14. At peak load, P_{max}, the material conforms to the shape of the indenter. The total displacement h_{max} is the sum of the contact depth h_c (the vertical distance along which contact is made) and the displacement of the surface at the perimeter of contact h_s, due to elastic deformation of the flat surface:

$$h_c = h_{max} - h_s \tag{3-1}$$

During unloading, the elastic displacements are recovered, and the final depth of the residual impression is h_f when the indenter is fully withdrawn. To determine the contact depth h_c from the experimental data, the displacement of the surface at the contact perimeter h_s, must be obtained. This displacement h_s depends on the geometry of the indenter.

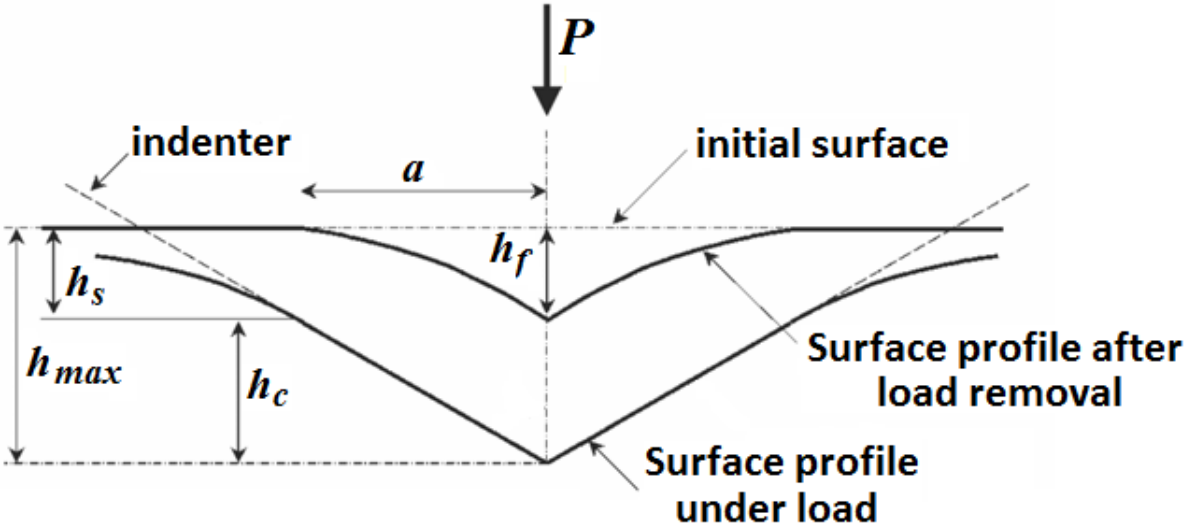

Figure 3-14: Cross-section of nanoindentation profile at peak load and at full unloading for an elasto-plastic material.

Oliver and Pharr assumed that the equations describing the elastic unloading of a flat, semi-infinite half space are the same as those for an indented surface. That is, Sneddon's solutions [103] can be applied to a flat surface or to a surface with a hardness impression. Sneddon derived general relationships among the load, elastic displacement and contact area for any indenter that can be described as a solid of

revolution of a smooth function. Sneddon's expressions for the shape of the surface outside the area of contact can be used to obtain h_s:

$$h_s = \varepsilon \frac{P}{S} \tag{3-2}$$

where P is the indentation load, S the stiffness of the contact, $S = dP/dh$, and ε a indenter geometrical constant that has a value of 1 for a flat punch, 0.75 for a paraboloidal indenter and 0.72 for a conical indenter. Oliver and Pharr obtained that the value of ε that best described the unloading behavior of a Berkovich indenter was 0.75.

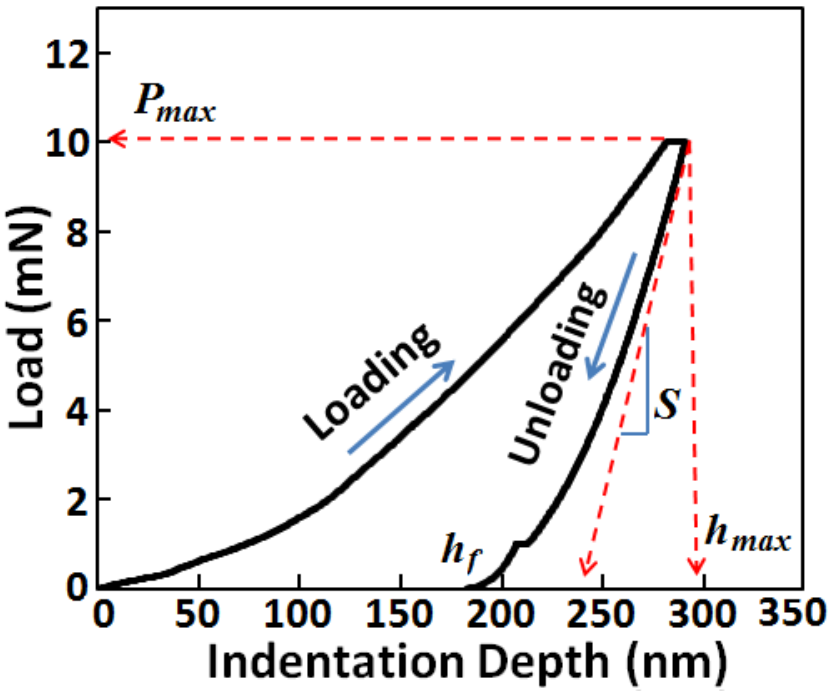

Figure 3-15: A loading-unloading sequence for an indentation in an Al/SiC nanolaminate, indicating the parameters used to estimate the contact depth h_c.

The maximum depth, h_{max}, and the maximum stiffness of the unloading curve, S, can be obtained from the loading and unloading sequence of an indentation, as shown in figure 3-15. They can be used to estimate the contact depth h_c according to equation 3-2. The contact area A_c at peak load is determined from the geometry of the indenter and the contact depth h_c. The indenter geometry is described by an area function $F(h)$ which relates the cross-sectional area of the indenter to the distance from its tip h. The projected contact area A_c is then determined using the relation:

$$A_c = F(h_c) \tag{3-3}$$

whereas the functional form of F must be estimated experimentally prior to the analysis using a standard calibration material (fused quartz) with a well-known elastic modulus. Alternatively, the shape function can be determined directly by careful measurement of the dimensions of the tip using a traceably calibrated, precision metrology device such as an Atomic Force Microscope (AFM).

Both the hardness and the elastic modulus can be determined as follows:

(a) Hardness determination

The hardness can be determined as:

$$H = \frac{P}{A(h_c)} \tag{3-4}$$

where P is the load and $A(h_c)$ is the cross-sectional area of the indenter at a distance h_c from its tip. According to this definition, the measured hardness may be different from the one obtained from the more conventional definition in which the contact area is determined by direct measurement of the size of the residual impression.

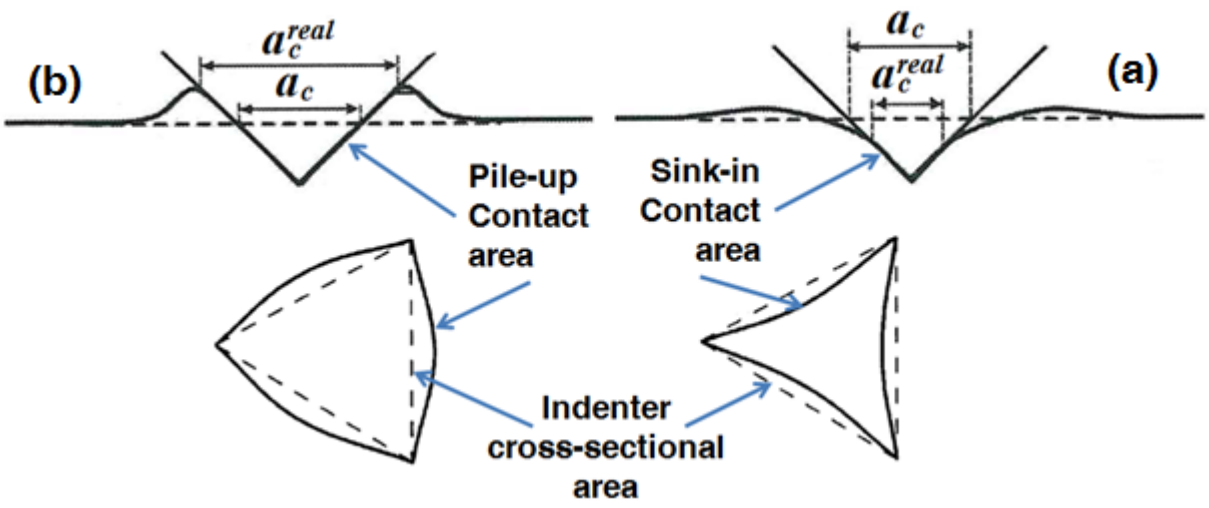

Figure 3-16: Effect of (a) pile-up and (b) sink-in on the real contact area a_c^{real} compared to the contact area a_c derived from instrumented nanoindentation. The dashed line indicates the height of the original surface.

There are two reasons for this difference. Firstly, the material around the indentation may pile-up (or sink-in), as shown in figure 3-16, and the real contact area will be larger (or smaller) than the one derived from equation 3-4. As a result the hardness will be overestimated (underestimated). Secondly, elastic recovery at the sides of the

indentation mark may happen, and therefore the residual size of the indentation will be smaller than that in equation 3-4. However, the size of the residual hardness imprint coincides with the size of contact area *a* at peak load for metals, whose deformation is mainly controlled by plastic deformation. Elastic recovery during unloading in this case usually affects the depth of the residual indentation mark, which decreases from h_{max} to h_f, while the size of contact area a remains constant during unloading. However, this may not be true when elastic recovery is important, as in the case of materials with a very high E/σ_y ratio (> 20) [104]. To avoid uncertainties, the real contact area for most nanolaminates tested in this work was actually measured by direct observation of the residual imprints by either SEM or AFM.

(b) Elastic Modulus determination

The elastic modulus E can be calculated from:

$$S = \frac{2}{\sqrt{\pi}} E_r \sqrt{A(h_c)} \tag{3-5}$$

where S is the initial slope of the unloading curve, as shown in figure 3-15, and E_r the reduced modulus that accounts for the elastic deformation of both the specimen and the indenter and is given by:

$$\frac{1}{E_r} = \frac{1-\upsilon^2}{E} + \frac{1-\upsilon_i^2}{E_i} \tag{3-6}$$

where E_i and E are the elastic modulus and υ_i and υ are the Poisson`s ratio of the indenter and the specimen, respectively.

3.4.3. Micropillar compression

The micropillar compression testing technique was introduced by Uchic and his colleagues [43, 44] to evaluate plastic flow of specimens ranging in size from about 1 μm to several μm. A schematic illustration of the experiment is shown in figure 3-17. This test simulates the compression experiment commonly performed on macroscopic samples, with some modifications to facilitate both the fabrication of the micrometer size specimens and their subsequent manipulation into the testing system. The most remarkable difference is that the microcompression specimens are not freestanding;

rather, they remain integrally attached to the bulk substrate in order to eliminate the need for micromanipulation. Therefore, the substrate acts as the bottom compression platen during the test.

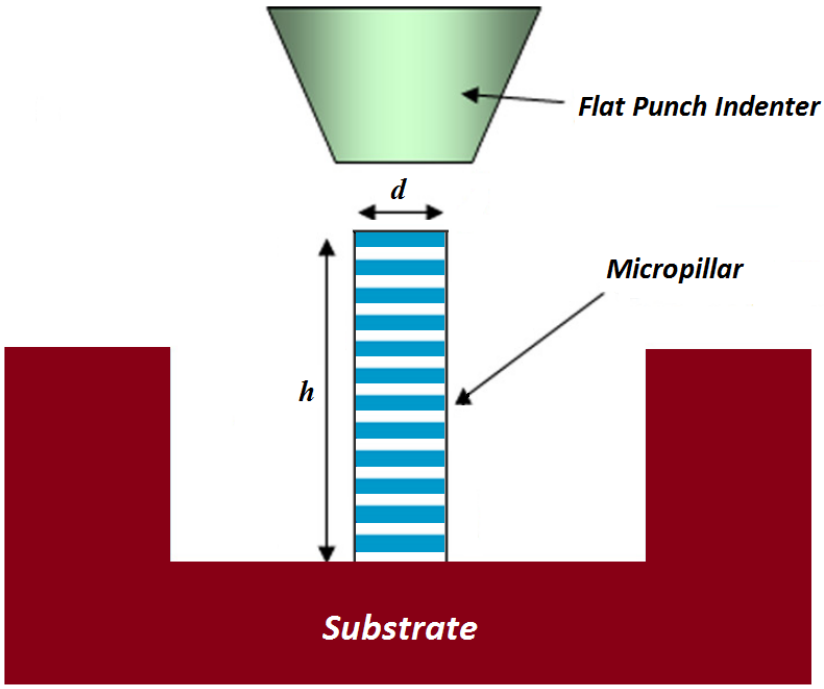

Figure 3-17: Schematic of compression test on a micropillar.

Commercial nanoindentation systems are usually used as the mechanical test frame, where the sharp indentation tip is substituted with a flat punch tip. The load and displacement resolution of many nanoindentation machines are appropriate for microcompression tests. In the last ten years, micropillar compression has been widely applied to study size effects in the mechanical strength of single crystalline metals, such as Ni, Au, Al, Cu, Nb, W, and Mo [42, 105-108], by testing micropillars with diameters ranging from 200 nm to ≈ 20 μm. Most studies used FIB milling to fabricate the micropillars, allowing accurate control of location and size, using the methodology described in section 3.3.3. In most cases, micropillars with a circular cross-section were studied, but others, like square cross-sections are also possible.

3.4.3.1. Challenges

Some of the challenges and/or concerns associated with micropillar compression are summarized below in the context of the application of this test to Al/SiC nanolaminates:

(a) FIB irradiation damage: it is recognized that the use of highly accelerated Ga^+ ions associated with FIB milling creates some surface damage. The depth and nature of this

damaged layer depends on a number of parameters, including the atomic weight and bonding nature of the material, the angle of the incident beam, and the ion energy [87, 90, 92, 94, 109]. Depending on these parameters, several damage types have been reported, from the formation of a thin amorphous layer to the introduction of point and line defects, as well as to the precipitation of Ga-containing phases [93, 110]. While these surface defects might play a major role on single-crystal micropillars, where the strength is very dependent on micropillar diameter, this work relies on the hypothesis that the effect of surface damage should be negligible in Al/SiC nanolaminates. This is because the length scale that controls the strength of Al/SiC nanolaminates, the individual layer thickness, is orders of magnitude smaller than the pillar diameter. As a matter of fact, and as will be shown in chapter 5, and contrary to the single-crystal behavior, the strength was found to be independent of the micropillar diameter in the case of Al/SiC nanolaminates, corroborating the initial hypothesis.

(b) Tapering effect: as explained in section 3.3.3, tapering effects induce a non-uniform stress field that might create artifacts on the determination of stress-strain curves. The results presented in this work were mainly obtained on micropillars fabricated by lathe milling, to minimize these problems.

(c) Elastic deflection of the substrate: the compliance contribution coming from the elastic deflection of the substrate at the base of the pillar should be accounted for to obtain accurate strain measurements. The method for correcting the measured displacement will be discussed in next section.

(d) Misalignment between the flat punch tip and the top surface of the pillar: when the misalignment is greater than 1 degree, stress concentration at the top of the pillar can lead to an underestimation of the yield point and elastic modulus, changes in strain hardening response and buckling [111, 112]. To ensure minimum alignment errors, the nanoindentation apparatus was fitted with a double-tilt stage and a procedure was developed to align the pillars, as will be explained in the next section.

3.4.3.2. Methodology

The uniaxial micropillar compression tests were conducted using the Hysitron TriboIndenter™ and the Micro Materials NanoTest™ platforms described in section 3.4.1. The samples were mounted in such a way as to allow for high temperature testing:

- Hysitron TriboIndenter: In this system, the samples were mounted by mechanical clips. A flat diamond punch with a diameter of 8 μm was used to apply the load. The flat punch tip was brazed to a low thermal expansion coefficient Eclipse® shaft, attached directly to a load transducer.
- Micro Materials NanoTest: Thermally conductive cement was used in this system to mount the samples. The tests were carried out using a sapphire flat punch tip with a diameter of 10 μm, compatible with high temperature testing.

To reduce alignment errors, a novel in-situ method was developed by using the nanoindenter head as a high resolution displacement gauge to determine the surface profile to the sample. The indenter tip was brought in contact with the sample surface at various X-Y locations of the positioning table, and the raw Z displacement measured. The Z displacements at different X-Y locations provided the initial slope of the sample surface, which was corrected by the use of a double-tilt stage mounted between the X-Y table of the instrument and the sample, as schematically illustrated in figure 3-18.

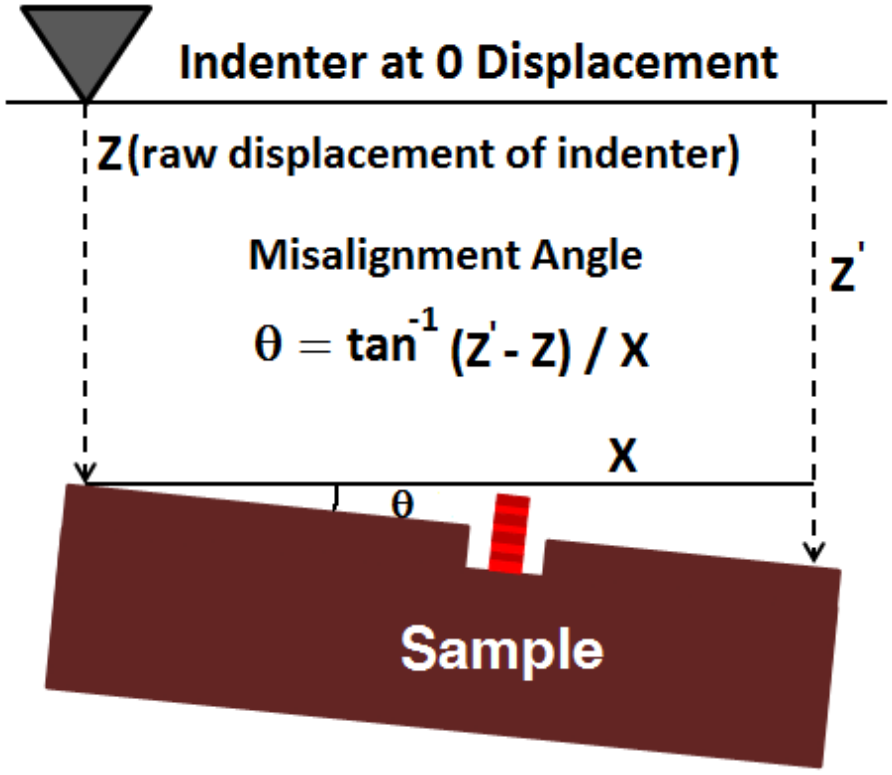

Figure 3-18: Measuring misalignment of sample for micro-compression testing.

3.4.3.3. Stress and strain determination

In order to compute stress and strain from the load-displacement data, the micropillars were considered perfect cylindrical rods of length L_0 and constant cross-sectional area A_0. The true stress and true strain will be given by [84, 85]:

$$\varepsilon = ln\frac{L_0 - u_{pillar}}{L_0} \tag{3-7}$$

and

$$\sigma = \frac{P}{A_0\left(1 - u_{pillar}/L_0\right)} \tag{3-8}$$

where u_{pillar} is the pillar contraction and P the measured load.

The measured displacement of the flat punch, u_{TOTAL}, is different from u_{pillar} because it includes contributions from the elastic sink-in effect of the surrounding material at the base of pillar (u_{sink}) as well as a small contribution from the diamond indenter itself (u_{punch}). So,

$$u_{TOTAL} = u_{pillar} + u_{sink} + u_{punch} \tag{3-9}$$

The sink-in contribution to the measured displacement can be easily corrected using Sneddon's equation [85] for the deflection of an elastic surface by a flat punch, in which the micropillar itself is assimilated to the flat punch, according to:

$$C_{Sneddon} = \frac{du_{sink}}{dP} = \frac{\sqrt{\pi}(1 - \upsilon^2)}{2E_{base}\sqrt{A_P}} \tag{3-10}$$

where $C_{Sneddon}$ is the Sneddon compliance associated with elastic deflection of the surface at the base of the pillar, E_{base} and υ_{base} are the elastic and Poisson's modulus of the base material and A_P is the micropillar cross-sectional area. Sneddon's equation assumes that the pillar is completely rigid, which may result in a slight overestimation of the compliance.

The relative magnitude of each contribution is plotted in figure 3-19. While the contribution of the elastic deformation of the flat-punch (u_{punch}) is negligible, an

accurate determination of the elastic and plastic deformation of the pillar requires the correction of Sneddon's sink-in effect. Figure 3-20 shows the load-displacement curve corresponding to micropillar compression of Al/SiC nanolaminates before and after sink-in correction.

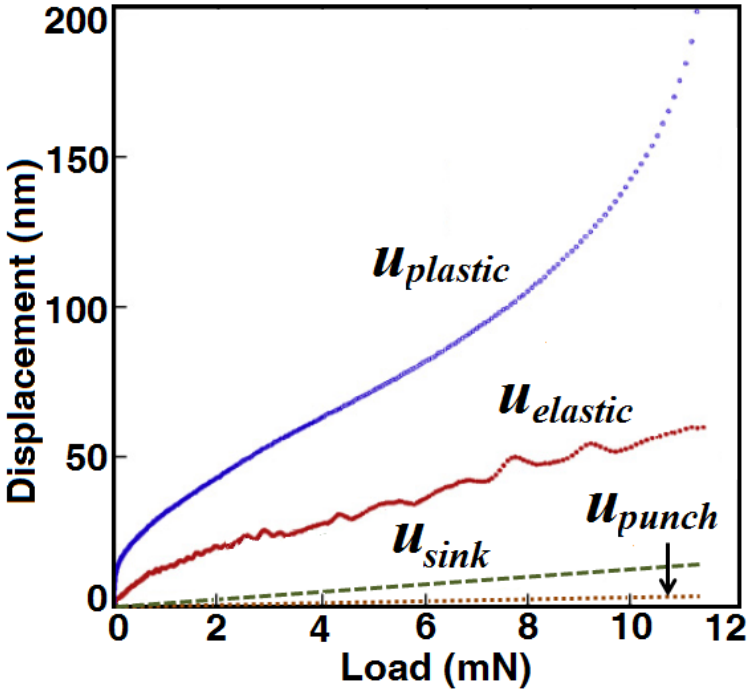

Figure 3-19: Different contributions to the deformation of a micropillar in compression [85].

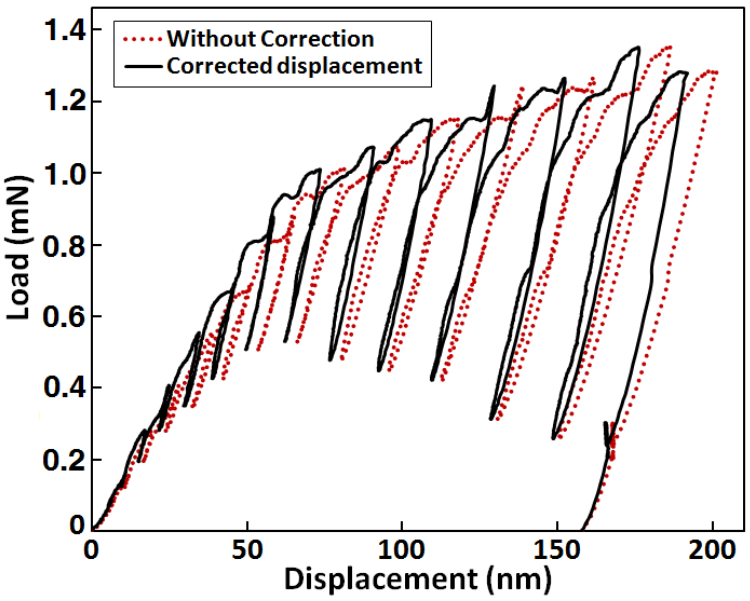

Figure 3-20: Load-displacement curve for micropillar compression of Al/SiC nanolaminates before and after sink-in correction.

So, the pillar contraction was estimated in this work according to:

$$u_{pillar} = u_{total} - u_{sink-in} = u_{total} - C_{Sneddon}P \quad (3\text{-}11)$$

3.4.4. Indentation creep

Indentation creep was used to study the creep behavior of the Al/SiC nanolaminates. Creep is essentially the time-dependent plastic response of a material under stress. In the case of depth-sensing indentation tests, the nominal pressure in the zone under the indenter is often very high, and can easily reach a few percent of the shear modulus of the material. Under these conditions, nearly all materials, including metals and even ceramics, are known to creep to more or less extent at low homologous temperatures. Depth-sensing indentation measurements can be conveniently applied to the study of strain-rate effects on deformation behavior and the creep properties of materials in small volumes [113-120].

In uniaxial tensile creep tests, the steady-state creep behavior of a wide range of materials can be described by a power-law equation of the type:

$$\dot{\varepsilon} = A\sigma^n exp\left(\frac{-Q}{RT}\right) \quad (3\text{-}12)$$

where $\dot{\varepsilon}$ is the strain rate, σ the applied stress, n the stress exponent, Q the activation energy and A some pre-factor. The stress exponent n, given by the slope of $\dot{\varepsilon}$ versus σ in a log-log plot under isothermal conditions, can provide useful information on the rate-controlling deformation mechanism.

Although still a topic of debate in the scientific community, it is possible to draw analogies between uniaxial creep and indentation creep when using self-similar indenters [119]. It has been shown by dimensional analysis that the following scaling relationships are obeyed during indentation of power-law creeping solids with self-similar indenters:

$$\dot{\varepsilon} \propto \dot{h}/h \propto \dot{a}/a \propto \dot{A}_c/A_c \quad (3\text{-}13)$$

and

$$\sigma \propto P/h^2 \quad (3\text{-}14)$$

where P is the indentation load, h the instantaneous indenter displacement and a the radius of the contact zone. Manipulating equations 3-12 to 3-14 leads to:

$$\dot{\varepsilon}_{ind} = CH^n exp\left(\frac{-Q}{RT}\right) \tag{3-15}$$

where the indentation strain rate is defined as $\dot{\varepsilon}_{ind} = \frac{\dot{h}}{h}$, the hardness $H = \frac{P}{A_c}$, and the pre-factor C depends on the material and the indenter geometry.

A typical nanoindentation creep curve can be divided into two regimes: an initial transient regime where the depth increases suddenly and a steady state regime in which the rate of penetration reaches a constant value. This is similar to the primary and steady state creep regimes observed during uniaxial tensile testing. However, there are certain fundamental differences that should be kept in mind when analyzing indentation creep data:

- The specimen is under a uniform stress field during uniaxial creep testing. During indentation, the material under the tip experiences a very complicated triaxial stress state with a strong gradient from the vicinity of the tip to the undeformed surrounding material.
- The creep strain is uniformly distributed over the entire specimen in the steady state regime during uniaxial creep without contribution from the primary transient regime to the overall strain rate. In contrast, during indentation creep, the deformation fields under the indenter tip act as an expanding hemispherical volume. As deformation proceeds, the elastic-plastic boundary expands and new undeformed material enters into the plastic zone. This new material will exhibit primary creep deformation that will be added to the steady-state creep strain present in the already deformed volume. Hence, there will always be a contribution from both primary and steady state creep stages in indentation creep measurements.
- The third fundamental difference is that indentation creep will not show a tertiary stage leading to rupture due to the constraint imposed by the surrounding material to the deforming volume. On the contrary, the penetration rate will decrease over time.

3.4.4.1. Analysis of indentation creep data

Several methods can be found in the literature for the analysis of indentation creep data. They include the depth-sensing, constant-load (*h-CL*) method; the continuous-stiffness, constant-load (*S-CL*) method; the constant loading rate method; and the exponential loading rate method [115, 116, 121, 122]. The *h-CL* method can be easily applied and it has been frequently used to investigate the creep properties of materials. It was selected to measure the creep properties of the Al/SiC nanolaminates in this thesis. The displacement change in this method is monitored at a constant indentation load. Since the contact area increases during the hold period as creep takes place, the indentation hardness and the indentation strain rate will continuously decrease with time. The determination of strain rate and hardness during the hold period thus enables the calculation of the stress exponent.

The indentation strain rate $\dot{\varepsilon}$ can expressed as:

$$\dot{\varepsilon} = \frac{1}{h}\left(\frac{dh}{dt}\right) \tag{3-16}$$

where h is the indentation depth and t the time. dh/dt can be determined by fitting the experimental $h - t$ curve during the holding time to the empirical law:

$$h(t) = h_0 + x(t - t_0)^y + zt \tag{3-17}$$

where h_0, x, y and z are fitting constants, and t_0 is the time necessary to reach the maximum load. The fitting protocol is found to produce very good fits to all the results in Al/SiC nanoscale multilayers. The choice of the fitting equation does not affect the computation of the creep parameters as long as a good fit to the data can be obtained. Figure 3-21 shows the fitting curve for the Al50SiC50 nanolaminate tested at ambient temperature. Differentiation of equation 3-17 allows the calculation of indentation strain rate $\dot{\varepsilon}$ according to equation 3.16.

3.4.4.2. Strain rate sensitivity

Based on the depth-sensing, constant-load (*h-CL*) method, the strain-rate sensitivity m is given by the slope of the double logarithmic plot of hardness H *vs.* $\dot{\varepsilon}$ under isothermal conditions according to the following equation:

$$m = \frac{\partial\, ln(H)}{\partial\, ln(\dot{\varepsilon})} \tag{3-18}$$

while the stress exponent n, defined in equation 3-12, is just the inverse of the strain rate sensitivity, m, and the activation volume is determined as:

$$V^* = \frac{2.8 \times \sqrt{3}\, kT}{H}\left(\frac{\partial\, ln(\dot{\varepsilon})}{\partial\, ln(H)}\right) \tag{3-19}$$

where k is the Boltzmann constant and T is the absolute temperature. In this equation, the yield strength of the nanolaminates is assumed to be given by $\approx H/2.8$.

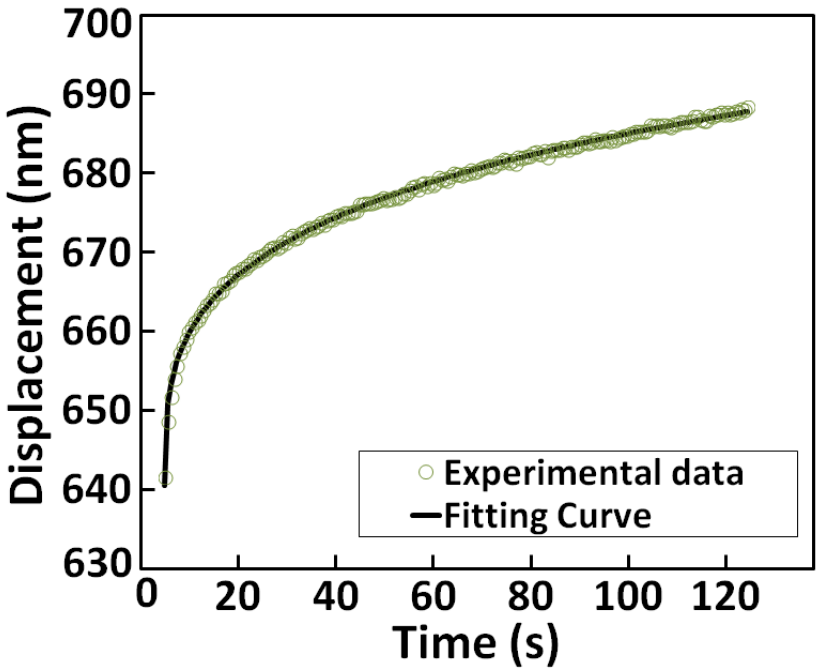

Figure 3-21: Experimental creep curve and fitting with equation 3-17 for the Al50SiC50 nanolaminate tested at ambient temperature.

The corresponding double logarithmic plots of stress *vs.* strain rate and strain rate *vs.* stress for the Al50SiC50 nanolaminate tested at room temperature are plotted in figures 3-22 (a) and (b), respectively. The strain rate sensitivity and the activation volume can be computed from the slope of these plots.

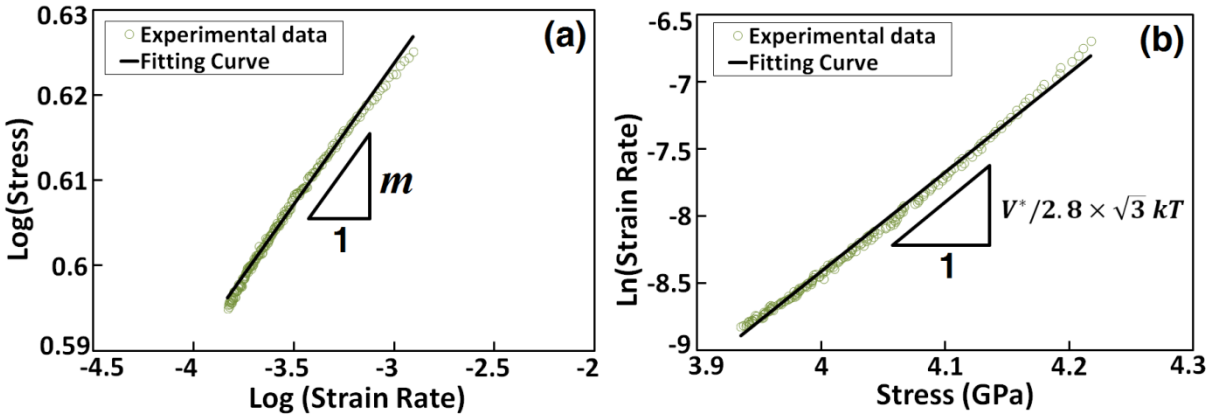

Figure 3-22: Determination of (a) strain rate sensitivity, m, and (b) activation volume, V^*, for the experimental results of the Al50SiC50 nanolaminate tested at ambient temperature.

Strain rate sensitivity and activation volume provide information about the thermally activated deformation mechanisms that control plastic flow. Recent investigations in nanostructured metals have shown that the influence of grain size on the strain rate sensitivity is closely related to the lattice structure of the metals, as summarized by Niu *et al*. [123] in figure 3-23, which shows the evolution of the strain rate sensitivity with the average grain size, for face centered cubic (fcc), body center cubic (bcc), and hexagonal close packed (hcp) metals, respectively.

The data of three representative fcc metals, Cu, Al, and Ni, show a consistent trend with the strain rate sensitivity increasing with decreasing grain size from the micrometer to the submicrometer scale, followed by a sharp rise when the grain size is reduced below a couple of hundreds nanometers (figure 3-23 (a)). The present explanation for this phenomenon is that the highly localized dislocation activity (*e.g.* dislocation nucleation) at the grain boundaries (GBs) is responsible for the enhanced strain rate sensitivity in nanocrystalline fcc metals. On the contrary, the strain rate sensitivity of bcc metals (Fe, Ta, W, V) decreases with grain size from the submicrometer to the nanocrystalline regime. It has been claimed that this behavior is related to the low mobility of screw dislocations in bcc metals, as well as to the increasing prevalence of GB strengthening in the smaller size regime. The strain rate sensitivity of bcc metals is only about ~0.004 when the grain size is below 100 nm, which is 5- to 10-fold smaller than that of fcc metals having the same grain size (figures 3-23 (a) *vs*. 3-23 (b)). Finally, no definitive conclusions can be drawn for hcp metals due to the scatter in the limited experimental data (figure 3-23 (c)).

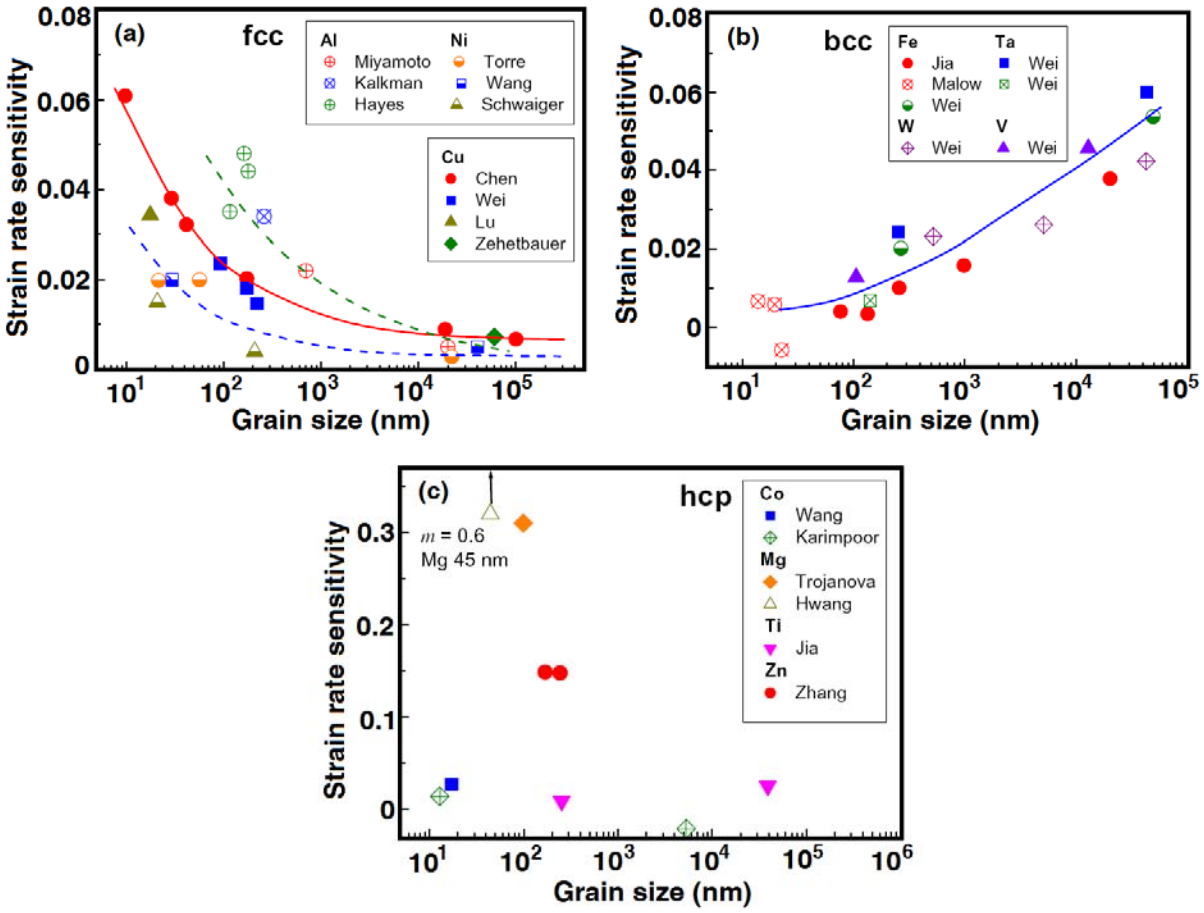

Figure 3-23: Strain rate sensitivity of (a) fcc metals, (b) bcc metals, and (c) hcp metals as a function of grain size [123].

In the case of nanolaminates, and as explained in chapter 2, the layer thickness is the most relevant microstructural parameter controlling strength. However, the strain rate sensitivity of nanolaminates and its thickness dependence are far from clear. Only a very limited number of papers addressing size effects on strain rate sensitivity have been published in nanolaminates. The most relevant results are reviewed below, and they are limited to room temperature studies in metallic multilayers.

Wen *et al*. [124] used the depth-sensing, constant-load (h-CL) method at room temperature to study the strain rate sensitivity of Ag/Co nanolaminates with modulation period from 4 to 60 nm. The total creep depth decreased with increasing hardness of multilayers (figure 3-24), which indicates that the creep resistance increased with hardness. Stress exponent values in the range from 2.5 to 5 determined by dimensional analysis suggested that creep was controlled by dislocation climbing.

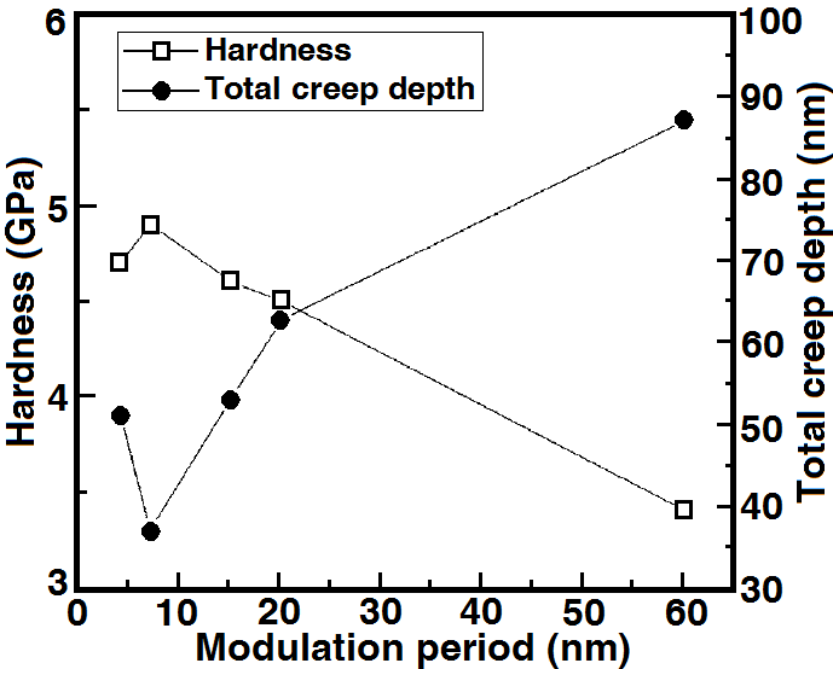

Figure 3-24: Hardness and total creep depth as a function of the modulation period in Ag/Co nanolaminates [124].

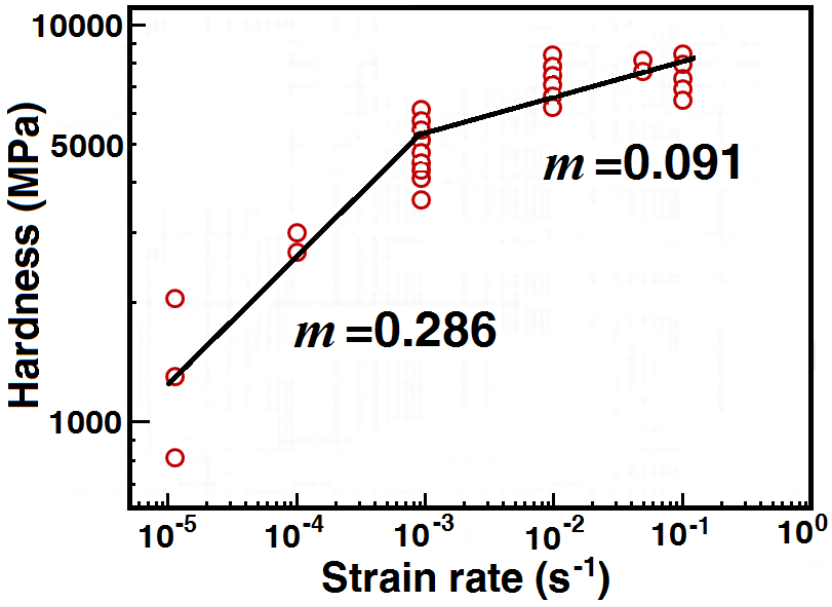

Figure 3-25: Hardness of Cu/Ta multilayers as a function of strain rate [125].

Huang *et al.* [125] investigated the strain rate sensitivity of Cu/Ta nanolaminates at strain rates between 10^{-1} s^{-1} and 10^{-5} s^{-1} at room temperature. The individual Cu and Ta layers had equal thickness (~ 30 nm) but different grain sizes: 26-28 nm for Cu and 9.5-10 nm for Ta. A transition in strain rate sensitivity was found at a strain rate of 10^{-3} s^{-1} (figure 3-25), indicating a competition between dislocation-mediated and GB-mediated

mechanisms in Cu and Ta layers. At higher strain rates (>10^{-3} s^{-1}), plastic deformation of the Cu/Ta multilayer was dominated by dislocation-mediated mechanisms in Cu. At low strain rates (<10^{-3} s^{-1}), the GB-mediated mechanisms in Ta dominated, increasing significantly the strain rate sensitivity of the Cu/Ta multilayers.

Carpenter *et al*. [126] measured the strain rate sensitivity and activation volume of a Cu/Ni metallic multilayer with a modulation period of 42 nm by the strain-rate jump test, using micropillar compression tests at room temperature. The average values for strain rate sensitivity and activation volume are summarized in table 3-2. The values for Cu/Ni nanolaminates were near to the lower range found in nanocrystalline Cu and Ni. It was concluded that the interfaces served as the primary sources and sinks for dislocations, similar to the grain boundaries in nanocrystalline materials.

Table 3-2: Strain rate sensitivities and activation volumes for selected materials [126].

Material	Strain rate jump (s^{-1})	Strain rate sensitivity	Activation volume (b^3)
Nanocrystalline Ni, Cu	-	0.01 to 0.04	8-12
21 nm/21 nm Cu/Ni multilayers	$10^{-4} \rightarrow 10^{-5}$	0.017 ± 0.003	15 ± 9
	$10^{-5} \rightarrow 10^{-4}$	0.010 ± 0.001	22 ± 8
	$10^{-4} \rightarrow 10^{-3}$	0.011 ± 0.002	19 ± 7
	$10^{-3} \rightarrow 10^{-4}$	0.018 ± 0.002	11 ± 4
Coarse grain Ni, Cu	-	0.001 to 0.005	1000

4 Nanomechanical testing at elevated temperature

The main aim of this work was to study the mechanical properties of Al/SiC nanolaminates at high temperature. Since these nanolaminates are grown as thin-films on a substrate, mechanical characterization relays on instrumented nanoindentation and/or other novel nanomechanical testing methods, like micropillar compression. Even though several instrumented nanoindentation instruments capable of operating at elevated temperature have been commercialized recently, the technique itself is by no means well established. This is due to several critical problems that need to be overcome in order to obtain reliable results. They include heat management inside the instrument, thermal drift effects on the measurements and sample and indenter stability as a function of testing conditions. A large part of the research work in this thesis was dedicated to overcome these challenges and to find the best high temperature testing procedure depending on the experimental setup. The most important results are summarized in this chapter.

4.1. Experimental set-up for high temperature nanomechanical testing

The high temperature nanoindentation studies were performed in the two commercial platforms described in section 3.4.1. Since the load and displacement transducers are only capable of operating at room temperature, high temperature nanoindentation relies on heating locally the sample, while appropriate heat shields and active cooling systems are placed to protect the critical components of the instrument. The design of the heating system in each platform is described below.

4.1.1. Hysitron TI 950 TriboIndenter™

Heating of the specimens was achieved through a commercial heating stage with integrated cooling, shown in figures 4-1 and 4-2, coupled to a PID temperature controller. The heater was designed with a small profile to enable concentrated heating of the sample without heating other components of the system. This is important, not only to protect some sensitive components, like the load transducer and the motorized stages, but also to reduce the potential for uncontrolled thermal drift due to expansion and contraction of the elements in the load frame. The heater consisted on a resistive heating wire embedded in a copper cartridge to take advantage of the high thermal conductivity of copper for fast and uniform heating. The heater cartridge lays on the cooling stage by three small ceramic balls arranged in a symmetric tripod configuration, rather than a ceramic layer, to minimize thermal conduction. A ceramic spacer ring reduced heat transfer between the heater and the steel ring that was used to clamp the whole assembly to the main plate (figure 4-1).

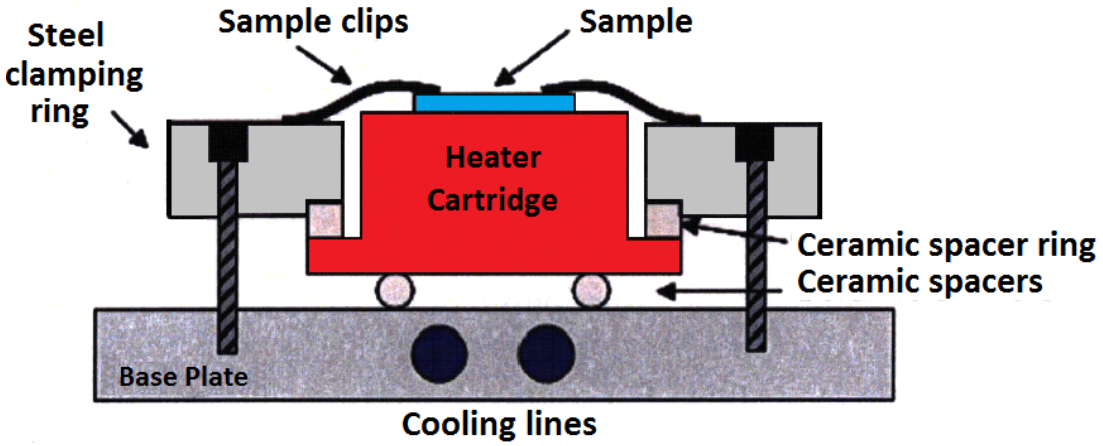

Figure 4-1: Schematic of heating stage in the Triboindenter platform. The steel ring clamps the copper heater cartridge between ceramic spacers which limit thermal conduction between the heater and the rest of the stage.

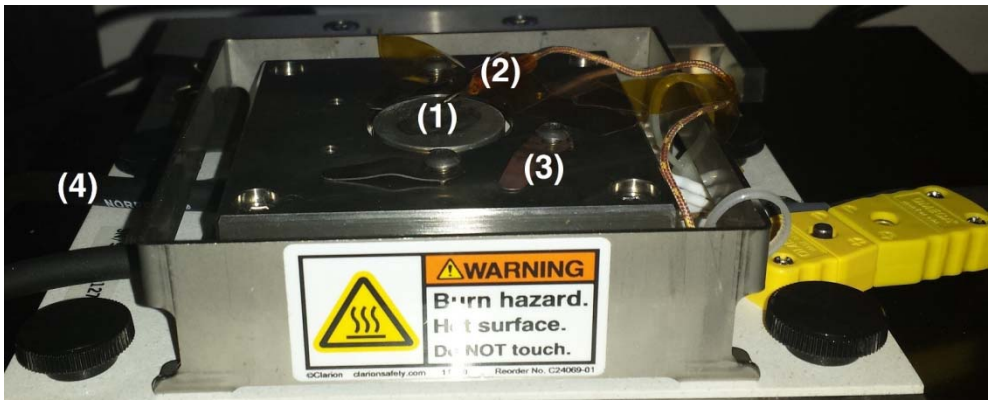

Figure 4-2: Heating stage in the TriboIndenter. (1) Surface of heater cartridge, (2) thermocouple, (3) sample clips, (4) cooling lines.

Considering that this system displays a vertical loading configuration, the transducer must be protected from radiation, conduction and convection heating. This is achieved through an actively cooled heat shield with a small central hole for the indenter assembly, as schematically shown in figure 4-3. Finally, a temperature controlled close-circuit chiller ensures active cooling of both the heat shield and the sample stage (figure 4-4).

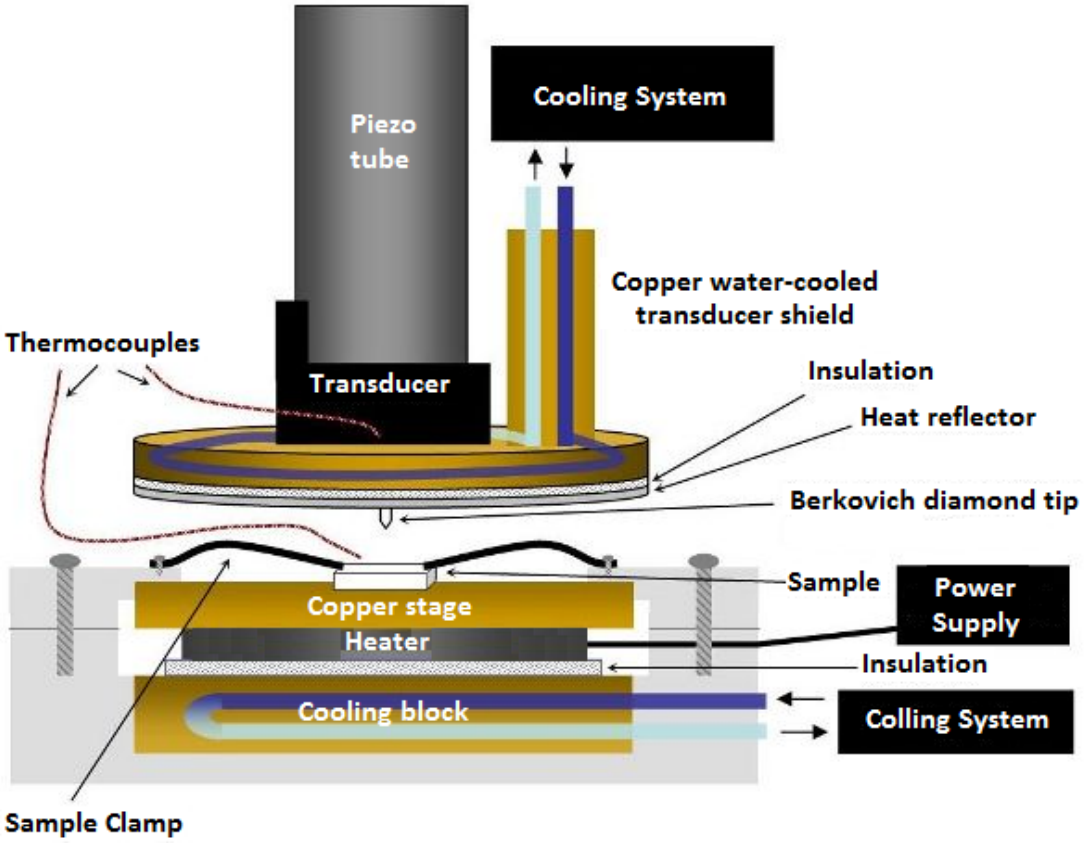

Figure 4-3: Heating system used in the Hysitron high temperature nanoindentation system [127].

This system does not use active heating of the indenter tip, but it rather relies on the principle of passive heating. Heat will flow from the heated sample to the colder indenter tip when contact is first established, until some equilibrium is reached. For this reason, the indenter tip itself should be attached to a special shaft made of a special glass-ceramic with low thermal conductivity and low thermal expansion coefficient.

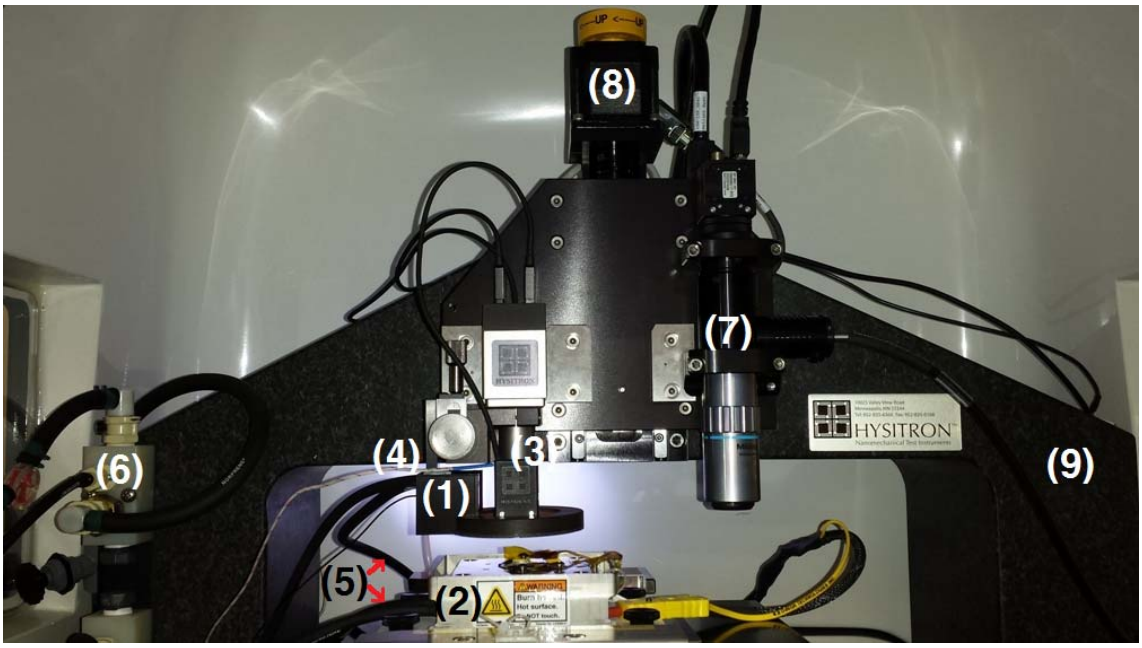

Figure 4-4: Inside view of the TriboIndenter during high temperature testing, (1) heat shield, (2) heating stage, (3) Triboscanner (Piezo tube and transducer), (4) thermocouple, (5) cooling lines, (6) cooling system, (7) optical objective, (8) Z-axis stage, (9) granite bridge.

4.1.2. Micro Materials NanoTest™ platform III

This system also uses a resistive heating stage for mounting the sample while actively cooled heat shields protect the electronics. There are, however, three important differences with the previous system that makes it more adequate for elevated temperature nanoindentation:

a) The system uses a horizontal loading configuration so that convection heating of the electronics is minimized.
b) The principle of active indenter tip heating. The indenter tip itself is independently heated to the test temperature, as shown schematically in figure 4-5. This strategy helps to minimize thermal drift, as explained in section 4.2; figure 4-6 shown the heating set-up for Micro Materials NanoTest system.

c) The entire system is placed inside a chamber that can be purged with Ar down to oxygen contents < 0.1%, minimizing oxidation of the sample surface and tip degradation as well as contamination effects.

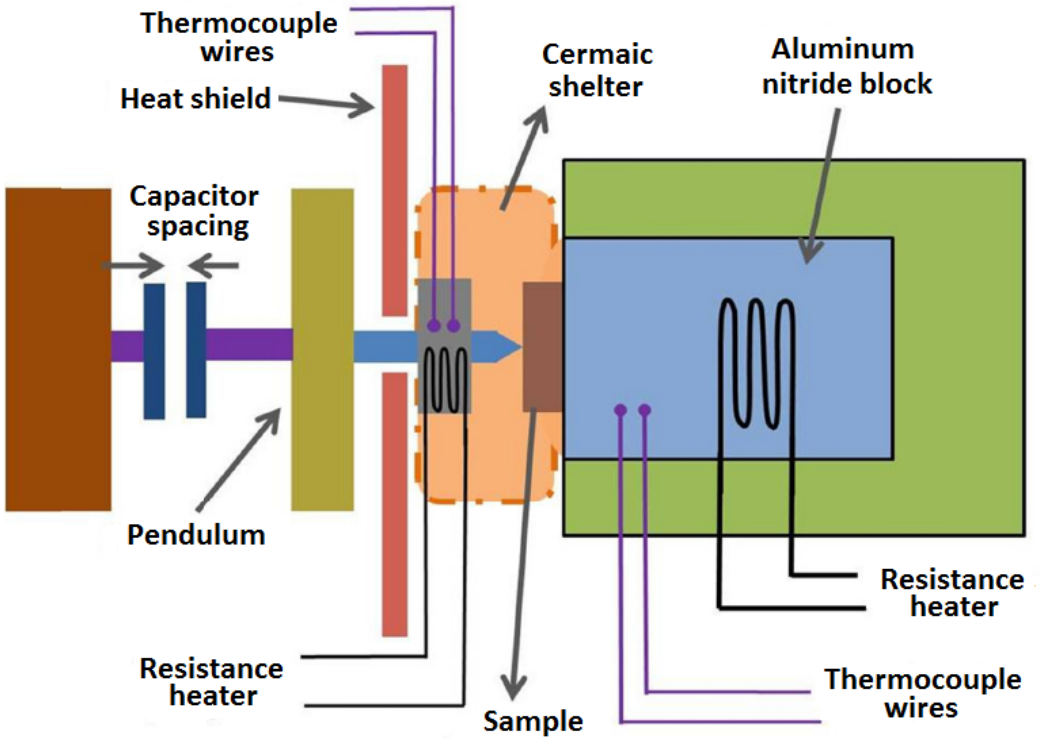

Figure 4-5: Schematic of the hot stage and heated tip set-up for the Micro Materials NanoTest system.

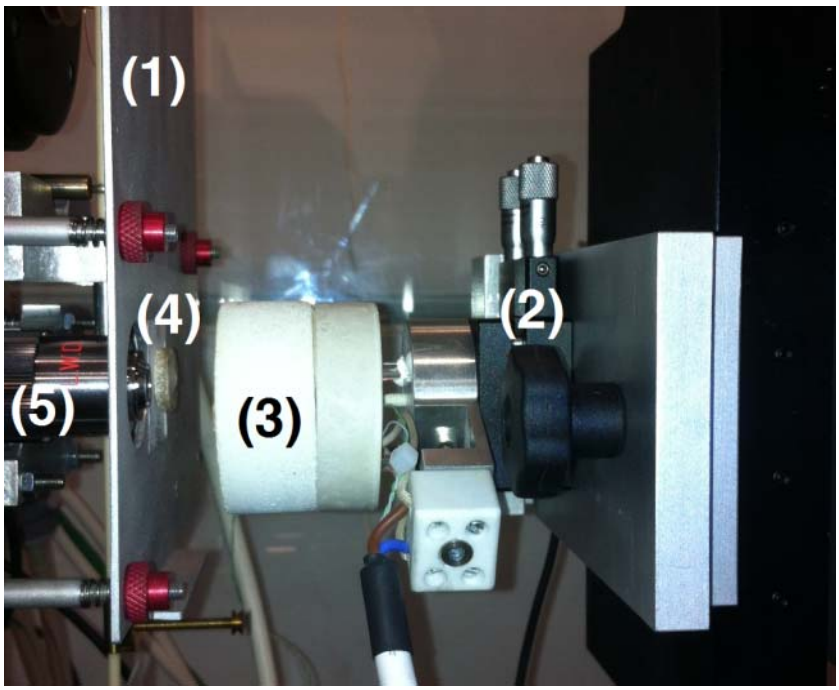

Figure 4-6: Close view of heating set-up for Micro Materials NanoTest system, (1) heating shield, (2) tilt stage, (3) heating stage, (4) heated tip set-up, (5) optical objective.

4.2. Thermal Drift

Thermal drift refers to changes in the measured displacement even when the indenter is maintained at a constant depth within the sample. Thermal drift arises due to electronic drift or small contractions or extensions of different parts of the system motivated by thermal fluctuations inside the chamber. As a result, nanoindentation systems are extremely sensitive to thermal fluctuations as small as 1ºC, and this is the biggest challenge to obtain accurate results during elevated temperature nanoindentation.

Thermal drift must be continuously monitored and corrected during indentation, even at ambient temperature. The most extended procedure to measure thermal drift is to monitor the displacement signal when the contact between the indenter and the sample surface is purely elastic, and therefore, the depth should remain constant with time. During a regular indentation experiment, this is achieved in two stages: when contact is established at a very small load, typically a few μN, and upon elastic unloading, at a small fraction of the maximum load. An estimate of the pre-indentation and post-indentation drift rates can be obtained by monitoring depth over time during both stages, respectively.

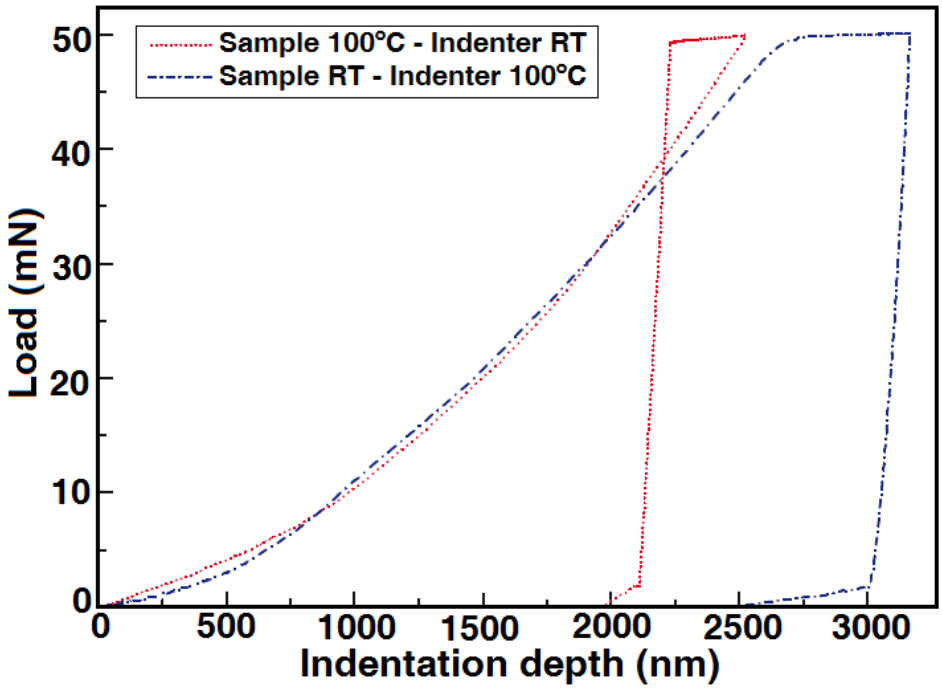

Figure 4-7: Load-indentation depth curves for indentations performed under load control in Al with a temperature gap of 75ºC between the indenter and the sample. The red curves stand for the case in which the sample was heated to 100ºC while the indenter was mantained at ambient temperature. The blue curves stand for the opposite situation (indenter at 100ºC, sample at ambient temperature) [128].

For reliable results, drift rates before and after the test should be equal and small, typically < 0.1 nm s^{-1}. This condition is routinely achieved during nanoindentation at ambient temperature in any commercial system, but it becomes a challenge at elevated temperature. For this reason, a large effort was dedicated in this work to minimize thermal drift.

It was found that the major source of thermal drift is actually thermal flow between the indenter and the sample motivated by temperature difference between the two. The temperature gradient between the indenter and sample can be reduced by holding the indenter in contact with the sample for a stabilization period, but this method cannot achieve complete thermal equilibrium. The effect of a temperature gap of ≈ 75ºC between sample and indenter on the load – penetration depth curves is shown in figure 4-7. All curves were obtained under load control. The red curves stand for the case in which the sample was heated to 100ºC while the indenter was mantained at ambient temperature. The blue curves in figure 4-7 stand for the opposite situation (indenter at 100ºC, sample at ambient temperature). Heat will flow towards the indenter if the indenter tip is colder than the sample (red curves). The indenter temperature will rise, inducing the thermal expansion of the tip and of the indenter shaft. In order to maintain a constant load, the system will react withdrawing the indenter, giving rise to a spurious decrease in indentation depth. The opposite behavior (increasing penetration depth with time at constant load) will be found when the indenter is hotter than the sample [128].

Similar effects are observed when the tests are carried out in displacement control, as shown in figure 4-8. In this case, the particular outcome depends on the frame compliance of the system. If heat transfer occurs from the sample to the indenter (hotter sample), the indenter and the indenter shaft will expand, and the system will react by reducing the load proportional to the frame compliance. The opposite behavior (increasing the load proportional to the frame compliance) will take place if the indenter is hotter than the sample. This results in differences in the slope of the load-Indentation depth during loading, as shown in the red and blue curves in figure 4-8.

The analysis of the geometry of the contact suggests that the main factor influencing thermal drift during elevated temperature nanoindentation is the indenter tip assembly. Samples are typically flat and have much larger lateral dimension than the indenter, so the sample surface will constrain any thermal expansion or contraction.

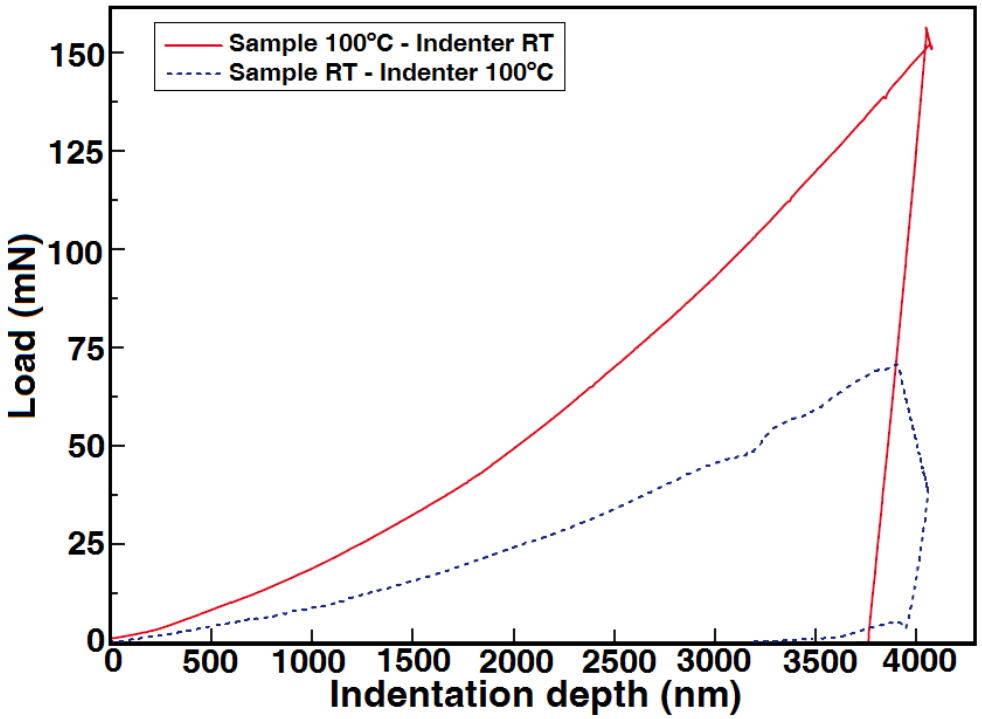

Figure 4-8: Load-indentation depth curves obtained under displacement control for indentations performed under load control in Al with a temperature gap of 75ºC between the indenter and the sample. The red curves stand for the case in which the sample was heated to 100ºC while the indenter was mantained at ambient temperature. The blue curves stand for the opposite situation (indenter at 100ºC, sample at ambient temperature) [128].

Regarding the indenter tip assembly, the main components that can contribute to the thermal expansion are the indenter itself, the shaft and the brazing between indenter and shaft, as schematically illustrated in figure 4-9. Diamond indenters present a very high thermal conductivity and are expected to achieve a constant temperature immediately after being brought in contact with the sample. The contribution of the brazing is also expected to be negligible due to its small dimensions. Therefore, the thermal expansion of shaft is thought to dominate thermal drift when passive heating is used. Two different glass-ceramic indenter shafts (extended length Macor® and super extended length Zerodur®) were used in this investigation, with the second providing the most reliable results. The thermal properties of the corresponding glass-ceramics are found in table 4-1.

Table 4-1: Thermal properties of Macor and Zerodur glass ceramics.

Thermal Properties	Macor®	Zerodur®
Thermal conductivity (W m^{-1} K^{-1})	1.46	1.46
Thermal expansion coefficient (10^{-6} K^{-1})	9.3	0 ± 0.007

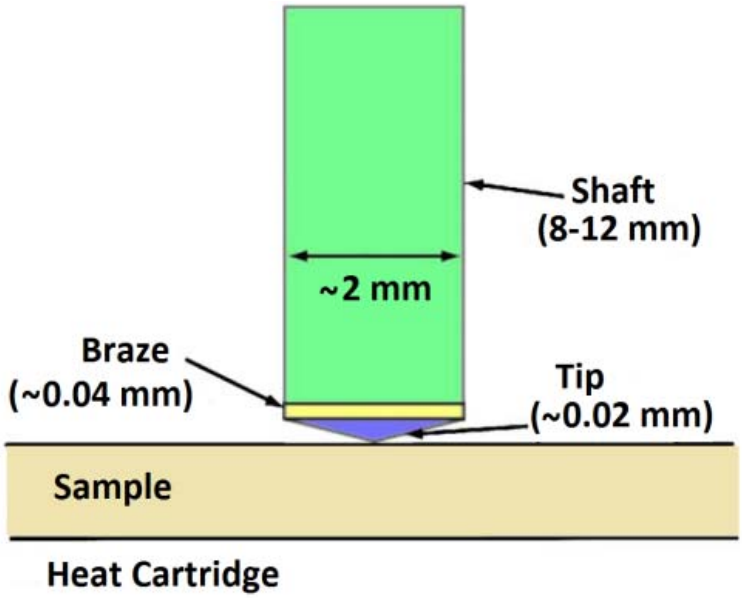

Figure 4-9: Schematic illustration of the indenter tip assembly [127].

Despite of these improvements with the selection of the shaft material, passive indenter heating systems tend to give unreliable results, especially when the contact area is changing during indentation. Under these conditions, the heat transfer by conduction between the sample and the indenter tip is continuously changing during the test and thermal stability cannot be achieved. Additionally, the thermo-mechanical properties of the sample play a very important role. For instance, by comparison of the drift rates during nanoindentation of Al and fused silica, it was concluded that materials with high thermal conductivity and low hardness give rise to higher drift rates. While the effect of higher thermal conductivity is obvious (facilitates heat transfer and thus thermal drift), softer materials lead to larger contact areas and also enhance the heat transfer between sample and indenter. Thus, the influence of the different parameters (indenter and sample temperature, thermo-mechanical properties of the sample) on the magnitude and direction of thermal drift during elevated temperature nanoindentation is summarized in figure 4-10.

Considering all these factors, active indenter heating is thought to be the only alternative to minimize and control thermal drift during high temperature nanoindentation. This is particularly critical if the tests are carried over long periods of time (creep tests) because it is the only method that allows achieving thermal equilibrium and negligible heat transfer between the sample and the indenter independently of the properties of the indented material.

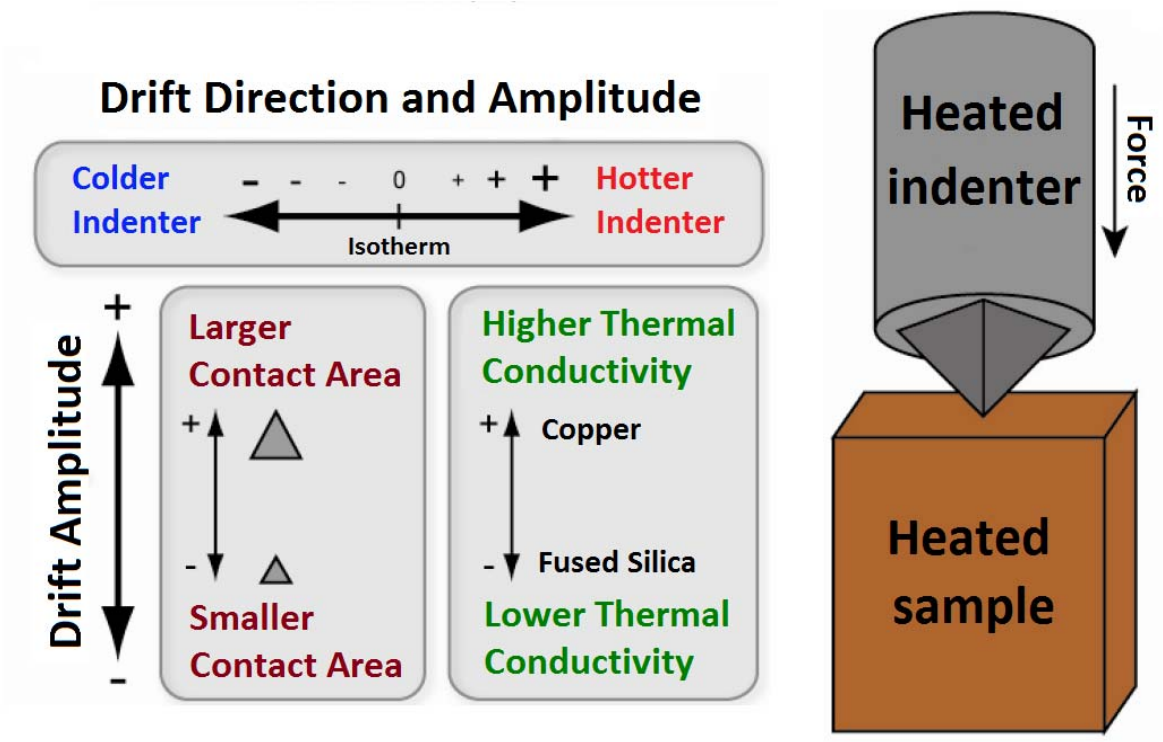

Figure 4-10: Schematic diagram showing the influence of different parameters (indenter and sample temperature, thermo-mechanical properties of the sample) on the magnitude and direction of thermal drift during elevated temperature nanoindentation.

4.3. Sample oxidation

Sample oxidation can be one of the most important challenges associated with testing at elevated temperatures. However, this was not a critical issue for Al/SiC nanolaminates, in which tests could be carried out in air at temperatures up to 300ºC. The most limiting factor in this case is the growth of the native oxide layer of Al_2O_3, which can contribute to errors in the determination of the hardness and modulus at low indentation depths. AFM images of indents carried out 100ºC, 200ºC and 300ºC in a 1 μm monolithic Al coating in air are shown in figure 4-11. The maximum indentation depth was 250 nm in all cases. They show that surface oxidation becomes apparent at 100ºC and affects considerably the surface topography at 300ºC. However, these effects were limited in monolithic SiC coatings as well as in the Al/SiC multilayers, even in air that were indented up to 300 ºC without any oxidation effects.

4.4. Indenter tip effects

The most important indenter tip effects to be taken into account when performing elevated temperature nanoindentation are:

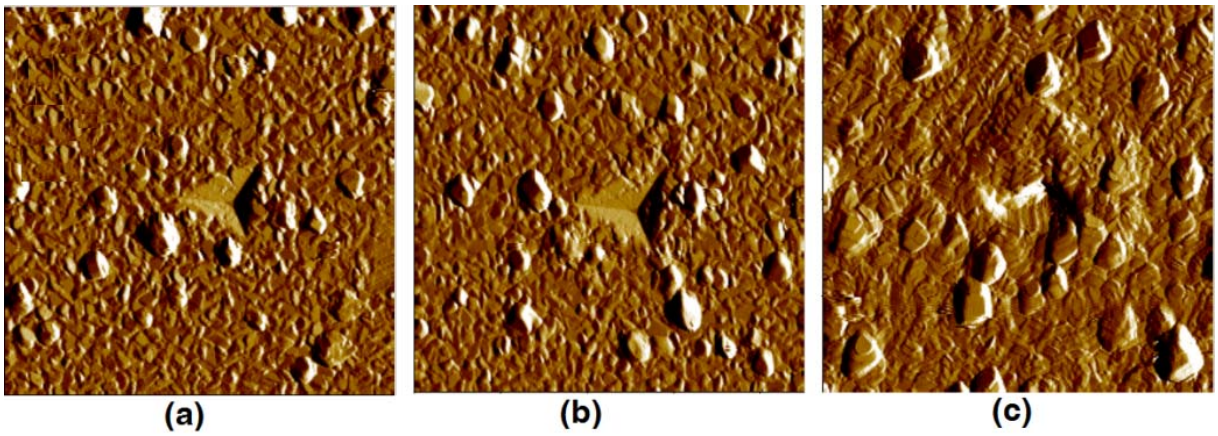

Figure 4-11: AFM topography images (8 μm scan size) of the indentation imprint of a monolithic Al coating at (a) 100°C, (b) 200°C, and (c) 300°C.

(a) Thermal expansion of the indenter: it can lead to errors in the tip area function which is usually calibrated at room temperature. However, in the case of diamond indenters, properties like hardness and reduced modulus can be accurately extracted from high temperature data using area calibrations performed at ambient temperature because the thermal expansion of the diamond geometry is less than 0.04% at 400°C [129].

(b) High temperature degradation of the tip: transformation to graphite of diamond indenters can occur above 400ºC. Thus, sapphire and cubic boron nitride indenters are recommended above 400ºC.

(c) Interaction between indenter material and specimen: This interaction can occur due to chemical reactions between the indenter and the tip, accelerated wear of the indenter tip as well as adhesion effects that might result on loss of material from the tip and/or material transfer from the specimen to the indenter tip, resulting in indenter tip contamination. Chemical indenter-material interactions that have been observed so far during elevated temperature nanoindentation are summarized in table 4-2 [130]. Figure 4-12 shows an example of severe material loss in a diamond tip after indenting a steel sample at 500ºC. It should be noted that this kind of interactions are often the most limiting factor to carry out high temperature nanoindentation of a given material.

In this work, a diamond indenter was used to carry out nanoindentation of the Al/SiC nanolaminates as well as the monolithic Al and SiC layers at 300ºC. Different tip effects were observed in each case:

Table 4-2: Chemical indenter-materials interactions during high temperature nanoindentation [130].

Indenter Material	*Sample Material Classes*						
	Alkali Metals Li, Na, K, Rb, Cs	*Alkaline Earth Metals* Be, Mg, Ca, Sr	*Early Transition Metals* Se, Ti, V, Cr, Y, Zr, Nb Mo Hf Ta W	*Ferrous Metals* Mn, Fe, Co, Ni	*Noble Metals* Ru, Rh, Pd, Re Os Ir Pt	*Coinage Metals* Cu, Zn, Ag, Cd, In Sn Au Pb Bi	*Metalloids* Al, Si, Ge
Diamond	Inert	Inert	Dissolves carbon/Forms carbides	Dissolves carbon *e.g. Fe ~400°C*	Dissolves carbon >1000°C	Inert	Forms Al_4C_3>700°C with Al Forms SiC>1200°C with Si
Carbides *B_4C*	Unknown	Inert	B4C reacts with Ti & Zr	B4C forms borides/carbides	Inert	Inert	Forms borides
SiC	Unknown	Inert	Inert	Dissolves SiC	Inert	Inert	Forms Al_4C_3 with Al
WC	Unknown	Inert	Mostly Inert – may lose carbon by diffusion	Mostly Inert – may lose carbon by diffusion	Inert	Inert	Inert
Nitrides *cBN*	Unknown	Inert	Mostly Inert Mo, Ti & Cr may form nitrides/borides	Dissolves *e.g. Ni ~300°C*	Inert	Inert	Forms borides & nitrides
Oxides *Al_2O_3*	Dissolves	May reduce oxide	Mostly Inert Ti & Cr may reduce oxide *e.g. High Cr steel ~700°C*	Dissolves *e.g. Ni ~300°C*	Dissolves in Pd & Pt	Dissolves in Zn & Bi	Reduces oxide e g. Al ~400°C

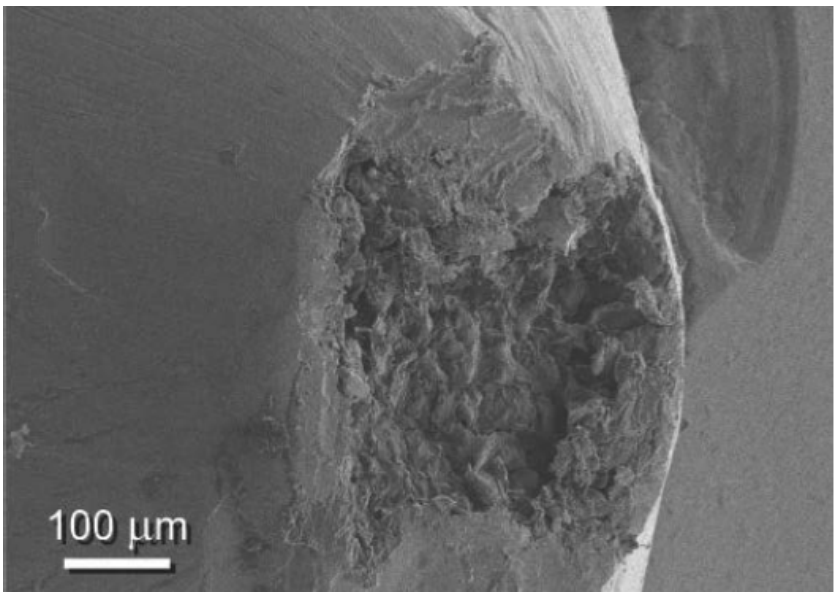

Figure 4-12: SEM image of a degraded diamond tip after indenting a steel sample at 500°C [130].

- In the case of the Al/SiC nanolaminates (with hardnesses in the range 3 to 10 GPa depending on individual layer thickness), the diamond tip could be used to carry out a large number of indents (up to 300°C) without dimensional changes, tip degradation and/or contamination.
- In the case of monolithic SiC coating (with hardness around 30 GPa), accelerated wear of the diamond tip was observed after a small number of

indentations at 300ºC. Continuous re-calibration of the indenter tip was required to account for the change in the tip shape to obtain accurate results afterwards (figure 4-13).

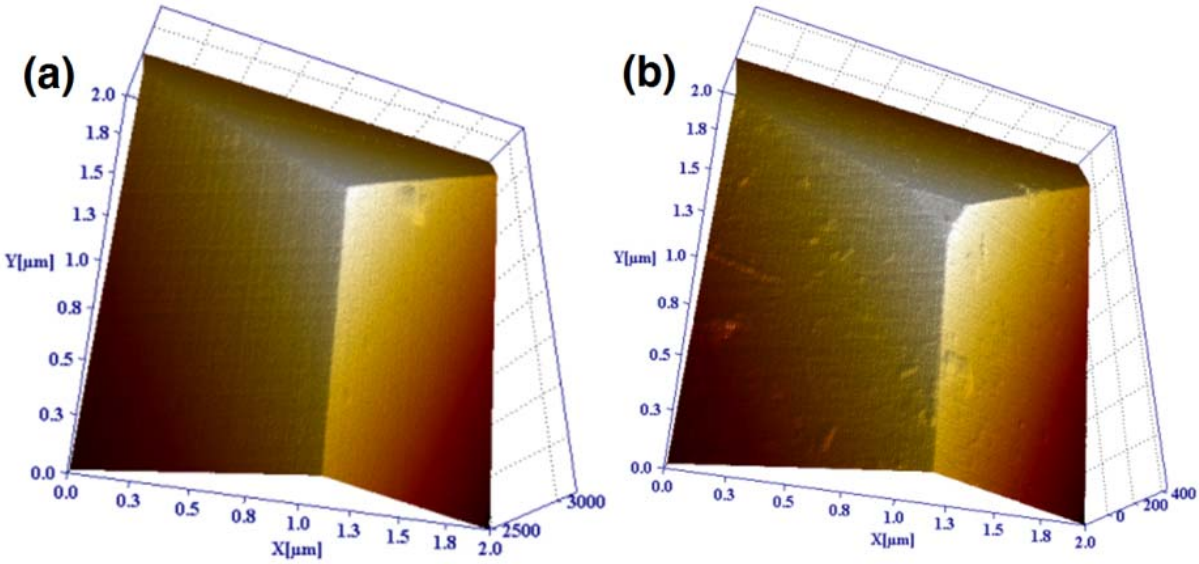

Figure 4-13: AFM 3D topography images of (a) a new diamond Berkovich tip and (b) after nanoindentations in SiC monolithic coating at 300ºC (2 μm scan size).

- In the case of the monolithic Al coatings, severe degradation of the tip was observed after indentation at 300ºC, resulting in irregular hardness impressions, as shown in Figure 4-14 (c).

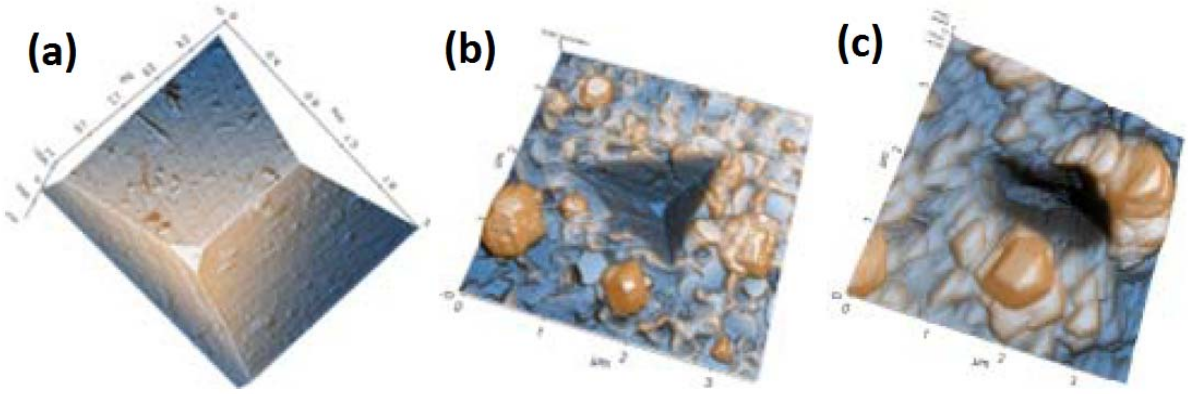

Figure 4-14: (a) AFM 3D topography images of (a) diamond Berkovich tip (2 μm scan size), and hardness impressions on a monolithic Al coating at (b) 200 °C and (c) 300 °C (3.5 μm scan size).

Degradation of the tip after indentation of Al at 300ºC occurred due to transfer of material from the coating to the indenter tip, as shown in figure 4-15 (b), presumably coming from the oxidation of the Al surface. Several strategies were followed to clean

the diamond indenter tip after high temperature nanoindentation, such as the use of different solvents (ethanol, acetone), sliding a piece of scotch tape through the indenter tip and performing large indents in wood and Si surfaces. The most successful cleaning procedure began with the application of small drops of hot phosphoric acid to the tip using a cocktail stick for a few seconds, taking care of not attacking the diamond holder. This was followed by indentation on a wood surface and final washing in ethanol. This cleaning procedure was repeated several times until most of the oxide was removed, as shown in figure 4-15 (c), allowing the re-utilization of the tip after severe contamination.

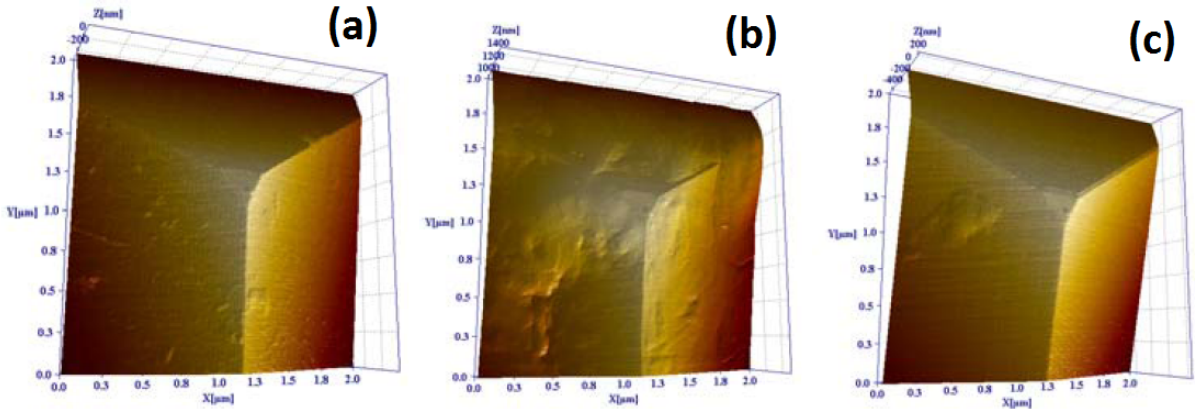

Figure 4-15: AFM 3D topography images (2 µm scan size) of the diamond Berkovich tip used for high temperature nanoindentation of monolithic Al coatings: (a) before testing, (b) after several nanoindentations 300°C and (c) after cleaning to remove the oxide contamination.

4.5. High temperature testing of Al/SiC nanolaminates

The testing procedure to minimize thermal drift, sample oxidation and tip degradation under either passive heating or active heating is described in detail in this section. The tests were carried out between ambient temperature and 300ºC using diamond indenters. Sample oxidation and tip degradation were minimum even when the tests were carried out in air, with the exception of the monolithic Al coatings, as described above. So, the most critical issues to obtain reliable results under active or passive heating were:

- Mounting of the samples: mechanical clips to fix the samples (available in the Hysitron platform) gave rise to an increase in system compliance at high temperature. So, thermally conductive cement, “Omega Bond 400”, was used in all cases to mount the samples.

- Control of surface temperature: the use of hot plates to heat up the specimens introduces some uncertainty when the heater temperature is used as reference. This is particularly important for thick coatings of low thermal conductivity materials, because a large thermal gradient can develop between the bottom and the top coating surfaces. A good recommendation is therefore to limit the sample thickness to less than 1 mm. In this case, sample thickness was limited by the thickness of the Si substrate (0.7 mm) and an additional thermocouple was attached to the sample surface using the same thermally conductive cement, so that the surface temperature was continuously monitored. The temperature gap observed between the bottom and the top surface of the coating was typically of the order of 5ºC for a target temperature of 100°C, 10°C for 200°C, and 20°C for 300°C.
- Thermal drift: control of thermal drift was by far the most critical factor to obtain reliable results. The procedure followed is described below, depending on the use of passive or active heating of the indenter tip.

4.5.1. Passive indenter heating

This was the approach followed in the Hysitron TI950 TriboIndenter system:

1) Sample temperature was gradually increased using the PID controller using a heating rate of 10 ºC/min;
2) Once the sample temperature was stabilized (temperature changes were below 1ºC per 10 minutes), the indenter was brought into contact with the sample with a small contact force of 2 μN. The extension of the piezoscanner was monitored and the vertical displacement was compensated with the Z-motor of the stage to ensure that thermal expansion of any part of the system did not lead the scanner out of its vertical range (~3 μm). The time required to reach thermal equilibrium was of the order of 60 minutes. Afterwards, the PID controller of the heater was disabled and operated at constant power, in order to avoid small fluctuations in sample temperature caused by the feedback loop.
3) To minimize thermal transient effects, a series of indents at different locations were performed by moving the sample without losing contact between the indenter and the sample surface.

4) For each indent, both pre-loading and unloading thermal drift rates were measured using the procedure described in section 4.2. Only those tests with a drift rate < 0.1 nm s^{-1} were considered for analysis.
5) Despite of these precautions, it was found that, thermal transients do actually occur during indentation when using passive indenter heating due to the continuous change of the contact area, and hence thermal conduction between sample and indenter during loading and unloading. So, reliable results were only possible when using fast loading and unloading rates to minimize drift rate effects. In particular, a loading time of 1 s and an unloading time of 0.5 s were used thorough this work. Interestingly, thermal drift during loading and unloading was less pronounced in micropillar compression compared with indentation. This is probably due to the fact that, contrary to indentation tests, the contact area between the flat punch and the micropillar remains constant during loading and unloading.

4.5.2. Active indenter heating

This was the approach followed in the Micro Materials NanoTest system, providing a much better control of thermal drift. The procedure must ensure that both tip and sample are heated to the same temperature, so that thermal transient effects are negligible even when the contact area is changing. The procedure followed in this case is briefly described below:

1) The system was purged in Ar overnight, achieving an atmosphere with oxygen content < 0.1 %.
2) Sample and indenter temperature were gradually increased using the two independent PID controllers using a very low heating rate of 2-5 ºC/s, to avoid thermal shock.
3) Depending on sample and indenter combination, the temperature may vary when they are brought into contact due to thermal flow between them. So, some preliminary indents were performed in order to fine tune the parameters of the PID controllers to achieve the same temperature and minimize the drift rate, which was monitored both at the beginning and at the end of the test. It is actually possible to generate a calibration plot of measured indenter-sample surface temperature as a function of indenter temperature set point [128]. After

fine tuning, the PID controllers were disabled and the heaters operated at constant power to avoid any temperature fluctuations.

4) Using this approach, it was actually possible to carry out indentations at elevated temperature with negligible drift rates (<0.01 nm s^{-1}) over periods of several minutes. This approach was used to carry out the indentation creep tests described in section 3.4.4 during 10 minutes at 150ºC.

5 Nanoindentation of Al/SiC nanolaminates

This thesis is aimed at providing a detailed study of the relationship between the microstructure and the mechanical properties of Al/SiC nanolaminates. Taking into account the current state of the art in this field, this information is important to understand the critical deformation and fracture mechanisms in this novel class of materials. Many important mechanical properties (such as the elastic modulus, the hardness and the time-dependent behavior) can be obtained by means on nanoindentation and they are presented below.

This chapter begins with the analysis of the morphology and microstructural features of the Al/SiC nanolaminates manufactured by magnetron sputtering. Afterwards, the elastic modulus and hardness of Al and SiC monolithic layers are reported as a function of temperature. This is followed by a systematic analysis of the influence of Al and SiC

layer thickness and volume fraction on the mechanical properties at ambient temperature. After that, the mechanical properties of one nanolaminate containing Al and SiC layers on 40 nm in thickness were measured from ambient temperature up to 300ºC. Following these tests, it was decided to focus the systematic analysis of the influence of Al and SiC layer thickness and volume fraction on the mechanical properties to the temperature range between 50ºC and 150ºC. Finally, the strain rate sensitivity of the Al/SiC nanolaminates was determined from 50ºC to 150ºC as a function of the layer thickness/volume fraction.

5.1. Morphology and microstructure of Al/SiC nanolaminates

Al/SiC nanolaminates were deposited by magnetron sputtering on a Si (111). The layers were relatively uniform throughout the thickness of the laminate (figure 5-1). Analysis by TEM showed that the Al/SiC interfaces were clean with no evidence of any chemical reaction, figure 5-1 (b). The first layer deposited on the atomically smooth thermally grown SiO_2 substrate layer was Al.

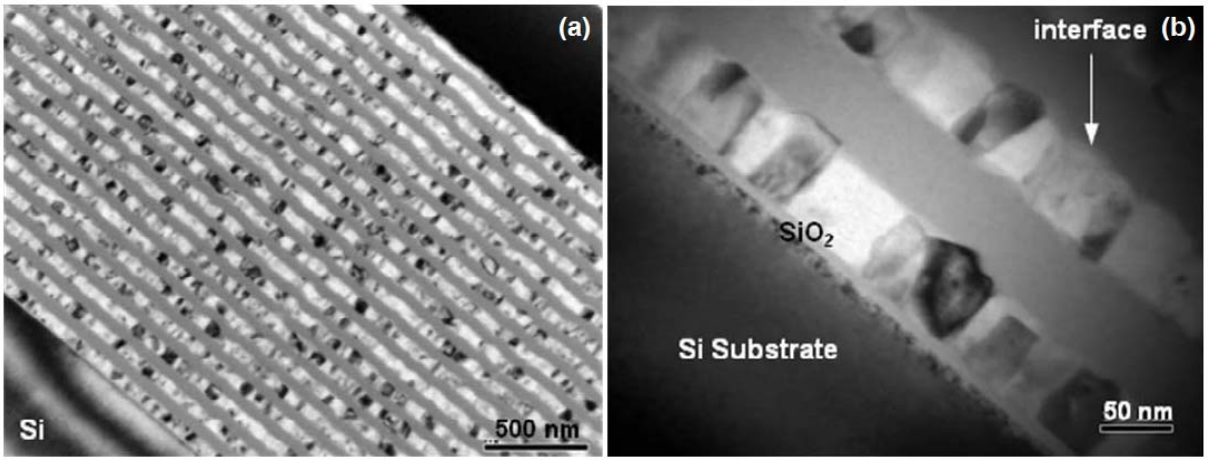

Figure 5-1: (a) Microstructure of Al/SiC nanolaminate. (b) The interface between Al and SiC are chemically abrupt, with no evidence of chemical reaction.

The amorphous structure of SiC can be attributed to the relatively low deposition temperature (below 100°C). The Al layers were nanocrystalline, with columnar grains whose average width (parallel to the layers) was of the order of 2-3 times the layer thickness. A small degree of roughness is associated with the individual layers due to the columnar grain structure of the Al layers. The roughness of the SiC appears to

follow the roughness of the previously deposited Al layer. The total degree of roughness also increases with the distance from the Si substrate.

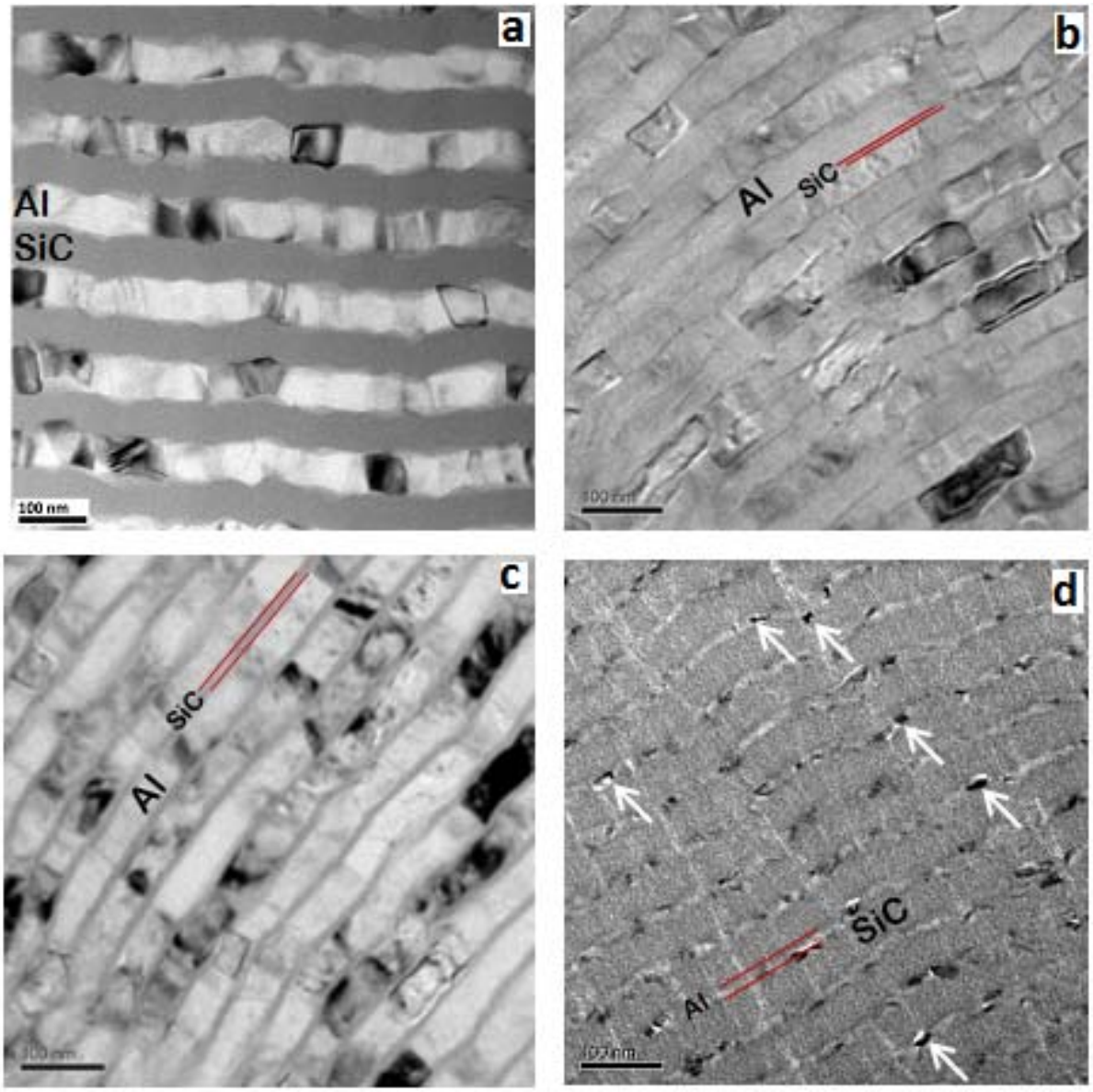

Figure 5-2: TEM bright-field images of the cross-section of various Al/SiC nanolaminates. (a) Al50SiC50, (b) Al50SiC2, (c) Al50SiC10, and (d) Al10SiC50. The arrows indicate pores.

Representative TEM bright-field images of the cross-section of various nanolaminates are shown in figure 5-2. They include (a) Al50SiC50, (b) Al50SiC2, (c) Al50SiC10, and (d) Al10SiC50. All multilayers with different layer thickness are physically rough as a result of the competitive columnar grain growth during deposition of each Al layer. The layer roughness was not large enough to break up the layered structure, even in the case of the Al50SiC2 nanolaminate, where the SiC layers were only 2 nm thick, figure

5-2 (b). The actual layer thicknesses, as measured by TEM, compared well with the nominal layer thicknesses and were uniform through the entire thickness of each nanolaminate. All nanolaminates were apparently pore free, except for the nanolaminate Al10SiC50. It showed evidence of porosity, presumably aligned along columnar grain boundaries, as indicated by the arrows in figure 5-2 (d). This TEM image was recorded at slightly under focused conditions to reveal the Fresnel contrast associated with the pores.

5.2. Mechanical properties of Al and SiC monolithic layers

In order to understand the influence of the nanolaminate architecture on the mechanical behavior, it is important to know the properties of the individual constituents (Al and SiC). This is not always possible because the nanolaminate structure changes the microstructure (*e.g.*, the Al grain size) as well as the deformation mechanisms but other properties (such as the elastic modulus of Al and SiC or the hardness of SiC) should not be significantly modified. Thus, 1 μm thick SiC and Al thin films were grown by magnetron sputtering on a Si (111) substrate under the same conditions used to deposit the nanolaminates.

The Al thin film was made of columnar nanograins with the <111> orientation mostly perpendicular to the substrate, while the SiC thin film was amorphous. The mechanical properties (elastic modulus and hardness) were measured as function of temperature in square samples of 1 x 1 cm^2 using the TriboIndenter platform. Indentations were carried out using fast loading cycles in order to minimize the influence of thermal drift on load-indentation depth curves. Tests were performed with a loading rate of 5 mN sec^{-1} up to a maximum load of 10 mN. The maximum load was held constant for a dwell period of 0.5 s at peak load prior to unloading at 20 mN sec^{-1}. In the case of the Al thin film, maximum loads of 1, 2.5, 5, 7.5 and 10 mN were used in order to get a better estimation of the hardness and modulus by extracting the substrate contribution using the extrapolation method described in the standard ISO 14577 parts four. The elastic modulus and hardness of the SiC and Al thin films were determined as a function of temperature by means of the Oliver and Pharr method as well as from AFM images of the residual indents. At least 20 indentations were performed for each sample and temperature.

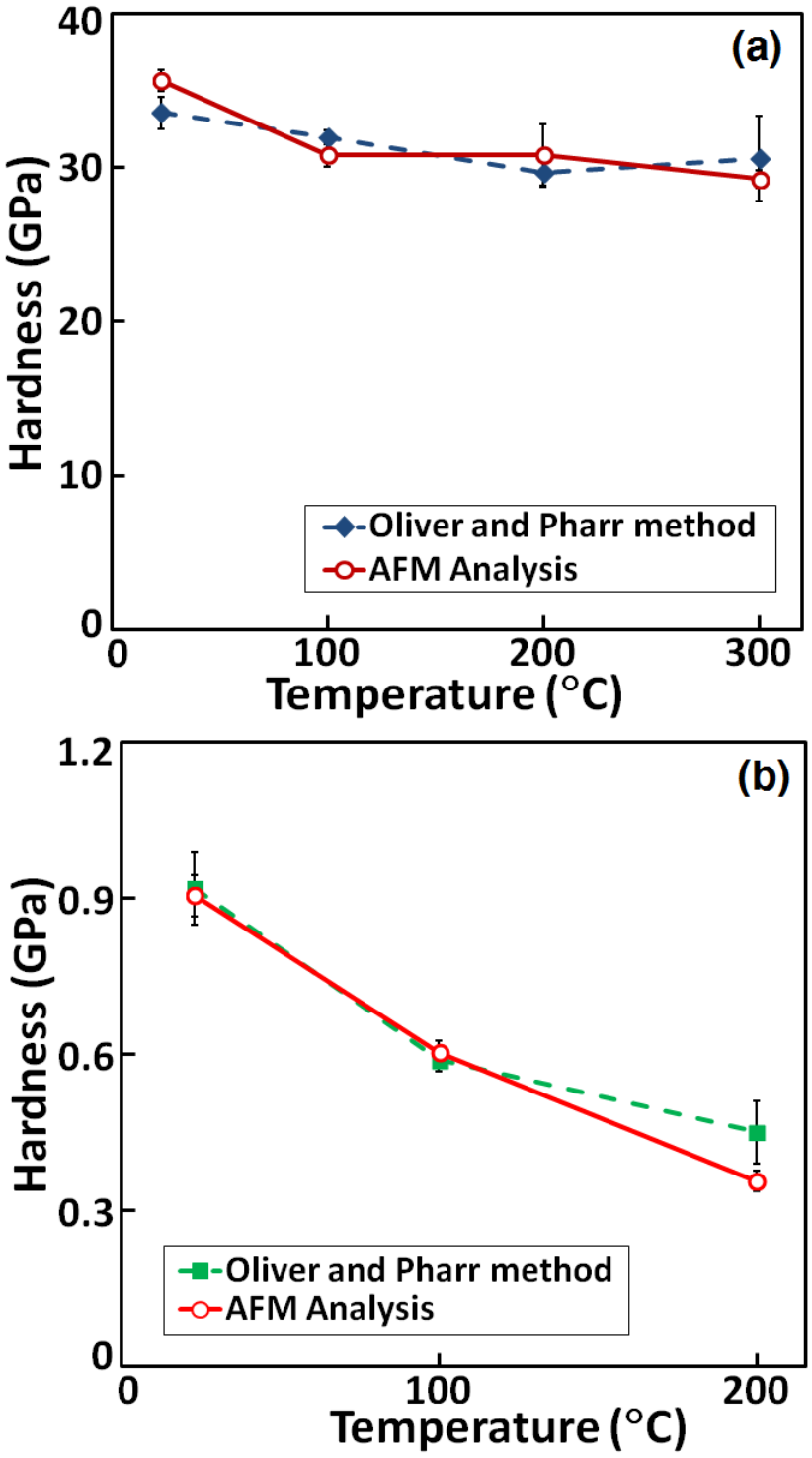

Figure 5-3: Hardness of (a) SiC and (b) Al thin films as a function of temperature. Hardness was determined using the Oliver and Pharr method and the AFM images of the residual indents.

The evolution of the hardness of SiC and Al with temperature is plotted in figures 5-3 (a) and (b), respectively. No significant differences were found in the results obtained using either the Oliver and Pharr method or the area of the residual indents. The hardness of

SiC decreased slightly from 35 ± 0.7 GPa at ambient temperature to 29 ± 0.6 GPa at 300ºC, while the hardness of the Al thin film dropped from 0.9 ± 0.04 GPa to 0.4 ± 0.02 GPa from ambient temperature to 200ºC.

The Poisson's ratio of SiC and Al were taken as 0.14 and 0.34 to compute their elastic moduli from the indentation tests [131, 132]. The evolution of the elastic modulus of SiC and Al with temperature is plotted in figure 5-4. There was a slight increase in the elastic modulus of SiC with temperature from 297 ± 7 GPa at ambient temperature to 320 ± 3 GPa at 300ºC, which was attributed to the densification of the thin film because no evidence of crystallization was found. The elastic modulus of Al decreased from 88 ± 6 GPa at ambient temperature 70 ± 3 GPa at 100ºC. The thermal drift was too large at 200ºC and accurate values of the elastic modulus of Al could not be obtained.

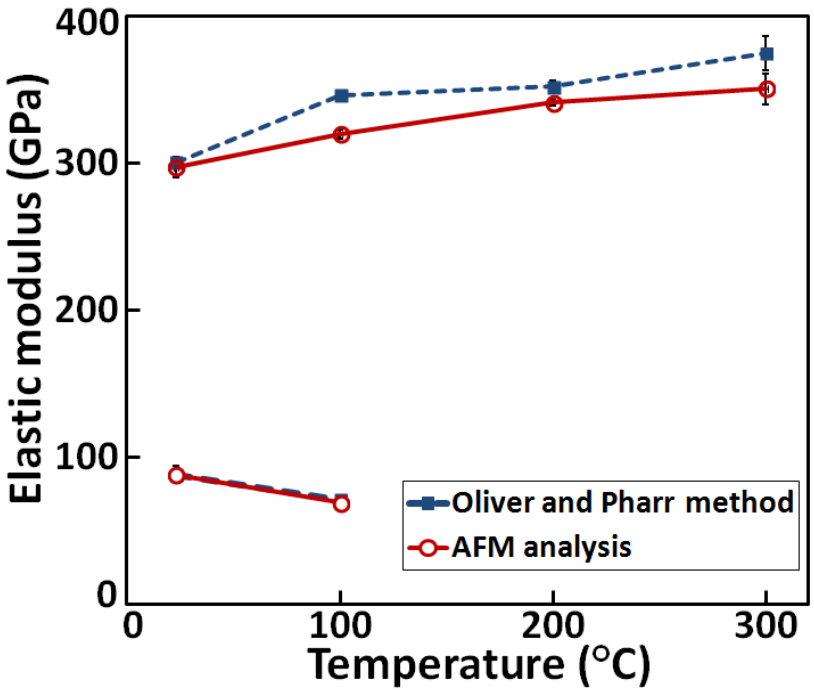

Figure 5-4: Evolution of the elastic modulus of SiC and Al thin films as a function of temperature. Elastic modulus was determined using the Oliver and Pharr method and the AFM images of the residual indents.

5.3. Mechanical behavior of nanolaminates at room temperature

The elastic modulus and hardness of Al/SiC nanolaminates were measured by means of nanoindentation as a function of the layer thicknesses/volume fraction of Al and SiC. The total number of layers of each nanolaminate was selected to reach a total film thickness above 10 μm. This large film thickness ensured negligible substrate effects

during indentation testing. Nanoindentation was carried out at room temperature using the NanoTest platform. Drift rates lower than 0.01 nm sec^{-1} was achieved prior to testing. Tests were performed with a loading rate of 10 mN sec^{-1} up to a maximum load of 100 mN. The maximum load was held constant for a dwell period of 5 seconds at peak load prior to unloading at 20 mN sec^{-1}. The creep rate was computed in all cases at the end of the hold period and it was always below 0.1 nm sec^{-1}, ensuring negligible creep effects on the determination of the elastic modulus from the unloading stiffness. Upon unloading, thermal drift was measured again by introducing a 60 second hold segment at 10% of the maximum load. The drift rate was measured over the last 40 seconds of the hold segment. At least 8 indentations were performed in each sample.

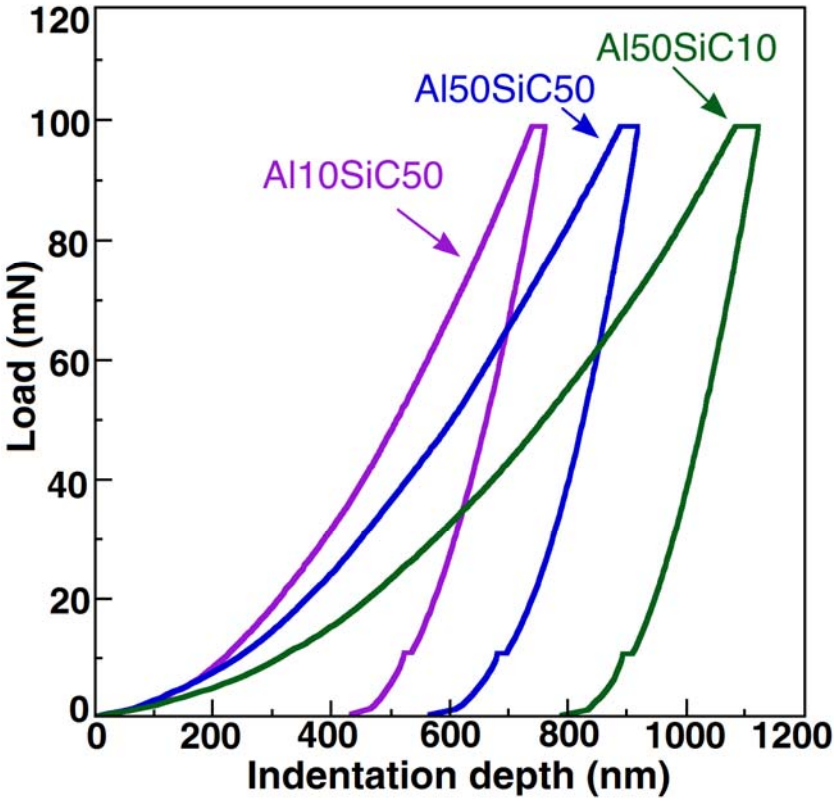

Figure 5-5: Load-indentation depth of Al-SiC nanolaminates with different layer thickness at room temperature.

Representative load-indentation depth curves at room temperature of three different nanolaminates are plotted in figure 5-5. They correspond to Al10SiC50, Al50SiC50 and Al50SiC10 and the Al volume fractions were 0.17, 0.50 and 0.83, respectively. As expected, the resistance to the indenter penetration decreased with the Al content due to the much higher hardness of SiC. The maximum indentation depth was always below 1200 nm and, therefore, within 10% of the total film thickness, which is a widely

accepted rule-of-thumb to avoid substrate effects in the indentation response. The load-indentation depth curves of all the nanolaminates were similar to those shown in figure 5-5. They were analyzed using the Oliver and Pharr method to compute the hardness and the elastic modulus of the different nanolaminates. The Poisson's ratio of each nanolaminate was estimated as the average of the direct and the inverse rule of mixtures assuming that the Poisson's ratio of Al and SiC were 0.34 and 0.14, respectively. The hardness and elastic modulus of all the nanolaminates are summarized in table 5-1.

Table 5-1: Elastic modulus and hardness of Al/SiC nanoscale multilayers at room temperature.

Series	Sample	H(GPa)	E(GPa)
S1	Al10SiC50	9.7 ± 0.1	172 ± 1
	Al25SiC50	8.1 ± 0.5	161 ± 4
	Al50SiC50	5.7 ± 0.3	141 ± 3
	Al100SiC50	5.5 ± 0.4	127 ± 5
S2	Al50SiC2	3.3 ± 0.2	92 ± 4
	Al50SiC10	4.1 ± 0.1	105 ± 2
	Al50SiC25	4.8 ± 0.1	113 ± 2
	Al50SiC100	7.6 ± 0.3	152 ± 3
S3	Al100SiC100	5.7 ± 0.1	140 ± 2
	Al25SiC25	6.8 ± 0.2	141 ± 2
	Al10SiC10	6.5 ± 0.3	142 ± 3

It is well known that the Oliver and Pharr method may not provide accurate values of the hardness and elastic modulus if significant pile-up takes place around the indentations. The contact area was measured from the surface profile of indentation imprints by means of AFM in all nanoscale multilayer series in order to confirm the applicability of the Oliver and Pharr method to these materials. The topography around the residual indents is shown in figure 5-6 for two nanolaminates with different Al/SiC volume fraction ratios (Al10SiC50 and Al50SiC10). No significant pile-up was found around the indentations, confirming the accuracy of the data in table 5-1.

To ascertain the actual deformation and fracture mechanisms, selected indentation imprints were cross-sectioned using FIB and analyzed by TEM. An indentation cross-section in the Al50SiC10 nanolaminate is shown in figure 5-7. Remarkably, the layered structure was preserved in the deformed region and the strain imposed by the indenter was accommodated by the plastic deformation of the Al layers, plus the elastic deflection of the SiC layers. No dislocations could be found in the Al layers, but their

thickness was reduced under the indented area, evidencing that they deformed plastically under the constraint of the stiff and hard SiC layers.

It is also worth noting that the SiC layers underwent substantial bending under the indenter, because their small thickness allowed large elastic deformations without fracture. Nevertheless the SiC layers could not always accommodate the shear deformation imposed by the indenter, and were broken, as shown by the arrow in figure 5-7 (b). Similar observations in other Al/SiC nanoscale multilayers [17, 83, 133], together with the results of the numerical simulations [84, 134, 135], led to the conclusion that the high hardness of Al/SiC nanolaminates is a consequence of constrain imposed by the SiC layers to the plastic deformation of the Al layers.

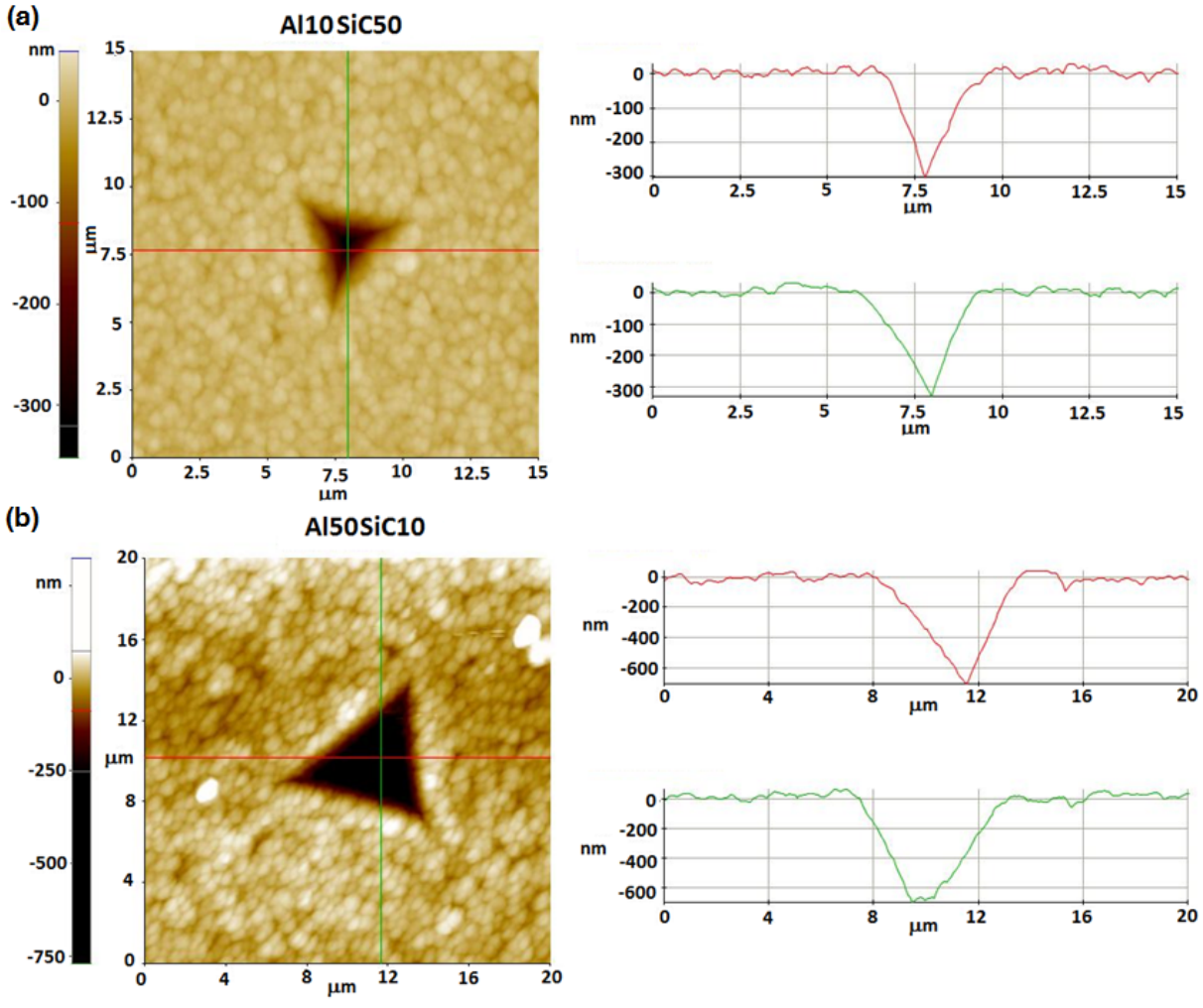

Figure 5-6: AFM topography scans of residual indents of (a) Al10SiC50 and (b) Al50SiC10. No evidence of any significant pile-up was found.

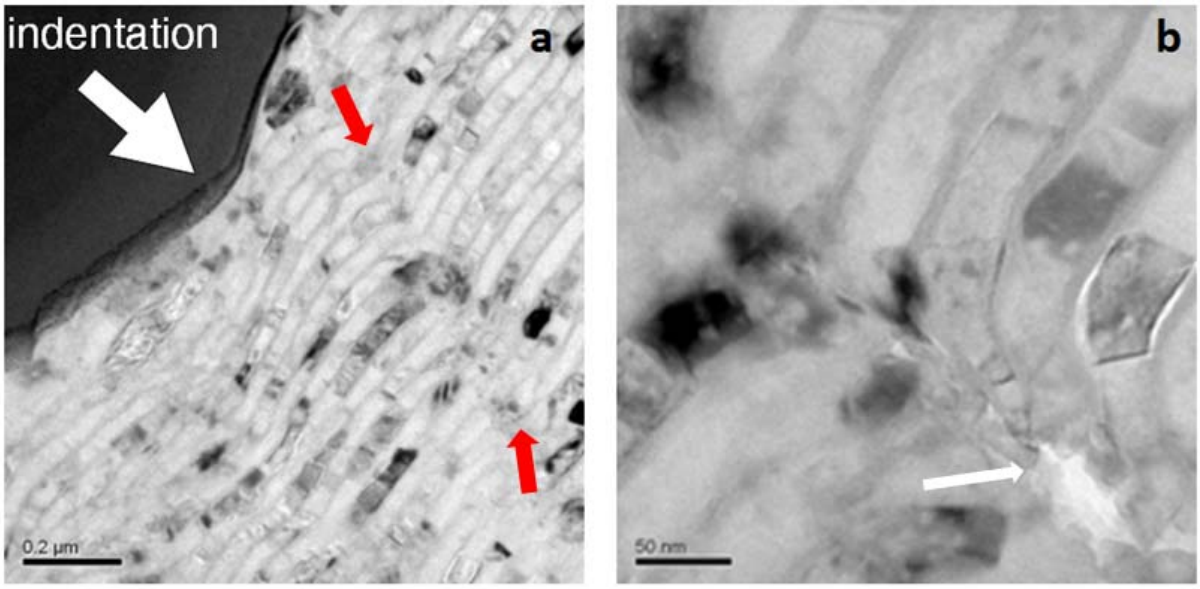

Figure 5-7: Indentation cross-section in the Al50SiC10 nanolaminate. (a) General view. (b) Detail of the fracture of SiC layers.

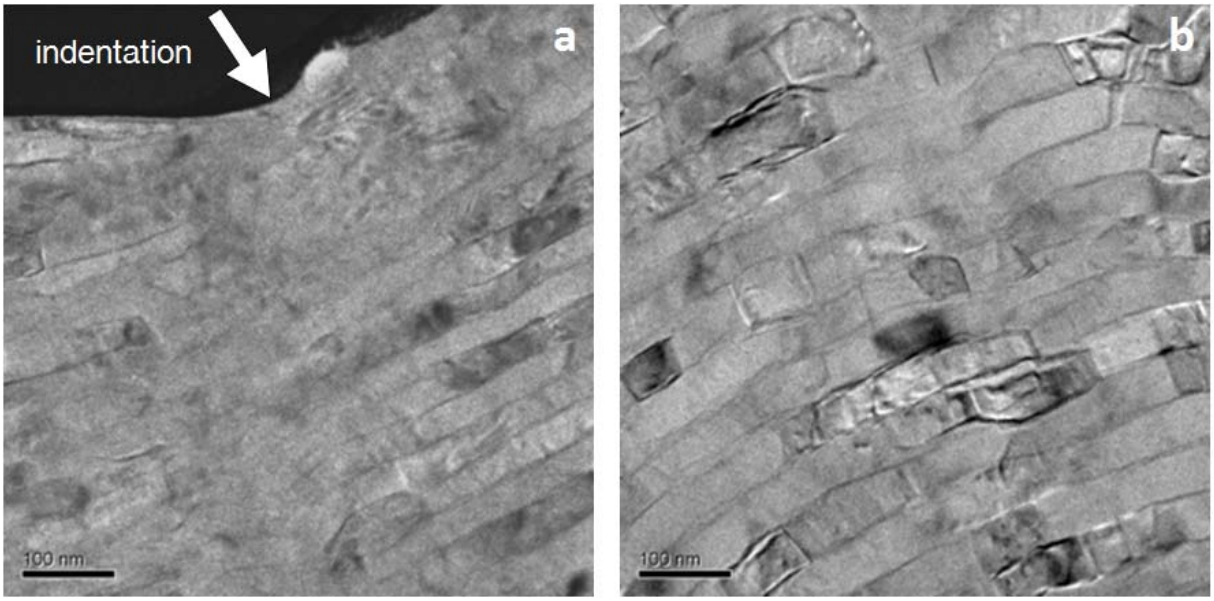

Figure 5-8: Indentation cross-section in nanolaminate Al50SiC2. (a) General view. (b) Underneath the indented area, but far away from the surface.

TEM observations of the remaining nanolaminates were similar. Changes in the deformation and fracture mechanisms with layer thicknesses were not found, except in the nanolaminate Al50SiC2. In this particular case, the SiC layer thickness was so small, 2 nm, that the layered structure was apparently not preserved under the indenter (figure 5-8).

5.3.1. Effect of the layer thickness on the elastic modulus

The elastic moduli of the Al/SiC nanolaminates of series 1 and 2 are plotted in figure 5-9 as a function of the Al volume fraction. The data clearly show that, as expected, the elastic modulus only depends on the volume fraction of the constituents and is independent of the individual layer thicknesses. For instance, Al25SiC50 and Al50SiC100 nanolaminates, both with an Al volume fraction of 0.33, present the same elastic modulus even though the layer thickness in the latter is twice that of the former. The same behavior was found in Al50SiC25 and Al100SiC50, both with an Al volume fraction of 0.67. Moreover, the nanolaminates of series 3, which contained the same volume fraction of Al and SiC but with different layer thickness (10, 25 and 100 nm), presented the same elastic modulus, see table 5-1.

Due to the layered structure, the nanolaminates are expected to display a very anisotropic behavior, with bounds given by the Voigt and Reuss averages. Assuming a perfect interface, Al and SiC deform under isostrain conditions in the longitudinal direction, and therefore, the longitudinal nanolaminate elastic modulus will approach the Voigt average given by:

$$E_l = E_{Al}V_{Al} + E_{SiC}V_{SiC} \tag{5-1}$$

while the nanolaminate deform under isostress conditions in the transverse direction, and the elastic modulus approaches the Reuss average:

$$E_t = \frac{1}{\frac{V_{Al}}{E_{Al}} + \frac{V_{SiC}}{E_{SiC}}} \tag{5-2}$$

where V represents the volume fraction of each constituent, as indicated by the subscripts. The dotted and solid lines in figures 5-9 represent the Voigt and Reuss averages, respectively, as obtained from the elastic moduli of Al and SiC at room temperature. The agreement of the nanoindentation modulus with the Reuss average was excellent, with the only exception of the Al10SiC50 nanolaminate, which was below the Reuss average. This result can be explained by the intercolumnar porosity observed by TEM (figure 5-2 (d)). The origin of this porosity is not clear but it could be the result of some problem during deposition.

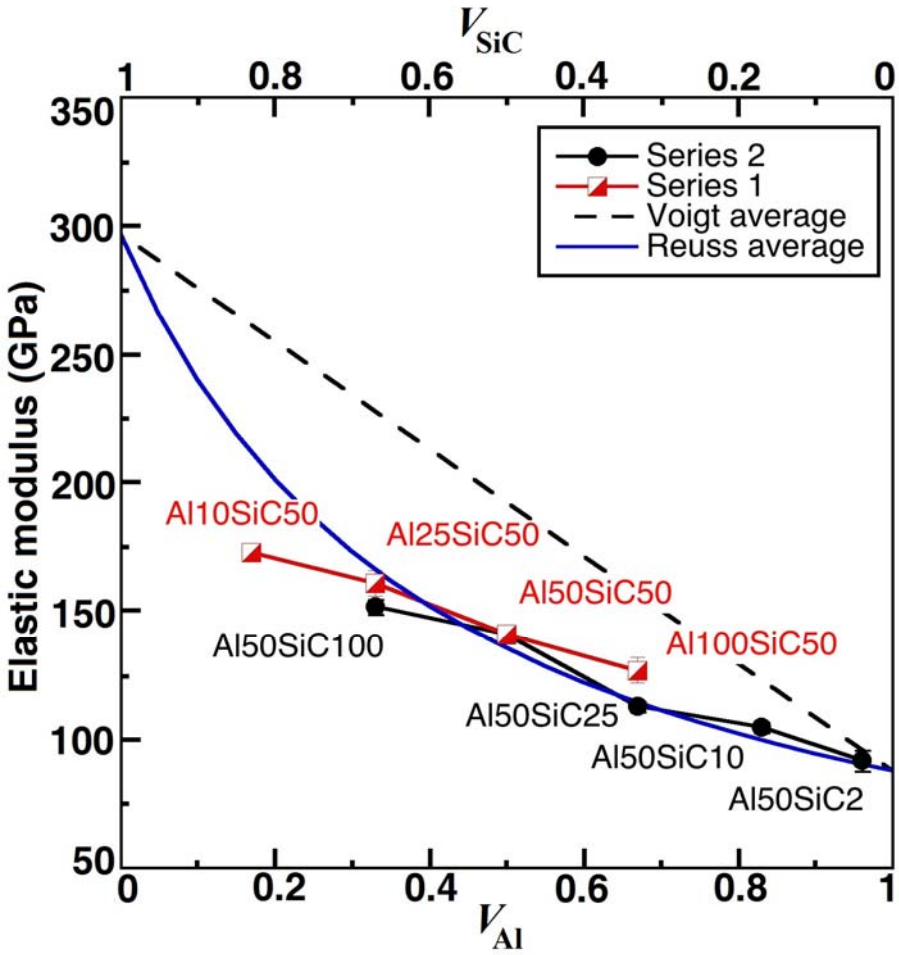

Figure 5-9: Elastic modulus of the nanolaminates as a function of Al volume fraction at ambient temperature. The dotted and solid lines stand for the predictions of the Voigt (rule of mixtures) and Reuss (inverse rule of mixtures) averages, respectively.

The excellent agreement of the nanoindentation elastic modulus with the Reuss average was somewhat surprising. Even though the indentation loading direction is perpendicular to the layers, the stress field under the indenter is very complex, and substantial deformation is expected to take place both in the longitudinal and transverse directions. Therefore, the indentation modulus was expected to be somewhere between the Voigt and Reuss averages. In any case, the results are in good agreement with previous results on Al/SiC nanolaminates with equal Al and SiC layer thicknesses [17, 83, 136]. Moreover, the elastic modulus measured by nanoindentation is in good agreement with that obtained by micropillar compression in the next chapter, with the former only being slightly larger than the latter, even though loading during micropillar compression is uniaxial and transverse to the layers. There might be two explanations for this. Firstly, even though the nanoindentation stress field is very complex, the major contribution to the elastic recovery takes place in the indentation direction [137]. As a

matter of fact, it is well known that the projected area of the indentation imprint remains fairly constant and that only the depth is recovered during elastic unloading. Secondly, the assumption of a perfect interface between the layers may not be accurate. In fact, micropillar compression studies in Al/SiC nanolaminates, shown in the next chapter, demonstrated that slight interface sliding might take place during deformation at room temperature.

5.3.2. Effect of the layer thickness on hardness

The evolution of the ambient temperature hardness with the Al volume fraction is plotted in figure 5-10 for the nanolaminates of series 1 and 2. These results show that the hardness of the nanolaminates decreased more or less linearly as the Al volume fraction increased from 9.7 GPa for V_{Al}=16% down to 3.3 GPa for V_{Al}=96%. The hardness of the nanolaminates was not given by some rule of mixtures of the hardness and volume fraction of the constituents but it did not depend either on the layer thickness. This result was surprising because the hardness should be controlled by the dominant deformation mechanisms, which involve the elastic bending of SiC layers and the plastic deformation of Al constrained by the SiC layers. It is well established that the yield stress of the Al layers increases rapidly as the layer thickness decreases (following a potential law with a power exponent in the range -1 to -0.5) [138], and thus it should be expected that (for a given volume fraction of Al) the nanolaminate with thinner Al layers should be stronger. However, since the indentation also involves substantial elastic bending of the SiC layers, thinner SiC layers might require lower loads to bend, because the flexural modulus of a plate scales with the cube of the plate thickness. Moreover, if interface sliding also occurs during deformation, the area fraction of interfaces (which is inversely proportional to the layer thickness) should also play a role.

Therefore, the surprising observation in figure 5-10 showing that, in the range of layer thicknesses studied, the room temperature hardness is determined by the volume fraction of the constituents might be due to the fact that the increase in the yield stress of Al upon the reduction of layer thickness is balanced by the reduction in the flexural modulus of the thinner SiC layers. As such, nanolaminates Al25SiC50 and Al50SiC100, both with V_{Al}=0.33, display the same hardness within experimental error, and so do Al50SiC25 and Al100Si50, both with V_{Al}=0.67, even though the layer thicknesses and the interface densities vary by a factor of 2.

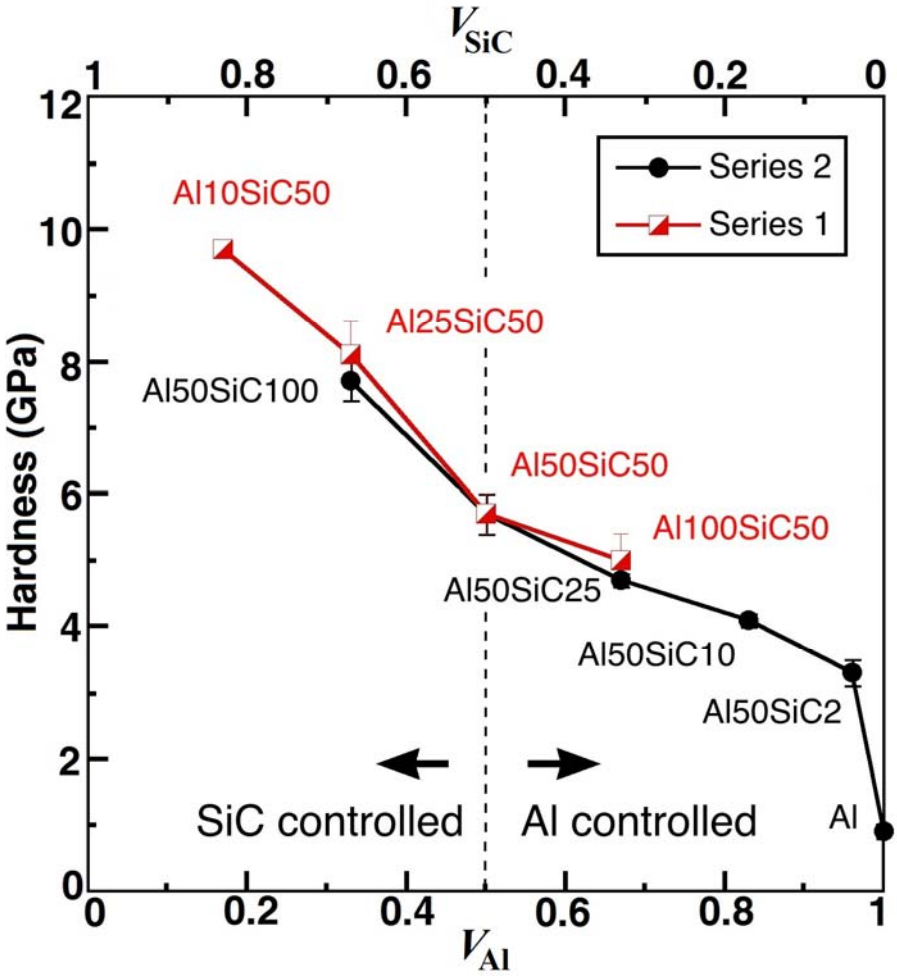

Figure 5-10: Influence of Al (and SiC) volume fraction on the ambient temperature hardness of Al/SiC nanolaminates.

It is also worth noting the difference in hardness between the monolithic Al coating and the Al50SiC2 nanolaminate. Introducing 2 nm thick SiC interlayers between 50 nm thick Al layers increased the hardness from 0.9 GPa for Al up to 3.3 GPa for Al50SiC2. As shown in figure 5-2 (b), the thin SiC interlayer interrupts the growth of the columnar grains of Al, forcing the Al layers to re-nucleate on each SiC layer. The impact of this microstructural change on the elastic modulus is negligible, as shown in figure 5-9, yet the hardness increased by more than a factor of 3 that has to be attributed to an increase in the yield strength of Al because the thin SiC layers are not expected to constrain the deformation of the Al layers, as evidenced in figure 5-8. Further increase of the SiC layer thickness in series 2, keeping the Al layer thickness at 50 nm, led to an increase in the hardness, due to the contribution of the constraint imposed by the SiC layers.

In this regard, it is interesting to follow the evolution of the so-called plasticity index, *i.e.*, the ratio H/E, with the volume fraction of Al (and SiC), which is plotted in figure 5-11. Two different regimes are found in this plot. The ratio H/E remains constant at roughly 0.4 (compare with H/E=0.01 for monolithic Al coatings) when V_{Al}>0.5, while H/E increases as V_{Al} decreases towards the H/E=0.1 (the ratio corresponding to monolithic SiC) when V_{Al}<0.5. These results seem to indicate that hardness is mainly controlled by the plastic flow of the Al layers and the constraint imposed by the SiC layers when V_{Al}>0.5, so that H and E follow the same trend with V_{Al}. However, the deformation is controlled by the elastic deformation of the SiC layers, rather than by the constrained plastic deformation of Al, when V_{Al}<0.5. As a result, H increases more rapidly than E and the ratio H/E increases as V_{Al} decreases.

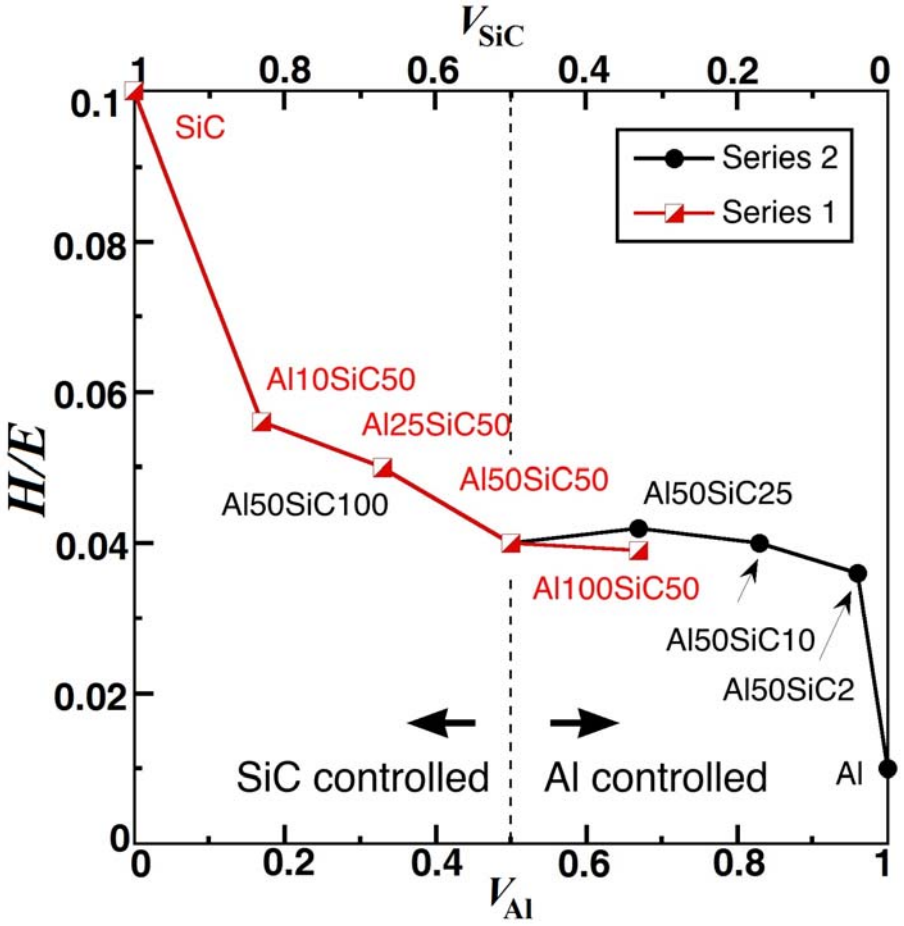

Figure 5-11: Influence of Al (and SiC) volume fraction on the ambient temperature H/E ratio of Al/SiC nanolaminates.

Finally, the evolution of the hardness with the layer thickness in plotted in figure 5-12 for the nanolaminates of series 3, which contain the same volume fraction of Al and SiC.

According to figure 5-11, the deformation is mainly controlled by the constrained plastic flow of Al and the hardness is expected to increase as the layer thickness decreases because of the smaller grain size of Al. Figure 5-12 confirms that this is the case, showing a reduced hardness of the nanolaminates with 100 and 50 nm layer thicknesses with respect to the nanolaminates with 10 and 25 nm layer thicknesses. Nevertheless, other factors that would lead to a reduction in hardness for smaller layer thickness (such as interface sliding or the development of an inverse Hall-Petch effect for Al layer thicknesses of the order of ≈ 10 nm) could also be active, explaining the plateau in hardness achieved for layer thicknesses below 25 nm.

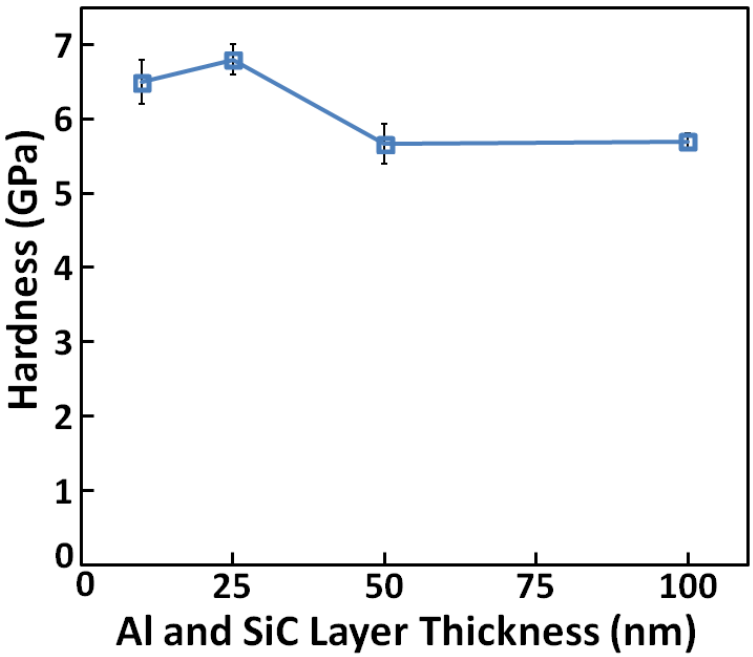

Figure 5-12: Ambient temperature hardness *vs.* Al and SiC layer thickness for the nanolaminates of series 3.

5.4. High temperature stability of Al/SiC nanolaminates

The mechanical properties and deformation and fracture mechanisms from ambient temperature up to 300ºC were studied in an Al/SiC nanolaminate made up by alternate layers of 40 nm in thickness. The nanolaminate was grown by magnetron sputtering on a (111) Si, as explained in chapter 3, and included 40 layers. The mechanical properties were obtained at ambient temperature, 100, 200 and 300ºC by nanoindentation using the TriboIndenter platform, using the approach detailed in chapter 4. Two types of indentation tests were carried out: conventional loading-unloading up to a maximum

load of 10 mN and multiple loading-unloading cycles to extract hardness and modulus as a function of indentation depth. At least 10 indentations were performed at each temperature and the samples were kept at the test temperature for at least 4 hours. After cooling down, nanoindentations were carried out at ambient temperature on each sample to measure the post-annealing hardness and modulus.

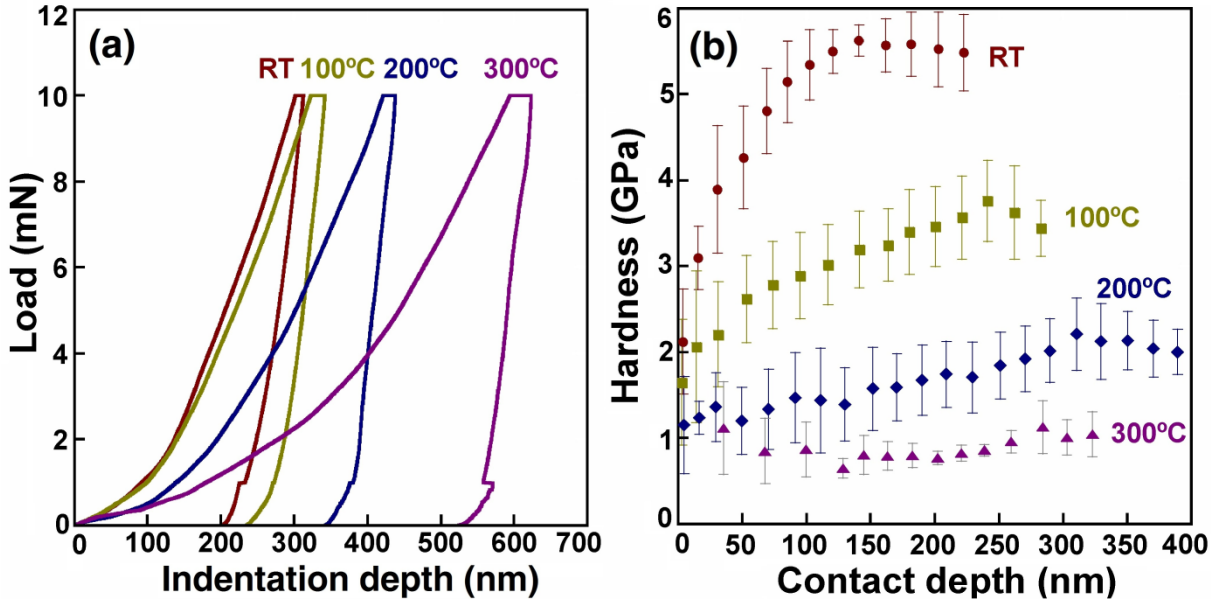

Figure 5-13: (a) Representative load-indentation depth curves for different test temperatures. (b) Hardness *vs.* contact depth at each test temperature.

Representative load-indentation depth curves at each test temperature are plotted in figure 5-13 (a), while the hardness evolution with contact depth is shown in figure 5-13 (b). In this figure, the data for each temperature correspond to the average value from five multiple loading-unloading curves, while the error bars represent one standard deviation. It is evident that the test temperature had a marked influence on the indentation response, especially at 200°C and above. Figure 5-13 (b) shows that the hardness slightly increased with contact depth in the range between 100 and 400 nm, ruling out any substrate effects. For very shallow indents, below 100 nm, lower hardness values were measured probably due to the surface roughness of the multilayers.

The evolution of hardness and elastic modulus with temperature is shown in figure 5-14 (solid symbols). Both exhibited a marked reduction with temperature, particularly at and above 200°C. The drop in modulus was much larger than the one that could be expected from the temperature dependence of the elastic moduli of Al and SiC. Thus,

the reduction by ≈ 50% of the Al/SiC nanolaminate elastic modulus at 200°C has to be attributed to changes in the microstructure and/or the deformation micromechanisms.

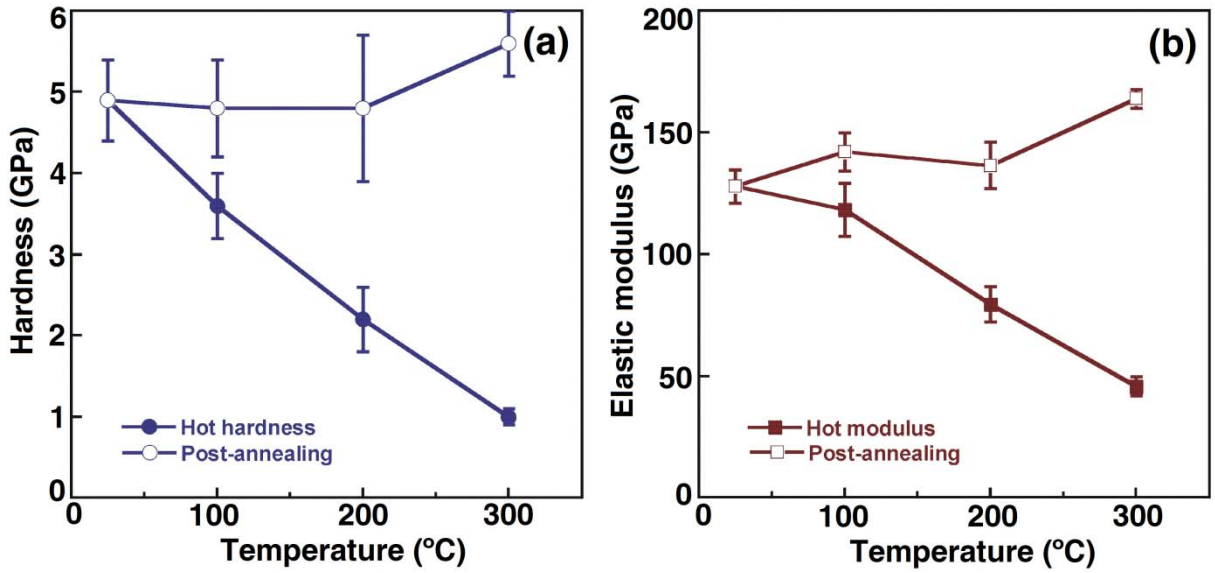

Figure 5-14: (a) Hardness and (b) elastic modulus as a function of test temperature, in solid symbols. The open symbols represent the post-annealing hardness and modulus at ambient temperature.

Interestingly, the ambient hardness and modulus of samples annealed at 100, 200, and 300°C during the 4 h were comparable to those measured in the as-received samples, as shown in figure 5-14 (open symbols), and exhibited a slight increase at 300°C. Interestingly, the post-annealing hardness results demonstrate the need of high-temperature nanoindentation to ascertain the thermal stability of nanostructured coatings. Traditionally, the hardness after annealing has been used as a parameter to assess the thermal stability of coatings. However, in this particular case, post-annealing nanoindentation of Al/SiC did not reveal any effect of temperature on mechanical properties, while high temperature nanoindentation did show marked differences.

Cross-sections across the indentations were prepared by FIB and examined in the SEM. The SEM micrographs of two indentation cross sections at ambient temperature and 300°C are shown in figures 5-15 (a) and (b), respectively. The small imprint of the 10 mN indentation at ambient temperature is pointed out by the arrow and the typical microstructure of Al/SiC multilayers is observed. Both Al (light grey) and SiC (dark grey) layers were 40 nm in thickness and the layers were wavy (albeit continuous) due to the inherent columnar growth of the Al layers. Although SiC is brittle, the SiC layers

exhibited a considerable compliance due to their small thickness and sandwiching effect between the ductile Al layers. No cracking was observed at this indentation load, but it is known that the SiC layers tend to crack at ambient at larger indentation depths [17]. The residual imprint at 300°C was much larger at the same indentation load (figure 5-15 (b)) as the hardness was reduced by a factor of five in comparison with the ambient temperature value. This drop in hardness could be attributed to several factors.

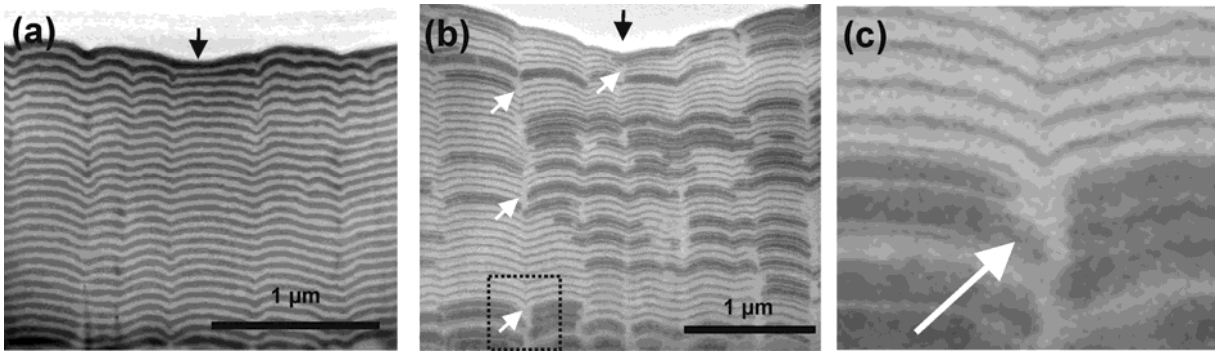

Figure 5-15: Scanning electron microscope (SEM) images of indentation cross sections (a) at ambient temperature (dark grey: SiC; light grey: Al) and (b) at 300°C. Some reaction between Al and SiC can be observed at 300°C (dark areas). The white arrows in (b) indicate areas where the SiC layers were broken and the Al has plastically flown to heal the cracks, as shown in more detail in (c).

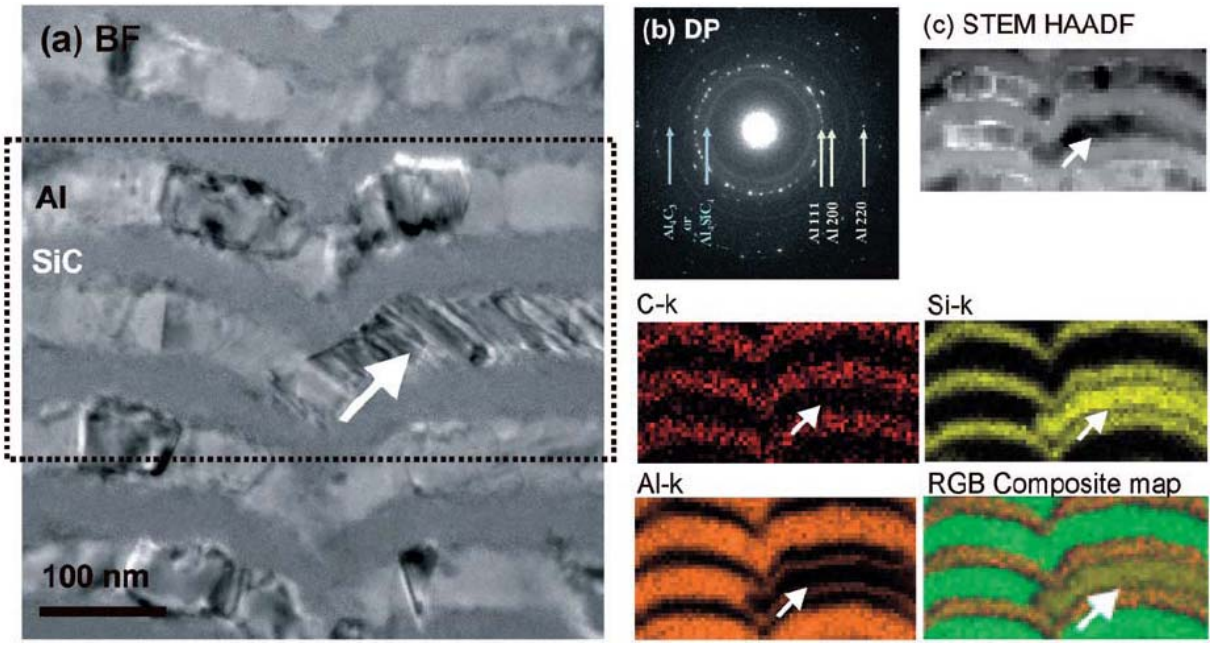

Figure 5-16: (a) BF TEM image of the Al/SiC nanolaminate after annealing at 300°C. The white arrow indicates one of the layers that appear dark in the SEM image of figure 5-15(b). (b) SADP, indicating the presence of reaction products between Al and SiC. (c) The element maps measured in the dashed rectangle indicate that the dark layer corresponds to a Si-rich area, presumably as a reaction product between Al and SiC.

Firstly, the flow stress of nanostructured Al decreases rapidly with temperature and the indentation load has to be mainly borne by the SiC layers as Al exhibits significant plastic flow. This led to the cracking of the SiC layers, especially at columnar boundaries (marked with white arrows in figure 5-15 (b)), further reducing the strength (as well as the stiffness) of the nanolaminate. Finally, it should be noted that the cracks in SiC layers tested at high temperature were always filled in by Al that plastically flowed to fill the gaps (see detail in figure 5-15 (c)). This is an indication of the development of a self-healing mechanism in these nanolaminates, which results from the small size of the Al grains (easy flow at high temperature) together with small layer thickness.

Secondly, the FIB cross section at 300°C (figure 5-15 (b)) revealed many dark areas indicative of the development of chemical reactions between Al and SiC. Moreover, the SiC layers appear much thinner, enforcing the reaction hypothesis. Very little is known about the reactivity and diffusivity between Al and amorphous SiC when the layers are at the nanoscale and a detailed analysis is beyond the scope of this thesis [139]. Nevertheless, TEM foils were prepared by FIB from the region below the indenter in the samples tested at different temperature. Figure 5-16 (a) shows a high magnification bright-field (BF) TEM image of an area encompassing one dark layer (indicated by the white arrow). The selected area diffraction pattern (SADP) in figure 5-16 (b) shows the expected Al diffraction rings plus several rings that can be attributed to either Al_4C_3 or Al_4SiC_4, common reaction products between Al and SiC. According to previous works on SiC-particle-reinforced Al composites [140], the common reaction product between Al and SiC is Al_4C_3 through the following reaction:

$$4\mathrm{Al} + 3\mathrm{SiC} \rightarrow \mathrm{Al_4C_3} + 3\mathrm{Si} \tag{5-3}$$

but these results were obtained at higher temperatures and with crystalline SiC particles of much larger size. Therefore, other reactions such as:

$$4\mathrm{Al} + 4\mathrm{SiC} \rightarrow \mathrm{Al_4SiC_4} + 3\mathrm{Si} \tag{5-4}$$

cannot be ruled out. In both cases, carbides plus some free Si are expected as reaction products resulting in interface embrittlement. The energy-dispersive X-ray spectroscopy mapping of figure 5-16 (c) of the nanolaminate tested at 300°C clearly shows the thinning of the SiC layers together with regions in which a complete layer of Al has been substituted by Si and carbides as a result of the reaction process (marked with white arrows).

Our TEM studies suggest that chemical reaction between the Al and the SiC layers did take place at 200°C and was widespread at 300°C. Thus, extensive chemical reaction between Al and SiC, leading to brittle reaction products, could also be responsible for the reduction in hardness and modulus beyond 200°C. It should be noted, however, that annealing of the nanolaminates for 4 h at high temperature did not modify either the hardness or the modulus (figure 5-14) at ambient temperature, so apparently they are not severely modified by the interface embrittlement. Therefore, the flow stress of Al together with the chemical reactions at the interface determines the high-temperature nanoindentation behavior of the Al/SiC nanolaminates.

5.5. Effect of layer thickness on thermomechanical properties

The effect of Al and SiC layer thickness and/or volume fraction on the high temperature mechanical properties was also studied by means of nanoindentation at 50°C, 100°C, and 150°C. Tests were not carried out at higher temperature because the properties become controlled by the chemical reaction between Al and SiC at higher temperatures (200°C). Nanoindentation was carried out using the NanoTest platform and the loading conditions were identical to those reported in section 5.3 to characterize the ambient temperature properties. As explained before, the samples were bonded to the heater plate using the high temperature adhesive and both sample and indenter were heated independently to the target temperature. The drift rates were lower than 0.01 nm sec^{-1} prior to testing. The samples were kept at the test temperature for at least 4 hours prior to testing. A minimum of 8 indentations were carried out at each temperature in each sample.

Representative load-indentation depth curves of Al50SiC50 nanolaminate at different temperatures are shown in figure 5-17. As expected, the indenter tip penetration increased with temperature. The maximum indentation depth was always below 10% of the total laminate thickness to avoid substrate effects. The Oliver and Pharr method was used to determine the elastic modulus and hardness from these curves. The topography of the residual imprints was measured by AFM and did not show significant pile-up around the indentation. The hardness and elastic modulus of all the nanolaminates of series 1, 2 and 3 are reported in table 5-2.

TEM observation of the nanolaminates deformed at different temperatures (up to 150°C) showed similar mechanisms than those tested at ambient temperature. The

deformation under the indenter was accommodated by the plastic deformation of Al layers and the elastic deflection of the SiC layers. No dislocations were found in Al layers after deformation.

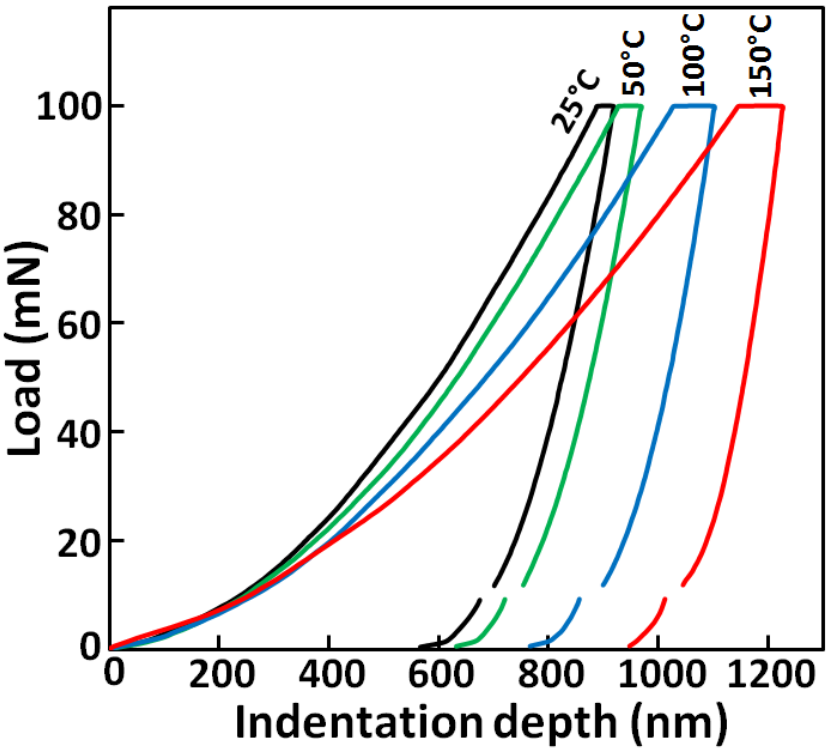

Figure 5-17: Load-indentation depth curves of the Al50SiC50 nanolaminate at different temperatures.

Table 5-2: Average values and standard deviation of the elastic modulus (E) and hardness (H) of the Al-SiC nanoscale multilayers at 50ºC, 100ºC, and 150ºC. Hardness and elastic modulus are expressed in GPa.

Series	Sample	50°C		100°C		150°C	
		H	*E*	*H*	*E*	*H*	*E*
S1	Al10SiC50	9.2 ± 0.3	173 ± 5	7.4 ± 0.1	166 ± 4	6.1 ± 0.2	141 ± 2
	Al25SiC50	7.2 ± 0.2	153 ± 3	5.2 ± 0.1	141 ± 4	4.0 ± 0.1	149 ± 2
	Al50SiC50	5.3 ± 0.1	135 ± 1	3.9 ± 0.2	130 ± 3	3.1 ± 0.3	141 ± 7
	Al100SiC50	5.2 ± 0.4	122 ± 5	4.2 ± 0.3	116 ± 6	3.6 ± 0.2	116 ± 4
S2	Al50SiC2	2.8 ± 0.1	91 ± 1	1.5 ± 0.1	84 ± 6	1.2 ± 0.1	80 ± 8
	Al50SiC10	3.6 ± 0.2	101 ± 3	2.6 ± 0.1	104 ± 1	2.0 ± 0.1	106 ± 2
	Al50SiC25	4.4 ± 0.2	113 ± 3	3.5 ± 0.2	117 ± 4	2.7 ± 0.2	116 ± 5
	Al50SiC100	7.2 ± 0.3	144 ± 3	5.4 ± 0.1	135 ± 2	4.0 ± 0.2	140 ± 5
S3	Al100SiC100	5.4 ± 0.4	138 ± 6	4.7 ± 0.2	138 ± 6	3.4 ± 0.1	133 ± 3
	Al25SiC25	6.3 ± 0.3	134 ± 3	4.5 ± 0.1	126 ± 3	3.5 ± 0.2	122 ± 4
	Al10SiC10	5.8 ± 0.1	136 ± 0	4.3 ± 0.3	125 ± 5	3.9 ± 0.2	125 ± 3

The elastic modulus of series 1 and 2 Al/SiC nanolaminates at 100°C is plotted in figure 5-18 as a function of Al volume fraction. The elastic modulus lies between the Voigt and Reuss averages. Laminates with higher Al volume fraction were closer to the Voigt average and the experimental results moved towards to the Reuss average as the SiC content increased. As at ambient temperature, only the Al10SiC50 nanolaminate was outside these bounds and this low modulus could be due to the intercolumnar porosity, figure 5-2 (d).

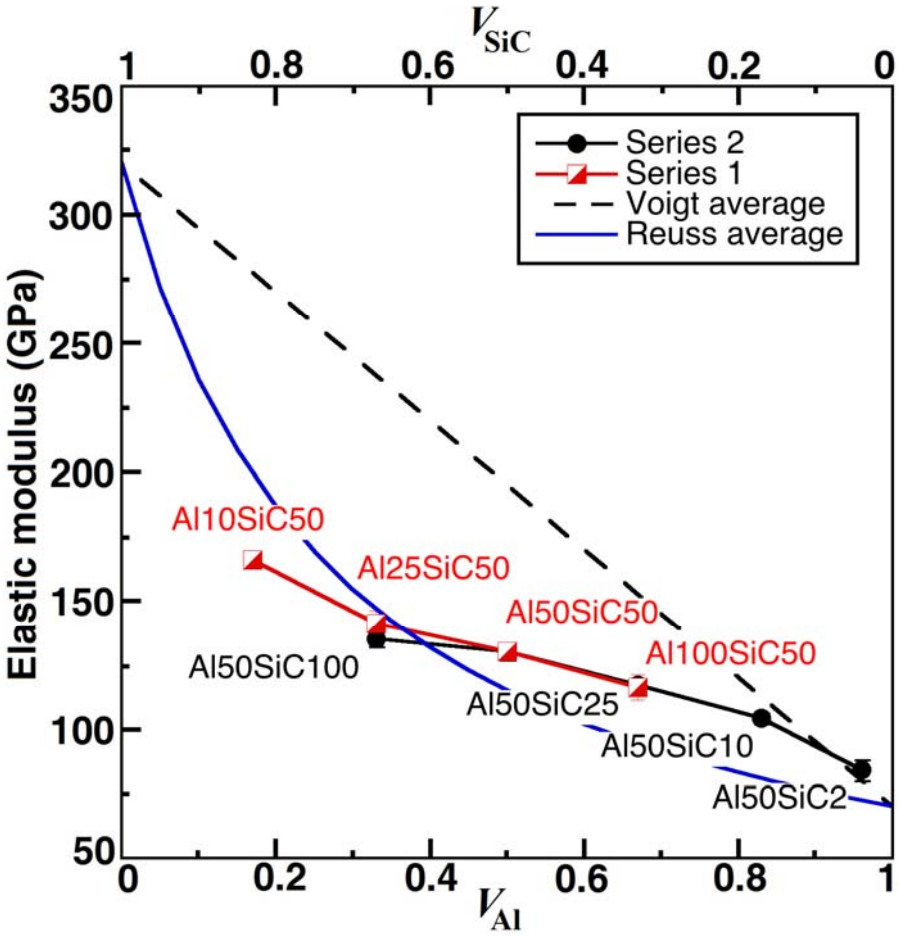

Figure 5-18: Evolution of the elastic modulus as a function of Al volume fraction at 100ºC.

The evolution of hardness with temperature is depicted in figures 5-19 (a) and 5-19 (b) for Series 1 and 2 nanolaminates, respectively. There was a marked reduction of the hardness with temperature in all cases but there were some distinctive effects of the layer thickness that were not evident at ambient temperature. For instance, the influence of the temperature on the mechanical properties of Al25SiC50 and Al100SiC50 nanolaminates was very different. The hardness of the former was 2 GPa higher at ambient temperature, while both presented very similar hardness at 150ºC.

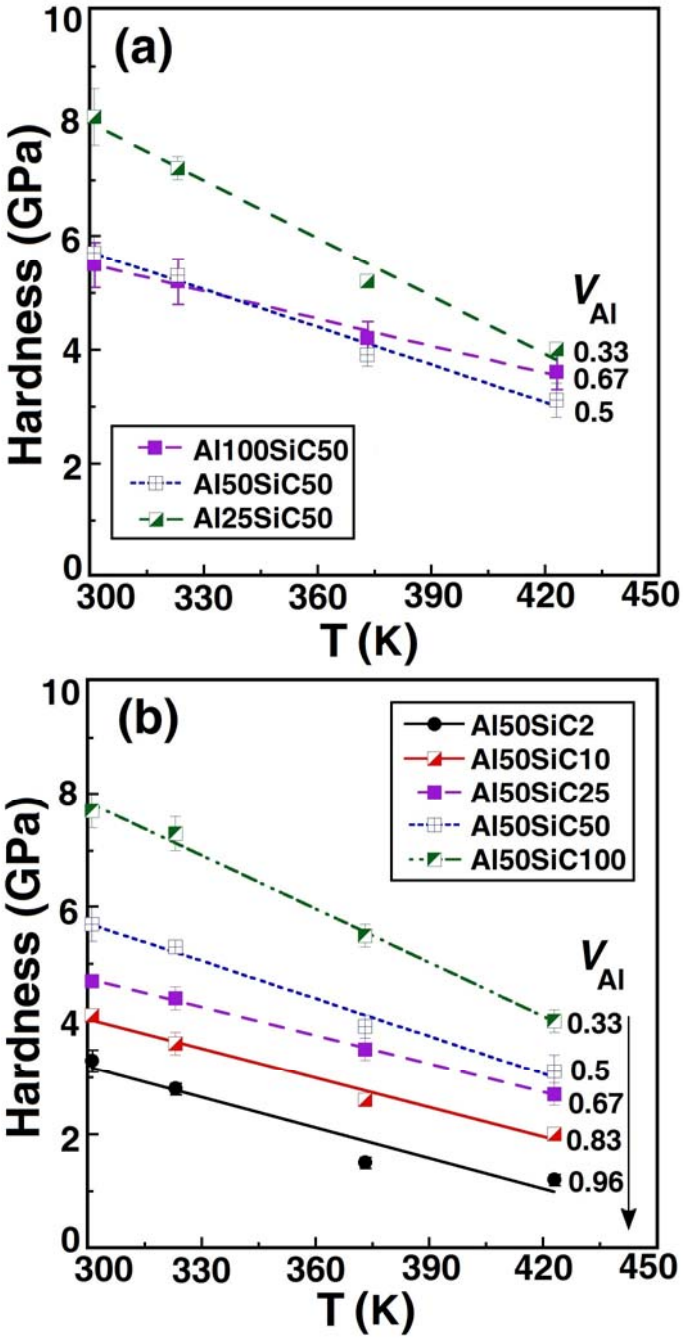

Figure 5-19: Evolution of hardness with temperature for Al/SiC nanolaminates. (a) Series 1. (b) Series 2.

It is instructive to analyze the influence of temperature on the hardness using an Arrhenius type equation:

$$H = H_0 exp\left(\frac{E_a}{RT}\right) \tag{5-5}$$

where H_0 is the extrapolated hardness at 0 K, E_a some apparent activation energy for hardness and R the universal gas constant. Figures 5-20 (a) and 5-20 (b) show the

corresponding Arrhenius plots and activation energies for each nanolaminate. The variation of the SiC layer thickness between 100 nm and 25 nm had no influence in E_a when the Al layer thickness was held constant and equal to 50 nm, figure 5-20 (b).

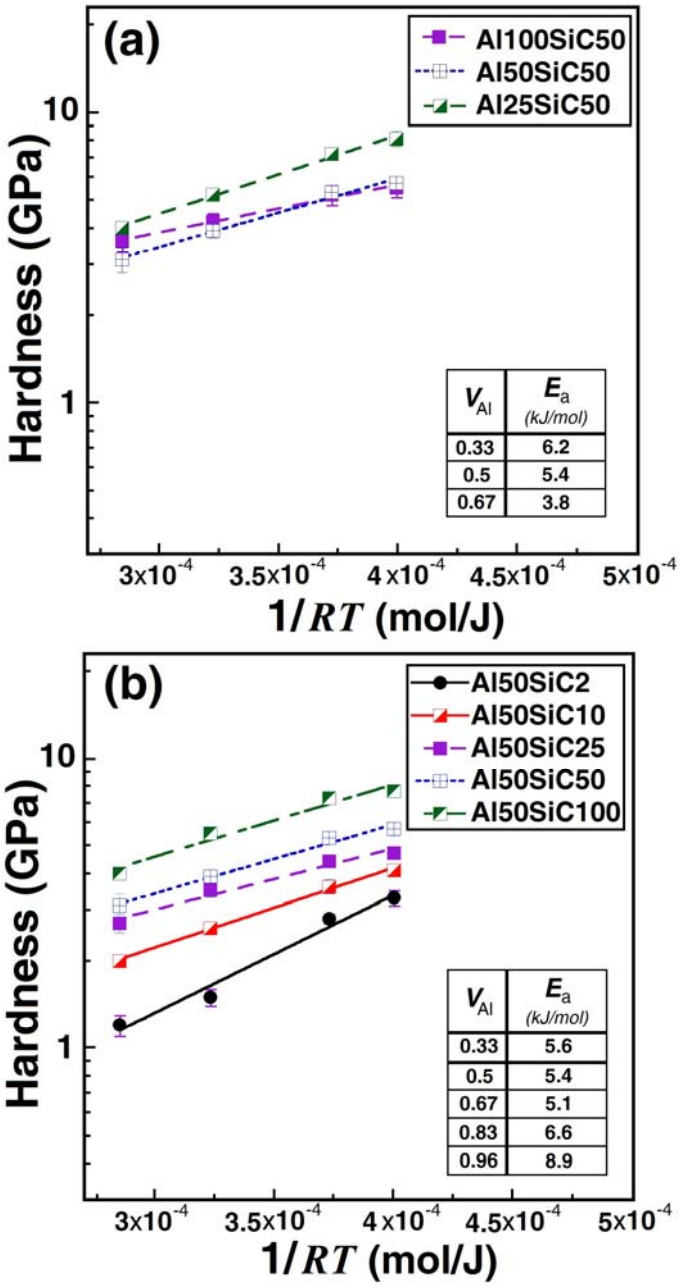

Figure 5-20: Arrhenius plots to determine the apparent activation energy for hardness of the Al/SiC nanolaminates. (a) Series 1. (b) Series 2.

This is not surprising because only Al should contribute to the drop in hardness with temperature as SiC is deforming elastically. The activation energy only increased considerably when the SiC layer thickness was reduced below 10 nm, and especially at 2 nm. This can only be explained as a consequence of the increase in interface area,

meaning that some interface-mediated deformation mechanism, like interface diffusion or dislocation climbing at the interfaces [141], might become the critical processes influencing the strength reduction with temperature.

The same trend was observed in the case of Series 1 nanolaminates. Excluding nanolaminate Al10SiC50 that presented a large porosity, E_a increased as the Al layer thickness decreased when the SiC layer thickness was equal to 50 nm. As a consequence, even though Al100SiC50 and Al50SiC25 nanolaminates, both with V_{Al}=0.67, presented the same ambient temperature hardness, the reduction of hardness with temperature was much higher in the Al50SiC25 nanolaminate because of the higher interface density. Similar trends were found for Al50SiC100 and Al25Si50 nanolaminates. The role of the interface in the deformation at high temperature is supported by the high temperature micropillar compression tests in Al50SiC50 nanolaminates presented in the next chapter. They showed a marked increase in the contribution of interface sliding to the deformation as temperature increased from ambient temperature to 100ºC.

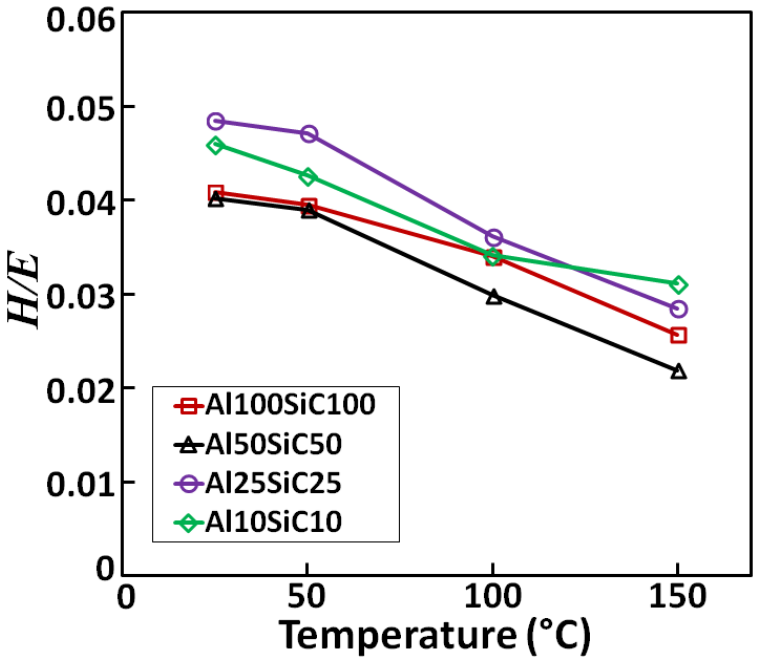

Figure 5-21: Evolution of the plasticity index H/E with temperature for series 3 nanolaminates.

Finally, the evolution of the plasticity index (ratio H/E) with temperature is plotted in figure 5-21 for the series 3 nanolaminates, which contain the same volume fraction of Al and SiC. The plasticity index decreased with temperature in all cases and this trend was

particularly important at 100ºC and above. The softening of the nanocrystalline Al layers together with the activation of interface sliding during deformation would contribute to the reduction of the plasticity index at high temperature.

5.6. Strain rate sensitivity

As explained in chapter 3, the depth-sensing, constant-load (*h-CL*) method was used to study the strain rate sensitivity of the Al/SiC nanoscale multilayers. Nanoindentation tests were performed at ambient, 50°C, 75°C, 100°C, 125°C, and 150°C using the NanoTest platform with a standard Berkovich tip. The indentations were carried out at a loading rate of 10 mN sec^{-1} until a maximum load of 50 mN, which was held constant for 120 s. The maximum load was chosen according to two requirements: the indentation depth should be smaller than 1/10 of the laminates thickness in order to avoid any substrate effect, and the indentation depth should be larger than the bilayer thickness even in the case of laminates in which the thickness of each layer is 100 nm. At least 5 tests were carried at each temperature.

Table 5-3: Average value and standard deviation of the strain rate sensitivity (*m*) of series 1, 2 and 3 nanolaminates at different temperatures.

Series	Sample	25ºC	50°C	75°C	100°C	125°C	150°C
S1	Al10SiC50	0.04 (±0.003)	0.04 (±0.002)	0.05 (±0.004)	0.05 (±0.004)	0.08 (±0.003)	0.07 (±0.021)
	Al25SiC50	0.05 (±0.006)	0.07 (±0.003)	0.06 (±0.003)	0.07 (±0.002)	0.09 (±0.006)	0.15 (±0.007)
	Al50SiC50	0.04 (±0.007)	0.07 (±0.010)	0.09 (±0.009)	0.10 (±0.008)	0.09 (±0.003)	0.13 (±0.008)
	Al100SiC50	0.04 (±0.000)	0.04 (±0.000)	0.05 (±0.004)	0.06 (±0.003)	0.06 (±0.006)	0.08 (±0.003)
S2	Al50SiC2	0.04 (±0.002)	0.07 (±0.004)	0.07 (±0.005)	0.06 (±0.003)	0.07 (±0.005)	0.08 (±0.009)
	Al50SiC10	0.05 (±0.004)	0.07 (±0.003)	0.07 (±0.007)	0.07 (±0.006)	0.07 (±0.004)	0.11 (±0.008)
	Al50SiC25	0.05 (±0.005)	0.07 (±0.004)	0.08 (±0.008)	0.08 (±0.003)	0.08 (±0.003)	0.12 (±0.015)
	Al50SiC100	0.04 (±0.004)	0.06 (±0.007)	0.09 (±0.009)	0.11 (±0.063)	0.12 (±0.030)	0.12 (±0.071)
S3	Al100SiC100	0.04 (±0.000)	0.04 (±0.000)	0.05 (±0.004)	0.06 (±0.003)	0.06 (±0.003)	0.08 (±0.005)
	Al25SiC25	0.06 (±0.011)	0.06 (±0.001)	0.06 (±0.009)	0.05 (±0.004)	0.08 (±0.007)	0.10 (±0.008)
	Al10SiC10	0.04 (±0.002)	0.04 (±0.003)	0.04 (±0.002)	0.04 (±0.002)	0.04 (±0.003)	0.05 (±0.005)

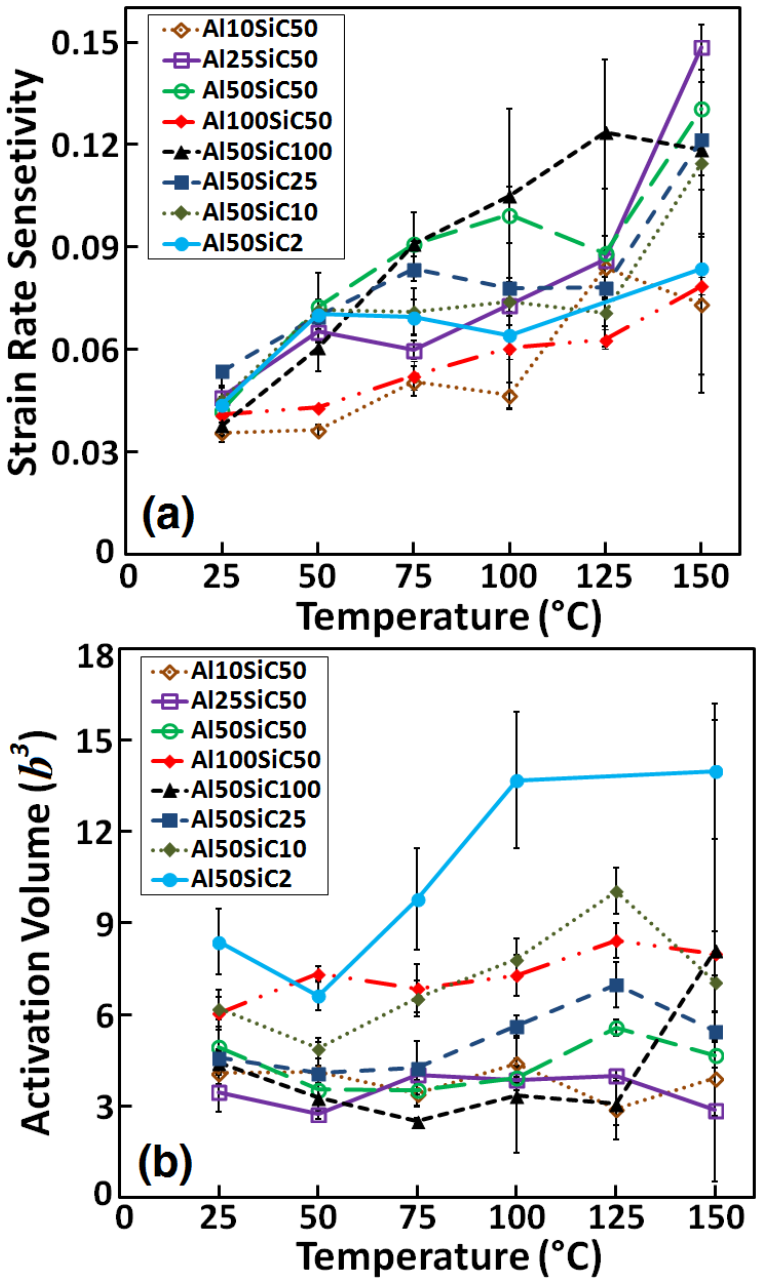

Figure 5-22: Experimental results of (a) strain rate sensitivity, and (b) activation volume, as a function of temperature for series 1 and 2 nanolaminates.

The experimental results of strain rate sensitivity of the series 1, 2 and 3 nanolaminates at different temperatures are summarized in table 5-3 and figures 5-22 (a) and 5-23 (a). All the nanolaminates presented similar strain rate sensitivity ($0.04 < m < 0.05$) at ambient temperature. In addition, the strain rate sensitivity increased slightly with temperature in all cases. No consistent pattern with layer thicknesses was found. The strain rate sensitivities at ambient temperature were in good agreement with those reported previously for ultrafine grain aluminum by Hayes *et al*. [142] and support the

hypothesis that the creep deformation of the multilayer was controlled by the plastic deformation of Al with negligible contributions from SiC or interface sliding.

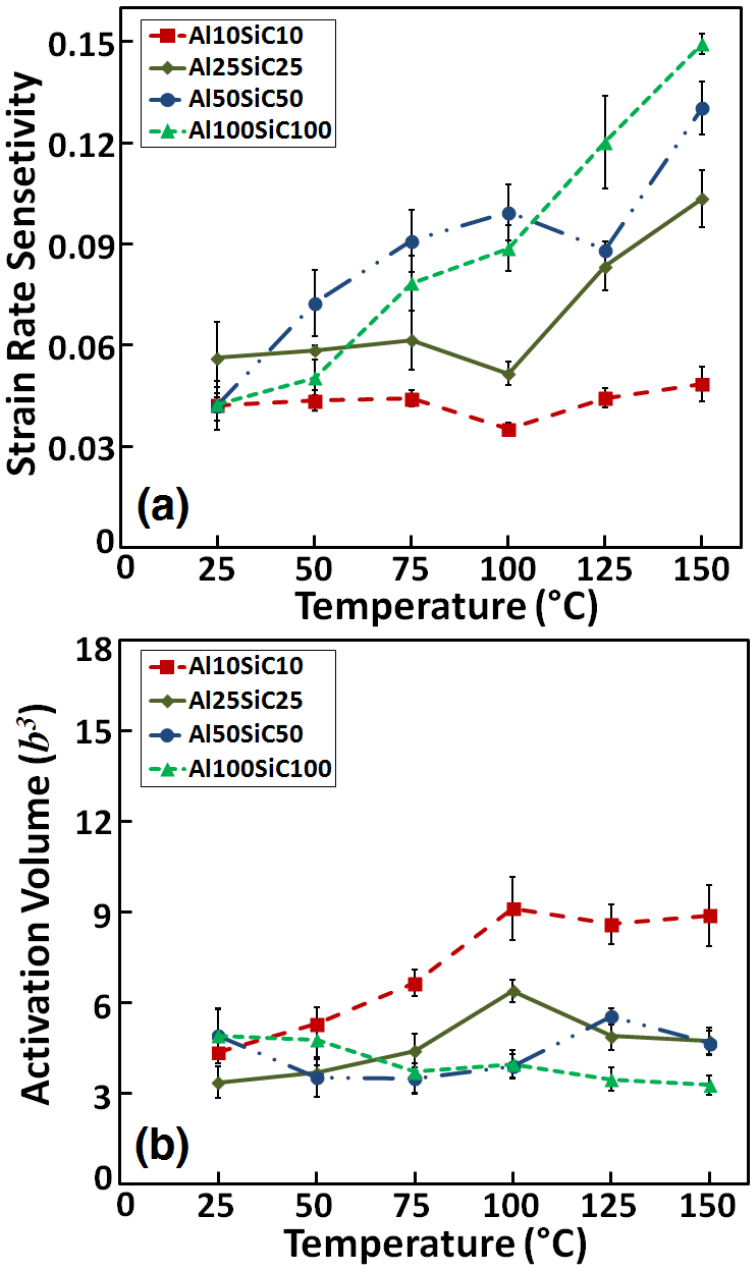

Figure 5-23: Experimental results of (a) strain rate sensitivity, and (b) activation volume, as a function of temperature for nanolaminates with same volume fraction of Al and SiC.

At higher temperatures, the strain rate sensitivity increased in the range between 0.07 and 0.15. The increase in strain rate sensitivity with temperature could support the hypothesis that deformation at higher temperature is controlled by the balance between strain hardening/dislocation multiplication and dynamic recovery in the Al layers, with less constraint effects from the SiC layers. The strain rate sensitivity values reported by Semiatin *et al*. [143] and Hayes *et al*. [142] for nanocrystalline Al were in the same

range, between 0.04 at RT and 0.16 at 200°C. They associated their strain rate sensitivity values with dislocation nucleation and annihilation processes at the grain boundaries. Since, dislocation sources no longer reside within the grains at grain sizes of 100 nm or less, dislocations are nucleated within grain boundaries, glide across the grain and absorbed into the opposite grain boundary. One could imagine the same scenario in the Al/SiC nanoscale multilayers, where the Al grain size is less than 100 nm and the Al layers are sandwiched between two SiC layers, with both the grain boundaries and the Al/SiC interfaces acting as sources and sinks for dislocations.

The activation volume for all the nanolaminates ranged between $1b^3$ and $15b^3$ in the whole temperature interval (25ºC to 150ºC), as shown in figures 5-22 (b) and 5-23 (b). These values are also consistent with an interface/grain boundary controlled deformation mechanism, as dislocation-dislocation interactions typically yield much larger activation volumes (>$100b^3$) [142, 144, 145].This result is in agreement with the fact that no dislocations were observed in any of the deformed Al/SiC nanolaminates, even after substantial plastic deformation of the Al layers, as shown in figures 5-7 and 5-8, supporting a deformation mechanism mediated by the nucleation of dislocations at grain boundaries and/or crystalline/amorphous interfaces.

5.6.1. Activation energy

Since creep is a thermally activated process, activation energies can provide valuable insights into the mechanisms that control the deformation behavior. Based on equation 3-15, the determination of activation energy requires computing the strain rate at a constant stress value as a function of temperature. Unfortunately, the stress is determined by the nanolaminate hardness in the case of indentation creep, and, it is not possible to follow this approach because (as shown in the $ln\,\dot{\varepsilon}_{ind}$ *vs*. hardness plot in figure 5-24 for one of the nanolaminates under study) the stress varies with temperature. Each line in figure 5-24 corresponds to the average of at least 5 indentations at each temperature.

To overcome this limitation, the stress exponent was determined from the slope of the corresponding line at each temperature. Next, all data in between the two dash lines of figure 5-24, were represented in a graph of $ln(\dot{\varepsilon}_{ind}) - n\,ln(H)$ *vs*. $1/T$, as shown in figure 5-25. Following this approach, all data at each temperature between the two dash lines of figure 5-24 collapse into a single point, as shown in figure 5-25, and the

activation energy could be computed from the linear slope the data across the whole temperature range.

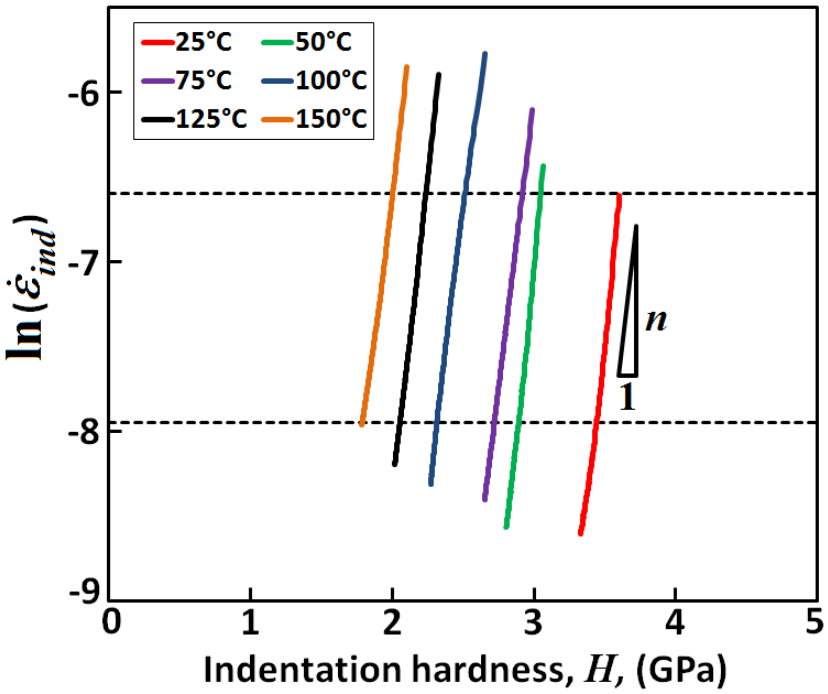

Figure 5-24: Experimental evolution of $ln\,\dot{\varepsilon}_{ind}$ *vs.* hardness for Al100SiC50 nanolaminates tested at different temperatures.

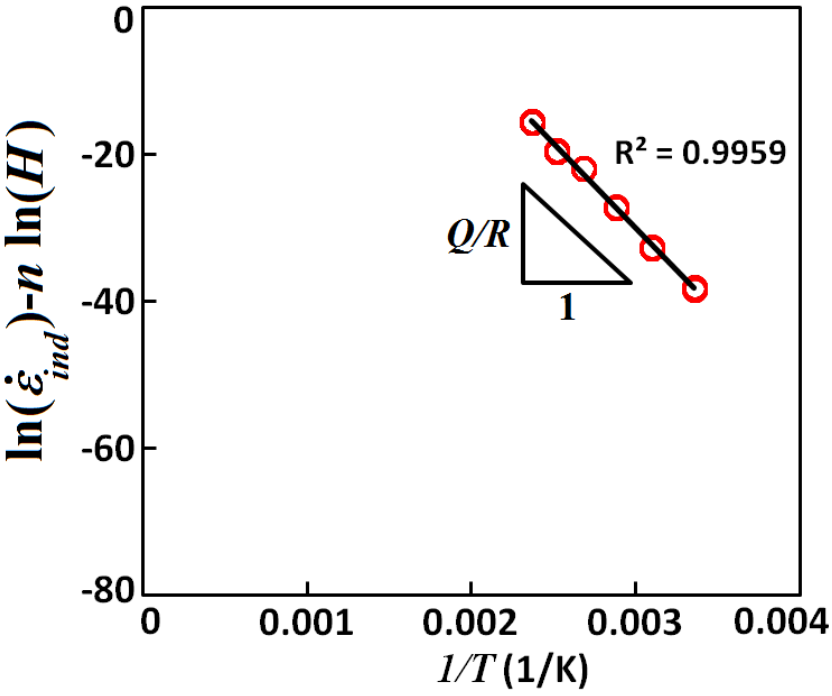

Figure 5-25: The best fit to the experimental results for Al100SiC50 nanolaminate to calculate the activation energy for creep, Q.

The computed activation energies of each nanolaminate are summarized in table 5-4. The results indicate a complex temperature dependency of the activation energy with the layer thickness. For instance, the results for series 1 and 2 in figure 5-26 show that the activation energy decreases with the Al volume fraction from above 300 kJ/mol for an Al volume fraction of 16% to a around 150 kJ/mol for nanolaminates with an Al layer thickness of 50 nm and Al volume fraction larger than 66%. It is instructive to compare these values with the creep activation energies for SiC and Al. The, activation energy of bulk SiC is higher than 800 kJ/mol [146], while the activation energy of pure Al is in the range between the activation energies for self-diffusion (150 kJ/mol) [147, 148] and for grain-boundary diffusion (80 kJ/mol) [148, 149]. The trend observed in figure 5-26 might therefore arise from the increasing contribution of plastic flow in the SiC layers as the Al volume fraction decreases, which must necessarily take place to accommodate the indentation imprint.

Additionally, and comparing the activation energies for nanolaminates with equal volume fraction, Al25SiC50 shows a lower activation energy than Al50/SiC100, and so does Al50SiC25 compared with Al100SiC50. They are re-plotted in figure 5-27, together with the activation energies for the nanolaminates in series 3, as a function of Al layer thickness.

Table 5-4: Activation energies for creep deformation of Al/SiC nanolaminates in the temperature range 25ºC to 150ºC.

Series	Sample	Activation Energy (kJ/mol)
S1	Al10SiC50	314
	Al25SiC50	231
	Al50SiC50	192
	Al100SiC50	191
S2	Al50SiC2	140
	Al50SiC10	150
	Al50SiC25	144
	Al50SiC100	270
S3	Al100SiC100	236
	Al25SiC25	158
	Al10SiC10	112

Figure 5-27 demonstrates that, keeping the Al volume fraction constant, the activation energy decreases with decreasing the Al layer thickness. In particular, the Al10SiC10 nanolaminate displays an activation energy of 112 kJ/mol, getting close to the activation energy for grain boundary diffusion in Al, and suggesting a larger contribution from

interfaces (grain boundaries and Al-SiC interfaces) to creep deformation of Al/SiC nanolaminates.

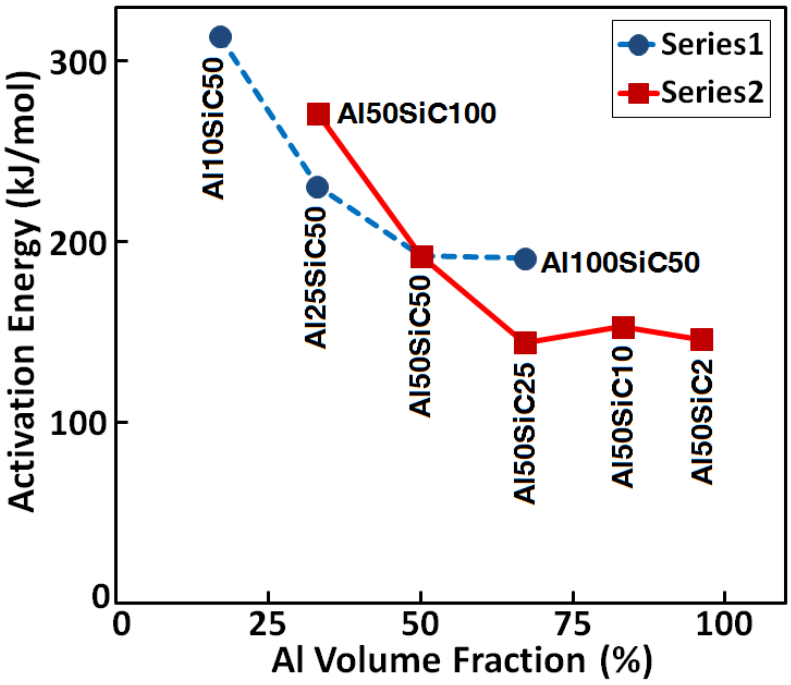

Figure 5-26: Activation energy for indentation creep deformation for series 1 and 2 Al/SiC nanolaminates as a function of Al volume fraction.

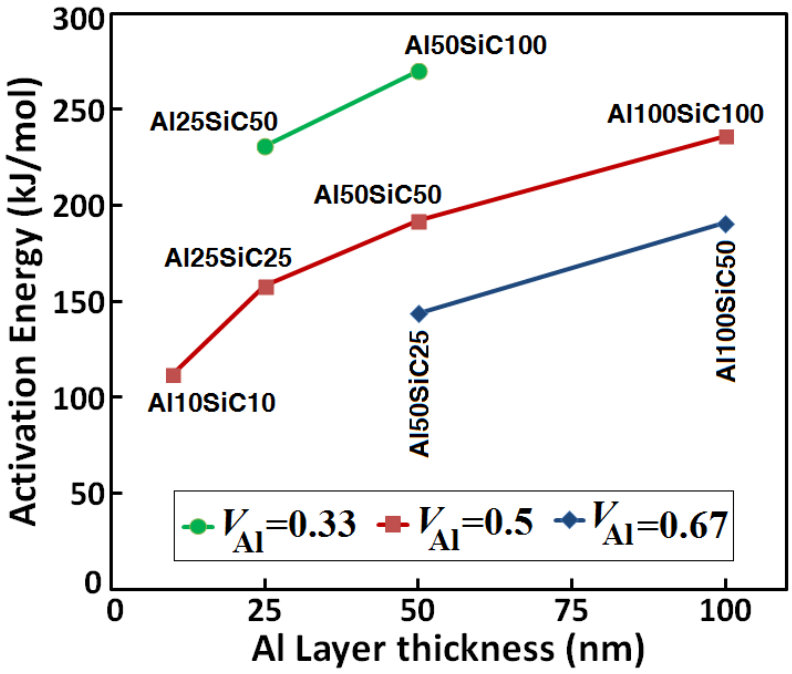

Figure 5-27: Activation energy for indentation creep deformation of Al/SiC nanolaminates as a function of Al layer thickness at different Al volume fraction.

6 Micropillar compression of Al/SiC nanolaminates

The characterization of the mechanical properties of Al/SiC nanolaminates by high temperature nanoindentation –presented in the previous chapter– showed that the hardness decreased rapidly with temperature. At 200ºC and above, this reduction was the result of the chemical reactions at the SiC/Al interface. However, it was also found a marked reduction in hardness from ambient temperature to 100ºC (in the range of 1.5 GPa to 2.0 GPa, see figure 5.19) that could not be attributed to the chemical reactions at the interface. The apparent activation energies for hardness, computed from the variation of hardness with temperature for different nanolaminates, suggested the interface sliding could be responsible for the reduction in hardness at 100ºC but this could not be confirmed by the TEM analysis of the deformation mechanisms under the indenter. It should be noted that indentation is not the ideal test to check the influence of the interface sliding on the mechanical properties of nanolaminates because of the constraint induced by the elastic material surrounding the indented volume. Thus, it was

decided to study the influence of the temperature on the mechanical properties by means of micropillar compression tests. The free surfaces of the micropillar should provide clear evidence of interface sliding if this mechanism was operative at high temperature.

Al/SiC nanolaminates with a total number of 40 layers (20 Al and 20 SiC) were deposited by magnetron sputtering on Si (111). A high magnification cross-sectional bright-field TEM image of the as-processed Al/SiC nanolaminate near the Si (111) substrate is shown in figure 6-1. The individual layer thickness was 60 ± 2 nm for Al and 59 ± 3 nm for SiC. Focused Ion Beam (FIB) milling was used to manufacture the micropillars, with a diameter of 1 μm and a length of 2 μm, following the techniques indicated in chapter 3. Two micropillars machined by FIB using annular milling and lathe milling are shown in figures 6-2 (a) and 6-2 (b), respectively. As expected, the pillars fabricated by annular milling showed a slight taper, of ~ 2.5º in average, while the pillars fabricated by lathe milling showed virtually no taper.

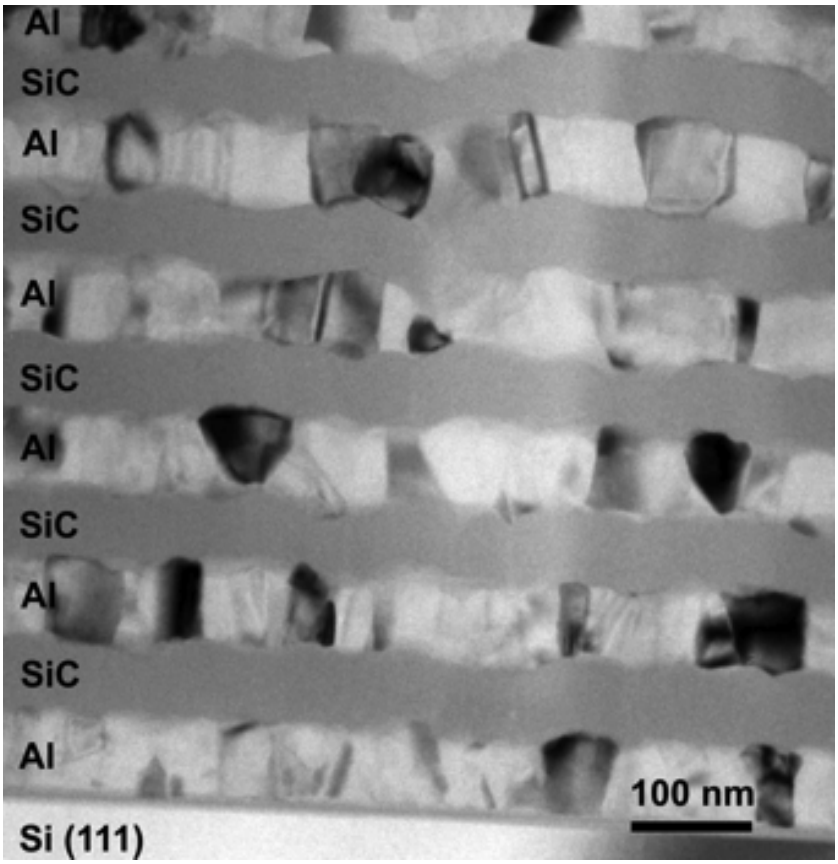

Figure 6-1: Bright-field TEM cross-section image of the as-processed Al/SiC nanolaminate.

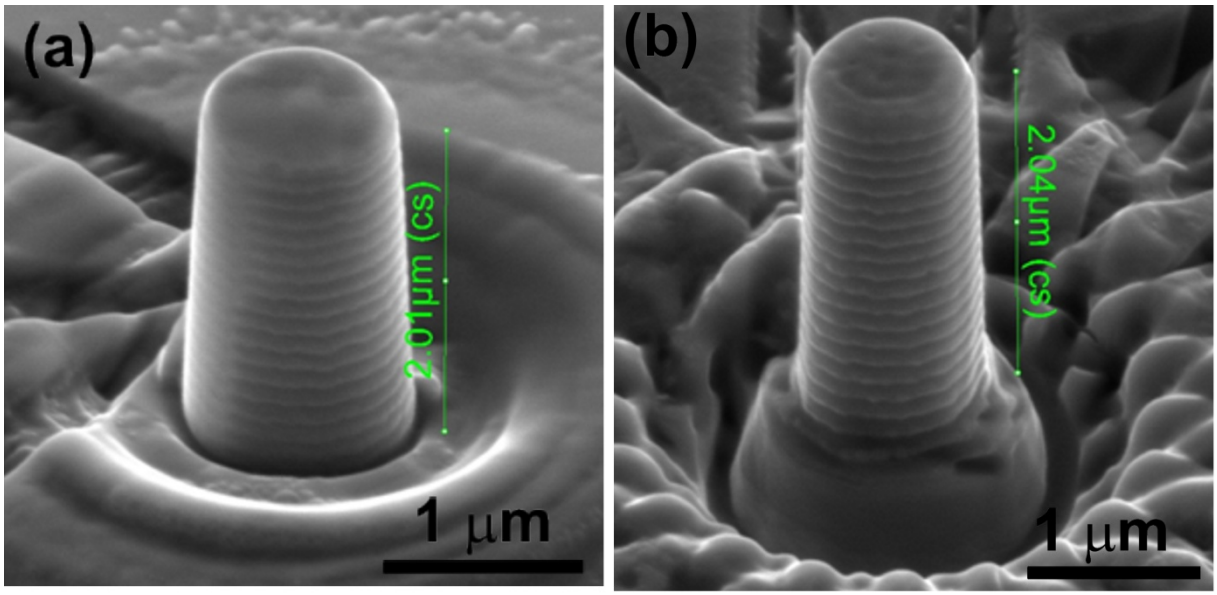

Figure 6-2: SEM images of Al/SiC nanolaminate micropillars fabricated by (a) annular milling, with slight taper (≈ 2º) and (b) lathe milling, without taper.

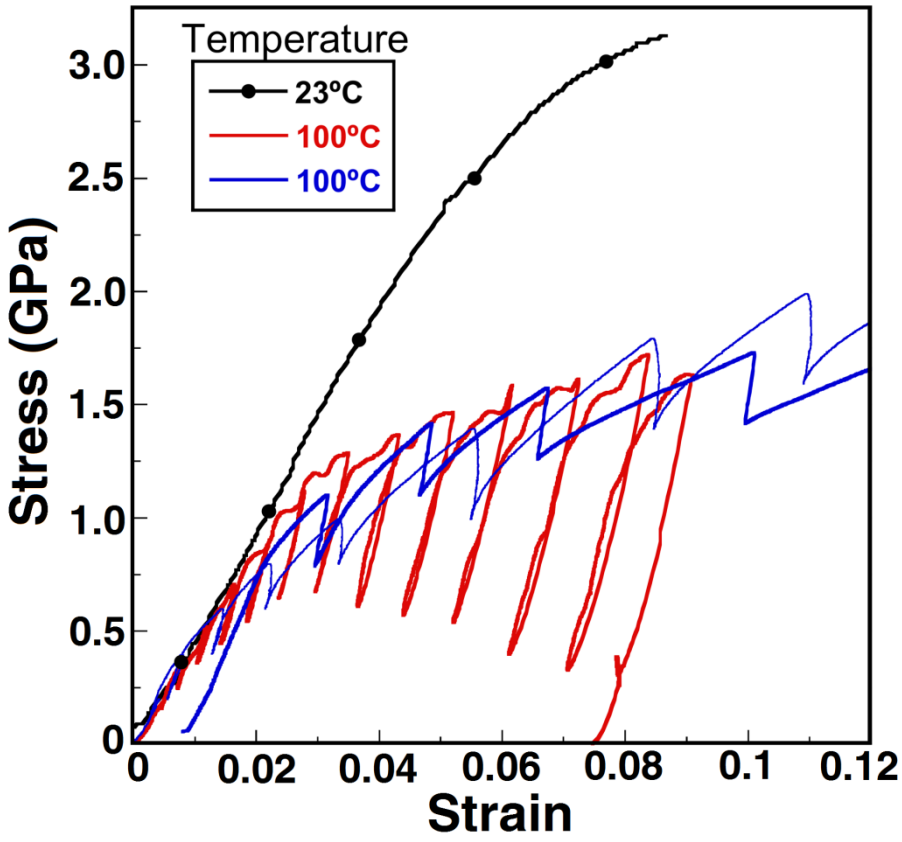

Figure 6-3: Compression stress-strain curves at 23ºC and 100ºC. The colors in the curves at 100ºC indicate that the tests were carried out either under displacement control (red) or load control (blue).

Uniaxial compression tests of the micropillars were conducted using the TriboIndenter platform. The samples were mounted on a heating stage using mechanical clips. A flat diamond punch with a diameter of 8 μm was used to apply the load. The tests were carried out at 23ºC and 100ºC. The flat tip was maintained in contact with the pillar surface using a very low force (2 μN) for 1 hour prior to testing to attain thermal equilibrium and minimize thermal drift. Thermal drift was then measured both before loading and during unloading over a 20 s hold segment. Typical thermal drift values at 23ºC and 100 ºC were 0.1 and 0.15 nm s^{-1} respectively. Experiments were performed under displacement control at a strain rate of 10^{-3} s^{-1} and under load control. The initial strain rate in the latter was 10^{-3} s^{-1}, but the strain rate varied significantly upon plastic yield. A multiple loading-unloading strategy was used in most cases to measure the elastic stiffness of the micropillar during the test from unloading segments. The stresses and strains, including the Sneddon correction for the sink-in effect at the base of the pillar, were calculated using the methods detailed in chapter 3.

The engineering stress-strain curves in compression at 23ºC and 100ºC are plotted in figure 6-3. They correspond to taper-free micropillars to avoid any artifacts (strain hardening) coming from tapering. The elastic modulus and the flow stress at 8% plastic strain, σ_f, at 23ºC and 100ºC are summarized in table 6-1, together with the hardness H and the ratio H/σ_f.

Table 6-1: Elastic modulus, E, flow stress at 8% plastic strain, σ_f, and H/σ_f ratio of Al/SiC nanolaminates as function of temperature.

T=23 ºC			T=100 ºC		
E (GPa)	σ_f (GPa)	H / σ_f	E (GPa)	σ_f (GPa)	H / σ_f
123 ± 2	3.1 ± 0.2	1.6	111 ± 3	1.6 ± 0.2	2.3

The initial loading slope of the stress-strain curves at 23ºC and 100ºC was much more compliant than the one expected from purely elastic loading. This behavior was attributed to the local plastic yielding at the top of the micropillar, due to slight misalignments between the micropillar surface and the flat punch, before full contact is established between the two. This effect is clearly seen in the variation of elastic modulus of the micropillar, determined from the slope of the unloading steps during the test, as a function of the applied displacement (figure 6-4). The elastic modulus

increases until the applied displacement has reached 50 to 100 nm and full contact was established between the top of the pillar and the flat punch, leading to a constant value, independent of the applied displacement (table 6-1).

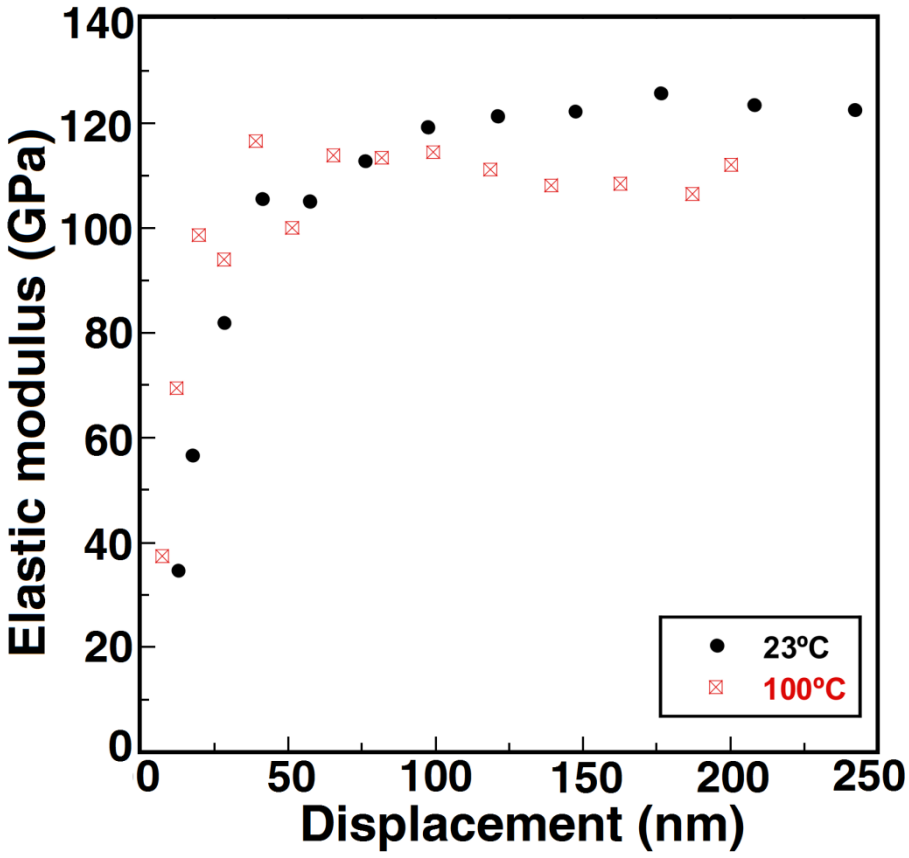

Figure 6-4: Elastic modulus of the Al/SiC nanolaminate obtained from slope of the unloading steps during the micropillar compression tests as a function of the applied displacement.

The theoretical transverse elastic modulus of the Al/SiC multilayer, E, can be computed from laminate theory according to this equation:

$$\frac{1}{E} = \frac{V_{Al}}{E_{Al}} + \frac{V_{SiC}}{E_{SiC}} \tag{6-1}$$

where V_{Al} and V_{SiC} stand for the volume fraction of Al and SiC (50% in this case), and E_{Al} and E_{SiC} are the corresponding elastic moduli. They were determined from instrumented nanoindentation tests in the monolithic films at 23ºC and 100ºC (see section 5.2) and can be found in table 6-2. The theoretical values of transverse modulus according to equation 6-1 were 135 GPa and 114 GPa at 23ºC and 100ºC, respectively, which are very close to the experimental results.

Table 6-2: Hardness, H, and elastic modulus, E, measured from instrumented indentation tests in monolithic Al and SiC films and the Al/SiC nanolaminate.

Materials	T=23ºC		T=100ºC	
	E (GPa)	H (GPa)	E (GPa)	H (GPa)
Al	88 ± 6	0.91 ± 0.04	70 ± 3	0.60 ± 0.02
SiC	297 ± 7	35.6 ± 0.7	320 ± 3	30.8 ± 0.8
Al/SiC	128 ± 7	4.9 ± 0.5	118 ± 11	3.7 ± 0.4

Interestingly, the elastic modulus of the Al/SiC nanolaminates determined from micropillar compression tests were similar, albeit slightly lower, than those determined from instrumented nanoindentation, shown in table 6-2. The difference, although very small, is very likely caused by the elastic anisotropy of Al/SiC laminates due to the layer orientation. While the transverse elastic modulus is measured directly during micropillar compression, nanoindentation tests perpendicular to the layers are be influenced both by the transverse and the longitudinal elastic moduli due to the multiaxial stress state. Thus, when loading perpendicular to the layers, in nanoindentation one would expect a slightly higher modulus because of the contribution from loading parallel to the layers.

While elastic moduli at 23ºC and 100ºC were very similar, the differences in plastic behavior were dramatic, considering the small variation in temperature. The micropillars tested at 23ºC presented a very high strain hardening rate, reaching 3.1 GPa at 8% applied strain, while the micropillars tested at 100ºC displayed a much softer behavior and the flow stress seemed to saturate at 1.6 GPa when the applied strain reached ~8% (figure 6-3). It is worth noting that these marked differences in the strain hardening capacity and in the flow stress were triggered by small changes in the homologous temperature T/T_m from 0.3 (23ºC) to 0.4 (100ºC) in Al.

Nanoindentation experiments in monolithic films of both materials showed no variation in the properties of SiC between 23ºC and 100ºC while the hardness of Al dropped by 30%, from 0.9 GPa to 0.6 GPa (table 2). These hardness values cannot be extrapolated directly to the properties of the Al layers within the nanolaminate because the thickness of the monolithic Al film was 1 μm, while the Al layers within the nanolaminate were only 60 nm thick. In this temperature range, the hardness of Al/SiC nanolaminate was also reduced by ~ 30%, the same percentage that in the monolithic Al coatings (table 6-2).

6.1. Deformation mechanisms

The compressed micropillars were studied by SEM to get a better understanding of the mechanisms of deformation as a function of temperature. The micrographs corresponding to two micropillars deformed up to a plastic strain of 8% at 23ºC and 100ºC are shown in figures 6-5 (a) and 6-5 (b), respectively. The differences are obvious and correspond well with the differences in the stress-strain curve. The micropillars deformed at 23ºC showed evidence that the plastic deformation of the Al layers was constrained by the elastic SiC layers. Limited extrusion of the Al layers at the edges of the pillar was observed, especially towards the top, where the stresses are expected to be larger. On the contrary, Al was flowing out of the multilayer structure in the form of “tongues” at 100ºC, and this behavior can be a result of either a large reduction in the flow stress of the nanocrystalline Al, as compared with the behavior at 23ºC, or of a substantial difference in the constrain imposed by the SiC layers as a result of interface sliding.

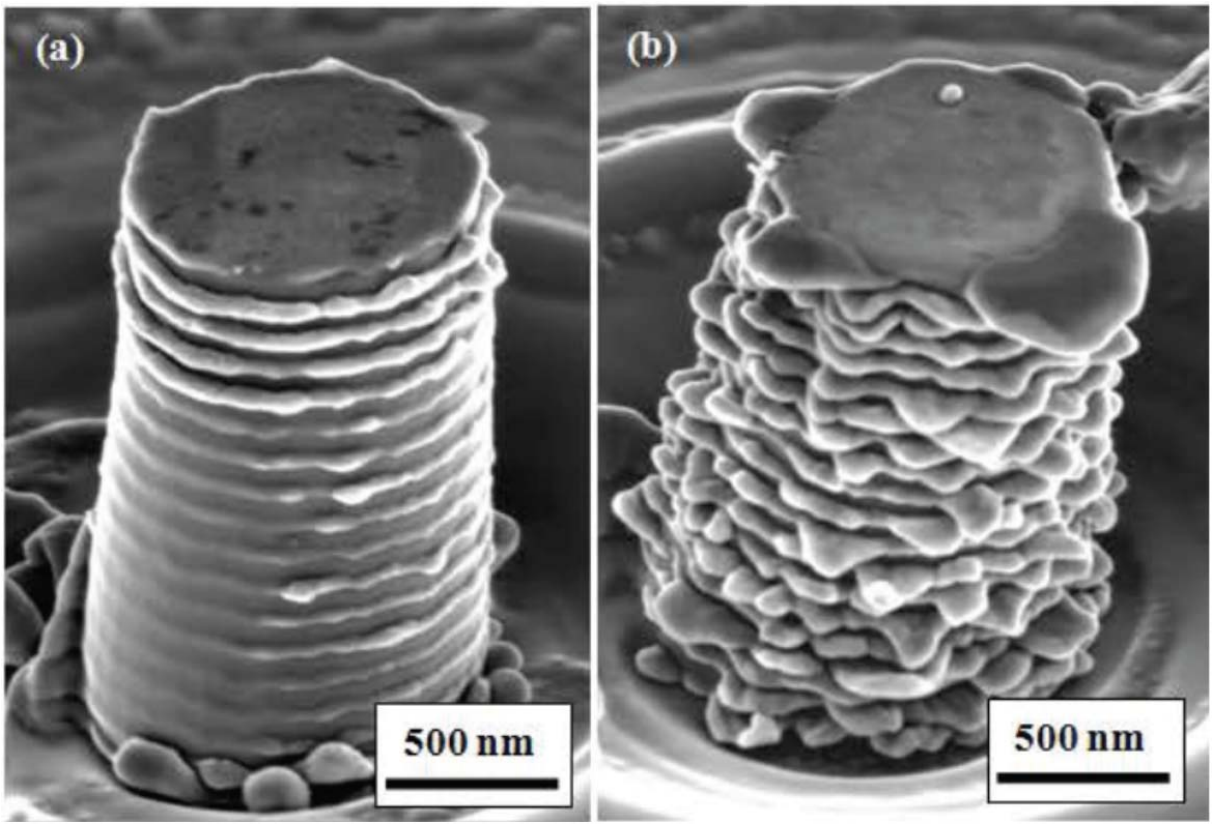

Figure 6-5: SEM micrograph of Al/SiC nanolaminate micropillars deformed up to a plastic strain of 8% at (a) 23ºC and (b) 100ºC.

TEM analysis of the deformed pillars, made by extracting thin foils through the center of the pillar using FIB, provided additional information about the different deformation micromechanisms. A bright-field (BF) image of the full pillar deformed at ambient temperature up to 8% strain is depicted in figure 6-6 (a). It shows that the plastic strain of the nanolaminate was accommodated by the plastic deformation of the Al layers. The strain was homogenously distributed along the different Al layers, except for the Al layer just at the micropillar base that showed extensive plastic deformation due to the stress concentration in this area.

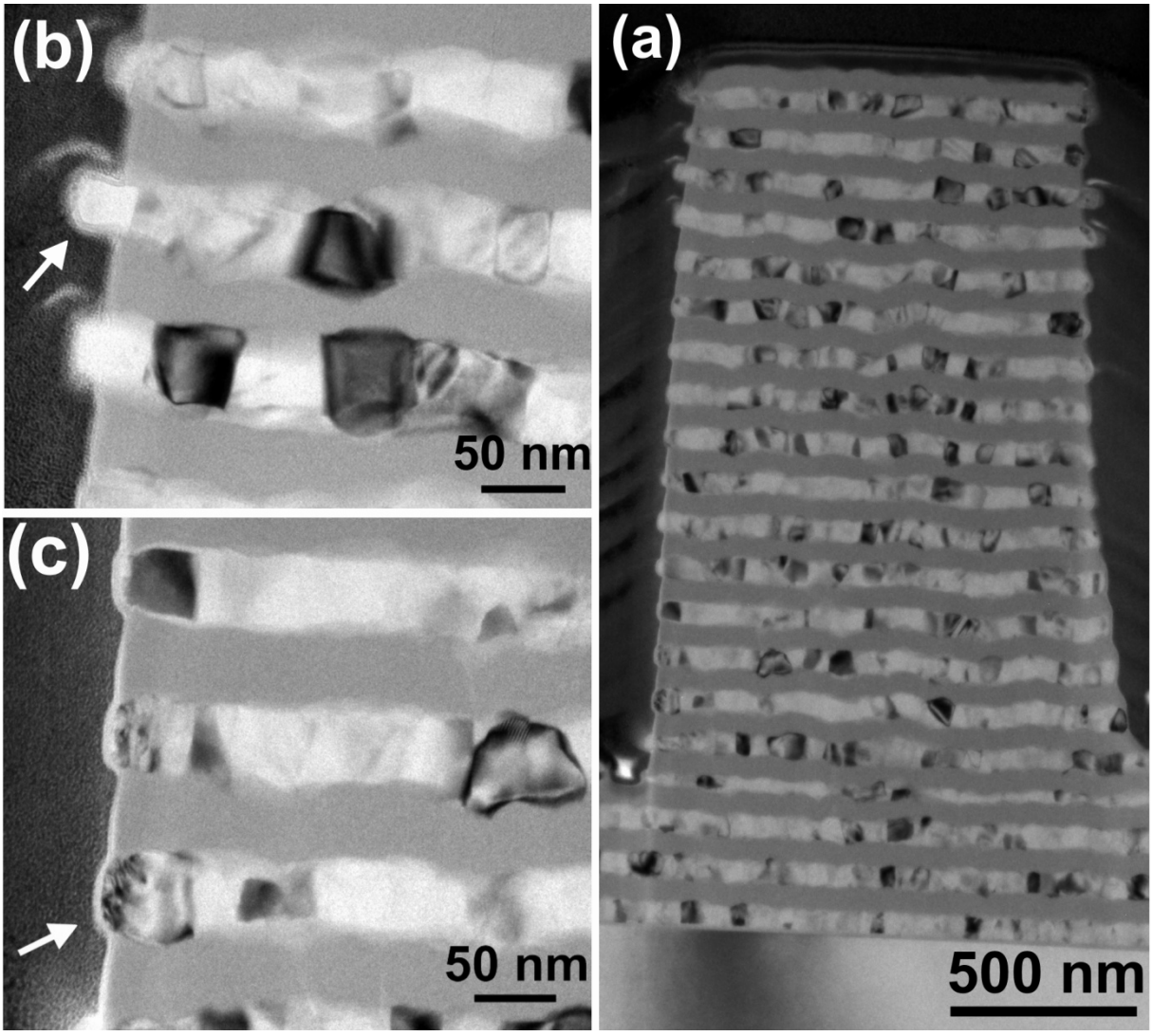

Figure 6-6: TEM images of Al/SiC nanolaminate micropillar deformed up to 8% at 23ºC. (a) Full view. (b) Detail of upper region of the micropillar. (c) Detail of the lower region of the micropillar.

As a result of plastic deformation, the Al grains were slightly elongated perpendicular to the compression axis as compared with as-deposited grains (figure 6-1), and some Al

was extruded out at the free surfaces. The Al extrusion was more predominant towards the top of the pillar where the stresses were higher as a result of the slight taper of this particular pillar, as can be seen in figure 6-6 (b). This image also shows one grain (see arrow) which has been extruded out of the multilayer indicating that interface sliding was also present during deformation. This result is in agreement with the lack of chemical bonding between Al and amorphous SiC, which should be able to accommodate sliding. It should be noted, however, that extrusion of Al at 23ºC was limited and most of the Al layers did not extrude out in the pillar deformed at room temperature, as shown in figure 6-6 (c).

It is not clear from the TEM images whether the deformation of the nanocrystalline Al layers at room temperature was diffusion or dislocation flow controlled. As a matter of fact, no dislocations could be found in the deformed Al layers, except for some dislocation pile-ups at the free surface of some layers, as pointed out by the white arrow in figure 6-6 (c). It is interesting to note that the only evidence of any dislocations was in these areas of no constraint from the brittle SiC layers. This is consistent with the work of Sun *et al*. [150] who showed no dislocations after indentation of Al/SiC nanolaminates at room temperature. It is possible that some dislocations could be annihilated at the numerous grain boundaries and Al/SiC interfaces after slip, although this does not explain the complete absence of dislocations in the Al layers. We can hypothesize that the fine grain size of the Al layers and the large degree of interfacial area would be conducive to interfacial and/or grain boundary diffusion at this temperature, contributing to a large degree of plastic flow in the Al layers.

The pillar deformed at 100ºC showed widespread extrusion of the Al layers at the free surfaces along the micropillar (figure 6-7). Plastic deformation was also homogenously distributed along all the Al layers, except for the bottom layer that underwent more extensive plastic deformation. No dislocations were found either at 100ºC but Al grain extrusion was prevalent along the surfaces of the micropillar, indicating that interface sliding was dominant at 100ºC, as compared with the behavior at 23ºC.

It is important to point out that this change in the interface sliding behavior was not due to any chemical reactions at the Al/SiC interface. The interfaces between the crystalline Al and the amorphous SiC layers remained clean of any reaction products after testing at 100ºC, as shown in the high resolution TEM image of Figure 6-8.

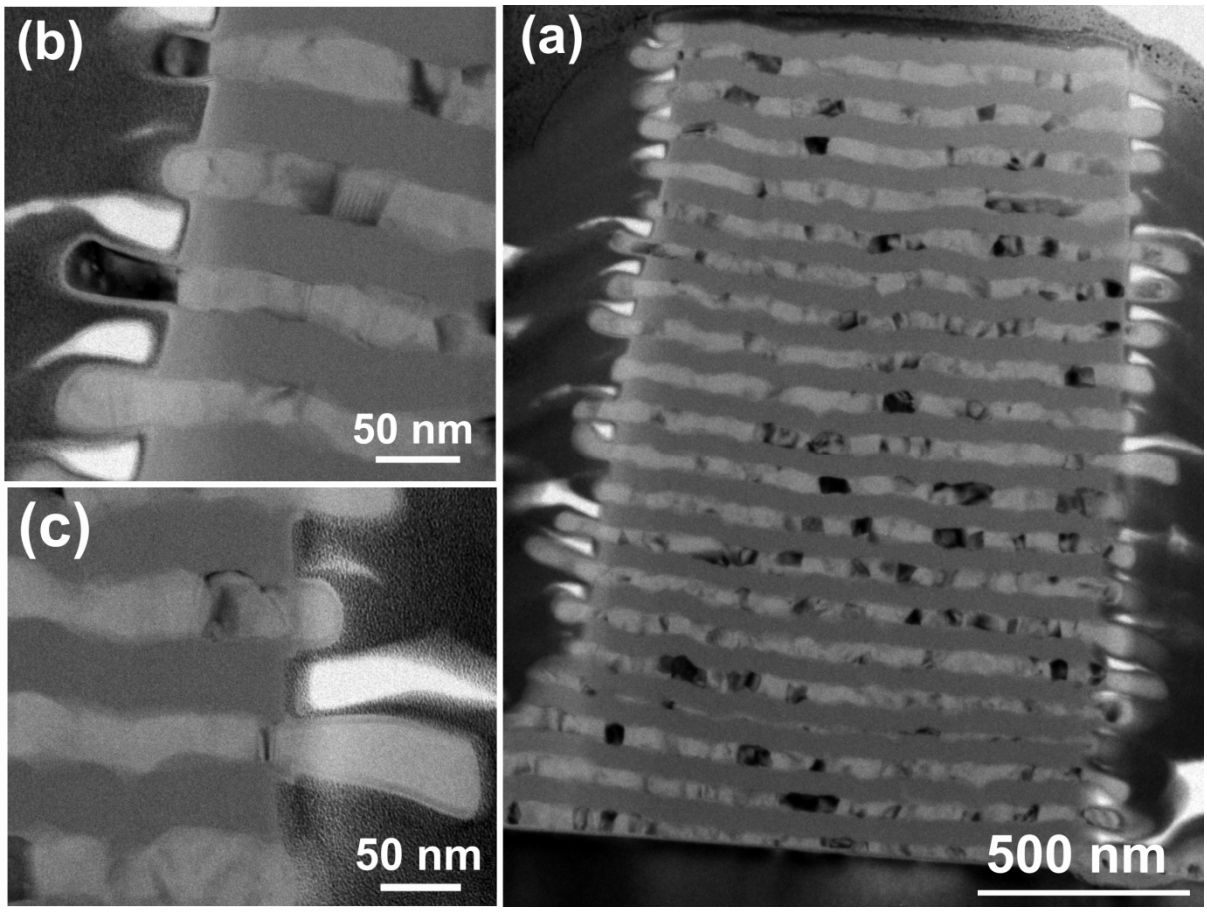

Figure 6-7: TEM images of Al/SiC nanolaminate micropillar deformed up to 8% at 100ºC. (a) Full view. (b) and (c) Details of lateral surface showing extrusion of the Al grains out of the micropillar.

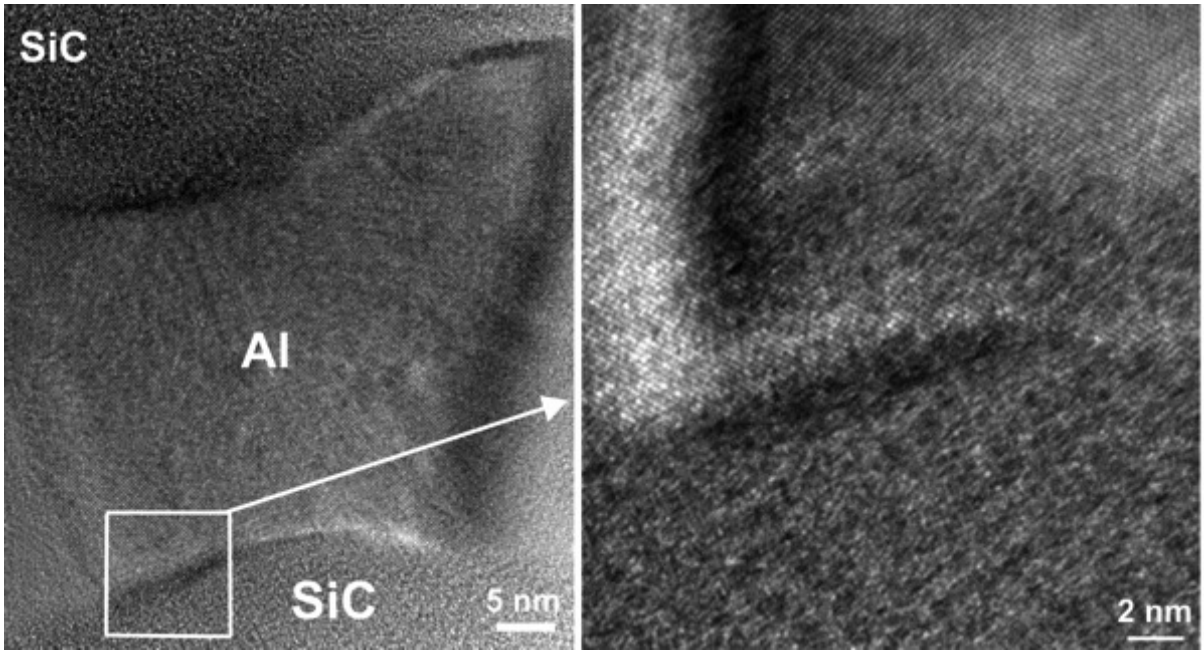

Figure 6-8: High resolution TEM image of the Al/SiC interface after micropillar compression at 100ºC. The interface is clean of any chemical reaction products.

In summary, micropillar compression tests of the Al/SiC nanolaminates showed a dramatic reduction in the strain hardening rate and in the flow stress from 23ºC to 100ºC, while the nanoindentation hardness was only reduced by 30% in this temperature range. It is obvious that the temperature increase will lead to some softening of the nanocrystalline Al layers, as shown by the nanoindentation experiments performed in monolithic Al thin-films (table 6-2), but this mechanism cannot explain the reduction in the strain hardening rate, nor the variation in the indentation constrain factor H/σ_f from ~ 1.6 at 23ºC to ~ 2.3 at 100ºC (table 6-1).

SEM and TEM analysis confirmed that the deformation of the Al/SiC micropillars was controlled by the plastic deformation of the nanocrystalline Al layers constrained by the elastic amorphous SiC layers. The TEM studies did not provide any evidence of dislocations in the Al layers. TEM analysis also demonstrated that interface sliding was limited at 23ºC and important at 100ºC. These observations, together with the changes in indentation constrain factor H/σ_f, suggest that changes in the elastic constrain of the Al flow by the SiC layers with temperature was also an important factor leading to the differences in the mechanical behavior between 23ºC and 100ºC. However, the role played by Al softening and interface sliding could not be quantified from the experimental observations. The numerical simulations presented in next chapter were aimed at clarifying this point.

7 Numerical simulation of micropillar compression

Finite element simulations of the micropillar compression tests were carried out to determine the influence of the Al flow stress and the interface properties (strength, friction coefficient) on the overall stress-strain response of the Al/SiC micropillars. The combination of micropillar compression experiments, TEM observations and numerical simulations were used to obtain a systematic and thorough understanding of the high temperature mechanical behavior of Al/SiC nanolaminates.

7.1. Geometrical model and materials properties

Numerical simulations of the micropillar compression test of Al/SiC nanolaminates were performed using the commercial finite element software Abaqus [151]. The simulations were not aimed at predicting the stress-strain behavior but at elucidating the influence of the flow stress of the Al layers and of the Al/SiC interface properties on the overall mechanical behavior of the micropillars under compression.

The geometrical model of the micropillar compression tests as well as the boundary conditions are depicted in figure 7-1. It consists of a cylindrical pillar with a length of 2 μm and radius of 0.5 μm (the dimensions of the experimental micropillars) and a circular flat punch. The pillar was composed of 30 alternative layers of Al and SiC with identical thickness. The bottom of the pillar was bonded to a semi-infinite elastic homogeneous medium with the effective properties of the Al/SiC nanolaminate to simulate accurately the testing conditions. The dimensions of the semi-infinite medium were large enough to avoid any effect of the boundary conditions on the simulated load-displacement curves. The flat punch was modeled as a rigid body assuming frictionless contact between the micropillar and the flat punch.

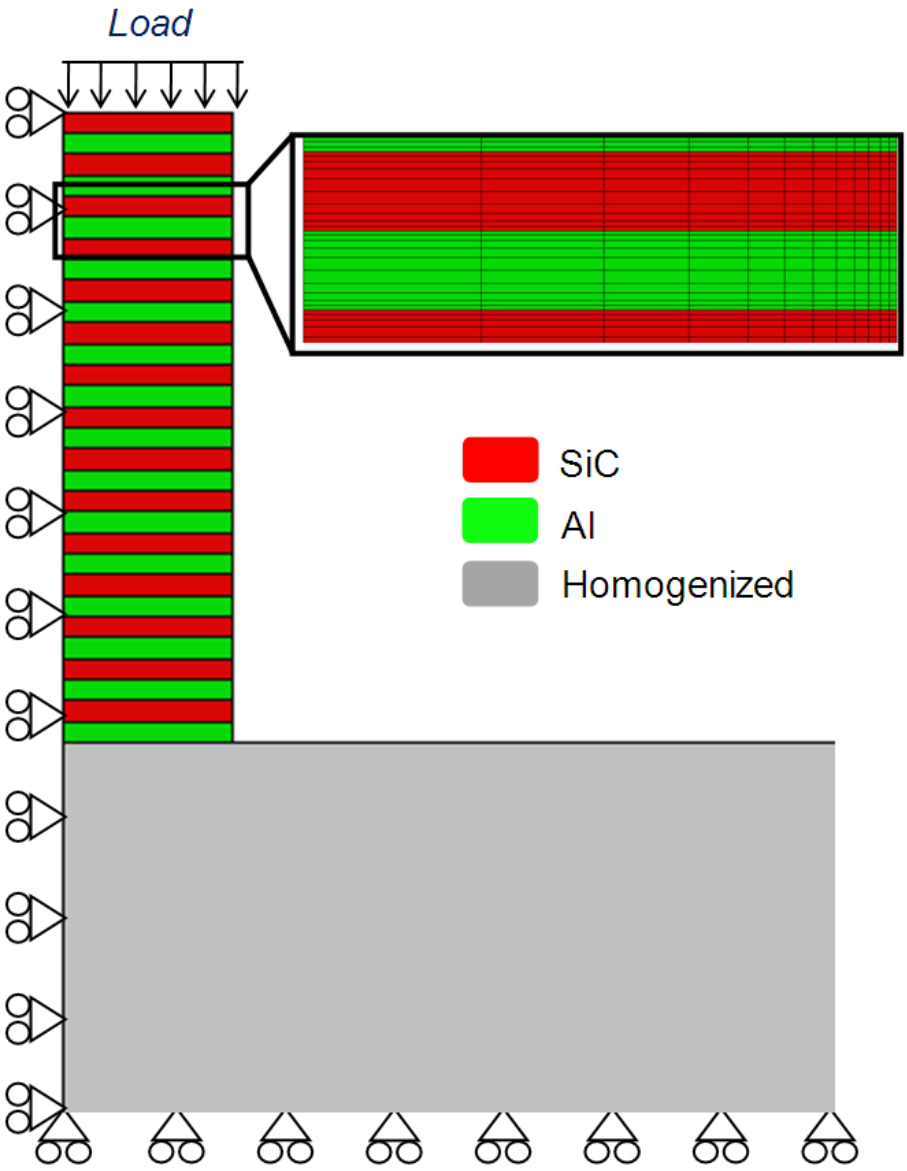

Figure 7-1: Axisymmetric finite element model of micropillar compression composed of 15 bilayers of Al/SiC with a total height of 2 μm and 1 μm in diameter.

Taking advantage of the axial symmetry, the model was meshed using two-dimensional four–node linear axisymmetric elements with reduced integration (CAX4R). 3600 elements were used to mesh the pillar and 14440 elements for the semi-infinite medium. The mesh was refined at the edges of the Al layers to capture accurately their extrusion during the compression test. Finally, cohesive surfaces were inserted between the Al and the SiC layers to account for the effects of interface fracture and sliding.

The model included three different bulk materials, namely SiC, Al and the homogenized nanolaminate, and the Al/SiC interface. The SiC layers were modeled as elastic isotropic solids with an elastic modulus of 300 GPa and a Poisson's ratio of 0.14. The Al layers were modeled as elastoplastic, isotropic solid following the Von Misses yield criterion. The elastic modulus and Poisson's ratio were, respectively, 88 GPa and 0.34. It was assumed that the strain hardening capacity of the Al layers was negligible due to their nanocrystalline structure and the small layer thickness. The homogenized elastic medium at the base of the pillar was assumed to be transversally isotropic and the five independent elastic constants, estimated from laminate theory, are found table 7-1 [132, 138].

Table 7-1: Elastic constants of the transversally isotropic homogenized medium. The direction 1 is perpendicular to the isotropy plane 23.

E_1 (GPa)	E_2 (GPa)	G_{12} (GPa)	ν_{12}	ν_{23}
114	185	60.3	0.24	0.21

To account for the effect of interface sliding, the Al-SiC interface was modeled phenomenologically as a cohesive crack. In this model, the total stress acting on the interface, $t = \sqrt{\langle t_n \rangle^2 + t_s^2}$, is related with the corresponding displacement jump $\delta = \sqrt{\langle \delta_n \rangle^2 + \delta_s^2}$, where t_n and t_s stand for, respectively, the normal and shear stresses transferred through cohesive crack while δ_n and δ_s are the corresponding normal and shear displacement jumps across the cohesive interface. The $\langle \quad \rangle$ symbol stands for the Macaulay brackets, which returns the argument, if positive, and zero otherwise because compressive normal stresses do not open the crack. The simplest constitutive equation for the cohesive crack is the bilinear model, figure 7-2. In the absence of damage, the interface behavior is linear with an initial stiffness, K (10^{12} GPa/m), which is a numerical parameter large enough to ensure the displacement continuity at the interface and to avoid any modification of the stress fields in the

absence of damage. The onset of damage is attained when the total stress acting on the interface reaches a critical value t^c given by a quadratic criterion according to:

$$\left\{\frac{\langle t_n \rangle}{t_n^c}\right\}^2 + \left\{\frac{t_s}{t_s^c}\right\}^2 = 1 \tag{7-1}$$

where t_n^c and t_s^c stand for, respectively, the normal and shear interface strength [152]. In the case of the micropillar compression test, the normal stresses are always compressive and thus $\langle t_n \rangle = 0$ and the actual value of t_n^c is not relevant. Shear stresses parallel to the interface developed as a result of the mismatch in the mechanical properties of the Al and SiC layers and interface damage occurred when $t_s = t_s^c = t^c$.

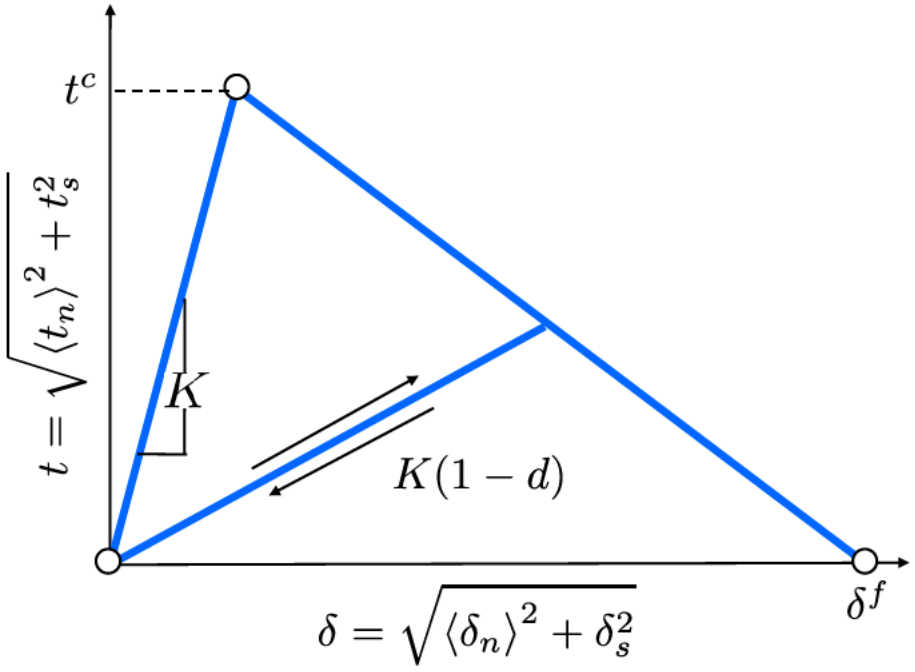

Figure 7-2: Constitutive equation for the cohesive interface crack under mixed-mode loading.

Once damage begins, the stress transferred through the interface and the interface stiffness are reduced depending on the interface damage parameter, d, which evolves from 0 (in the absence of damage) to 1 (no stresses transmitted across the interface). The evolution of d is controlled by the displacement jump across the interface, δ, the total stress acting at the interface at the onset of damage, t^c, and the interface fracture toughness $\Gamma = 0.5\, t^c\, \delta^f$ (the area under the curve), which is independent of the loading path in this model. Once the cohesive crack is completely broken, interface

sliding was opposed by Columbian friction, with a friction coefficient, μ, which together with the interface shear strength, t_s^c, and the interface toughness, Γ, determine the interface properties. More details about the cohesive crack model can be found elsewhere [98, 153, 154].

7.2. Numerical results

A parametric study was carried out using the model outlined in previous section to ascertain the influence of the Al yield stress σ_y (in the range 50-1000 MPa), and of the interface shear strength, t^c (between 0 and 1 GPa) and friction coefficient, μ (in the range 0 to 0.3) on the compressive stress-strain curve of the nanoscale multilayer. Nanocrystalline Al was assumed to have a negligible strain hardening capacity. Moreover, interface toughness was set to $\Gamma = 100$ J/m^2 in all cases, in good agreement with the available experimental data for this type of metal-ceramic interfaces [155].

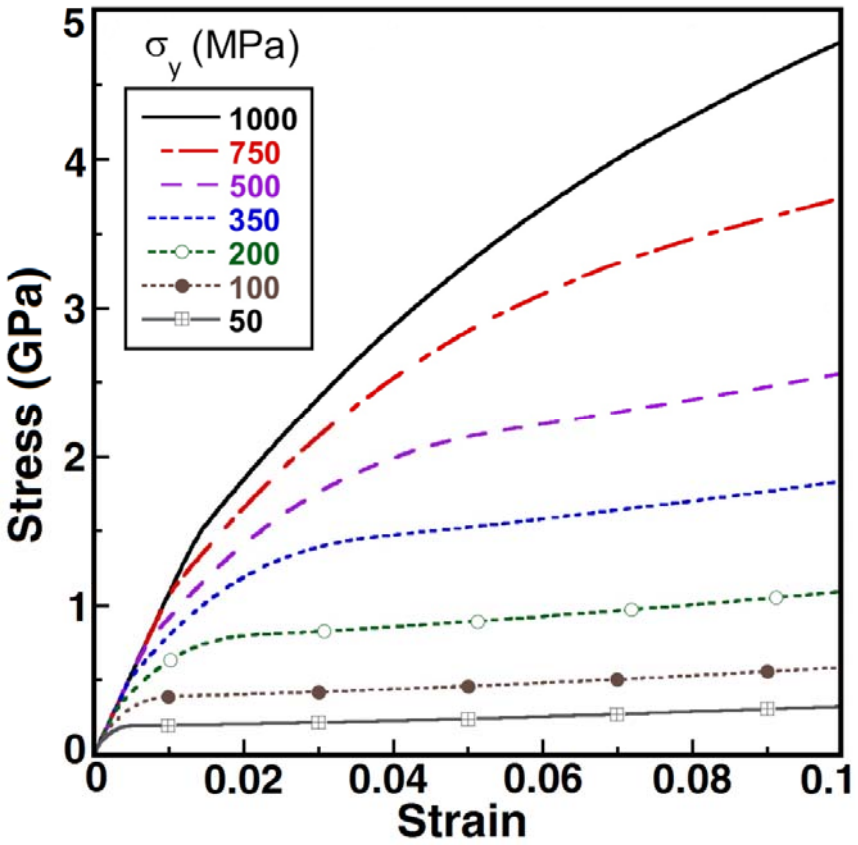

Figure 7-3: Simulation of micropillar compression: Effect of the Al yield stress σ_y for the case of a perfect interface.

The compressive stress-strain curves as a function of the Al yield stress σ_y are plotted in figure 7-3 in the case of a perfect interface between Al and SiC. The initial yield stress

of nanolaminate was proportional to the Al yield stress. After yielding, the micropillars showed a very substantial strain hardening capacity despite of the fact that Al flow stress was independent of the plastic strain. As a result, the compressive strength at 10% strain was approximately five times higher than the Al yield strength. This behavior comes about as a result of the elastic constrain imposed by the SiC layers on the plastic deformation of Al [156]. Constrain leads to the development of high compressive hydrostatic stresses, increasing the uniaxial applied stress required for yielding.

This is shown in figure 7-4, in which the contour plots of hydrostatic pressure are plotted as a function of the applied strain for the multilayer with σ_y = 350 MPa. They increased rapidly in the Al layers during the elasto-plastic transition (from 1.5% to 7.5% applied strain) and were maximum in the centre of the pillar. They were relieved at the free edges as a result of the extrusion of the Al out of the pillar, which took place in the absence of interface sliding.

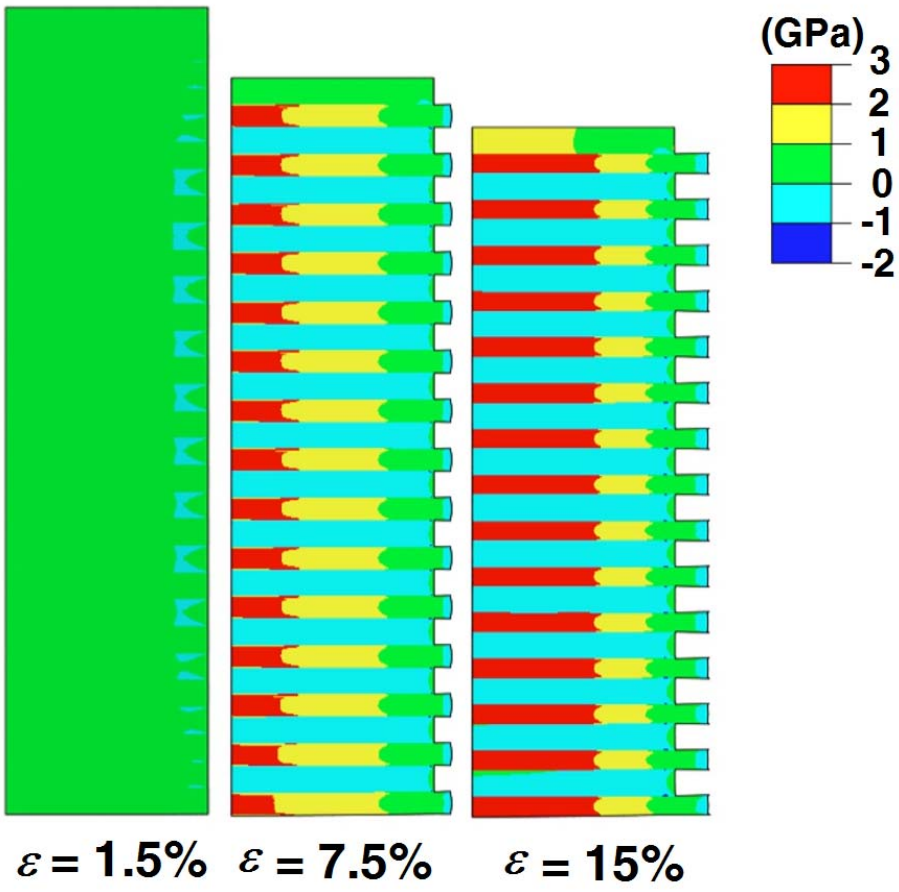

Figure 7-4: Contour plots of hydrostatic pressure as a function of the applied strain for nanolaminates with perfect interface.

The effect of the interface strength t^c on the compressive stress-strain curve is depicted in figure 7-5 assuming matrix yield strength of 350 MPa and a frictionless interface after fracture. Although the frictionless hypothesis is not realistic, it is useful to understand independently the effects of interface strength and friction. The curves are superposed until the shear stresses at the interface overcame the interface strength leading to free interface sliding in the absence of friction. As a result, no hydrostatic stresses were built-up in the Al layers during deformation after interface fracture and the strain hardening capability of the nanolaminate disappeared beyond this point. Thus, the nanolaminate strength depended on the interface shear strength which determined the critical strain for interface fracture. The influence of the elastic constrain on the mechanical behavior is readily appreciated in figure 7-5 if the curves of multilayers with different interface strength are compared with that of the material with a perfect interface.

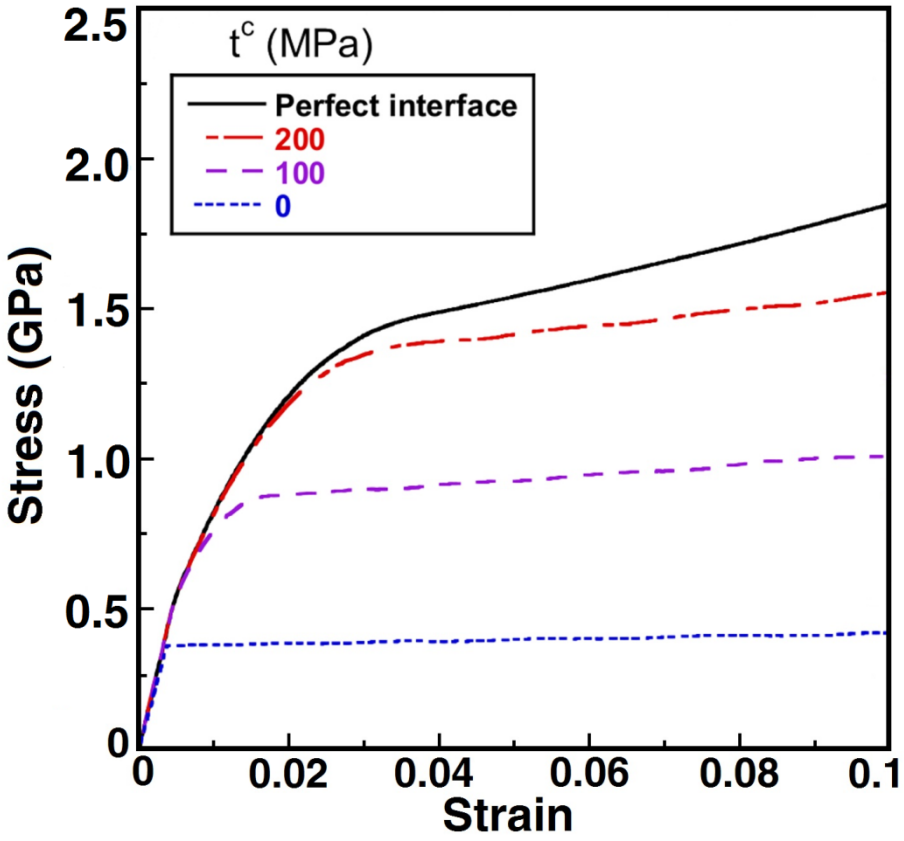

Figure 7-5: Simulation of micropillar compression: Effect of the interface strength t^c for σ_y=350 MPa and μ=0.

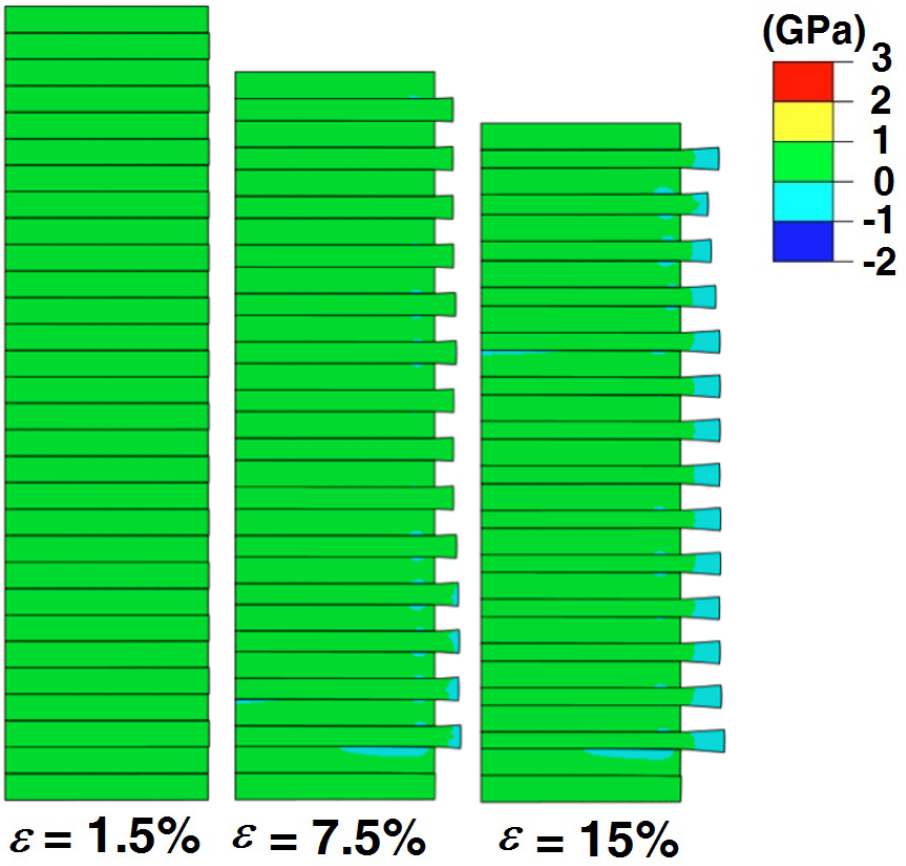

Figure 7-6: Contour plots of hydrostatic pressure as a function of the applied strain for nanoscale multilayers with Weak frictionless interface ($t^c = 0$ and $\mu = 0$).

In the limit of a very weak ($t^c = 0$) frictionless (μ = 0) interface, the constraint of the SiC layers was negligible (figure 7-6) and the Al/SiC micropillar would yield at the yield stress of Al without any strain hardening (figure 7-5).

Finally, the effect of the interface friction of the mechanical response is shown in figure 7-7 for an Al/SiC nanolaminate with Al yield strength of 450 MPa and a weak interface ($t^c = 0$). Even though the interface strength is negligible, the constraint imposed by frictional stresses on interface sliding leads to the build-up of hydrostatic stresses and to the development of strain hardening in the nanolaminate. It is worth noting that a friction coefficient above 0.25 induces a constrain equivalent to that of a perfect interface.

7.3. Comparison with experiments

The simulations above demonstrated that the compressive behavior of Al/SiC nanolaminate micropillars was controlled both by the yield stress of the Al layers (σ_y) and the interface properties (t^c, μ). Assuming a reasonable value of the interface

friction coefficient (μ =0.1-0.3), the simulations also show that the interface strength is not a critical parameter, since even for a very weak interface, sliding will be dominated by frictional forces.

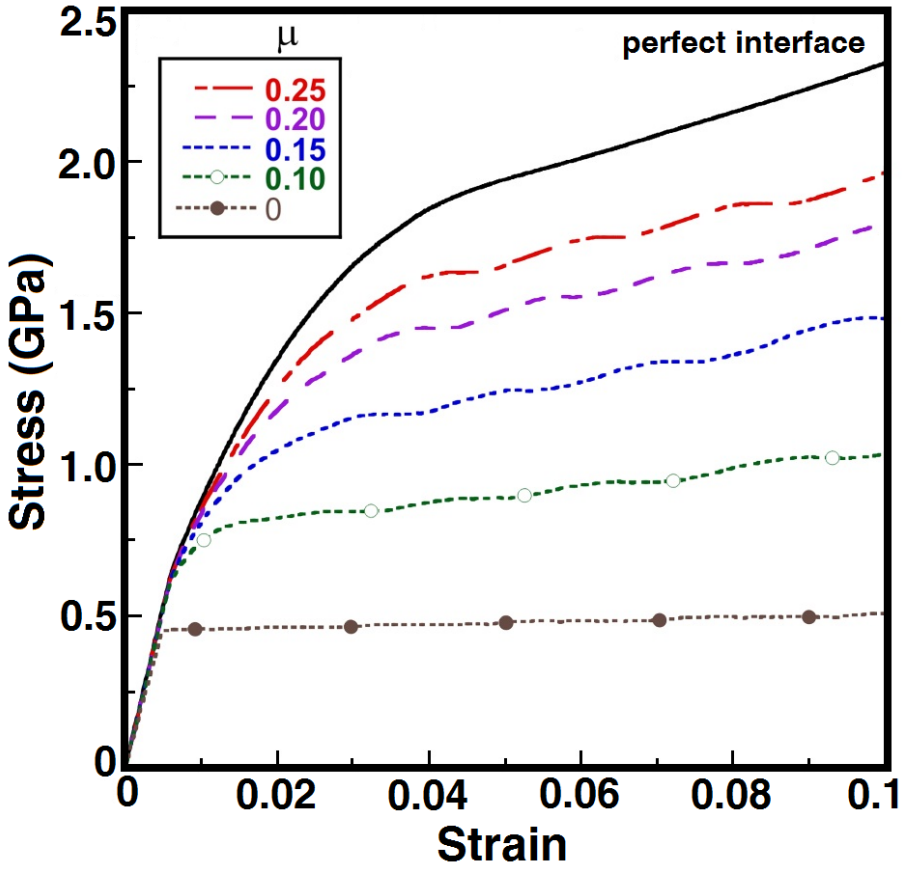

Figure 7-7: Simulation of micropillar compression: Effect of the interface friction μ for $\sigma_y = 450$ MPa and $t^c = 0$ MPa.

Interface sliding affects the constrain imposed by the SiC layers, which in turn determines the ratio of compressive strain required for plastic flow of the Al/SiC micropillar with respect to the Al yield stress, which ranges between 1 for a frictionless weak interface to 5 for a perfect interface. So, in modifying the interface properties, only the frictional coefficient will be taken into account. Therefore, the Al yield stress and the friction coefficient have to be chosen as a function of temperature in order to reproduce the experimental results. The experimental curves of figure 6-3 in previous chapter, clearly show that the strain hardening rate at 23ºC was much more pronounced than at 100ºC, indicating different levels of constrain and thus differences in the amount of interface sliding during deformation. This conclusion is supported by the limited interface sliding observed at 23ºC by TEM (figure 6-6), as opposed to the behavior found at 100ºC (figure 6-7).

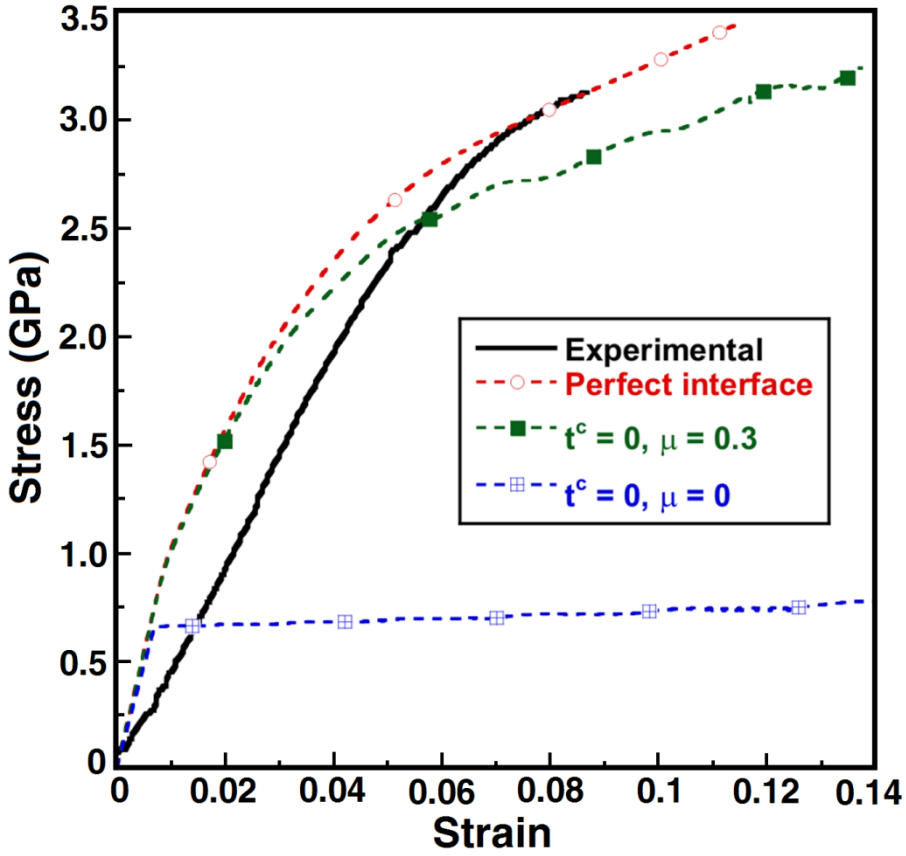

Figure 7-8: Comparison between experimental and numerical compressive stress-strain curves at 23ºC. The yield stress of Al was set to 650 MPa while the interface properties were varied considering either a perfect interface or a weak interface ($t^c = 0$) with a friction coefficient μ of 0 or 0.3.

Based on this information, and assuming a perfect interface at 23ºC (no sliding), a good correlation between experimental results and simulations at 23ºC could be obtained for $\sigma_y = 650$ MPa, as shown in figure 7-8, which also depicts simulation results for different friction coefficients (0.3 and 0). This value of the Al yield strength is reasonable for a 60 nm thick Al layer, considering that the yield stress of a 1 μm thick Al thin-film deposited in the same conditions should be of the order of 340 MPa, as estimated from its hardness of 910 MPa (table 6-2) and using $H \approx 2.8\,\sigma_y$. It is important to note that the differences in the elastic slope between experiments and simulations are due to the imperfect contact between the flat indenter and the micropillar at the beginning of the test (figure 6-4).

Regarding the results at 100 ºC, it is difficult to provide an accurate estimation of yield strength of the Al layers at this temperature. Assuming a perfect interface, the

experimental results were well fitted with $\sigma_y = 350$ MPa, which would imply a reduction of ≈ 50% with respect to the room temperature yield stress (figure 7-9).

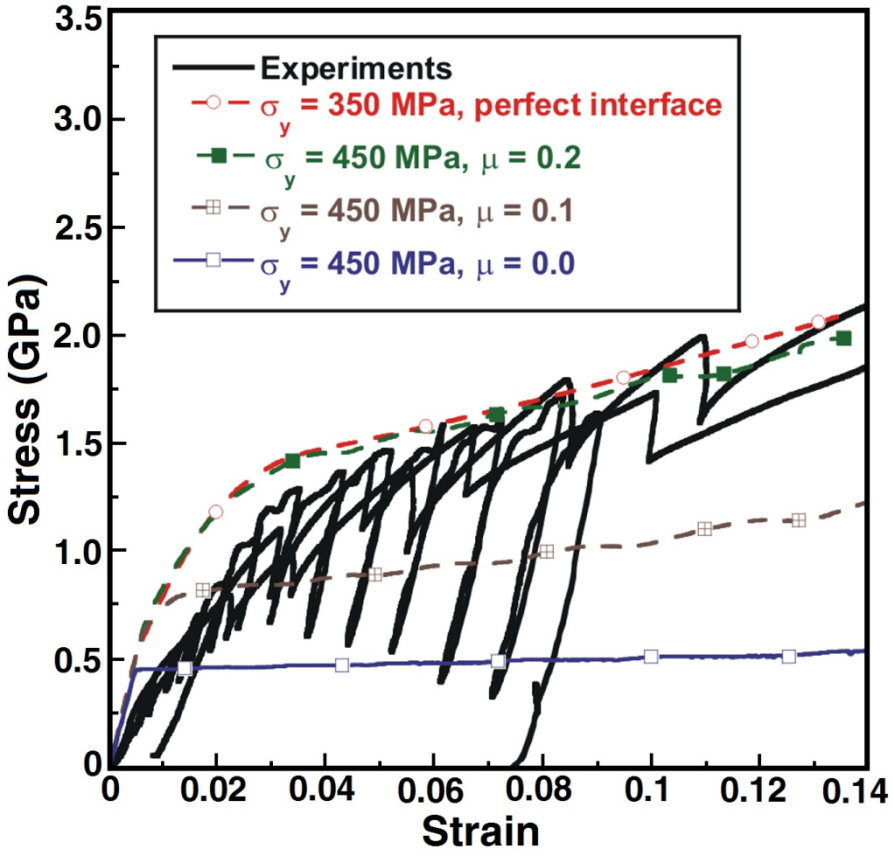

Figure 7-9: Comparison between experimental and numerical compressive stress-strain curves at 100ºC. The yield stress of Al was set to 350 MPa and a perfect interface or to 450 MPa with a weak interface ($t^c = 0$) and interface friction μ in the range 0 to 0.2.

The experimental TEM observations of extended interface sliding at 100ºC (figure 6-7) favored, however, the selection of an interface friction $\mu = 0.2$ in combination with $\sigma_y = 450$ MPa. This choice led to a very good fit of the experimental data and was compatible with the extended interface sliding observed experimentally. Moreover, it is interesting to note that the reduction in the yield stress of the Al layers of ≈ 30% at 100ºC is equivalent to the reduction in hardness determined for 1 μm thick Al thin-films, although this should not necessarily be the case for Al films of different thicknesses, and thus, different grain sizes (table 6-2). All in all, the large reduction in the flow stress and the strain hardening rate of Al/SiC nanolaminates from 23ºC to 100 ºC can be explained by a combination of two mechanisms: the drop in the yield stress of nanocrystalline Al together with easier interface sliding at the Al/SiC interfaces. This is likely to occur in

nanocrystalline Al as a result of the increased activation of dislocation climb and/or interface diffusion, as the homologous temperature was raised from 0.3 to 0.4.

Finally, it is worth noting that these combinations of changes in yield stress and interface friction can explain the discrepancy between the H/σ_y ratios between 23ºC and 100ºC. (table 6-1). The simulations showed that interface sliding was a controlling mechanism during micropillar compression and that Al was extruded out of the pillar due to the lack of constrain in the lateral surfaces. However, Al plastic flow during nanoindentation was constrained vertically by the SiC layers and laterally by the surrounding undeformed material. As a result, interface sliding contributes to a lesser extent and the hardness of Al/SiC at 100ºC was reduced by the same amount that the Al yield stress, *i.e.*, ≈ 30%. On the contrary, the flow stress during micropillar compression was reduced by ≈ 50% due to the additional effect of interface sliding leading to the unconstrained extrusion of Al at the free micropillar surfaces.

8 Concluding remarks

8.1. Summary of research findings

The work presented in this thesis can be summarized in three main blocks: the implementation of the optimum procedure to carry out nanomechanical testing at high temperature; the application of these methods to study the hardness of Al/SiC nanolaminates as a function of Al and SiC layer thickness; and a more throughout study of their deformation mechanisms by indentation creep, micropillar compression and numerical simulations. The main conclusions obtained in each block are summarized below:

Nanomechanical testing at high temperature

- The main challenges to carry out high temperature nanoindentation are thermal drift, environmental control and the sample-indentation tip interactions in the form of accelerated wear of the tip and tip contamination.
- Even though the use of passive tip heating can provide reliable results provided the testing time is low, active tip heating constitutes the only possible alternative to

carry out nanoindentation tests at elevated temperature for prolonged times (over minutes), without the drawbacks of thermal drift.

Thermomechanical behavior of Al/SiC nanolaminates

- Al/SiC multilayers grown by magnetron sputtering with individual layer thickness below 100 nm display amorphous SiC and nanocrystalline Al layers, with clean interfaces free of interfacial reaction products.
- The Al/SiC nanolaminates are thermally stable at temperatures up to 150ºC. Above 200ºC, thermal stability is impaired by chemical reactions between Al and SiC, leading to a dramatic drop in hardness and elastic modulus.
- The elastic modulus of the nanolaminates was in good agreement with the Reuss average (inverse rule-of-mixtures) of the constituents in the temperature range between 28ºC and 150ºC.
- The Al/SiC nanolaminates display very high room temperature hardness, between 3 and 10 GPa, mainly controlled by the volume fraction of the constituents and independent of the individual Al and SiC layer thicknesses, in the range between 10 and 100 nm.
- The hardness of all the nanolaminates decreased rapidly with temperature up to 150ºC, and the reduction in hardness increased as the layer thickness decreased (higher interface density) for nanolaminates with the same volume fraction of Al and SiC.
- The Al/SiC multilayers presented very high strain hardening rates at 23ºC, but the hardening rate decreased dramatically at 100ºC, as shown by micropillar compression.

Deformation mechanisms in Al/SiC nanolaminates

- The deformation of the Al/SiC nanolaminates at room temperature was controlled by the plastic deformation of the Al layers, constrained by the SiC layers, and the elastic bending of the SiC layers. At higher temperatures, loss of the SiC constrain has been observed, due to interface sliding, leading to marked reduction in strain hardening.
- The strain rate sensitivity and activation volume of the Al/SiC nanolaminates have also been determined in the temperature range between 28ºC and 150ºC. The strain rate sensitivity ranged between 0.04 and 0.15 and the activation volumes

between $1b^3$ and $15b^3$. These values agree well with those obtained in previous studies in nanocrystalline Al, indicating that deformation is controlled by interface-mediated dislocation flow in the Al layers, presumably due to the nucleation and annihilation of dislocations at grain boundaries and/or the Al-SiC interfaces.

- Indentation creep activation energies ranged between 112 and 314 kJ/mol, with the upper values associated with a higher SiC content. For a constant volume fraction, the activation energies were found to decrease with layer thickness, indicating a larger contribution from interface mediated plastic flow.
- Numerical simulations show that the compression of Al/SiC nanolaminates at room temperature is well explained by the plastic flow of the Al layers, constrained by the hard and stiff SiC layers. As a result of the constrain imposed by the SiC layers, the nanolaminates show a very large strain hardening rate, as a result of the build-up of hydrostatic stresses in the Al layers.
- The numerical simulations also suggest that that the constrain imposed by the SiC layers is reduced at high temperature, as a result of the onset of interface sliding at the Al-SiC interfaces. This is consistent with the increase in strain rate sensitivity and with the reduction in strain hardening with temperature.

8.2. Recommendations for future work

a) Even though the current Al/SiC nanolaminates were not prone to oxidation, it is highly recommended to establish the high temperature nanoindentation capability under high vacuum, instead of inside an environmental chamber. This will avoid potential oxidation problems at higher temperatures and/or in other materials, as found in this work for monolithic Al coatings.

b) Interface sliding was demonstrated to play a significant role in strength, strain hardening and creep resistance. The direct determination of interface strength and interface friction as a function of temperature is therefore recommended. The use of novel nanomechanical testing methods, such as testing the nanolaminates at different loading angles with respect to the layer orientation, would be of great interest.

c) Finally, the behavior of laminates under dynamic loading conditions such as fatigue remains to be investigated.

9 References

[1] A. Misra, H. Kung, D. Hammon, R. G. Hoagland, and M. Nastasi, "Damage Mechanisms in Nanolayered Metallic Composites," *International Journal of Damage Mechanics,* vol. 12, pp. 365-376, October 1, 2003 2003.

[2] A. Misra, M. Verdier, Y. C. Lu, H. Kung, T. E. Mitchell, M. Nastasi*, et al.*, "Structure and mechanical properties of Cu-X (X = Nb,Cr,Ni) nanolayered composites," *Scripta Materialia,* vol. 39, pp. 555-560, 1998.

[3] T. Foecke and D. E. Kramer, "In situ TEM observations of fracture in nanolaminated metallic thin films," *International Journal of Fracture,* vol. 119, pp. 351-357, 2003/01/01 2003.

[4] Y. C. Wang, A. Misra, and R. G. Hoagland, "Fatigue properties of nanoscale Cu/Nb multilayers," *Scripta Materialia,* vol. 54, pp. 1593-1598, 2006.

[5] A. Misra, M. F. Hundley, D. Hristova, H. Kung, T. E. Mitchell, M. Nastasi*, et al.*, "Electrical resistivity of sputtered Cu/Cr multilayered thin films," *Journal of Applied Physics,* vol. 85, pp. 302-309, 1999.

[6] A. Misra, X. Zhang, D. Hammon, and R. G. Hoagland, "Work hardening in rolled nanolayered metallic composites," *Acta Materialia,* vol. 53, pp. 221-226, 2005.

[7] J. McKeown, A. Misra, H. Kung, R. G. Hoagland, and M. Nastasi, "Microstructures and strength of nanoscale Cu-Ag multilayers," *Scripta Materialia,* vol. 46, pp. 593-598, Apr 2002.

[8] W. H. Soe and R. Yamamoto, "Mechanical properties of ceramic multilayers: TiN/CrN, TiN/ZrN, and TiN/TaN," *Materials Chemistry and Physics,* vol. 50, pp. 176-181, 1997.

[9] V. Teixeira, A. Monteiro, J. Duarte, and A. Portinha, "Deposition of composite and nanolaminate ceramic coatings by sputtering," *Vacuum,* vol. 67, pp. 477-483, 2002.

[10] L. Hultman, J. Bareño, A. Flink, H. Söderberg, K. Larsson, V. Petrova*, et al.*, "Interface structure in superhard TiN-SiN nanolaminates and nanocomposites: Film growth experiments and ab initio calculations," *Physical Review B,* vol. 75, p. 155437, 2007.

[11] Y. Long, F. Giuliani, S. J. Lloyd, J. Molina-Aldareguia, Z. H. Barber, and W. J. Clegg, "Deformation processes and the effects of microstructure in multilayered ceramics," *Composites Part B-Engineering,* vol. 37, pp. 542-549, 2006.

[12] J. M. Molina-aldareguia, S. J. Lloyd, M. Odén, T. Joelsson, L. Hultman, and W. J. Clegg, "Deformation structures under indentations in TiN/NbN single-crystal multilayers deposited by magnetron sputtering at different bombarding ion energies," *Philosophical Magazine A,* vol. 82, pp. 1983-1992, 2002/07/01 2002.

[13] X. Deng, C. Cleveland, N. Chawla, T. Karcher, M. Koopman, and K. K. Chawla, "Nanoindentation behavior of nanolayered metal-ceramic composites," *Journal of Materials Engineering and Performance,* vol. 14, pp. 417-423, 2005/08/01 2005.

[14] X. Deng, N. Chawla, K. K. Chawla, M. Koopman, and J. P. Chu, "Mechanical Behavior of Multilayered Nanoscale Metal-Ceramic Composites," *Advanced Engineering Materials,* vol. 7, pp. 1099-1108, 2005.

[15] R. M. Costescu, D. G. Cahill, F. H. Fabreguette, Z. A. Sechrist, and S. M. George, "Ultra-Low Thermal Conductivity in W/Al2O3 Nanolaminates," *Science,* vol. 303, pp. 989-990, February 13, 2004 2004.

[16] Y. Wang, J. Li, A. V. Hamza, and T. W. Barbee, "Ductile crystalline–amorphous nanolaminates," *Proceedings of the National Academy of Sciences,* vol. 104, pp. 11155-11160, July 3, 2007 2007.

[17] N. Chawla, D. R. P. Singh, Y. L. Shen, G. Tang, and K. K. Chawla, "Indentation mechanics and fracture behavior of metal/ceramic nanolaminate composites," *Journal of Materials Science,* vol. 43, pp. 4383-4390, 2008/07/01 2008.

[18] R. Banerjee, G. B. Thompson, P. M. Anderson, and H. L. Fraser, "Sputter deposited nanocrystalline Ni-25Al alloy thin films and Ni/Ni3Al multilayers," *Thin Solid Films,* vol. 424, pp. 93-98, 2003.

[19] S. PalDey and S. C. Deevi, "Single layer and multilayer wear resistant coatings of (Ti,Al)N: a review," *Materials Science and Engineering a-Structural Materials Properties Microstructure and Processing,* vol. 342, pp. 58-79, Feb 2003.

[20] N. J. M. Carvalho and J. T. M. De Hosson, "Deformation mechanisms in TiN/(Ti,Al)N multilayers under depth-sensing indentation," *Acta Materialia,* vol. 54, pp. 1857-1862, 2006.

[21] T. W. Barbee, Jr., "Nano-laminates: a new class of materials for aerospace applications," in *Aerospace Conference, 2003. Proceedings. 2003 IEEE*, 2003, pp. 4_1745-4_1754.

[22] M. T. Bohr, "Interconnect scaling - The real limiter to high performance ULSI," *Solid State Technology,* vol. 39, pp. 105-&, Sep 1996.

[23] A. Kajita, T. Usui, M. Yamada, E. Ogawa, T. Katata, A. Sakata*, et al.*, "Highly reliable Cu/low-k dual-damascene interconnect technology with hybrid (PAE/SiOC) dielectrics for 65 nm-node high performance eDRAM," in *Interconnect Technology Conference, 2003. Proceedings of the IEEE 2003 International*, 2003, pp. 9-11.

[24] I. A. Blech, "Electromigration in thin aluminum films on titanium nitride," *Journal of Applied Physics,* vol. 47, pp. 1203-1208, 1976.

[25] F. Bensebaa, D. Di Domenicantonio, L. Scoles, D. Kingston, P. Mercier, and G. Marshall, "Alternative coating technologies for metal–ceramic nanocomposite films: potential application for solar thermal absorber," *International Journal of Low-Carbon Technologies,* March 26, 2014 2014.

[26] T. Wang, X. H. Wang, T. H. Song, and L. T. Li, "Microstructures and dielectric characteristics of ultrafine-grained barium titanate-based ceramics for base-metal-electrode multilayer ceramic capacitors applications," *Japanese Journal of Applied Physics Part 1-Regular Papers Brief Communications & Review Papers,* vol. 46, pp. 6751-6754, Oct 2007.

[27] J. Bernard, D. Houivet, J. M. Haussonne, M. Pollet, F. Roulland, and S. Marinel, "Type I base-metal electrode multilayer ceramic capacitors," in *Developments in Dielectric Materials and Electronic Devices*. vol. 167, K. M. Nair, R. Guo, A. S. Bhalla, S. I. Hirano, and D. Suvorov, Eds., ed Westerville: Amer Ceramic Soc, 2005, pp. 291-310.

[28] H. Kishi, Y. Mizuno, and H. Chazono, "Base-metal electrode-multilayer ceramic capacitors: Past, present and future perspectives," *Japanese Journal of Applied Physics Part 1-Regular Papers Short Notes & Review Papers,* vol. 42, pp. 1-15, Jan 2003.

[29] N. A. Mara, D. Bhattacharyya, P. Dickerson, R. G. Hoagland, and A. Misra, "Deformability of ultrahigh strength 5 nm Cu/Nb nanolayered composites," *Applied Physics Letters,* vol. 92, Jun 9 2008.

[30] C. Reig, M. D. Cubells-Beltran, and D. R. Munoz, "Magnetic Field Sensors Based on Giant Magnetoresistance (GMR) Technology: Applications in Electrical Current Sensing," *Sensors,* vol. 9, pp. 7919-7942, Oct 2009.

[31] P. van Essen, R. Hoy, J. D. Kamming, A. P. Ehiasarian, and G. Janssen, "Scratch resistance and wear of CrNx coatings," *Surface & Coatings Technology,* vol. 200, pp. 3496-3502, Mar 2006.

[32] H. L. Aarshall, "Polarimetry with a soft X-ray spectrometer - art. no. 701129," in *Space Telescopes and Instrumentation 2008: Ultraviolet to Gamma Ray, Pts 1 and 2*. vol. 7011, M. J. L. Turner and K. A. Flanagan, Eds., ed Bellingham: Spie-Int Soc Optical Engineering, 2008, pp. 1129-1129.

[33] M. Henze, L. Bogdanic, K. Muehlbauer, and M. Schnieder, "Effect of the Biot Number on Metal Temperature of Thermal-Barrier-Coated Turbine Parts-Real Engine Measurements," *Journal of Turbomachinery-Transactions of the Asme,* vol. 135, p. 7, May 2013.

[34] M. Takahashi, J. Nakamura, F. Kirino, Y. Miyamura, N. Ohta, and R. Suzuki, "Magneto-optic disks for high-density recording with a shorter wavelength laser (abstract)," *Journal of Applied Physics,* vol. 69, p. 4773, 1991.

[35] N. Nomura, M. Abe, A. Kawamura, S. Fujinuma, A. Chiba, N. Masahashi*, et al.*, "Fabrication and mechanical properties of porous Co-Cr-Mo alloy compacts without Ni addition," *Materials Transactions,* vol. 47, pp. 283-286, Feb 2006.

[36] C.-S. Yang, C.-M. Chang, P.-H. Chen, P. Yu, and C.-L. Pan, "Broadband terahertz conductivity and optical transmission of indium-tin-oxide (ITO) nanomaterials," *Optics Express,* vol. 21, pp. 16670-16682, 2013/07/15 2013.

[37] J.-X. Feng, Q. Li, X.-F. Lu, Y.-X. Tong, and G.-R. Li, "Flexible symmetrical planar supercapacitors based on multi-layered MnO2/Ni/graphite/paper electrodes with high-efficient electrochemical energy storage," *Journal of Materials Chemistry A,* vol. 2, pp. 2985-2992, 2014.

[38] M. P. Casaletto, S. Kaciulis, G. Mattogno, L. Pandolfi, G. Scavia, L. Dori*, et al.*, "Surface study of thin film gas sensors on a Si micro-machined substrate," *Applied Surface Science,* vol. 189, pp. 39-52, Apr 2002.

[39] G. Shi, Y. Hanlumyuang, Z. Liu, Y. Gong, W. Gao, B. Li*, et al.*, "Boron Nitride–Graphene Nanocapacitor and the Origins of Anomalous Size-Dependent Increase of Capacitance," *Nano Letters,* vol. 14, pp. 1739-1744, 2014/04/09 2014.

[40] T. Khoperia, "Electroless Deposition for New Challenges in Nanoelectronics and Microelectronics," in *Nanotechnology*. vol. 35, W. Mustain and E. Traversa, Eds., ed, 2011, pp. 1-10.

[41] T. Juhola, B. Kerzar, M. Mokhtari, and L. F. Eastman, "High performance chip to substrate interconnects utilizing embedded structure," in *Electronic Components and Technology Conference, 1999. 1999 Proceedings. 49th*, 1999, pp. 167-173.

[42] M. Uchic, P. Shade, and D. Dimiduk, "Micro-compression testing of fcc metals: A selected overview of experiments and simulations," *JOM,* vol. 61, pp. 36-41, 2009/03/01 2009.

[43] M. D. Uchic and D. M. Dimiduk, "A methodology to investigate size scale effects in crystalline plasticity using uniaxial compression testing," *Materials Science and Engineering: A,* vol. 400–401, pp. 268-278, 2005.

[44] M. D. Uchic, D. M. Dimiduk, R. Wheeler, P. A. Shade, and H. L. Fraser, "Application of micro-sample testing to study fundamental aspects of plastic flow," *Scripta Materialia,* vol. 54, pp. 759-764, 2006.

[45] M. D. Uchic, P. A. Shade, and D. M. Dimiduk, "Plasticity of Micrometer-Scale Single Crystals in Compression," *Annual Review of Materials Research,* vol. 39, pp. 361-386, 2009.

[46] P. Jonnard, K. Le Guen, M. H. Hu, J. M. André, E. Meltchakov, C. Hecquet*, et al.*, "Optical, chemical, and depth characterization of Al/SiC periodic multilayers," 2009, pp. 73600O-73600O-9.

[47] D. L. Windt and J. A. Bellotti, "Performance, structure, and stability of SiC/Al multilayer films for extreme ultraviolet applications," *Applied Optics,* vol. 48, pp. 4932-4941, 2009/09/10 2009.

[48] J. S. Koehler, "Attempt to Design a Strong Solid," *Physical Review B,* vol. 2, pp. 547-551, 1970.

[49] D. R. Lesuer, C. K. Syn, O. D. Sherby, J. Wadsworth, J. J. Lewandowski, and W. H. Hunt, "Mechanical behaviour of laminated metal composites," *International Materials Reviews,* vol. 41, pp. 169-197, 1996.

[50] A. Misra and R. G. Hoagland, "Plastic flow stability of metallic nanolaminate composites," *Journal of Materials Science,* vol. 42, pp. 1765-1771, 2007/03/01 2007.

[51] A. Misra, "Mechanical behavior of metallic nanolaminates," in *Nanostructure control of materials*, R. H. J. Hannink and A. J. Hill, Eds., ed: CRC Press, 2006, pp. 146-177.

[52] J. W. Matthews, "Defects in epitaxial multilayers. I. Misfit dislocations," *Journal of crystal growth,* vol. 27, pp. 118-125, 1974.

[53] J. W. Matthews, "Defects in epitaxial multilayers. II. Dislocation pile-ups, threading dislocations, slip lines and cracks," *Journal of crystal growth,* vol. 29, pp. 273-280, 1975.

[54] J. W. Matthews, "Defects in epitaxial multilayers. III. Preparation of almost perfect multilayers," *Journal of crystal growth,* vol. 32, pp. 265-273, 1976.

[55] N. Q. Vo, R. S. Averback, Y. Ashkenazy, P. Bellon, and J. Wang, "Forced chemical mixing at Cu-Nb interfaces under severe plastic deformation," *Journal of Materials Research,* vol. 27, pp. 1621-1630, 2012.

[56] G. M. Luo, H. W. Jiang, C. X. Liu, Z. H. Mai, W. Y. Lai, J. Wang*, et al.*, "Chemical intermixing at FeMn/Co interfaces," *Journal of Applied Physics,* vol. 91, pp. 150-152, 2002.

[57] A. Misra and H. Kung, "Deformation behavior of nanostructured metallic multilayers," *Advanced Engineering Materials,* vol. 3, pp. 217-222, Apr 2001.

[58] N. Li, J. Wang, A. Misra, and J. Y. Huang, "Direct observations of confined layer slip in Cu/Nb multilayers," *Microscopy and Microanalysis,* vol. 18, p. 1155, 2012.
[59] H. Huang and F. Spaepen, "Tensile testing of free-standing Cu, Ag and Al thin films and Ag/Cu multilayers," *Acta Materialia,* vol. 48, pp. 3261-3269, 2000.
[60] J. M. Molina-Aldareguia and S. J. Lloyd, "Multilayered Materials: A Palette for the Materials Artist," in *Advances in Nanoengineering*, A. G. Davies and J. M. T. Thompson, Eds., ed: Imperial College Press, 2007, pp. 55-79.
[61] F. Giuliani, A. Goruppa, S. J. Lloyd, D. Teer, and W. J. Clegg, "High Temperature Deformation of AlN/CrN Multilayers using Nanoindentation," *MRS Online Proceedings Library,* vol. 841, pp. null-null, 2004.
[62] U. Helmersson, S. Todorova, S. A. Barnett, J. E. Sundgren, L. C. Markert, and J. E. Greene, "Growth of single-crystal TiN/VN strained-layer superlattices with extremely high mechanical hardness," *Journal of Applied Physics,* vol. 62, pp. 481-484, 1987.
[63] H. C. Barshilia, M. S. Prakash, A. Jain, and K. S. Rajam, "Structure, hardness and thermal stability of TiAlN and nanolayered TiAlN/CrN multilayer films," *Vacuum,* vol. 77, pp. 169-179, 2005.
[64] C. A. Freyman and Y.-W. Chung, "Synthesis and characterization of hardness-enhanced multilayer oxide films for high-temperature applications," *Surface and Coatings Technology,* vol. 202, pp. 4702-4708, 2008.
[65] P. C. Yashar, S. A. Barnett, L. Hultman, and W. D. Sproul, "Deposition and mechanical properties of polycrystalline Y2O3/ZrO2 superlattices," *Journal of Materials Research,* vol. 14, pp. 3614-3622, 1999.
[66] X. Miao and B. Ben-Nissan, "Microstructure and properties of zirconia-alumina nanolaminate sol-gel coatings," *Journal of Materials Science,* vol. 35, pp. 497-502, 2000/01/01 2000.
[67] S. Zhang, "Toughening of hard nanostructural thin films: a critical review," *Surface & coatings technology,* vol. 198, pp. 2-8, 2005.
[68] D. E. Wolfe, J. Singh, and K. Narasimhan, "Synthesis of titanium carbide/chromium carbide multilayers by the co-evaporation of multiple ingots by electron beam physical vapor deposition," *Surface and Coatings Technology,* vol. 160, pp. 206-218, 10/22/ 2002.
[69] L. Chih-Ming, C. Yung-Yu, V. F. Valery, L. Wei-Cheng, R. Tommi, G. S. Debbie*, et al.*, "Surface acoustic wave devices on AlN/3C–SiC/Si multilayer structures," *Journal of Micromechanics and Microengineering,* vol. 23, p. 025019, 2013.
[70] J. W. Lim, J. J. Lee, H. Ahn, and K. T. Rie, "Mechanical properties of TiN/TiB2 multilayers deposited by plasma enhanced chemical vapor deposition," *Surface & Coatings Technology,* vol. 174, pp. 720-724, Sep-Oct 2003.
[71] M. Shinn, L. Hultman, and S. A. Barnett, "Growth, structure, and microhardness of epitaxial TiN/NbN superlattices," *Journal of Materials Research,* vol. 7, pp. 901-911, 1992.
[72] L. Hultman, "Synthesis, Structure, and Properties of Superhard Superlattice Coatings," in *Nanostructured Coatings*, A. Cavaleiro and J. T. M. D. Hosson, Eds., ed, 2006, pp. 539-554.
[73] T. S. Li, H. Li, and F. Pan, "Microstructure and nanoindentation hardness of Ti/TiN multilayered films," *Surface & Coatings Technology,* vol. 137, pp. 225-229, Mar 2001.
[74] J. Romero, J. Esteve, and A. Lousa, "Period dependence of hardness and microstructure on nanometric Cr/CrN multilayers," *Surface & Coatings Technology,* vol. 188, pp. 338-343, Nov-Dec 2004.
[75] G. Zhang, Z. Wu, M. Wang, X. Fan, J. Wang, and P. Yan, "Structure evolution and mechanical properties enhancement of Al/AlN multilayer," *Applied Surface Science,* vol. 253, pp. 8835-8840, 2007.
[76] Z. Wu, G. Zhang, M. Wang, X. Fan, P. Yan, and T. Xu, "Structure and mechanical properties of Al/AlN multilayer with different AlN layer thickness," *Applied Surface Science,* vol. 253, pp. 2733-2738, 2006.
[77] G. Abadias, A. Michel, C. Tromas, C. Jaouen, and S. N. Dub, "Stress, interfacial effects and mechanical properties of nanoscale multilayered coatings," *Surface and Coatings Technology,* vol. 202, pp. 844-853, 12/15/ 2007.
[78] Y. M. Wang, K. Wang, D. Pan, K. Lu, K. J. Hemker, and E. Ma, "Microsample tensile testing of nanocrystalline copper," *Scripta Materialia,* vol. 48, pp. 1581-1586, Jun 2003.

[79] N. Mara, A. Sergueeva, A. Misra, and A. K. Mukherjee, "Structure and high-temperature mechanical behavior relationship in nano-scaled multilayered materials," *Scripta Materialia,* vol. 50, pp. 803-806, 3// 2004.
[80] N. A. Mara, A. Misra, R. G. Hoagland, A. V. Sergueeva, T. Tamayo, P. Dickerson*, et al.*, "High-temperature mechanical behavior/microstructure correlation of Cu/Nb nanoscale multilayers," *Materials Science and Engineering: A,* vol. 493, pp. 274-282, 2008.
[81] M. A. Monclús, S. J. Zheng, J. R. Mayeur, I. J. Beyerlein, N. A. Mara, T. Polcar*, et al.*, "Optimum high temperature strength of two-dimensional nanocomposites," *APL Materials,* vol. 1, pp. -, 2013.
[82] K. K. Schuegraf, *Handbook of thin film deposition processes and techniques :principles, methods, equipment and applications*: Noyes Publications, 1988.
[83] S. Lotfian, J. M. Molina-Aldareguia, K. E. Yazzie, J. Llorca, and N. Chawla, "High-temperature nanoindentation behavior of Al/SiC multilayers," *Philosophical Magazine Letters,* vol. 92, pp. 362-367, 2012 2012.
[84] S. Lotfian, M. Rodríguez, K. E. Yazzie, N. Chawla, J. Llorca, and J. M. Molina-Aldareguía, "High temperature micropillar compression of Al/SiC nanolaminates," *Acta Materialia,* vol. 61, pp. 4439-4451, 2013.
[85] D. R. P. Singh, N. Chawla, G. Tang, and Y. L. Shen, "Micropillar compression of Al/SiC nanolaminates," *Acta Materialia,* vol. 58, pp. 6628-6636, 2010.
[86] K. Gamo, "Nanofabrication by FIB," *Microelectronic Engineering,* vol. 32, pp. 159-171, 1996.
[87] J. Orloff, L. Swanson, and M. Utlaut, *High Resolution Focused Ion Beams: FIB and its Applications*: Springer, 2003.
[88] E. Martínez, E. Engel, C. López-Iglesias, C. A. Mills, J. A. Planell, and J. Samitier, "Focused ion beam/scanning electron microscopy characterization of cell behavior on polymer micro-/nanopatterned substrates: A study of cell–substrate interactions," *Micron,* vol. 39, pp. 111-116, 2008.
[89] R. K. Bansal, A. Kubis, R. Hull, and J. M. Fitz-Gerald, "High-resolution three-dimensional reconstruction: A combined scanning electron microscope and focused ion-beam approach," *Journal of Vacuum Science & Technology B: Microelectronics and Nanometer Structures,* vol. 24, pp. 554-561, 2006.
[90] J. Orloff, "High-resolution focused ion beams," *Review of Scientific Instruments,* vol. 64, p. 1105, 1993.
[91] M. J. Vasile, R. Nassar, and J. Xie, "Focused ion beam technology applied to microstructure fabrication," *Journal of Vacuum Science & Technology B: Microelectronics and Nanometer Structures,* vol. 16, pp. 2499-2505, 1998.
[92] N. Yao, *Focused Ion Beam Systems*: Cambridge University Press, 2007.
[93] J. Yu, J. Liu, J. Zhang, and J. Wu, "TEM investigation of FIB induced damages in preparation of metal material TEM specimens by FIB," *Materials Letters,* vol. 60, pp. 206-209, 2006.
[94] L. A. Giannuzzi and F. A. Stevie, "A review of focused ion beam milling techniques for TEM specimen preparation," *Micron,* vol. 30, pp. 197-204, 1999.
[95] M. W. Phaneuf, "Applications of focused ion beam microscopy to materials science specimens," *Micron,* vol. 30, pp. 277-288, 1999.
[96] S. Reyntjens and R. Puers, "A review of focused ion beam applications in microsystem technology," *Journal of Micromechanics and Microengineering,* vol. 11, pp. 287-300, Jul 2001.
[97] H. Bei, S. Shim, M. K. Miller, G. M. Pharr, and E. P. George, "Effects of focused ion beam milling on the nanomechanical behavior of a molybdenum-alloy single crystal," *Applied Physics Letters,* vol. 91, pp. 111915-111915-3, 2007.
[98] C. Motz, T. Schöberl, and R. Pippan, "Mechanical properties of micro-sized copper bending beams machined by the focused ion beam technique," *Acta Materialia,* vol. 53, pp. 4269-4279, 2005.
[99] M. D. Uchic, D. M. Dimiduk, J. N. Florando, and W. D. Nix, "Sample Dimensions Influence Strength and Crystal Plasticity," *Science,* vol. 305, pp. 986-989, August 13, 2004 2004.
[100] Hysitron. (2014, 21/04/2014). *Hysitron's Patented Three-Plate Transducer: An Overview*. Available: http://hysitron.com/resources/core-techniques/hysitrons-patented-transducer

[101] MicroStarTech. (2014, 21/04/2014). *Nano Indenters from Micro Star Technologies* Available: http://www.microstartech.com/
[102] W. C. Oliver and G. M. Pharr, "An improved technique for determining hardness and elastic modulus using load and displacement sensing indentation experiments," *Journal of Materials Research,* vol. 7, pp. 1564-1583, 1992.
[103] I. N. Sneddon, "The relation between load and penetration in the axisymmetric boussinesq problem for a punch of arbitrary profile," *International Journal of Engineering Science,* vol. 3, pp. 47-57, 1965.
[104] Y.-T. Cheng and C.-M. Cheng, "Scaling, dimensional analysis, and indentation measurements," *Materials Science and Engineering: R: Reports,* vol. 44, pp. 91-149, 2004.
[105] B. E. Schuster, Q. Wei, H. Zhang, and K. T. Ramesh, "Microcompression of nanocrystalline nickel," *Applied Physics Letters,* vol. 88, pp. 103112-103112-3, 2006.
[106] D. Kiener, C. Motz, and G. Dehm, "Dislocation-induced crystal rotations in micro-compressed single crystal copper columns," *Journal of Materials Science,* vol. 43, pp. 2503-2506, 2008/04/01 2008.
[107] J. R. Greer and W. D. Nix, "Size dependence of mechanical properties of gold at the sub-micron scale," *Applied Physics a-Materials Science & Processing,* vol. 80, pp. 1625-1629, May 2005.
[108] A. T. Jennings and J. R. Greer, "Tensile deformation of electroplated copper nanopillars," *Philosophical Magazine,* vol. 91, pp. 1108-1120, 2011/03/01 2010.
[109] L. A. Giannuzzi and F. A. Stevie, *Introduction to Focused Ion Beams: Instrumentation, Theory, Techniques and Practice*: Springer, 2005.
[110] J. Marien, J. M. Plitzko, R. Spolenak, R. M. Keller, and J. Mayer, "Quantitative electron spectroscopic imaging studies of microelectronic metallization layers," *Journal of Microscopy-Oxford,* vol. 194, pp. 71-78, Apr 1999.
[111] H. Zhang, B. E. Schuster, Q. Wei, and K. T. Ramesh, "The design of accurate micro-compression experiments," *Scripta Materialia,* vol. 54, pp. 181-186, 2006.
[112] Y. S. Choi, M. D. Uchic, T. A. Parthasarathy, and D. M. Dimiduk, "Numerical study on microcompression tests of anisotropic single crystals," *Scripta Materialia,* vol. 57, pp. 849-852, 2007.
[113] W. Fei and X. Kewei, "An investigation of nanoindentation creep in polycrystalline Cu thin film," *Materials Letters,* vol. 58, pp. 2345-2349, 2004.
[114] G. Feng and A. H. W. Ngan, "Creep and strain burst in indium and aluminium during nanoindentation," *Scripta Materialia,* vol. 45, pp. 971-976, 2001.
[115] R. Goodall and T. W. Clyne, "A critical appraisal of the extraction of creep parameters from nanoindentation data obtained at room temperature," *Acta Materialia,* vol. 54, pp. 5489-5499, 2006.
[116] W. B. Li, J. L. Henshall, R. M. Hooper, and K. E. Easterling, "The mechanisms of indentation creep," *Acta Metallurgica et Materialia,* vol. 39, pp. 3099-3110, 1991.
[117] B. N. Lucas and W. C. Oliver, "Indentation power-law creep of high-purity indium," *Metallurgical and Materials Transactions A,* vol. 30, pp. 601-610, 1999/03/01 1999.
[118] S. A. Syed Asif and J. B. Pethica, "Nanoindentation creep of single-crystal tungsten and gallium arsenide," *Philosophical Magazine A,* vol. 76, pp. 1105-1118, 1997/12/01 1997.
[119] C. L. Wang, Y. H. Lai, J. C. Huang, and T. G. Nieh, "Creep of nanocrystalline nickel: A direct comparison between uniaxial and nanoindentation creep," *Scripta Materialia,* vol. 62, pp. 175-178, 2010.
[120] C. L. Wang, M. Zhang, and T. G. Nieh, "Nanoindentation creep of nanocrystalline nickel at elevated temperatures," *Journal of Physics D: Applied Physics,* vol. 42, p. 115405, 2009.
[121] X. Li and B. Bhushan, "A review of nanoindentation continuous stiffness measurement technique and its applications," *Materials Characterization,* vol. 48, pp. 11-36, 2002.
[122] A. H. W. Ngan, H. T. Wang, B. Tang, and K. Y. Sze, "Correcting power-law viscoelastic effects in elastic modulus measurement using depth-sensing indentation," *International Journal of Solids and Structures,* vol. 42, pp. 1831-1846, 2005.
[123] J. Niu, J. Zhang, G. Liu, P. Zhang, S. Lei, G. Zhang, *et al.*, "Size-dependent deformation mechanisms and strain-rate sensitivity in nanostructured Cu/X (X= Cr, Zr) multilayer films," *Acta Materialia,* vol. 60, pp. 3677-3689, 2012.

[124] S. P. Wen, F. Zeng, Y. Gao, and F. Pan, "Indentation creep behavior of nano-scale Ag/Co multilayers," *Scripta Materialia,* vol. 55, pp. 187-190, Jul 2006.
[125] P. Huang, F. Wang, M. Xu, T. J. Lu, and K. W. Xu, "Strain rate sensitivity of unequal grained nano-multilayers," *Materials Science and Engineering: A,* vol. 528, pp. 5908-5913, 7/15/ 2011.
[126] J. S. Carpenter, A. Misra, M. D. Uchic, and P. M. Anderson, "Strain rate sensitivity and activation volume of Cu/Ni metallic multilayer thin films measured via micropillar compression," *Applied Physics Letters,* vol. 101, pp. -, 2012.
[127] J. C. Trenkle, C. E. Packard, and C. A. Schuh, "Hot nanoindentation in inert environments," *Review of Scientific Instruments,* vol. 81, pp. 073901-13, 2010.
[128] J. M. Wheeler, P. Brodard, and J. Michler, "Elevated temperature, in situ indentation with calibrated contact temperatures," *Philosophical Magazine,* vol. 92, pp. 3128-3141, 2012.
[129] C. A. Schuh, C. E. Packard, and A. C. Lund, "Nanoindentation and contact-mode imaging at high temperatures," *Journal of Materials Research,* vol. 21, pp. 725-736, 2006.
[130] J. Wheeler and J. Michler, "Invited Article: Indenter materials for high temperature nanoindentation," *Review of Scientific Instruments,* vol. 84, p. 101301, 2013.
[131] G. Dehm, T. J. Balk, H. Edongué, and E. Arzt, "Small-scale plasticity in thin Cu and Al films," *Microelectronic Engineering,* vol. 70, pp. 412-424, 2003.
[132] L. L. Snead, T. Nozawa, Y. Katoh, T.-S. Byun, S. Kondo, and D. A. Petti, "Handbook of SiC properties for fuel performance modeling," *Journal of Nuclear Materials,* vol. 371, pp. 329-377, 2007.
[133] D. R. P. Singh, N. Chawla, and Y. L. Shen, "Focused Ion Beam (FIB) tomography of nanoindentation damage in nanoscale metal/ceramic multilayers," *Materials Characterization,* vol. 61, pp. 481-488, Apr 2010.
[134] G. Tang, Y. L. Shen, D. R. P. Singh, and N. Chawla, "Indentation behavior of metal-ceramic multilayers at the nanoscale: Numerical analysis and experimental verification," *Acta Materialia,* vol. 58, pp. 2033-2044, Apr 2010.
[135] D. Bhattacharyya, N. A. Mara, P. Dickerson, R. G. Hoagland, and A. Misra, "A transmission electron microscopy study of the deformation behavior underneath nanoindents in nanoscale Al–TiN multilayered composites," *Philosophical Magazine,* vol. 90, pp. 1711-1724, 2010/05/07 2010.
[136] G. Tang, D. R. P. Singh, Y. L. Shen, and N. Chawla, "Elastic properties of metal–ceramic nanolaminates measured by nanoindentation," *Materials Science and Engineering: A,* vol. 502, pp. 79-84, 2009.
[137] I. Knorr, N. Cordero, E. T. Lilleodden, and C. A. Volkert, "Mechanical behavior of nanoscale Cu/PdSi multilayers," *Acta Materialia,* vol. 61, pp. 4984-4995, 2013.
[138] G. Dehm, "Miniaturized single-crystalline fcc metals deformed in tension: New insights in size-dependent plasticity," *Progress in Materials Science,* vol. 54, pp. 664-688, 2009.
[139] I. Dahan, N. Frage, and M. P. Dariel, "Structural evolution of Ti/TiC multilayers," *Journal of Applied Physics,* vol. 95, pp. 4662-4669, 2004.
[140] T. Sritharan, L. Chan, L. Tan, and N. Hung, "A feature of the reaction between Al and SiC particles in an MMC," *Materials characterization,* vol. 47, pp. 75-77, 2001.
[141] J. Wang, R. G. Hoagland, and A. Misra, "Room-temperature dislocation climb in metallic interfaces," *Applied Physics Letters,* vol. 94, p. 131910, 2009.
[142] R. W. Hayes, D. Witkin, F. Zhou, and E. J. Lavernia, "Deformation and activation volumes of cryomilled ultrafine-grained aluminum," *Acta Materialia,* vol. 52, pp. 4259-4271, 8/16/ 2004.
[143] S. L. Semiatin, K. V. Jata, M. D. Uchic, P. B. Berbon, D. E. Matejczyk, and C. C. Bampton, "Plastic flow and fracture behavior of an Al-Ti-Cu nanocomposite," *Scripta Materialia,* vol. 44, pp. 395-400, Mar 2001.
[144] A. J. Kalkman, A. H. Verbruggen, and S. Radelaar, "High-temperature tensile tests and activation volume measurement of free-standing submicron Al films," *Journal of Applied Physics,* vol. 92, pp. 6612-6615, 2002.
[145] H. Miyamoto, K. Ota, and T. Mimaki, "Viscous nature of deformation of ultra-fine grain aluminum processed by equal-channel angular pressing," *Scripta Materialia,* vol. 54, pp. 1721-1725, 5// 2006.

[146] S. M. Wiederhorn, B. Hockey, and J. French, "Mechanisms of deformation of silicon nitride and silicon carbide at high temperatures," *Journal of the European Ceramic Society,* vol. 19, pp. 2273-2284, 1999.
[147] R. Coble, "A model for boundary diffusion controlled creep in polycrystalline materials," *Journal of Applied Physics,* vol. 34, pp. 1679-1682, 1963.
[148] C. Xu, M. Kawasaki, and T. G. Langdon, "The high-temperature creep properties of materials processed using severe plastic deformation," *International Journal of Materials Research,* vol. 100, pp. 750-756, 2009.
[149] F. A. Mohamed and T. G. Langdon, "Deformation mechanism maps based on grain size," *Metallurgical transactions,* vol. 5, pp. 2339-2345, 1974.
[150] P. Sun, J. Chu, T. Lin, Y. Shen, and N. Chawla, "Characterization of nanoindentation damage in metal/ceramic multilayered films by transmission electron microscopy (TEM)," *Materials Science and Engineering: A,* vol. 527, pp. 2985-2992, 2010.
[151] Hibbit, Karlsson, and Sorensen, "Abaqus, Abaqus User's manual ", 6.10 ed, 2011.
[152] J. J. Williams, J. Segurado, J. Llorca, and N. Chawla, "Three dimensional (3D) microstructure-based modeling of interfacial decohesion in particle reinforced metal matrix composites," *Materials Science and Engineering: A,* vol. 557, pp. 113-118, 2012.
[153] L. P. Canal, C. González, J. Segurado, and J. Llorca, "Intraply fracture of fiber-reinforced composites: Microscopic mechanisms and modeling," *Composites Science and Technology,* vol. 72, pp. 1223-1232, 2012.
[154] L. P. Canal, J. Segurado, and J. Llorca, "Failure surface of epoxy-modified fiber-reinforced composites under transverse tension and out-of-plane shear," *International Journal of Solids and Structures,* vol. 46, pp. 2265-2274, 2009.
[155] B. J. Dalgleish, K. P. Trumble, and A. G. Evans, "The strength and fracture of alumina bonded with aluminum alloys," *Acta Metallurgica,* vol. 37, pp. 1923-1931, 1989.
[156] J. Llorca, A. Needleman, and S. Suresh, "An analysis of the effects of matrix void growth on deformation and ductility in metal-ceramic composites," *Acta Metallurgica et Materialia,* vol. 39, pp. 2317-2335, 1991.

10 Publications

❖ **Peer-Reviewed Journals**

- **S. Lotfian**, M. Rodríguez, K. E. Yazzie, N. Chawla, J. Llorca, and J. M. Molina-Aldareguía, "*High temperature micropillar compression of Al/SiC nanolaminates*," Acta Materialia, vol. 61, pp. 4439-4451, 2013.
- **S. Lotfian**, J. M. Molina-Aldareguia, K. E. Yazzie, J. Llorca, and N. Chawla, "*Mechanical Characterization of Lead-Free Sn-Ag-Cu Solder Joints by High-Temperature Nanoindentation*," Journal of Electronic Materials, vol. 42, pp. 1085-1091, 2013/03/05 2013.
- **S. Lotfian**, J. M. Molina-Aldareguia, K. E. Yazzie, J. Llorca, and N. Chawla, "*High-temperature nanoindentation behavior of Al/SiC multilayers*," Philosophical Magazine Letters, vol. 92, pp. 362-367, 2012/08/01 2012.
- **S Lotfian**, J Molina-Aldareguia, K Yazzie, J Llorca, A Misra, N Chawla, "*Mechanical Characterization of Nanolayered Al/SiC Composites by High Temperature Nanoindentation*," AIP Conference Proceedings. 2012.
- M.A. Monclus, **S. Lotfian**, J. M. Molina-Aldareguia, "*Tip shape effect on the hot indentation hardness and modulus of Al and SiC coatings*," International Journal of Precision Engineering and Manufacturing, Accepted.
- **S. Lotfian**, C. Mayer, N. Chawla, J. Llorca, A. Misra, and J. M. Molina-Aldareguia "*Effect of layer thickness on high temperature hardness of Al/SiC nanolaminates*," Thin Solid Films, Accepted.

❖ **Conferences**

➢ **Invited and Plenary Talk**

- C. Mayer, S. Lotfian, Nan Li, J.K. Baldwin, N. Chawla, N. Mara, A. Misra, J. Llorca, and J. Molina "*High Temperature Deformation Behaviour and modeling of Al/SiC Nanolaminates*," TMS Annual Meeting and Exhibition, San Diego, California, USA, February 16-20, 2014.
- S. Lotfian, J. Molina, C. Mayer, N. Chawla, J. Llorca, and A. Misra, "*High Temperature Mechanical Behaviour of Al/SiC Multilayers*," TMS Annual Meeting and Exhibition, San Diego, California, USA, February 16-20, 2014.
- S. Lotfian, J. Molina, M. Monclus, J. Llorca, C. Mayer, N. Chawla, I. Beyerlein, N. Mara, J. Mayeur, S. Zheng, and A. Misra " *High Temperature Mechanical Behaviour of Nanoscale Multilayers*," ECI Nanomechanical Testing in Materials Research and Development IV, Olhão, Faro, Portugal, October 6-13, 2013.
- S. Lotfian, J. Molina, J. Llorca, C. Mayer, N. Chawla, and A. Misra, "*High Temperature Mechanical Behaviour of Al/SiC Nanoscale Multilayers*," International Workshop On the Mechanical Behaviour of Nanoscale Multilayers, Madrid, Spain, October 1-4, 2013.
- S. Lotfian, J. Llorca, J. Molina, C. Mayer, N. Chawla, and A. Misra, "*Effect of Layer Thickness and Orientation on the Mechanical Response of Al/SiC Nanoscale Multilayers*," International Workshop On the Mechanical Behaviour of Nanoscale Multilayers, Madrid, Spain, October 1-4, 2013.
- S. Lotfian, J. Molina, K. E. Yazzie, H. Xie, C. Mayer, J. Llorca, J. K. Baldwin, A. Misra, and N. Chawla, " *High Temperature Mechanical Characterization and*

Modeling of Al/SiC Nanolaminates," 8th Pacific Rim International Congress on Advanced Materials and Processing (PRICM), Waikoloa, Hawaii, USA, August 4-9, 2013.

- S. Lotfian, M. Rodríguez, M. Monclus, J. Molina, and J. Llorca, "*Nanoscale metallic and metal-ceramic multilayers for radiation-resistant applications*," Trends in Nanotechnology (TNT), Madrid, Spain, Sept. 10-14, 2012.

➢ **Regular Contributions (Accepted as oral presentation)**

- S. Lotfian, M. Rodríguez, J. Molina, J. Llorca, C. Mayer, N. Chawla, and A. Misra, "*Effect of interface properties on the compressive behaviour of Al/SiC Nanolaminates at high Temperature*," EUROMAT2013, Seville, Spain, September 9-13, 2013.
- P. Frontini, S. Lotfian, M. Monclus, and J. Molina, "*Accounting for Drift Effects in High Temperature Nanoindentation of Glassy Polymers*," 13th International Congress of Science and Technology of Metallurgy and Materials, Pto. Iguazu, Argentina, August 20-23, 2013.
- S. Lotfian, J. Molina, M. Monclus, J. Llorca, N. Chawla, I. Beyerlein, and N. Mara, " *High Temperature Mechanical Behaviour of Nanoscale Multilayers*," TMS Annual Meeting and Exhibition, San Antonio, Texas, USA, March 3-7, 2013.
- S. Lotfian, J. Molina, K. E. Yazzie, J. Llorca, and N. Chawla, " *High Temperature Nanoindentation of Microstructural Constituents in a Sn-rich Pb-Free Solder*," TMS Annual Meeting and Exhibition, San Antonio, Texas, USA, March 3-7, 2013.
- S. Lotfian, J. Molina, K. E. Yazzie, H. Xie, J. Llorca, J. K. Baldwin, A. Misra, and N. Chawla, " *High Temperature Mechanical Characterization and Modeling of Al/SiC Nanolaminates*," TMS Annual Meeting and Exhibition, San Antonio, Texas, USA, March 3-7, 2013.
- M. Monclus, S. Lotfian, and J. Molina, "*High temperature mechanical properties of Al/SiC and Cu/Nb nanoscale multilayers*," 12th Micro Materials European Nanomechanical User Group Meeting, Valletta, Malta, October 24-25, 2012.
- J. Molina, M. Monclus, S. Lotfian, J. Llorca, K. E. Yazzie, N. Chawla, N. Mara, and I. Beyerlein, " *High Temperature Mechanical Behaviour of Nanoscale Multilayers*," 49th Annual Technical Meeting, Society of Engineering Science (SES), Atlanta, GA, USA, October 10-12, 2012.
- S. Lotfian, J. Molina, K. E. Yazzie, J. Llorca, and N. Chawla, " *High Temperature Nanoindentation Behavior of Al/SiC Nanoscale Multilayers*," 8 h European Solid Mechanics Conference (ESMC), Graz, Austria, July 9-13, 2012.
- S. Lotfian, J. Molina, K. E. Yazzie, J. Llorca, and N. Chawla, " *Mechanical Characterization of Pb-Free Solder and Sn-Based Intermetallics by High Temperature Nanoindentation*," IBEROMAT XII, Alicante, Spain, May 30-31 and June 1, 2012.
- S. Lotfian, M. Monclus, and J. Molina, "*Tip shape effect on the hot indentation hardness and modulus of Al and SiC*," Nanomechanical Testing Workshop, Nanobrücken II, Saarbrücken, Germany, March 20-22, 2012.
- S. Lotfian, J. Molina, K. E. Yazzie, J. Llorca, A. Misra, and N. Chawla, " *Mechanical Characterization of Nanolayered Al/SiC Composites by High Temperature Nanoindentation*," TMS Annual Meeting and Exhibition, Orlando, Florida, USA, March 11-15, 2012.

➢ **Poster**

- S. Lotfian, J. Molina, J. Llorca, C. Mayer, and N. Chawla " *Thermomechanical Behaviour of Lead-free Sn-Ag-Cu Solder Joints by Nanoindentation*," ECI Nanomechanical Testing in Materials Research and Development IV, Olhão, Faro, Portugal, October 6-13, 2013.